Spectroscopy and Photodissociation Dynamics of Diatomic Molecules

A thesis submitted to the University of Bristol in accordance with the requirement of the degree of Doctor of Philosophy in the School of Chemistry, Faculty of Science.

Martin James Cooper, September 1998.

Abstract

The Resonance Enhanced Multiphoton Ionisation Spectroscopy (REMPI) technique has been employed to investigate the Rydberg and ion pair states of ClO. High resolution REMPI spectra of the $C^2\Sigma^-$ Rydberg state was recorded. Analysis of the bands confirmed the previous assignment of the spectroscopic constants of the state. Spectra of the ClO radical following excitation in the wavelength range 276-261 nm, was obtained using both room temperature and rotationally cold samples. The 'cold' molecular beam spectra showed discrete rovibrational bands, with analysis of the rotational structure leading to the identification of excited levels of $^2\Pi$ symmetry resonant at the two photon energy (72200 - 76200 cm^{-1}). These were deduced to possess very extended equilibrium bond lengths ($R \sim 2.4$ Å), and thus were associated with one or more ion pair states. Full interpretation of the observed spectra was complicated by the effects of additional, wavelength dependent intensity enhancements due to predissociated levels of the $A^2\Pi$ state accidentally resonant at the energy of one absorbed photon.

Double Resonance Multiphoton Ionisation Spectroscopy was used to investigate Rydberg and ion pair states of S_2. The $B''^3\Pi_u$ valence state was used as an intermediate level in the double resonance process. Spectra of the radical were performed over the wavelength region 63400 - 71100 cm^{-1}. Analysis of the spectra resulted in extending the characterisation of the $^3\Delta_g$ Rydberg state (v = 3 - 10) with evidence of a second $^3\Sigma_g^+$ Rydberg state (v = 0 and 1). Spectra arising from ion pair states of the radical were also assigned. Spectroscopic constants were deduced for the $^5\Sigma_g^-$ (v=0 - 15), $^3\Pi_g$ (v=0 - 12) and $^3\Sigma_g^-$ (v=0 and 1) states. The magnitude of perturbation interactions between the various ion pair states were also calculated.

The technique of photofragment ion imaging was used to study the photodissociation of BrCl and Br_2 at various wavelengths in the range 235 - 580 nm. In both cases analysis of the photofragment images provided information on the spin orbit branching ratio in the atomic products, their mutual correlation and the anisotropy of the recoil velocity distribution as well as information on the roles of various excited states populated by the photoexcitation process. Over the wavelength region investigated BrCl dissociated to form Br + Cl, Br + Cl* and Br* + Cl, and Br_2 into Br + Br or Br + Br*. In both cases the images recorded were generally rationalised in terms of excitations to the states previously assigned as contributing to the UV/visible absorption spectrum, but with added interactions of these states with others as the molecule dissociated. In the case of Br_2 the branching ratios between the Br + Br* and Br + Br photodissociation channels were also calculated. The ratio was found to be ~3% Br + Br* at 435 nm increasing to ~79% at 500 nm. These values served to confirm and extend the previously reported measurements.

Authors Declaration

The work described in this thesis was carried out in the Department of Chemistry, University of Bristol between October 1995 and May 1998 under the supervision of Professor M.N.R. Ashfold. The work is original except where acknowledgement to other work is made and it has not been submitted for any other degree.

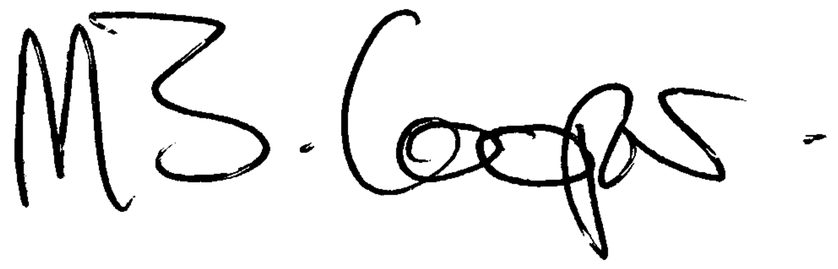

Martin J. Cooper, September 1998.

Acknowledgements

I would like to take this opportunity to thank everyone who has helped in this work:

Prof. Mike Ashfold, and Dr's Colín Western and Andrew Orr-Ewing for all their help, advice, motivation, enthusiasm, dedication, and patience over the past three years.

To Mum, Dad and Helen, for their constant support emotionally and financially.

To everyone who I worked with on the various experiments over the three years, Trinidad, Eckart, and Leon, and to Keith Rosser for helping to maintain the experiments and keep them running.

To Dr. Jeff Hudgens for allowing me to go and work him at the NIST laboratories in the USA (twice!).

To the NERC for funding my research, and to NATO for the money to go to the USA.

And finally to all my friends - Mat, Charles, Kirsty, Jon, Paul, Steve R., Rob, Stu, Steve L., Wendy, Alex, Neil, Phill, John, Ian, Martyn, Chris, Claire, and many others. You have all made my time in Bristol unforgettable.

"If we knew what it was we were doing, it would not be called research, would it?"

Albert Einstein.

Table of Contents

	Page
Chapter 1: Introduction	**1**
1.1 Introduction	2
1.2 Resonance Enhanced Multiphoton Ionisation (REMPI)	2
1.3 Double Resonance Multiphoton Ionisation	8
1.4 Rydberg and Ion Pair States	12
1.4.1 Rydberg States	12
1.4.2 Ion Pair States	14
1.4.3 Ion Pair States of I_2	16
1.5 Photofragment Ion Imaging	18
1.5.1 Experimental Overview	18
1.5.2 Analysis of the Collected Image	19
1.5.3 Ion Imaging of Methane	23
1.6 Thesis Overview	26
1.7 References	27
Chapter 2: Experimental	**29**
2.1 REMPI and Double Resonance Experiments in Bristol	30
2.1.1 Radical Generation	32
2.1.2 Light Generation	33
2.1.3 Time-of-Flight Mass Spectrometer	33
2.1.4 Data Collection and Calibration	35
2.2 REMPI Experiment at NIST	37
2.3 Ion Imaging Experiment at Bristol	39
2.3.1 Light Generation	39
2.3.1.1 OPO Laser System	41
2.3.2 Time-of-Flight Mass Spectrometer	43
2.3.3 Data Collection and Analysis	47
2.3.4 Ultraviolet/Visible Absorption Spectra	47
2.4 References	49

Chapter 3: Resonance Enhanced Multiphoton ionisation of ClO **50**

3.1 Introduction 51

3.2 Experimental 55

3.3 Results and Disscussion 56

3.3.1 2+1 REMPI of the $C^2\Sigma^-$ Rydberg State 56

3.3.2 Ion Pair States of ClO 57

3.3.3 Higher Rydberg States of ClO 68

3.4 Conclusions 69

3.5 References 71

Chapter 4: Double Resonance Multiphoton Ionisation of S_2 **73**

4.1 Introduction 74

4.2 Experimental 79

4.3 The $(3d\pi)^3\Delta_g$ Rydberg State 80

4.4 Ion Pair States 85

4.4.1 Ion Pair State Theory 85

4.4.2 Ion Pair State Spectra 89

4.4.2.1 The Isolated State Model 90

4.4.2.2 Deperturbation Analysis 102

4.5 Ionisation Threshold of S_2 via the $^5\Sigma_g^-$ State 112

4.6 Conclusions 115

4.7 References 116

Chapter 5: Photofragment Ion Imaging of Br_2 **118**

5.1 Introduction 119

5.2 Experimental 125

5.3 Results 126

5.4 Discussion 136

5.4.1 Slow Recoil Model 136

5.4.2 Predissociation Effects 138

5.4.3 Excited State Mixing 140

5.4.4 $\lambda > 510$ nm 142
5.4.5 $420 < \lambda < 510$ nm 143
5.4.6 $\lambda < 420$ nm 146
5.4.7 $\lambda = 260.662$ nm 146
5.5 Conclusions 148
5.6 References 149

Chapter 6: Photofragment Ion Imaging of BrCl **151**
6.1 Introduction 152
6.2 Experimental 159
6.3 Results 160
6.3.1 Absorption Spectra 160
6.3.2 Short-wavelength photodissociation: $\lambda \leq 262.5$ nm 162
6.3.3 Long wavelength photodissociation: $\lambda \geq 320$ nm 165
6.4 Discussion 170
6.4.1 $\lambda \sim 235$ nm and $\lambda \sim 260$ nm 170
6.4.2 $320 < \lambda < 400$ nm 172
6.4.3 $400 < \lambda < 540$ nm 172
6.4.4 Model for a weakly avoided crossing 180
6.4.5 Model for a strongly avoided crossing 181
6.4.6 The possible role of other dissociative states 184
6.4.7 Anisotropy parameters for Br formation 185
6.5 Conclusions 189
6.6 References 192

Appendices
A: Transformation of 2D Images into 3D Distributions 194
B: Wigner - Witmer Rules 197
C: Ion Pair State Vibrational Level Analysis 201
D: Rotational Hamiltonian Operator and Spin-Orbit Interactions 204

Chapter 1

Introduction

1.1 Introduction

The ability of the laser to deliver photons of a highly specific energy into a molecular system has made it the fundamental tool for research into the internal quantum states of molecules. Lasers have been employed in many studies to elucidate information on systems, such as potential energy curves, dissociation pathways, predissociation rates and the energetics of reaction products. Some of the simpler experiments use single photon excitation processes, such as laser induced fluorescence (LIF), and absorption spectroscopy, whereas more complicated processes like double resonance multiphoton ionisation spectroscopy and studies of reaction dynamics may employ a multiple photon excitation scheme.

In this work, Resonance Enhanced Multiphoton Ionisation (REMPI), and Double Resonance Multiphoton Ionisation, have been used to further the spectroscopic knowledge of the electronically excited states of the radicals ClO and S_2 respectively. Photofragment Ion Imaging has been employed to investigate and compare the photodissociation dynamics of the molecules Br_2 and BrCl.

1.2 Resonance Enhanced Multiphoton Ionisation (REMPI)

Resonance Enhanced Multiphoton Ionisation (REMPI) has become one of the most successful multiphoton methods used in spectroscopy today. REMPI satisfies the condition for multiphoton resonance excitation, $\Delta E = n h\nu$ where $n>1$, as first proposed by Goppert-Mayer[1] in 1931. The success of REMPI springs from the ability of the scheme to access high lying electronic states of molecules and atoms which have been previously unattainable, due to energetic difficulties or spectroscopic constraints. The fact that two or more photons are being used in the excitation process can change the relevant spectroscopic selection rules, compared with one photon methods. This allows REMPI to access states that cannot be studied via a single photon technique. This advantage plus many others have been highlighted in a number of multiphoton ionisation reviews along with a list of the large number of molecules which have been studied using REMPI.[2-5] REMPI is

now also being used not only to study the internal electronic structure of molecules, but as a tool in the detection of species from photodissociation processes,[6,7] reaction dynamic studies,[8] and surface chemistry investigations.[9,10]

Figure 1.1 shows an example of a REMPI scheme. A multiple number *n*, (in this case two) of identical photons are absorbed by the molecule simultaneously, to take the species to a state of energy *n*h*v*. The molecule is then ionised by the absorption of *m* photons (in this case 1), which enables easy mass selective detection of the species by time of flight methods. This scheme is commonly referred to as an [*n* + *m*] REMPI scheme, e.g. [2 + 1]. The molecule is only ionised when the energy of *n* photons matches that of the energy gap between two states. Therefore a spectrum of the total ion flux as the wavelength of the absorbing photon is scanned carries the signature of the high lying states of the neutral molecule. Measurement of the kinetic energy of the electrons ejected in the REMPI process provides information on the ion formed. This technique is called Resonance Enhanced Multiphoton Ionisation Photoelectron Spectroscopy, or REMPI -PES[11] and is also illustrated in figure 1.1. The photoelectrons produced are monitored at a fixed wavelength, and their kinetic energies recorded. Using conservation of energy arguments, information on the electronic, vibrational and rotational state of the ion can be calculated. Analysis of the vibrational structure of the ion can lead to information on the relative geometry change between the neutral and the ion. In the case of Rydberg states, which have similar properties to ions (as described later), information on the resonance enhancing excited state of the neutral molecule can be inferred.

It can be seen from fig. 1.1 that REMPI can be used to access high lying states that are difficult to access via a single photon absorption method. To study excited states with energies $\geq$ 6.5 eV above the ground state a single photon absorption method would have to employ vacuum ultraviolet wavelengths which is technically demanding and experimentally challenging, whereas the multiphoton technique can probe the same region, but by using the focused visible or near UV output of a dye laser.

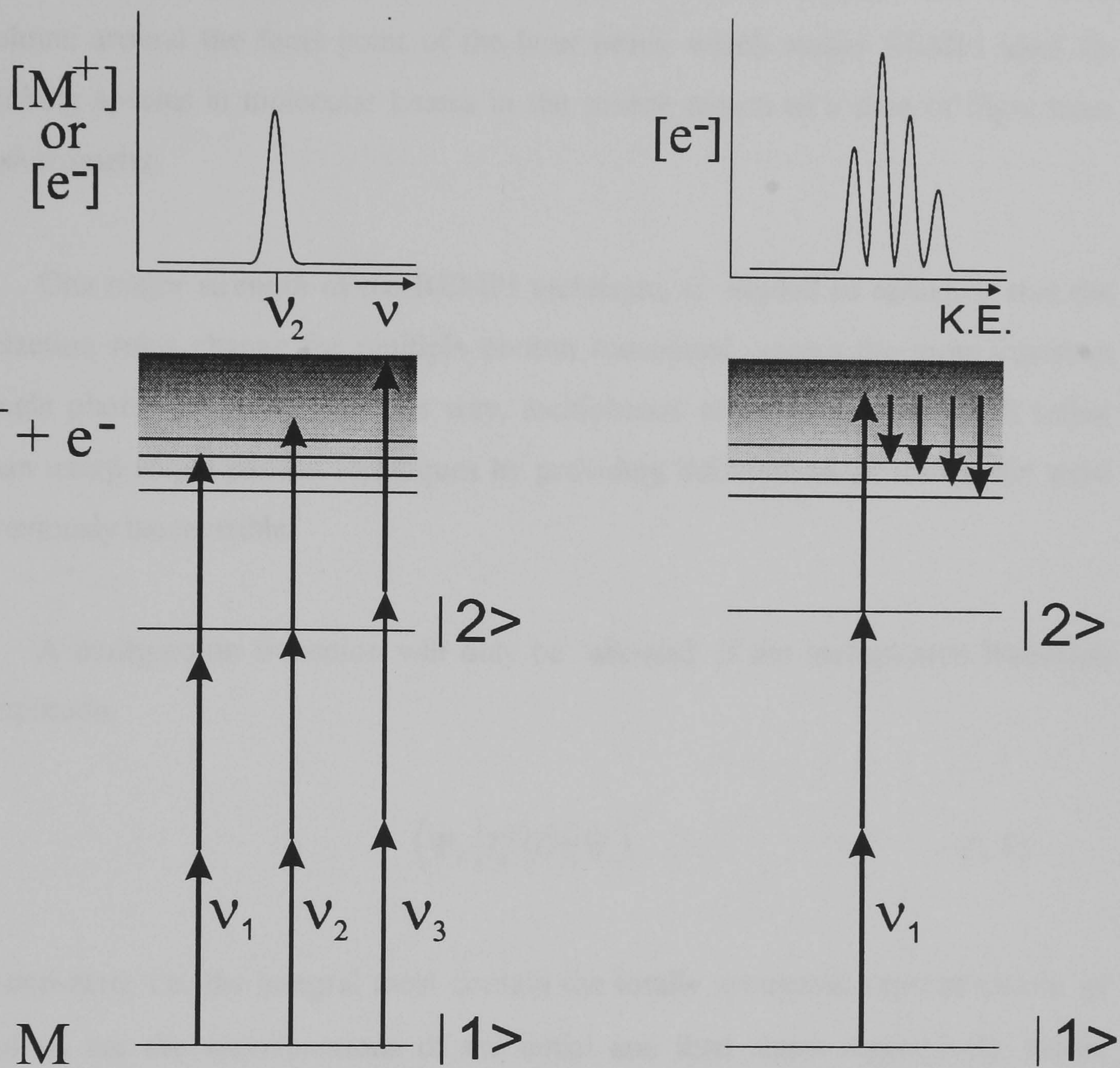

Figure 1.1: Schematic illustration of the REMPI and REMPI-PES excitation scheme. Ion or electron signal is only recorded when the sum of the energy of two incident photons is resonant with that of state |2>.

Compared to one photon transitions, multiphoton transitions are highly improbable, i.e. the absorption cross section for a multiphoton transition is small. This problem is overcome by using the high intensities that can be generated in the focus of a laser beam. This means that multiphoton transitions only occur in a small volume around the focal point of the laser beam, which makes REMPI ideal for probing species in molecular beams in the source region of a time of flight mass spectrometer.

One major strength of the REMPI technique, as alluded to earlier, is that the selection rules change for multiple photon transitions, versus the more common single photon transitions. In this way, multiphoton techniques complement rather than usurp single photon techniques by providing information on states that were previously inaccessible.

A multiphoton transition will only be 'allowed' if the multiphoton transition amplitude,

$$\left\langle \Psi_f \left| T_q^k(\hat{O}) \right| \Psi_i \right\rangle \qquad (1.1)$$

is non-zero, i.e. the integral must contain the totally symmetric representation. ψ_i and ψ_f are the wavefunctions of the initial and final states respectively, whilst $T_q^k(\hat{O})$ represents the qth component of the spherical tensor, of rank k, representing the multiphoton transition operator $\hat{O}$. Table 1.1 gives the representations of $T_q^k(\hat{O})$ for different n-photon transition operators for some common molecular point groups. Detailed consideration of eqn. 1.1 leads to the 'one-colour' multiphoton transition selection rules, which are summarised for 1, 2 and 3 photon transitions in Table 1.2. Table 1.2 shows that various transitions that are 'forbidden' in a one photon excitation process, become 'allowed' in a multiphoton excitation scheme.

number of photons, n	k	q	$D_{\infty h}$ [a]	C_{2v} [b]	C_s [b]
1	1	0	Σ_u^+	A_1	A”
		1	±1	Π_u	$B_1 + B_2$	2A’
2	0	0	Σ_g^+	A_1	A’
	2	0	Σ_g^+	A_1	A’
	2	±1	Π_g	$B_1 + B_2$	2A”
	2	±2	Δ_g	$A_1 + A_2$	2A’
3	1	0	Σ_u^+	A_1	A”
	1	±1	Π_u	$B_1 + B_2$	2A’
	3	0	Σ_u^+	A_1	A”
	3	±1	Π_u	$B_1 + B_2$	2A’
	3	±2	Δ_u	$A_1 + A_2$	2A”
	3	±3	Φ_u	$B_1 + B_2$	2A’

a Assuming Hund’s case (a) or (b) coupling.
Ignore u/g labels for non-centrosymmetric molecules.
b The z-axis of the point group corresponds to the q = 0 component of the k = 1 tensor.

Table 1.1: Representations of the spherical tensor components $T_q^k(\hat{O})$ of the one-colour, n-photon transition operator.

quantum number / property of interest	rank of transition tensor, k 0	1	2	3
atoms orbital angular momentum, l, of electron being excited	$\Delta l = 0$	$\Delta l = \pm 1$	$\Delta l = 0, \pm 2$ (but s $\not\leftrightarrow$ s)	$\Delta l = \pm 1, \pm 3$ (but s $\not\leftrightarrow$ p)
linear molecules [case (a)/(b)] axial projection of electronic orbital angular momentum, Λ	$\Delta\Lambda = 0$	$\Delta\Lambda = 0, \pm 1$	$\Delta\Lambda = 0, \pm 1, \pm 2$	$\Delta\Lambda = 0,...., \pm 3$
linear molecules [case (c)] axial projection of total electronic angular momentum, Ω	$\Delta\Omega = 0$	$\Delta\Omega = 0, \pm 1$	$\Delta\Omega = 0, \pm 1, \pm 2$	$\Delta\Omega = 0,...., \pm 3$
centrosymmetric molecules inversion symmetry, u/g	u $\leftrightarrow$ u g $\leftrightarrow$ g	u $\leftrightarrow$ g	u $\leftrightarrow$ u g $\leftrightarrow$ g	u $\leftrightarrow$ g
atoms and molecules total angular momentum, J	$\Delta J = 0$	$\Delta J = 0, \pm 1$ (J = 0 $\not\leftrightarrow$ J= 0)	$\Delta J = 0, \pm 1, \pm 2$ (J = 0 $\not\leftrightarrow$ J= 0,1)	$\Delta J = 0,...., \pm 3$ (J = 0,1,2 $\not\leftrightarrow$ J= 0; J = 1 $\not\leftrightarrow$ J= 1)
atoms and molecules total parity, +/-	+ $\leftrightarrow$ + − $\leftrightarrow$ −	+ $\leftrightarrow$ −	+ $\leftrightarrow$ + − $\leftrightarrow$ −	+ $\leftrightarrow$ −
atoms and molecules electron spin, S	$\Delta S = 0$	$\Delta S = 0$	$\Delta S = 0$	$\Delta S = 0$

Table 1.2: Allowed changes in some of the more important quantum numbers and symmetry descriptors for atoms and molecules undergoing one-colour multiphoton transitions involving one (k = 1), two (k = 2), and three (k = 1 and 3) photons.

1.3 Double Resonance Multiphoton Ionisation

Double Resonance Multiphoton Ionisation is very similar to REMPI in that a molecule is ionised by the absorption of multiple photons, but there are two key differences between the two techniques. Firstly the double resonance scheme uses two or more wavelengths in the overall excitation process, and secondly a real intermediate state (often a valence state) of the molecule is accessed during the excitation.[12,13]

Figure 1.2 illustrates the double resonance process. Firstly *n* 'pump' photons (in this case 1) of frequency ν_1, are absorbed by the molecule to access a known valence state. This resonance frequency is usually confirmed either by monitoring the absorption of laser light by the state, or by emission of LIF. Subsequently *m* 'probe' photons of a different frequency are absorbed to promote the molecule to the state of interest. The following double resonance excitation scheme illustrates the use of the $^3\Pi_u$ valence state of S_2 to access the $^3\Delta_g$ Rydberg state:

$$^3\Delta_g\,(v''', J''') \xleftarrow{h\nu_2} B''\,^3\Pi_u\,(v', J') \xleftarrow{h\nu_1} X\,^3\Sigma_g\,(v'', J'') \qquad (1.2)$$

As in REMPI spectroscopy a final number of photons '*o*' are absorbed to ionise the molecule for detection. This final ionisation can be by photons of the 'pump, or 'probe' beams, or even of a third wavelength. Overall the number and type of photons used in a double resonance scheme are summarised by [*n* + *m* + *o*] notation, e.g. [2 + 1' + 1']. Figure 1.2 shows a [1 + 1' + 1'] scheme as two different photons are used in the excitation process, with the 'probe' beam providing the final ionising photon. During a double resonance experiment the 'pump' wavelength is held constant, whereas the 'probe' wavelength is scanned and the ion flux monitored. This, as in the one colour REMPI process, creates a spectrum of the energy levels of the high lying states of the molecule.

The double resonance process has some advantages over the one colour REMPI process because of the different excitation scheme used. Firstly, a major

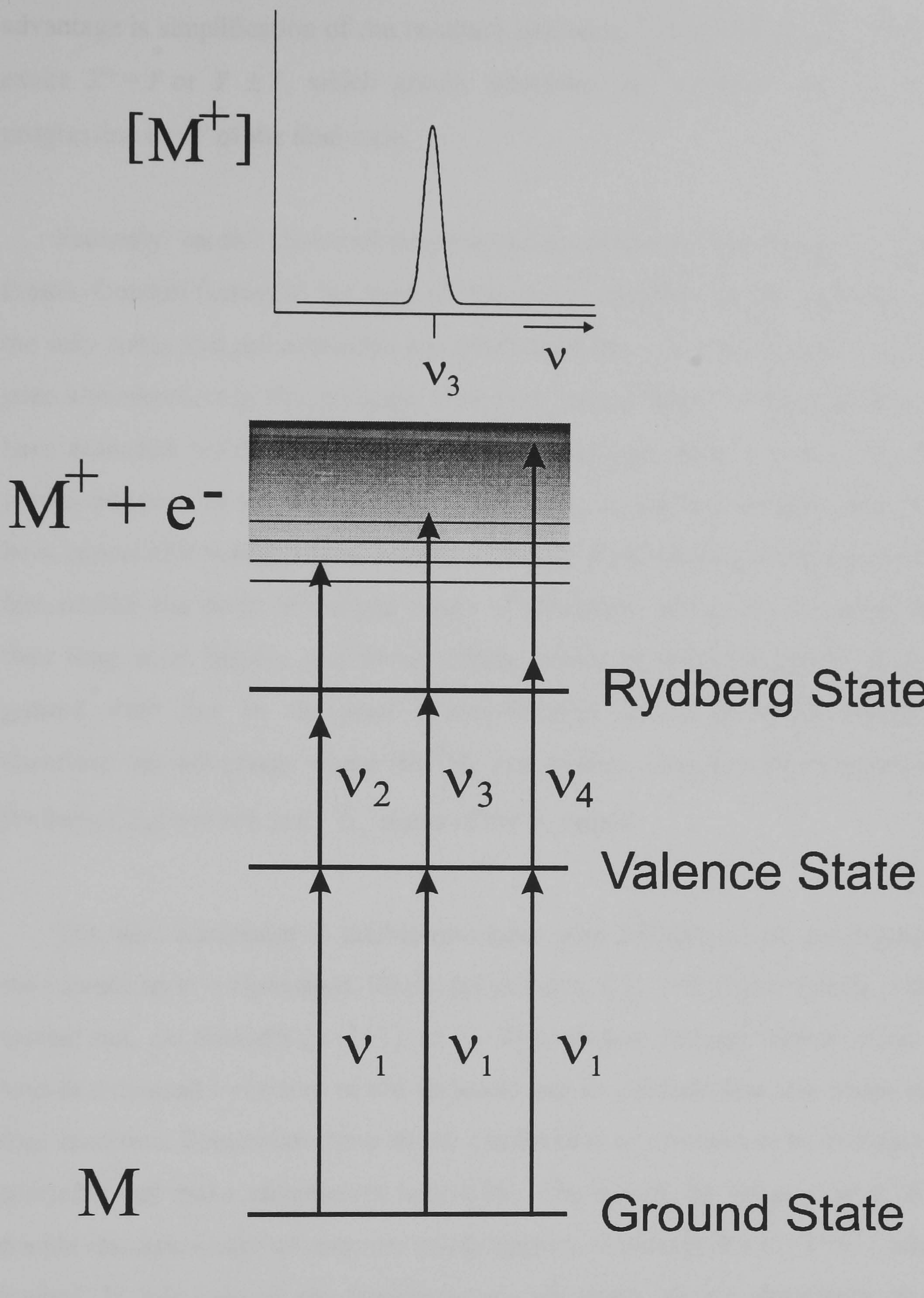

Figure 1.2: Schematic illustration of the double resonance excitation scheme

advantage is simplification of the resultant spectrum. The 'probe' photon can only excite $J''' = J'$ or $J' \pm 1$, which greatly simplifies the resultant spectrum into a progression in v''' of the final state.

Secondly, careful choice of the intermediate state used can change the overall Franck-Condon factors to the state of interest considerably. In the REMPI process the only states that are accessible are ones which have an overlap with the ground state wavefunction of the molecule. However, valence states of the molecule often have extended bond lengths compared to the ground state, and if a high lying vibrational state of the valance state is employed as the intermediate state, it will have appreciable wavefunction amplitude at both short and long bond lengths. This fact enables the study of ion pair states of molecules, which are characterised by their long bond lengths, and which usually cannot be accessed directly from the ground state due to the poor Franck-Condon factors involved. Figure 1.3 illustrates this advantage where the $^3\Pi_u$ intermediate state is used to access both Rydberg ($^3\Delta_g$) and ion pair $^5\Sigma_g^-$ states of the S_2 radical.

The third advantage of double resonance over REMPI is that interference at the valence level is eliminated. When, for instance, a [2 + 1] REMPI study is being carried out, occasionally [1+1+1], or [1+2] processes through valence states can lead to enhanced ionisation of the molecule and so produce spurious peaks in the final spectrum. Sometimes these effects can become so common as to dominate the spectrum and make assignments impossible. The use of the valence states in the double resonance scheme removes this possibility, especially if a [1+1'+1'] scheme is used. In this case all the transitions are via single photon absorption, as this enables a relaxation of the focusing conditions making simultaneous 2 photon absorption highly improbable.

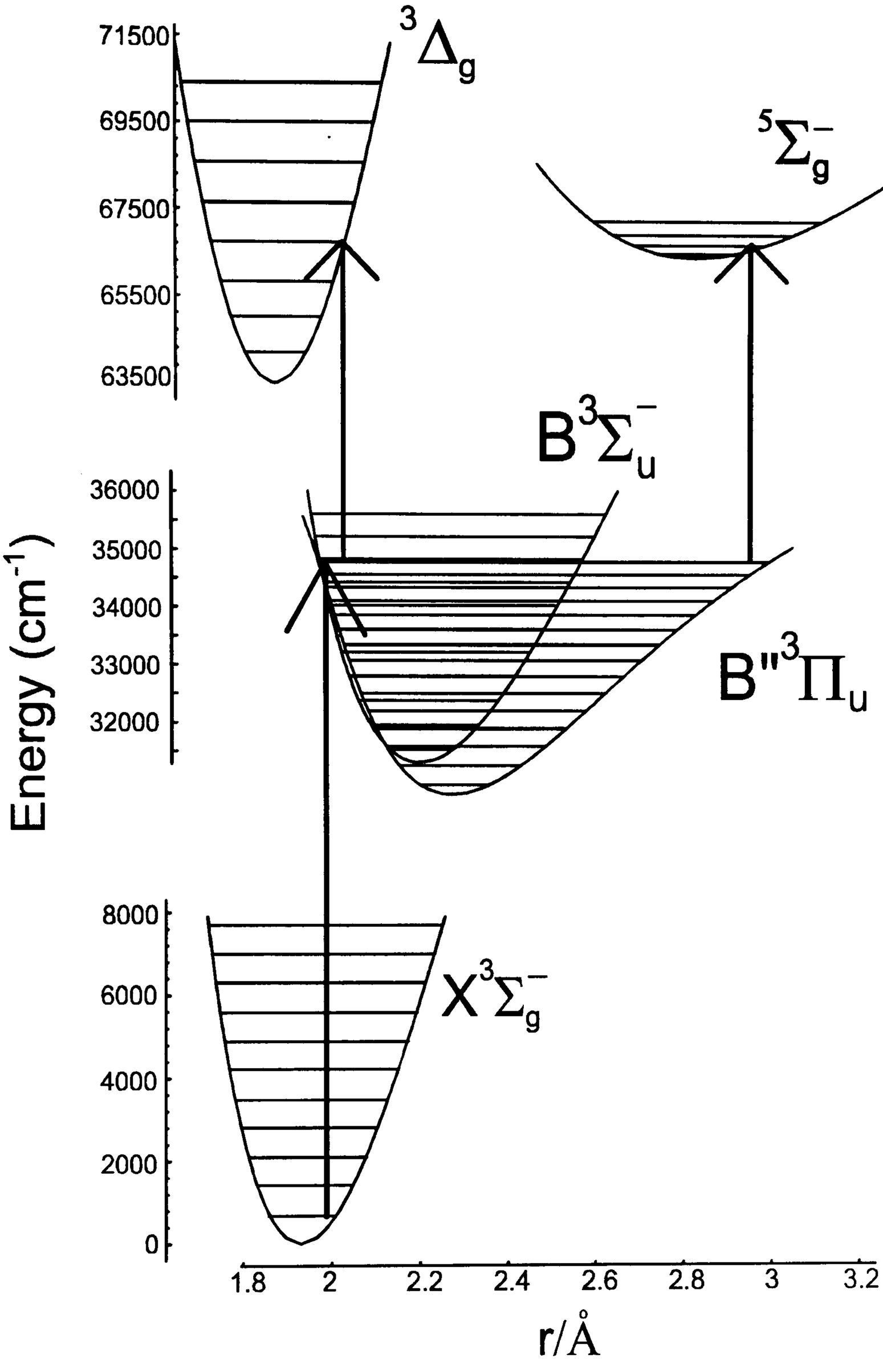

Figure 1.3: Example of a double resonance scheme for the S_2 radical. The $B''^3\Pi_u$ valence state is used as an intermediate to access both the $^3\Delta_g$ Rydberg and the $^5\Sigma_g^-$ ion pair states of S_2. The change in Franck-Condon overlap with the upper states by utilising the $^3\Pi_u$ state enables the transition to the $^5\Sigma_g^-$ state.

1.4 Rydberg and Ion Pair States

All of the spectroscopic work reported in this thesis is concerned with the study of either Rydberg or Ion Pair states of diatomic molecules. As an overview figure 1.4 shows the relative potential energy curves typically found for ground, valence, Rydberg and ion pair states of diatomic molecules.

1.4.1 Rydberg States

Rydberg states of atoms or molecules are high lying electronic states which are defined as having an electronic configuration which employs orbitals which have a value of the principal quantum number, *n*, which is greater than that of the highest orbital occupied in the ground state. For example the electronic distribution in the ground state and first Rydberg states of atomic sulphur are:

Ground State: $(1s)^2(2s)^2(2p)^6(3s)^2(3p)^4$ ^3P (1.3)

First Rydberg State: $(1s)^2(2s)^2(2p)^6(3s)^2(3p)^3(4s)^1$ ^5S (1.4)

A shorthand way of representing the electronic configuration of the first Rydberg state of atomic sulphur is $[^4S](4s)^1$ where $[^4S]$ represents the core electronic configuration, and $(4s)^1$ represents the orbital occupied by the Rydberg electron.

The Rydberg states of molecular systems are not so well defined, as *n* is not an ideal quantum number. The Rydberg states of atoms and molecules are consistent with the modified version of the Rydberg equation:[14]

$$\tilde{\nu} = E_i - \frac{R}{(n^*)^2} \qquad (1.5)$$

where $\tilde{\nu}$ is the term value relative to the ground state vibrationless level, E_i is the adiabatic ionisation potential, R is the Rydberg constant (109737 cm^{-1}) and n^* is the effective quantum number ($n^* = (n - \delta)$, where δ is the quantum defect). The value of the quantum defect varies with the degree to which the Rydberg orbital penetrates the core of the molecular ion. Where the Rydberg orbital can be described as being localised on one atom of the molecule, the value of the quantum defect can be approximated to the value for that of the atom, which aids in the assignment of n and l quantum numbers to the orbitals. The Rydberg states of a molecule can typically be ordered into several series of increasing n, each member of any one series having a common value of δ, that converges to an ionisation potential, E_i which corresponds to the energy threshold for forming some particular electronic state of the positive ion.

Molecular Rydberg states can be described in a similar way to those of atoms, by indicating the electronic configuration of the ion core, and then specifying the quantum numbers n, l, and λ of the Rydberg electron. For example the first doublet Rydberg state of ClO ($C^2\Sigma^-$) can be written, $[^3\Sigma^-]$ $(4s\sigma)^1$. The accuracy of this description generally increases with n, as the lower Rydberg levels can be subject to Rydberg-valence mixing.[15]

The properties of Rydberg states (bond lengths, bond angles, vibrational frequencies etc.) tend to mimic those of the molecular ion. This is due to the fact that the Rydberg electron is essentially non-bonding so the ion core dominates the electronic configuration. This general character often aids in the final ionisation step of the REMPI scheme, as the similarity between the Rydberg and ion states ensures a good Franck-Condon overlap for forming the ion.

Even though Rydberg states are high in energy, and are often above the dissociation limit(s) with the respect to the loss of one or more atoms, they are surprisingly stable. This is because, as figure 1.4 shows, Rydberg states correlate to highly excited atomic products. This long lived nature enables the ionisation step in the process to compete favourably with the other molecular processes, such as

photodissociation, which makes these states ideal candidates for studying via REMPI spectroscopy.

1.4.2 Ion Pair States

Ion-pair states of covalent diatomic molecules are generally characterised as having large dissociation energies, long bond lengths and a small vibrational spacing. Figure 1.4 shows that ion-pair states typically lie at energies similar to that of Rydberg states, but have extended bond lengths. For comparison however it is interesting to note that in the case of ionic structures, such as NaCl, the ground state is an ion pair state.

The form of the potential energy curves from ion-pair states can be rationalised by describing the electronic configuration, not as the sum of atomic orbitals from two neutral atoms, but from two atomic ions, one positive and one negative.[16] Therefore the potential energy curve at extended R can be described in terms of the Coulombic potential between two charges:

$$P.E. = -\frac{q_1 q_2}{4\pi\varepsilon_0 R} \qquad (1.6)$$

where q_1 and q_2 are the charges of the two ions, and R is the distance between them. This provides the basis for the deep, and very wide attractive well found in ion pair states. This well arises as Coulombic attraction has an effect over a much larger range of R than normal bonding attractive forces. The generally long bond length of ion-pair states can also be rationalised by the simple ion-ion model. The R_e of ion-pair states generally fall just slightly longer than the sum of the two ionic radii of the atoms involved. For example the S^+ and S^- ions have radii of 0.53 Å and 2.19 Å respectively, which gives a total of 2.62 Å. This is comparable with the $^5\Sigma_g^-$ ion-pair state of S_2 which has an R_e of 2.8 Å.

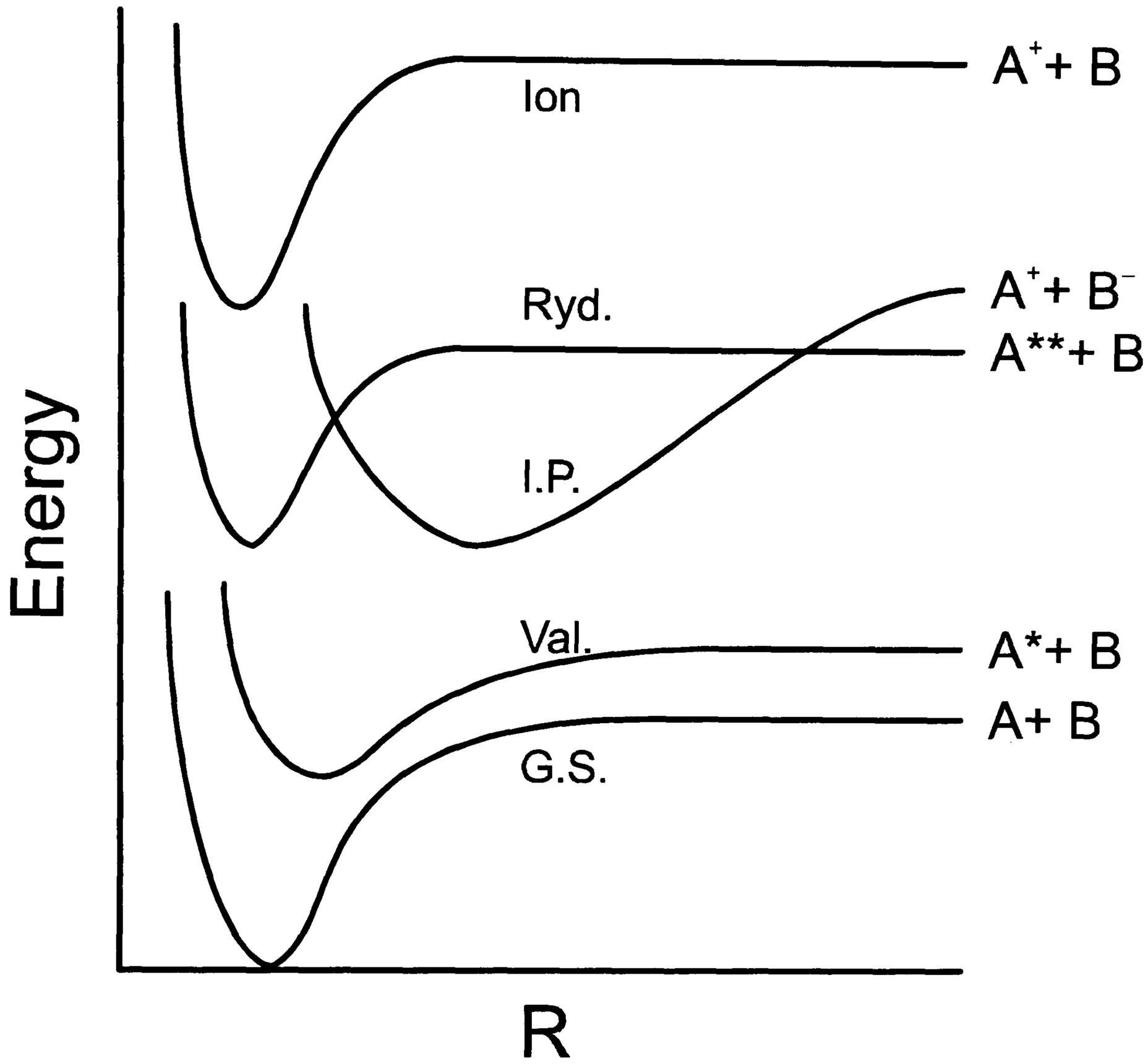

Figure 1.4: Typical potential energy curves for a diatomic molecule. Indicated are the relative positions of the ground (G.S.), valence (Val.), Rydberg (Ryd.), ion pair (I.P.) and ionic (Ion) states.

Most molecules are predicted to have a host of ion-pair states, just as most have a long series of Rydberg states, but with the long equilibrium bond lengths, and therefore poor Franck-Condon factors associated with transitions from the ground to ion pair states, it is easy to see why little spectroscopic data is available on them. Franck-Condon factors for direct excitation from the ground state to ion-pair states will only be suitable for exciting high into the vibrational manifold. Therefore the main tool for studying ion-pair states is double resonance spectroscopy as described previously. However, spectroscopic difficulties have not precluded the study of ion pair-states for a number of molecules, namely hydrogen halides[17,18] (HX), transition metal halides[19,20] and the halogens and inter-halogens.[21, 22]

1.4.3 Ion Pair States of I_2

Of all the molecules for which ion pair states have been characterised, the most extensive work has been carried out on iodine (I_2). The main reasons that have made I_2, and indeed the other halogens, agreeable to study is that the lowest ion pair states lie at energies that are easily accessible to modern spectroscopic techniques. Observations of ion pair states of I_2 were first reported in emission[23] following the electrical discharge of iodine vapour. The spectrum obtained in this work was extremely complex, which precluded a full spectroscopic assignment. This complexity is not unexpected for ion pair state spectra as the number and nature of the states often leads to overlapping band structure, with the complexity heightened in the case of the electrical discharge experiment where the technique offers a highly unselective excitation scheme.

High resolution data on the ion pair states have been recorded subsequently, mostly by double resonance techniques[24-27] utilising the $B^3\Pi_u(0^+)$ state, but also using more technically demanding methods, such as Degenerate Four Wave Mixing (DFWM).[28,29] These studies have led to at least partial characterisation of all 18 ion pair states that can arise from the 3 lowest ion pair limits of I_2, i.e. $I^+(^3P_2) + I^-(^1S_0)$, $I^+(^3P_{1,0}) + I^-(^1S_0)$ and $I^+(^1D_2) + I^-(^1S_0)$. The lowest lying ion pair states of I_2

have typical energies of *ca.* 40000 - 50000 cm^{-1}. For example the $E0_g^+$ ($^3P_2$) ion pair state of I_2 has been extensively investigated using double resonance spectoscopy,[26] with term values for vibrational levels v = 123 - 422 experimentally determined. At the lowest vibrational energies ($v \sim 130$) the vibrational spacing is of the order of 60 cm^{-1}, whereas at the highest energies reported ($v \sim 420$) the vibrational spacing has fallen to only 20 cm^{-1}. A potential energy curve of the state constructed from the data collected results in an $R_e \sim 3.7$ Å.

1.5 Photofragment Ion Imaging

The goal of many researchers studying molecular photodissociation is to quantify and understand how the energy placed in a molecular system to induce dissociation manages to dispose itself in the final photofragment products. The energy may end up in any of the degrees of freedom available to the molecule i.e. kinetic energy, vibrational and rotational excitation etc. of the photofragments. In the past techniques such as photofragment translational spectroscopy[30] and LIF studies[3132] on photofragments from photodissociation have been used to measure these quantities, and therefore elucidate information on the potential energy curves involved in the photodissociation process.

Photofragment ion imaging is a relatively new technique which was introduced by Chandler and Houston[33] in 1987. It provided a new way of probing the products of a molecular photodissociation. What makes photofragment ion imaging so powerful is that in a single experiment, the velocity, as well as quantum state distributions of products formed from a molecular dissociation can be determined. In ion imaging all the quantities of interest are monitored simultaneously, that means that accurate correlations can be drawn between two or more measured products from a photodissociation. For instance the branching ratio between two product channels containing differently excited photofragments can be accurately determined.

1.5.1 Experimental Overview

Ion imaging combines two older techniques in its experimental makeup: REMPI spectroscopy and translational time of flight spectroscopy.

REMPI is used to ionise a specific quantum state (electronic, vibrational and rotational) of the photofragments to enable detection. Coupling the knowledge of the REMPI transition linestrengths to the intensity of signal seen from a specific photofragment, enables accurate electronic, vibrational and rotational populations to be deduced. The only draw back with using REMPI is that the spectroscopy of

the photofragment to be probed must already be known if it is to be used for detection purposes. However, there is currently a wealth of spectroscopic REMPI data available on a large number of molecules and atoms.

The second technique of translational time of flight spectroscopy is used to determine the kinetic energy of the photofragments that have been selectively ionised in the REMPI process. This measurement is achieved by preserving the nascent recoil velocities of the photofragments produced by the photodissociation, perpendicular to the detector, as they are accelerated down a time of flight mass spectrometer. The key to the ion imaging technique then lies in the 2 dimensional (2D) position sensitive detection of the mass selected photofragments at the end of the flight tube. This is achieved by the coupling of a pair of matched micro-channel plates (MCP's), a fast phosphor screen and a charge-coupled device (CCD) camera. As the ionised photofragments impinge on the MCP's a shower of electrons is produced at the point of each impact, these then strike the phosphor screen to produce a bright spot or 'event'. The CCD camera records the position of all of the events on the screen every shot, and stores them on a PC ready for analysis. The CCD camera is time gated so as to record only those events that are related to the time of flight of the photofragment of interest.

One of the most elegant features of the image recorded by the CCD camera is that it shows directly the path and speed of the photofragments produced in the photodissociation, which makes the images produced by the experiment easy to interpret in terms of a molecule flying apart into two or more fragments.

1.5.2 Analysis of the Collected Image

The ion cloud that is initially formed expands in 3D, but the detector only views the image in 2D, therefore a mathematical manipulation is required to transform the recorded, squashed 2D image into the original 3D ion cloud distribution. Figure 1.5 shows an illustrative example of the recoiling 3D ion cloud, the detected 2D image and mathematically processed image. Generally the processed image is shown as a slice through the centre of the 3D ion cloud

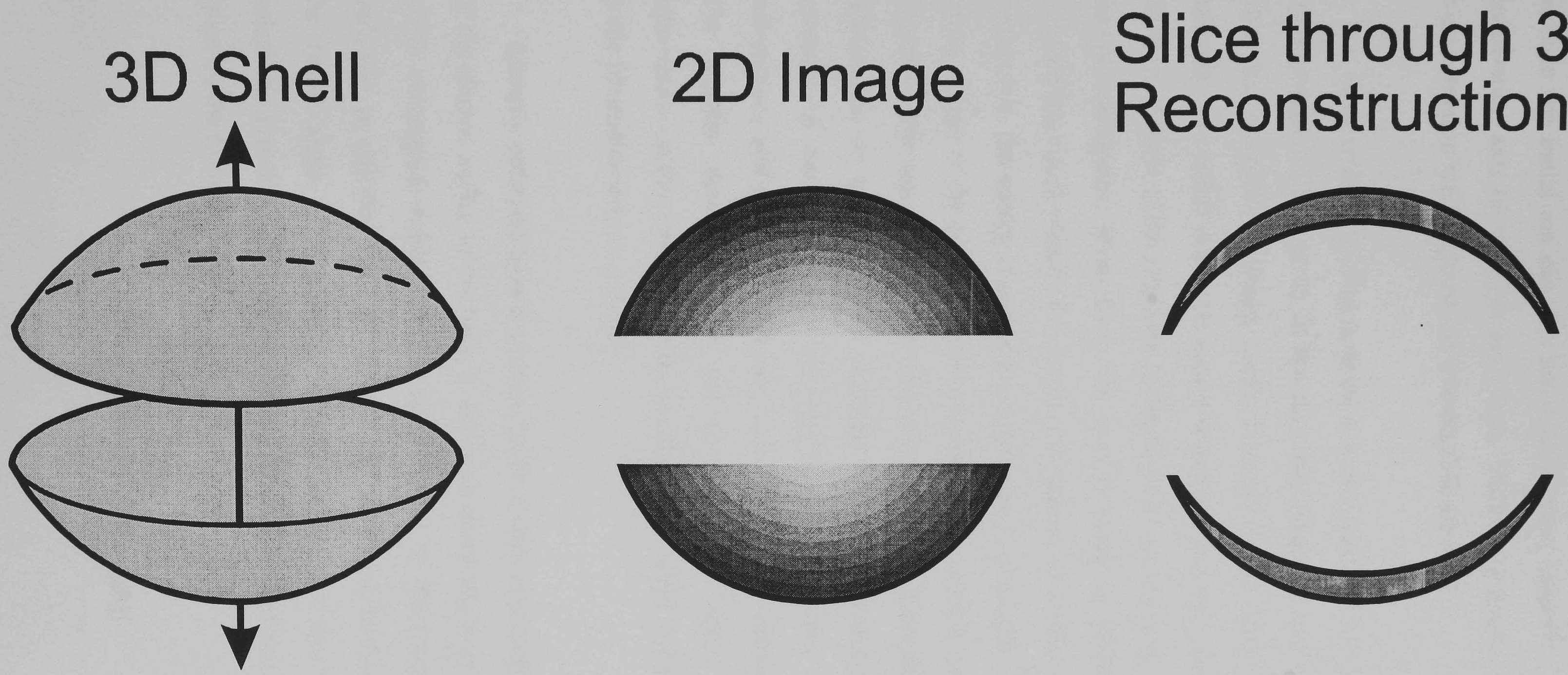

Figure 1.5: Schematic examples of a recoiling 3D cloud of ions, the resultant 2D image recorded by the detector and the 2D slice through the centre of the 3D mathematical reconstruction.

generated by the transformation. This mathematical reconstruction is possible because the initial ion cloud is assumed to have cylindrical symmetry about the polarisation axis of the photolysis laser beam. The mathematics involved in the transformation are discussed in more detail in appendix C.

A huge amount of data is present in the resultant 2D slice produced by the transformation. Each point in the slice has three associated parameters: radius, from the centre of the image, angle, from the central laser polarisation axis, and intensity. The radius is a direct measurement of the speed of the photofragment. As the time of flight of the fragment to the detector is known, the distance travelled by the photofragment away from the central point of photodissociation can be transformed into a velocity for the photofragment. From the known energies of the system (i.e. the energy levels of the fragments, wavelength of the photolysis laser beam, energy of the bond being broken, etc.), it is possible to calculate the amount of energy that has gone into internal energies of the photofragments and so glean information on active product channels at various photolysis wavelengths. The intensity of each point enables population distributions of different velocity sub-groups, and therefore branching ratios of product channels, to be calculated. The angular dependence of the photofragment recoil velocities provides information on the symmetry of the excited states of the molecule that are involved in the photodissociation process.

Linearly polarised light is used in the photodissociation process. The direction of the electric vector of the light, ε, defines a direction, in the laboratory frame, to which subsequent values such as the direction of the transition moment of the molecule, μ, and the recoil velocity, v, can be related. In the simplest case, where the recoil angle of a specific velocity subset is considered relative to the polarisation of the photolysis laser beam, the intensity at angle, θ, away from ε is given by the formula:[34]

$$I(\theta) = (1/4\pi) [1 + \beta P_2(\cos\theta)] \qquad (1.7)$$

where P_2 is the second order Legendre polynomial [$P_2(\cos\theta) = \frac{1}{2}(3\cos^2\theta - 1)$], and β is the anisotropy parameter. The value of β is determined by the symmetry of the ground and excited states involved in the photodissociation of the molecule.[35] β can have a value ranging anywhere from -1 to 2. A value of 2 is obtained if the photodissociation is a prompt process occurring with the transition moment parallel to the bond of the molecule (in the case of a diatomic). This leads to a $\cos^2\theta$ type distribution for the intensity of the recoiling flux as a function of θ, with the maximum photofragment flux at $\theta = 0^\circ$ and 180°, and with zero intensity at 90° and 270°. A value of -1 for β means that the photodissociation is occurring promptly with the transition dipole moment perpendicular to the bond of the diatomic molecule. This results in a $\sin^2\theta$ distribution of the recoiling photofragments, and a maximum in the photofragment flux at $\theta = 90^\circ$ and 270°, and zero intensity at 0° and 180°. If $\beta = 0$ then this corresponds to an isotropic distribution of the photofragments produced, i.e. the intensity if the photofragment flux is equal at all θ. Examples of photofragment flux distributions from a parallel and perpendicular photodissociation are shown in figure 1.6.

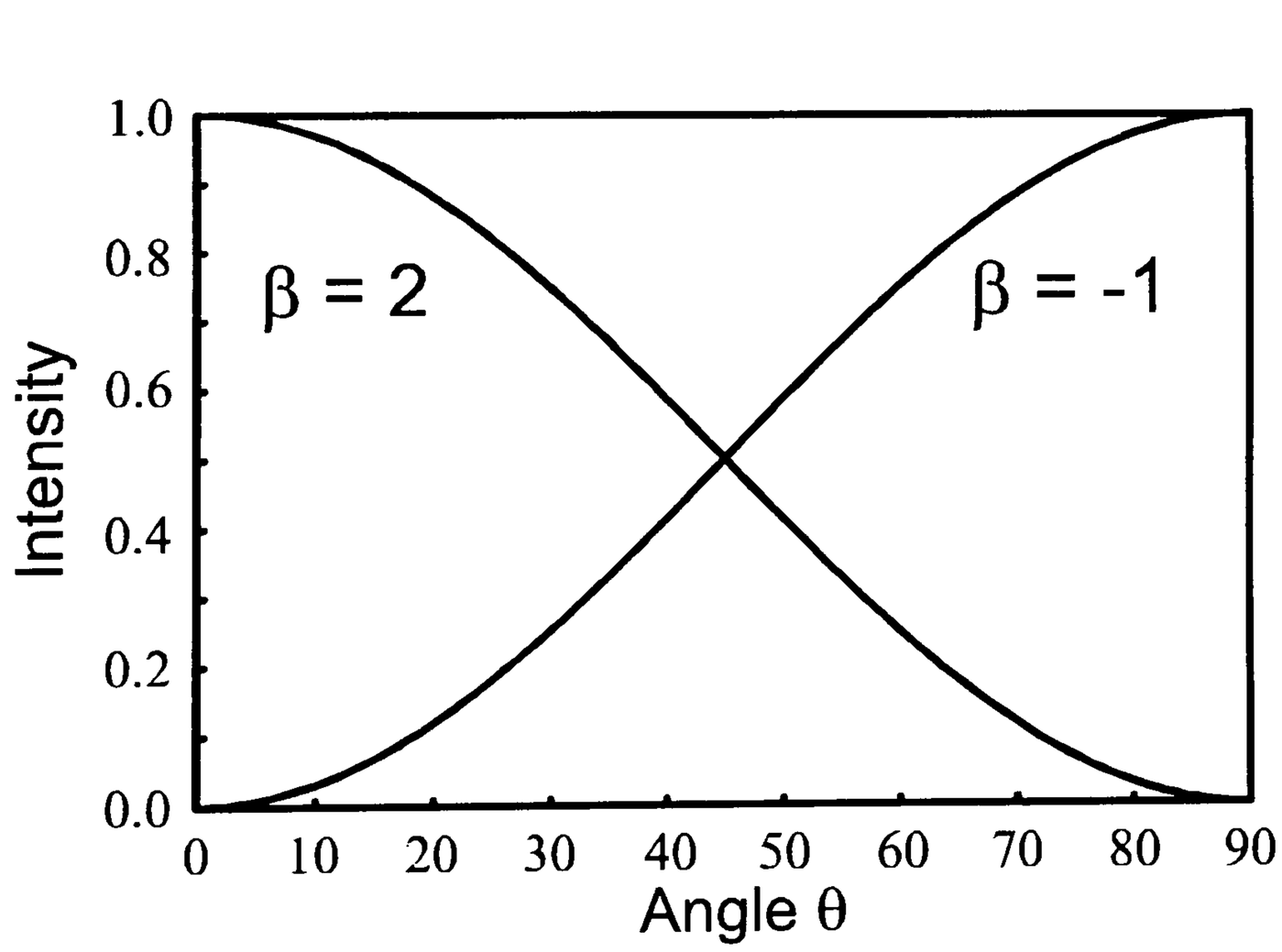

Figure 1.6: Expected photofragment ion flux distribution for a purely perpendicular ($\beta = -1$) and parallel ($\beta = 2$) photodissociation. θ is the angle between the polarisation of the photolysis laser, and the direction of the measured photofragment flux.

As mentioned previously β is determined by the symmetry of the ground and excited states involved in the dissociation, specifically β is determined by the change in Ω between the two states upon excitation.[35] Ω is defined as the projection of Λ + Σ onto the internuclear axis of the molecule (Appendix B.1 discusses the values of Λ, Σ and Ω in more detail). If β = 2, then a parallel photodissociation is occurring which is indicative of $\Delta\Omega = 0$, from the ground state to the excited state. If the ground state Ω is known, the value of β supplies information on the Ω of the excited state leading to dissociation. If β = -1, then a perpendicular photodissociation is occurring, which requires a $\Delta\Omega = \pm 1$ upon excitation from the ground state to the excited state.

The value of β must have a limiting value of 2 or -1 if the photodissociation is occurring promptly via a single excited state. If the value of β is found to be in the range from 2 to -1, then this can be due to a number of reasons such as predissociation, slow recoil velocities and excited state mixing, and can lead to extra information on the dissociation mechanism. Such effects on the β parameter will be discussed in detail in chapters 5 and 6.

The technique of photofragment ion imaging has now become established as one of the main tools in studying photodissociation processes. Many molecules have been studied via the technique since its introduction including diatomics such as HI (DI),[36] ICl [37] and H_2,[38] along with more complex polyatomics including CH_4 (CH_2D_2),[39,40] SO_2,[41] NO_2 [42-44] and many others.

1.5.3 Ion Imaging of Methane

The photodissociation of methane serves to illustrate how powerful the ion imaging technique can be.[39,40] Photodissociation of polyatomic molecules can lead to a host of different photofragment products such as atoms and small molecules. This results in a large number of energy channels in which the excitation photon energy may be taken up, such as rotation, vibration and translation, of the

photofragments. Elimination of H atoms from CH_4 and H and D atoms from CH_2D_2 was investigated following photolysis at the Lyman-α wavelength (λ = 121.6nm; 10.19 eV). At this wavelength, by energy conservation, 5 channels are available for the methane to dissociate into:

$$CH_4\ (^1A_1) \rightarrow CH_3\ (^2A_2'') + H \qquad \Delta E = 4.48\ eV \qquad (1.8)$$

$$CH_4\ (^1A_1) \rightarrow CH_2\ (a\ ^1A_1) + H_2 \qquad \Delta E = 5.01\ eV \qquad (1.9)$$

$$CH_4\ (^1A_1) \rightarrow CH_2\ (^3B_1) + H + H \qquad \Delta E = 9.21\ eV \qquad (1.10)$$

$$CH_4\ (^1A_1) \rightarrow CH_2\ (a\ ^1A_1) + H + H \qquad \Delta E = 9.48\ eV \qquad (1.11)$$

$$CH_4\ (^1A_1) \rightarrow CH\ (^2\Pi) + H_2 + H \qquad \Delta E = 9.07\ eV \qquad (1.12)$$

The H and D atom images for the two molecules are essentially the same, both showing two broad rings. Energy conservation assigns the faster ring to dissociation via channel (1.8), whereas the slower ring could arise from channels (1.10 - 1.12) and the contributions of each could not be assigned unambiguously. From the intensities of the images it was found that the elimination of H versus D from CH_2D_2 was favoured by a factor of 3.5:1, which is a large isotope effect, but is not so surprising given the observation of similar isotope effects in HOD[45] and CHD.[46] Elimination of H_2 via channels (1.9) and (1.12) after the absorption of two 210 -230 nm photons by CH_4 was also investigated. The same wavelength was used for REMPI detection of the H_2 products. This detection method enabled individual rovibrational levels of H_2 to be probed separately, to build up a picture of the energy disposal within the various degrees of freedom of the H_2 molecule produced. This study revealed that two channels, one 'fast' and one 'slow', were active in the photodissociation, and ignoring spin forbidden dissociations were assigned to channels (1.9) and (1.12). Dissociation via channel (1.9) led to 'hot' H_2, i.e. H_2 in excited v and J levels, whereas channel (1.12) led to cooler H_2 fragments. The relative contributions to the H_2 photofragment flux in its various excited states was deduced from the images recorded. The H_2 $v = 1$ photofragment flux was deconstructed into approximately equal contributions from both the fast and slow channels, whereas the H_2 $v = 2$ flux was made up of fast and slow H_2 in a 3:1 ratio. The degree of internal excitation of the H_2 molecule produced provides

information on the conformation of the transition state of the molecule as it dissociates. Generally it could be thought that 'cold' H_2 implies a specific pathway for forming H_2 that does not result in rotational and vibrational excitation, whereas a 'hot' H_2 suggests a different dissociation pathway leading to excited products. However, in the case of methane there must be careful consideration of the available energy after dissociation, and how that relates to the observed internal excitation of the H_2 fragment. In both cases (hot and cold) there is a linear correlation between the branching ratio and the H_2 photofragment internal energy, which has led to the conclusion that the two pathways (channels 1.9 and 1.12) are coupled, and that dissociation occurs on the same potential energy surface.

The brief description above of an investigation into the photodissociation of methane illustrates how powerful the ion imaging technique is. Information can be extracted from a single set of ion imaging experiments which would require a host of different experiments, such as Doppler spectroscopy and one dimensional time-of-flight techniques, to acquire.

1.6 Thesis Overview

The results presented in the following chapters are divided into two main sections. Firstly chapters 3 and 4 investigate the spectroscopy of ClO and S_2 by REMPI and double resonance techniques respectively. ClO is an important molecule in atmospheric chemistry as it is believed to be central to the catalytic destruction of ozone. Its production from the photodissociation of many atmospherically important chlorine and oxygen containing molecules is also of interest. S_2 is interesting as a spectroscopic analogue of O_2, and also the observation of ion pair states in molecules of group 6 elements has not been reported previously. The second section, chapters 5 and 6, deal with the photodissociation dynamics of Br_2 and BrCl. Interest in the photodissociation of molecules lies in the ability for such investigations to provide information on the interaction between the spectroscopically known states of molecules, and other states in the same energy region. In the case of Br_2 and BrCl the large value of the spin orbit splitting in Br coupled with the large number of electronic states correlating to each atomic limit makes them ideal for investigation and mutual comparison.

1.7 References

1 M. Goppert-Mayer, *Ann. Phys.* **9**, 273 (1931).

2 J.W. Hudgens, *Advances in Multiphoton Processes and Spectroscopy*, ed. S.H. Lin, World Scientific, Singapore. **4**, 117 (1988).

3 M.N.R. Ashfold, S.G. Clement, J.D. Howe and C.M. Western, *J. Chem. Soc Farad. Trans.* **89**, 1153 (1993).

4 M.N.R. Ashfold and J.D. Howe, *Ann. Rev. Phys. Chem.* **45**, 57 (1994).

5 P.M. Johnson and C.E. Otis, *Ann. Rev. Phys. Chem.* **32**, 139 (1981).

6 A.J.R. Heck and D.W. Chandler, *Annu. Rev. Phys. Chem.* **46**, 335 (1995).

7 A.J. Bell, S.A. Boggis, J.M. Dyke, J.G. Frey, R. Richter, N. Shaw and M. Tabrizchi, *J. Chem. Soc. Farad. Trans.* **90**, 17 (1994).

8 W.R. Simpson, T.P. Rakitzis, S.A. Kendell, A.J. Orr-Ewing and R.N. Zare, *J. Chem. Phys.* **103**, 7313 (1995).

9 A. de Meijere, K.W. Kolasinki and E. Hasselbrink, *Faraday Discussions.* **96**, 265 (1993).

10 C.T. Rettner, *J. Chem. Phys.* **101**, 1529 (1994).

11 K. Kimua, *Int. Rev. Phys. Chem.*, **6**, 195 (1987).

12 P.J. Jewsbury, T. Ridley, K.P. Lawley and R.J. Donovan, *J. Mol. Spectrosc.*, **157**, 33 (1993).

13 M.D. Danyluk and G.W. King, *Chem. Phys.*, **22**, 59 (1977).

14 M.B. Robin, *Higher Excited States of Polyatomic Molecules*, Academic Press, New York, 1974, vol 1 & 2, 1985, vol 3.

15 H. Lefebvre-Brion and R.W. Field, *Perturbations in the Spectra of Diatomic Molecules*, Academic Press (1986).

16 K.P. Lawley and R.J. Donovan, *J. Chem. Soc. Farad. Trans.*, **89**, 1885 (1993).

17 D.S. Ginter and M.L. Ginter, *J. Mol. Spectrosc.* **90**, 177 (1981).

18 G. de Londardo and and A.E. Douglas, *Can. J. Phys.* **51**, 434 (1973).

19 B. Pouilly, J. Schamps, D.J. Lumley and R.F. Barrow, *J. Phys. B*, **11**, 2289 (1987).

20 K.J. Jordan and R.H. Lipson, *J. Phys. Chem.* **95**, 7204 (1991).

21 J. Tellinghuisen, *J. Mol. Spectrosc.* **103**, 455 (1984).

22 J.C.D. Brand and A.R. Hoy, *Appl. Spectrosc. Rev.* **23**, 285 (1987).

23 R.S. Mulliken, *J. Chem. Phys.* **55**, 288 (1971).

24 T. Ishiwata, J. Yamada and K. Obi, *J. Mol. Spectrosc.* **158,** 237 (1993).

25 T. Ishiwata, H. Takekawa and K. Obi, *J. Mol. Spectrosc.* **159**, 443 (1993).

26 P.J. Wilson, T. Ridley, K.P. Lawley and R.J. Donovan, *Chem. Phys.* **182**, 325 (1994).

27 R.J. Donovan, K.P. Lawley, Z. Min, T. Ridley and A.J. Yarwood, *Chem. Phys. Lett.* **226**, 525 (1994).

28 M.D. Wheeler, I.R. Lambert and M.N.R. Ashfold, *Chem. Phys. Lett*, **229**, 285 (1994).

29 M.D. Wheeler, *Ph.D. Thesis*, University of Bristol (1997).

30 R.J. Oldman, R.K. Sander, and K.R. Wilson, *J. Chem. Phys.* **63**, 4252 (1975).

31 R.N. Dixon, J. Nightingale, C.M. Western, X. Yang, *Chem. Phys. Lett.*, **151**, 328 (1988).

32 M. Brouard, M.T. Martinez, J. O'Mahony and J.P. Simons, *Mol. Phys.*, **69**, 65 (1990).

33 D.W. Chandler and P.L. Houston, *J. Chem. Phys.* **87**, 1445 (1987).

34 R.N. Zare, *Angular Momentum*, (Wiley, New York, 1988).

35 R.N. Zare, *Mol. Photochem.*, **4**, 1 (1972).

36 T.N. Kitsopoulos, M.A. Buntine, D.P. Baldwin, R.N. Zare and D.W. Chandler, *SPIE.* **1858**, 2 (1993).

37 L.J. Rogers, M.N.R. Ashfold, Y. Matsumi, M. Kawasaki and B.J. Whitaker, *Chem. Phys. Lett.* **256**, 90 (1996).

38 M.A. Buntine, D.P. Baldwin and D.W. Chandler, *J. Chem. Phys.* **96**, 5843 (1992).

39 A.J.R. Heck, R.N. Zare and D.W. Chandler, *J. Chem. Phys.* **104**, 3399 (1996).

40 A.J.R. Heck, R.N. Zare and D.W. Chandler, *J. Chem. Phys.* **104**, 4019 (1996).

41 T. Sato, T. Kinugawa, T. Arikawa and M. Kawasaki, *Chem. Phys.* **165**, 173 (1992).

42 K. Tonokura and T. Suzuki, *Chem. Phys. Lett.* **224**, 1 (1994).

43 V.P. Hradil, T. Suzuki, S.A. Hewitt, P.L. Houston and B.J. Whitaker, *J. Chem. Phys.* **99**, 4455 (1993).

44 T. Suzuki, V.P. Hradil, S.A. Hewitt, P.L. Houston and B.J. Whitaker, *Chem. Phys. Lett.* **187**, 257 (1991).

45 N. Shafer, S. Satyapal and R. Bersohn, *J. Chem. Phys.* **90**, 6807 (1989).

46 R.A. Beärda, G.-K. Kroes, M.C. van Hemert, B. Heumann, R. Schinke and E.F. van Dishoeck, *J. Chem. Phys.* **100**, 1113 (1994).

PAGE NUMBERING AS ORIGINAL

Chapter 2

Experimental

Three different sets of apparatus were used to produce the results presented in this thesis. The low temperature time of flight (TOF) REMPI, Double Resonance and ion imaging work was performed at the University of Bristol, whereas the room temperature REMPI-TOF work was carried out at the National Institute of Standards and Technology (NIST) laboratories in Gaithersburg, Maryland, USA. The experimental details are outlined here and further specific details will be discussed at the appropriate points within the individual chapters.

2.1 REMPI and Double Resonance Experiments in Bristol

Figure 2.1 shows a schematic diagram of the experiment in Bristol which was used to record mass selective REMPI and double resonance spectra. In the case of the REMPI experiments the output from only a single Nd:YAG pumped dye laser was frequency doubled and focused into the source region of a TOF mass spectrometer. In the source region the laser beam crossed at right angles a pulsed molecular beam of the radical of interest. The ions produced by the REMPI process were then accelerated along the TOF tube towards the ion detector. The signal collected was then amplified, and fed into a digital oscilloscope where the ion count was displayed as a function of arrival time. The information from the oscilloscope was then read into a PC where it was processed and stored. In the case of the double resonance experiment a photomultiplier was used to monitor the LIF from the S_2 molecule. This enabled accurate frequency positioning of the 'pump' laser to populate the desired intermediate state.

The experimental set-up for the double resonance experiment was almost identical, except that the frequency doubled light from a second Nd:YAG pumped dye laser was used. The unfocused beams from the two dye lasers were then counter-propagated through the source region of the TOF mass spectrometer, again crossing

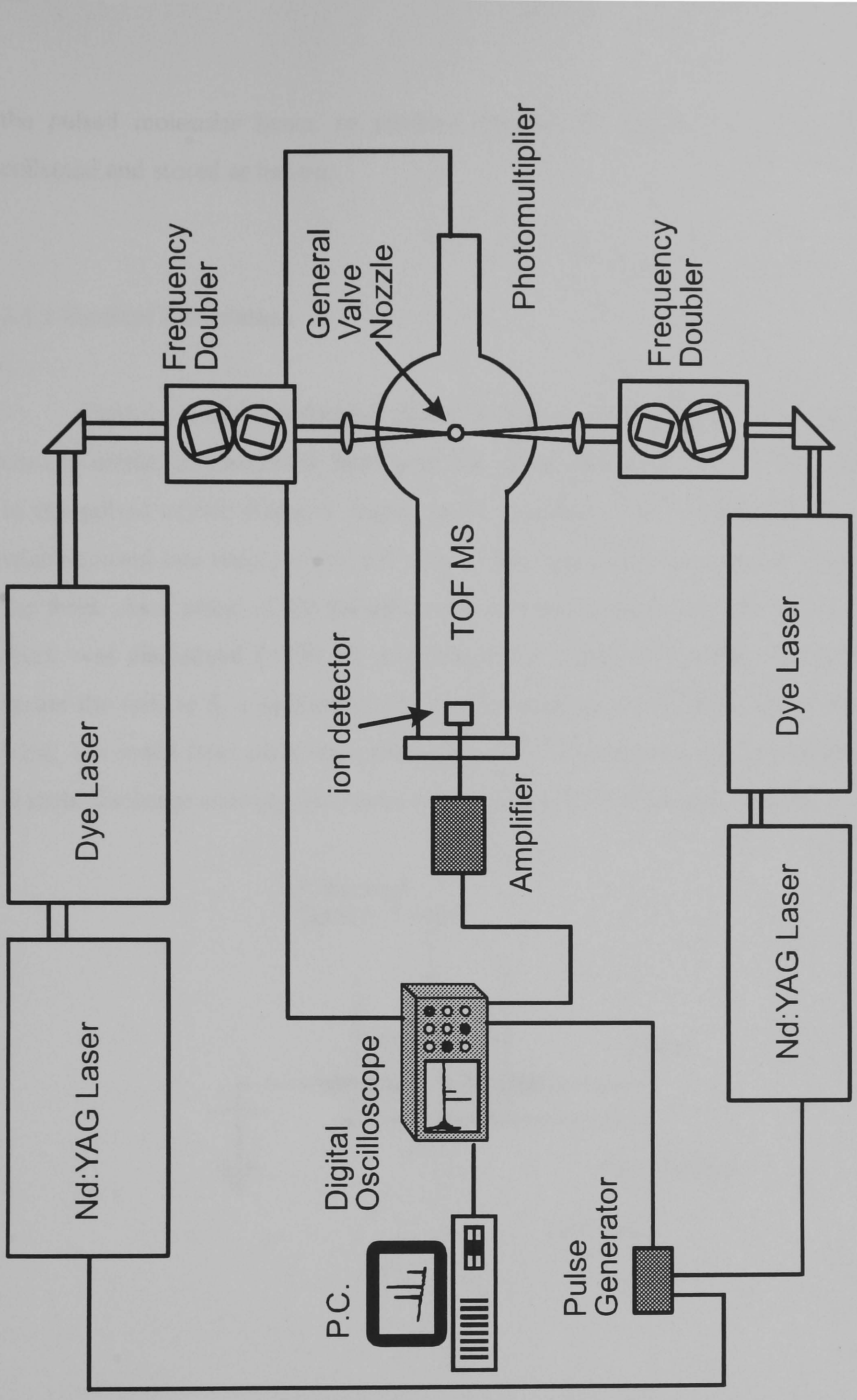

Figure 2.1: Schematic diagram of the experimental apparatus used to record REMPI and Double Resonance spectra in Bristol.

the pulsed molecular beam, to produce the ions of interest. The ion count was collected and stored as before.

2.1.1 Radical Generation

Figure 2.2 shows a diagram of the electric spark discharge attachment that was used to create the radicals of interest in the pulsed molecular beam.[1] The attachment to the pulsed nozzle (General Valve Series 9) consisted of a machined delrin block which housed two tungsten pins set about 1 mm apart, and had a metal plate fixed to the front. As a pulse of the precursor gas mixture passed over the pins an electric spark was discharged (~250 V) to produce the radical of interest. For example to create the radical S_2 a mixture of 5% H_2S in argon at a total pressure of 1 atm was used. The metal front plate was charged (~ -120 V) to prevent any ions created in the electric discharge entering the source region of the TOF mass spectrometer.

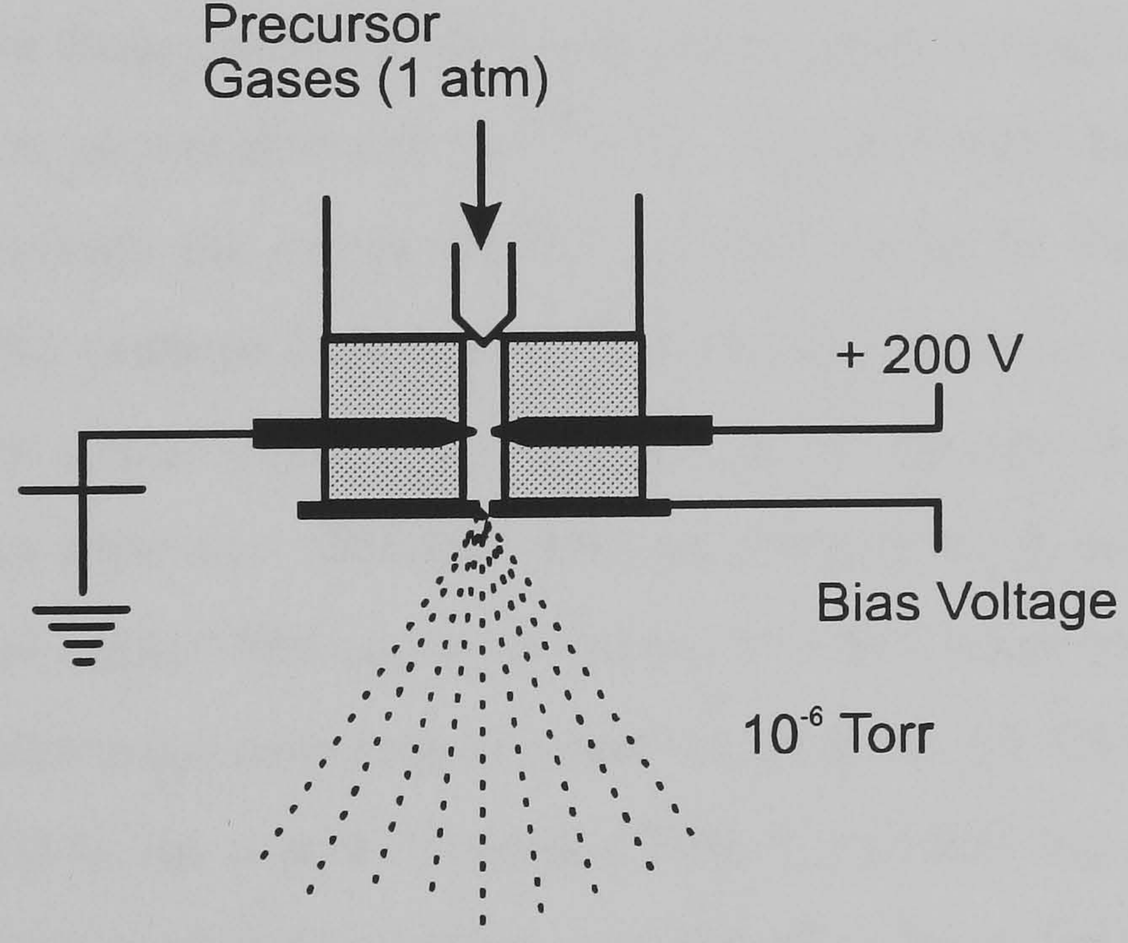

Figure 2.2: Electric spark discharge nozzle used to create radicals in a pulsed molecular beam.

2.1.2 Light Generation

The fundamental (1064 nm) light from two Nd:YAG lasers (Quanta-Ray and Spectron) was frequency doubled (532 nm), or tripled (355 nm) to pump two dye lasers (Spectra Physics PDL 1 and PDL 3) to generate the laser light used in both the experiments. A number of different dyes were used, and the outputs of the dye lasers were doubled using a selection of KDP and BBO crystals which were housed in a home made frequency doubling tracker. Typical pulse energies and bandwidths were ~1 μJ and 0.1 cm^{-1} respectively in the UV. If necessary the doubled and fundamental light were separated from each other by a selection of filters. When focusing was required quartz lenses were used with focal lengths varying from 30 cm to 100 cm.

2.1.3 Time-of-Flight Mass Spectrometer

Figure 2.3 shows a schematic of the Wiley-McLaren TOF mass spectrometer[2] used in Bristol. The design consists of two chambers which are each pumped by rotary backed oil diffusion pumps down to ~10^{-6} Torr. The molecular beam was expanded into the source through the pulsed nozzle and intercepted by the laser beam(s) to create the ions. The distance between the first of the accelerator and repeller plates which surround the source region was 10 cm to ensure that the plates did not hinder the molecular beam expansion. The ions were accelerated down the 75 cm long flight tube via a set of ion optics. The ions were subject to a two stage acceleration process. The first acceleration stage consisted of a field gradient of -30 V/mm over a distance of 10 cm, generated by the repeller plate at +3000 V and first ring of the extractor at ground. The second acceleration region was described by a field gradient of -150 V/mm over a distance of 5 cm, created by the five rings of extractor which are sequentially charged from ground to -7500 V. The third ring of the extractor had an additional user adjustable voltage control to optimise the electric fields. The ions were detected at the end of the flight tube by a Johnston multiplier which was typically held

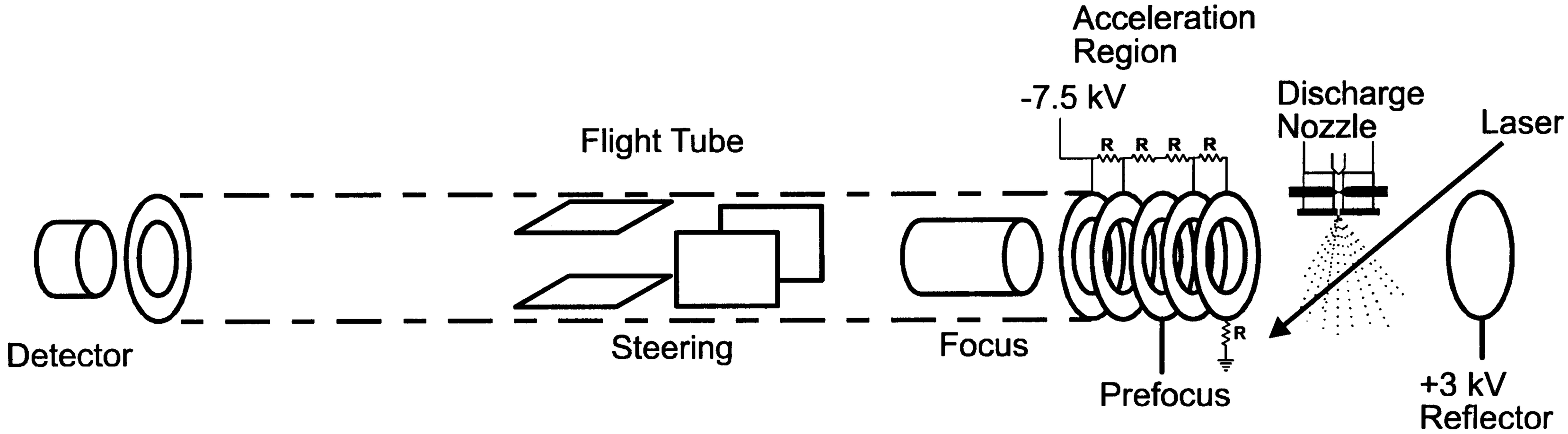

Figure 2.3: Schematic diagram of the Wiley-McLaren TOF tube used in the REMPI and Double resonance experiments in Bristol.

at -2.5 kV. The signal output from the detector was amplified and digitised by an oscilloscope (LeCroy 9310A) and collected by a PC.

2.1.4 Data Collection and Calibration

The TOF spectra were recorded and stored using the software package DRIVE written by Dr. Colin Western at the University of Bristol. Fig 2.4 shows a typical TOF spectrum. The peaks in the TOF were calibrated in terms of their mass using the following relationship:[2]

$$\text{Time of flight} \alpha \sqrt{\frac{mass}{charge}} \qquad (2.1)$$

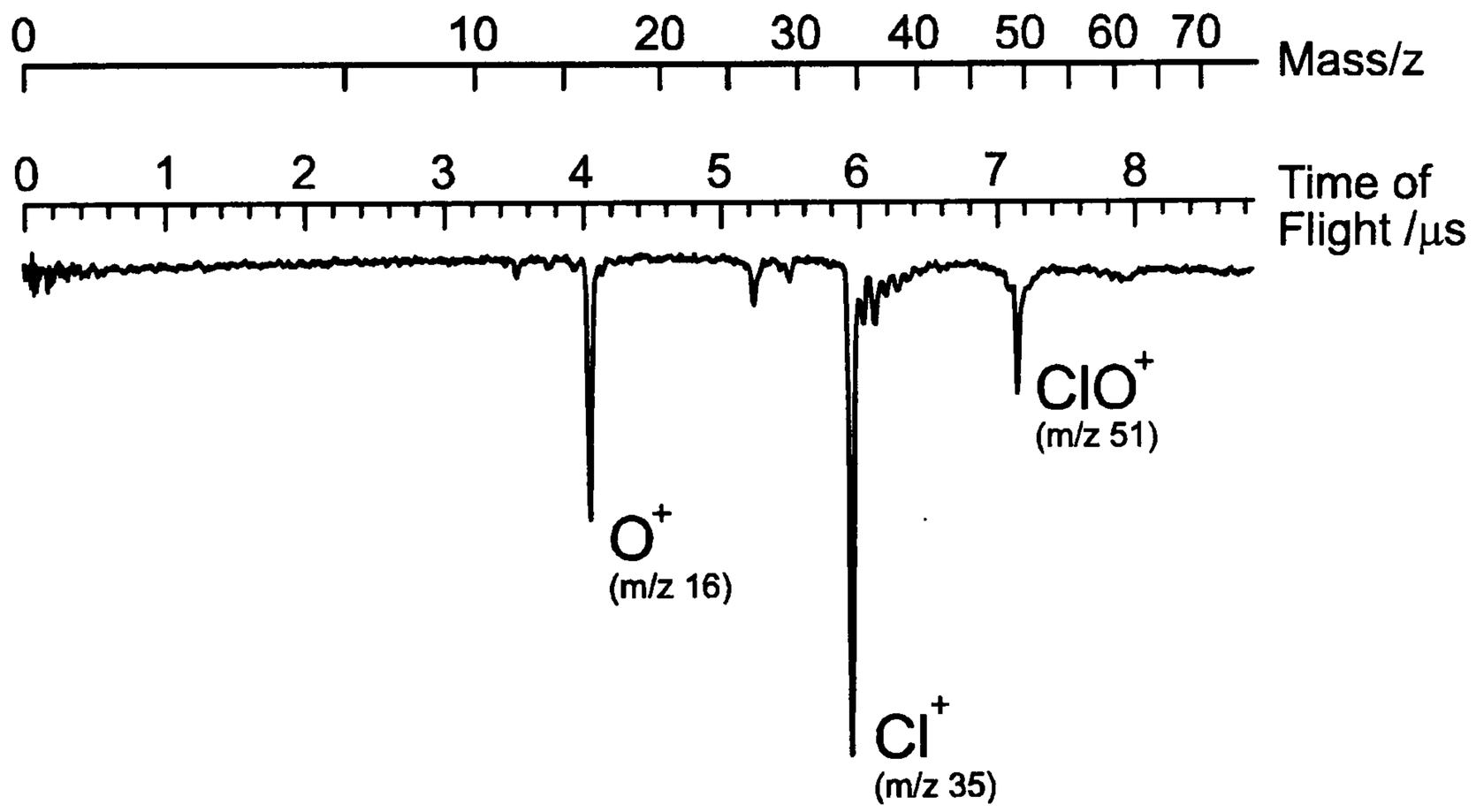

Figure 2.4: Typical TOF profile of the ions resulting from the 2+1 REMPI of ClO, showing the relationship between flight time and mass to charge ratio.

The REMPI spectra were recorded by scanning the wavelength of the laser and collecting only the portion of the ion yield which had the appropriate TOF. Typically 3 laser shots were averaged for each data point in the spectrum. Wavelength calibration of the spectra was achieved by simultaneously recording an LIF spectrum of I_2 and then comparing the recorded spectrum with the well documented B-X transition. A least squares fit of the observed vs. known line positions was performed in order to create an absolute wavenumber calibration for each spectrum. The transmission of a small portion of the laser beam through an etalon was used to linearise the scan to correct for any variations in the scan control motor speed during data acquisition.

2.2 REMPI Experiment at NIST

The apparatus at NIST[3,4] was used to produce room temperature REMPI spectra of ClO radicals. The gross design of the set-up was the same as that in Bristol, with a single laser beam being used to ionise the radicals, with mass selective detection of the ions via a TOF tube.

Figure 2.5 shows a diagram of the microwave discharge flow tube[5] used to generate the radicals for the room temperature study. The precursor gases were flowed constantly through the reactor and the radicals were created by passing a microwave discharge through the gas mixture. The resultant radicals then effused into the source region of the TOF mass spectrometer where they were probed by a laser beam propagating at right angles to it. The radicals were produced by this source with a rotational temperature of ~ 300K.

The output from an excimer (Lambda Physik XeCl 308 nm) pumped dye laser system (Lambda Physik) using various dyes was frequency doubled by either KDP or BBO doubling crystals housed in an Inrad auto tracker. The laser beam was focused into the source region of the TOF mass spectrometer with a 7.5 cm quartz lens.

The TOF considerations for the apparatus were the same as for that in Bristol, except an alternative detection method was employed. At the end of the TOF tube was a 'Daley doorknob' detector, which typically was held at 20 kV. As the ions impacted on the detector electrons were emitted which were accelerated into a fast phosphor screen. The subsequent light production was detected by a photomultiplier tube and monitored by an oscilloscope . This produced ion TOF spectra exactly analogous to that produced in the Bristol apparatus.

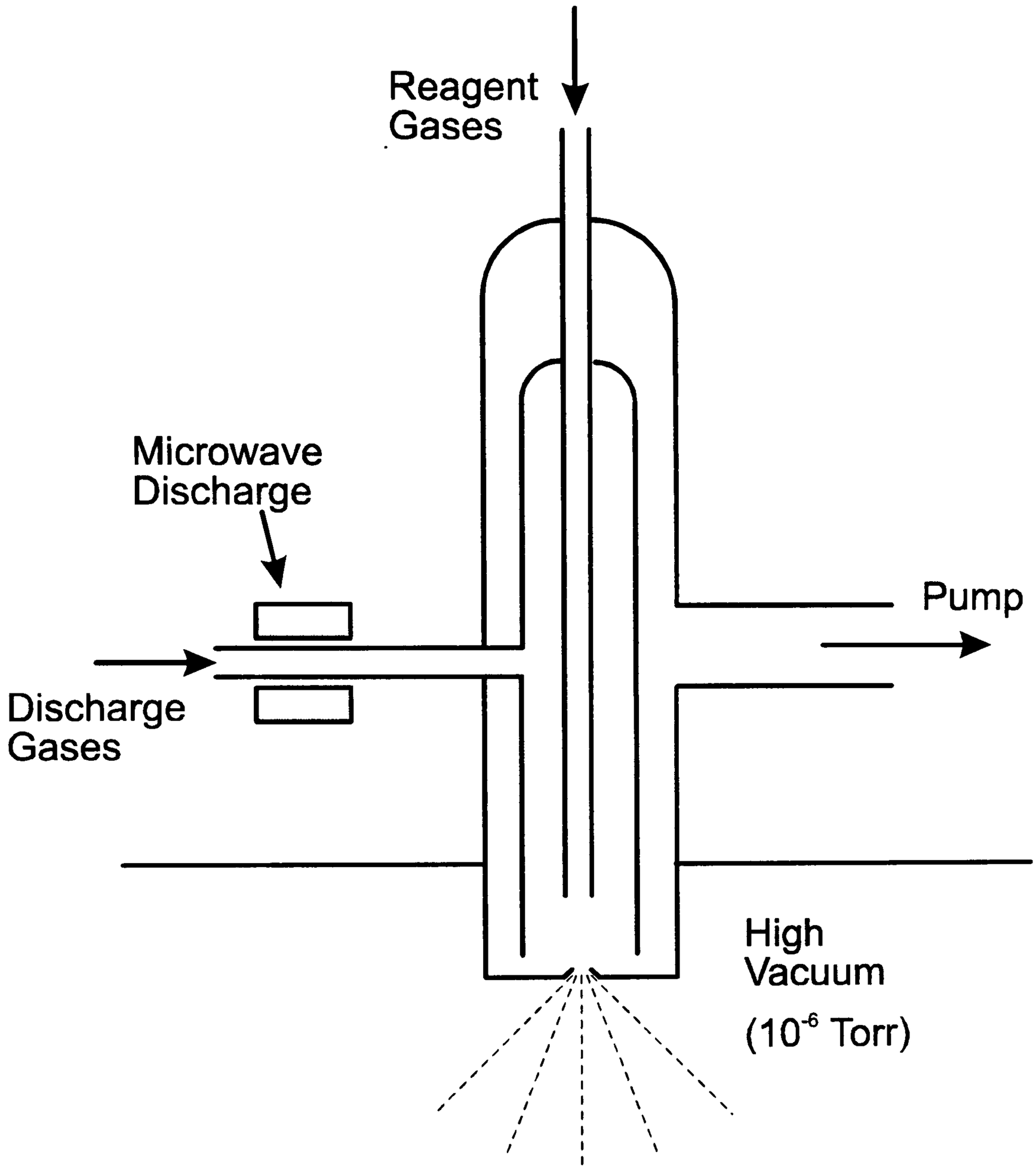

Figure 2.5: Microwave discharge flow reactor used a NIST to create room temperature ClO radicals from ozone and Cl_2 or O_2 and Cl_2.

2.3 Ion Imaging Experiment at Bristol

Figure 2.6 shows a schematic diagram of the ion imaging experiment at Bristol University which was used to record ion images from the photodissociation of Br_2 and BrCl at various wavelengths. The set-up consists of three pumped regions, one for the expansion and collimation of a molecular beam of species to be studied (typically ~90 Torr of the species in 700 Torr of Argon), the second region for photodissociation and ionisation of the photofragments to be studied, and the third for TOF mass separation and detection of the ions produced. The TOF tube, the counter propagating laser beams and the collimated molecular beam were all set-up mutually orthogonal to each other, so that the photofragments were collected along the TOF tube perpendicular to the laser beam. The ions were accelerated towards the detector, but their nascent velocity and angular distribution produced by the photodissociation process perpendicular to the detector face was preserved. Subsequent analysis of the images recorded then revealed information about the photodissociation dynamics of the molecule.

2.3.1 Light Generation.

Two laser beams were used in the ion image studies, one to photodissociate the molecule, and the second to ionise, via 2+1 REMPI, the fragments of interest for detection. In the experiments described here, atomic Br and Cl were probed using the well known 2+1 REMPI transitions.[6,7] For the photolysis wavelength regions 300 - 330 nm and 445 - 540 nm an Nd:YAG (Pro 250-10 YAG) pumped OPO (Spectra Physics MOPO 730-10) was used to photodissociate the molecules, and the output from an excimer (Lambda Physik XeCl 308 nm) pumped dye laser system (Lambda Physik) was frequency doubled using a BBO crystal to ionise the fragments of interest. The polarisation of the photolysis laser was manipulated by using a double Fresnel Rhomb, where for the majority of the images the polarisation was aligned vertically, i.e. with the electric vector perpendicular to the detector. For photodissociation over

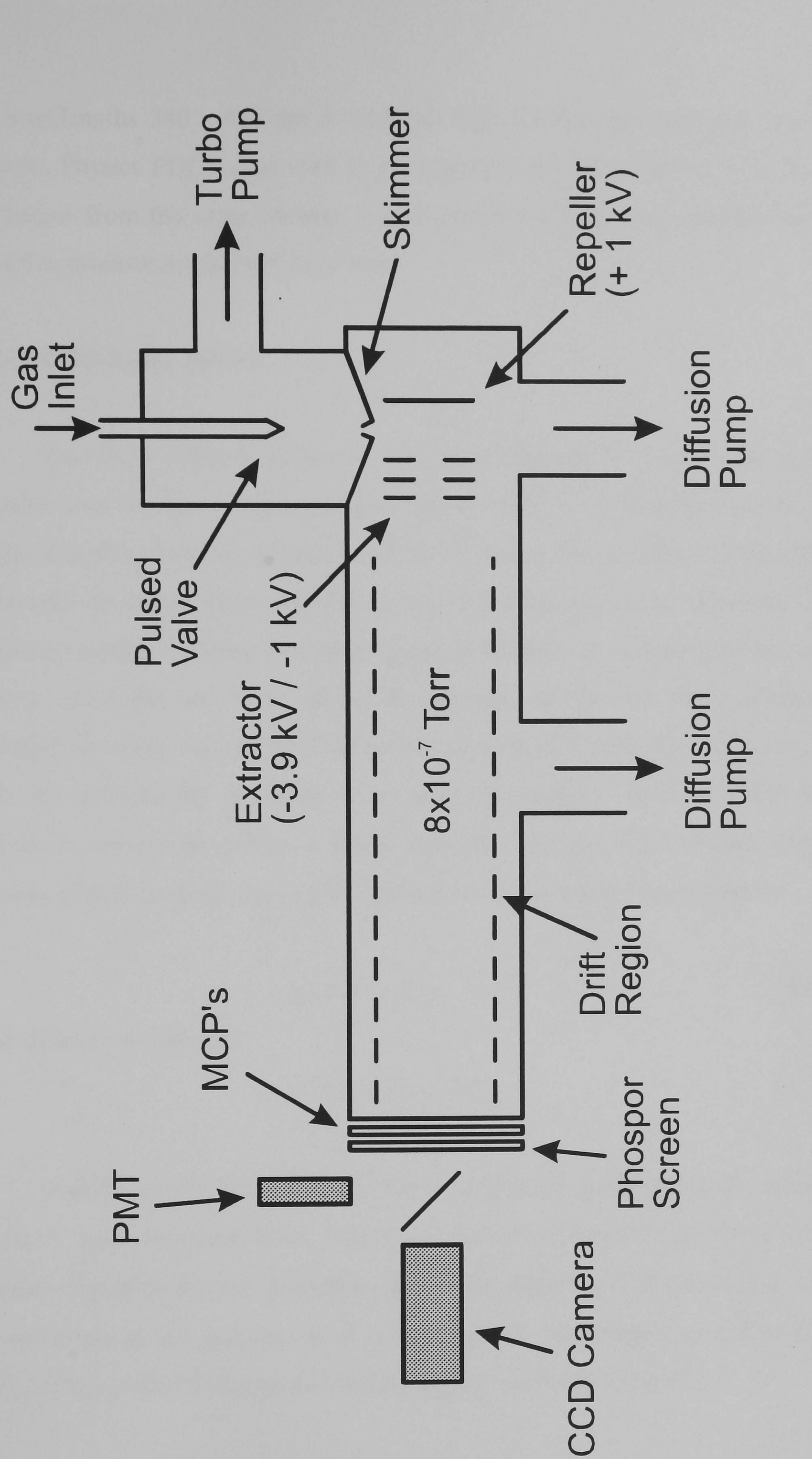

Figure 2.6: Schematic diagram of the photofragment ion imaging spectrometer used in Bristol to study the photodsissociation of Br_2 and BrCl.

the wavelengths 340 - 435 nm a Nd:YAG (Quanta Ray) pumped dye laser system (Spectra Physics PDL3) was used to generate the photodissociation laser beam, and the output from the same excimer system above was frequency doubled by a BBO crystal to produce the REMPI laser beam.

2.3.1.1 OPO Laser System

The OPO (Optical Parametric Oscillator) system[8] is a new way of creating tuneable laser radiation without the need for dye lasers. It is therefore worth spending a little time describing its operation and performance. The operation of the OPO laser can simply be described as nonlinear frequency mixing in reverse. Generally nonlinear frequency mixing combines two initial photons of different wavelengths into one final photon which has the same energy as the sum of the two initial photons. This technique is widely used in Nd:YAG lasers to produce 355 nm light where 532 nm and 1064 nm photons are combined in an optically nonlinear material. OPO uses this process in reverse by taking a single input photon (ω_p) and creating two output photons with frequencies, ω_s (signal) and ω_i (idler) that satisfy the condition:

$$\omega_p = \omega_s + \omega_i \tag{2.2}$$

or in terms of wavelength,

$$1/\lambda_p = 1/\lambda_s + 1/\lambda_i. \tag{2.3}$$

A β-Barium Borate (BBO) crystal is used as the parametric gain medium with which to 'split' the pump beam. Figure 2.7 illustrates the basic operation of the OPO process. Just as in normal frequency mixing, the angle (θ) of the crystal is critical to the operation of the process. As θ is changed the wavelengths of the two photons produced by the OPO change, but still satisfying equations 2.2 and 2.3.

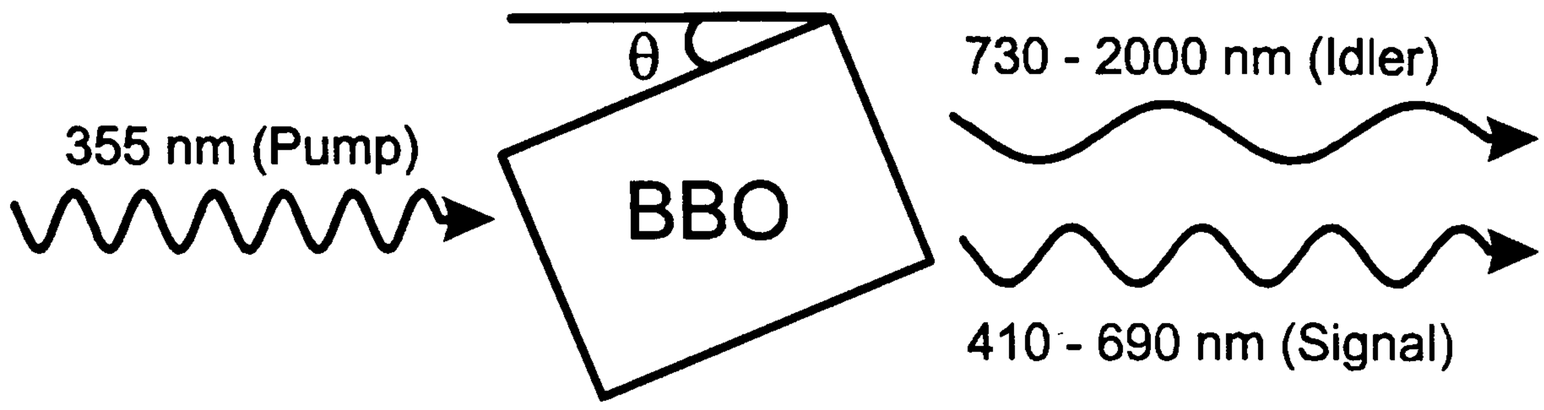

Figure 2.7: Illustration of the basic photon splitting process upon which the OPO laser system is based.

The two photons emerging from the mixing process will have a relatively broad bandwidth, so the BBO crystal is placed in a tuneable resonant cavity encompassing a diffraction grating so as to provide narrow bandwidth radiation (~ 0.15 cm^{-1}) at the desired wavelength. Figure 2.8 illustrates the resonant oscillator cavity and BBO pump configuration in the OPO system.

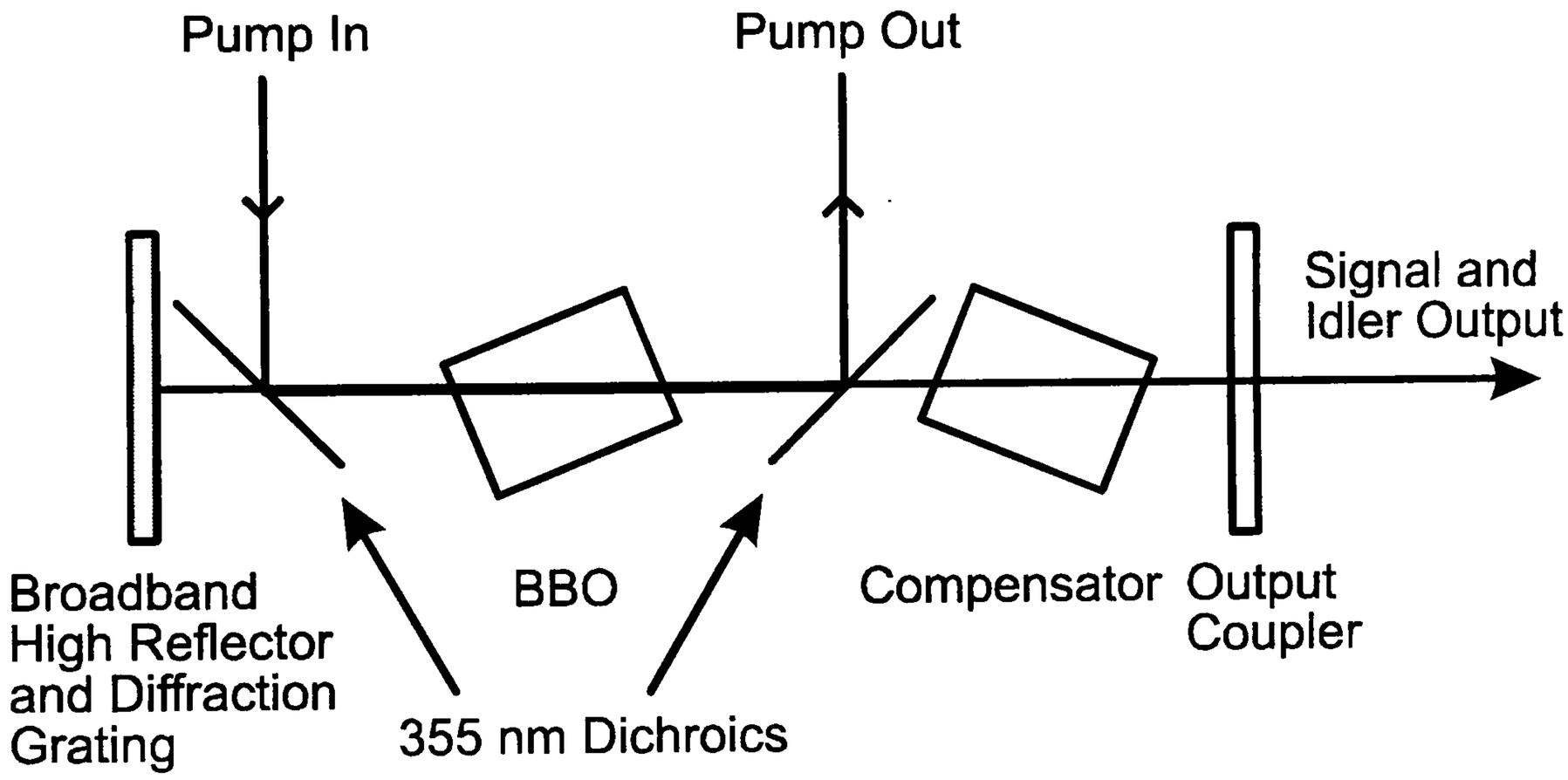

Figure 2.8: Schematic of the resonant cavity and pumping configuration in an OPO laser system. The signal and idler output exit the cavity together and are separated by a set of broadband dichroic mirrors.

In the case of the experiments described here the OPO was pumped with a 355 nm photon from a Nd:YAG laser, which enabled production of tuneable laser

radiation of 440 - 690 nm on the signal beam and 730 - 1800 nm on the idler beam, i.e. almost continuously from the near UV to the near infrared. The power of the laser radiation is enhanced by a second amplifier stage utilising a second BBO crystal which is seeded by the signal beam from the oscillator and pumped by the same 355 nm light from the Nd:YAG. This results in horizontally polarised radiation with typical pulse energies of ~ 70 mJ on the signal beam, and 35 - 10 mJ on the idler. The whole system is frequency locked by two feedback mechanisms, one which locks the path of the 355 nm pump photon from the Nd:YAG into the OPO, and a second which constantly monitors the efficiency of the OPO process. This second mechanism is crucial as it allows the wavelength of the system to be scanned which makes it of use in spectroscopic studies.

2.3.2 Time-of-Flight Mass Spectrometer

The ion optic lens arrangement in the TOF mass spectrometer is critical in providing high resolution velocity and mass selection of the photofragments prior to detection. This selectivity is achieved by designing the ion optics to fulfil the following criteria. Firstly the cloud of ions formed by the photodissociation and REMPI process should be collapsed in the dimension perpendicular to the detector. This ensures a minimum time spread over which the ions of particular interest arrive at the detector, and so minimises overlap with signal from ions of a similar mass. Secondly, the size of the image recorded on the detector should be proportional to the expansion speed of the ions formed perpendicular to the detector in the photodissociation process. In this way the kinetic energy of a photofragment formed by the photodissociation process can be deduced from the time of flight of the ion, and the size of the image recorded. Finally the ion optic set-up should minimise blurring of the image due to dependencies on the laser and molecular beam shapes, propagation directions and repulsion between the ions created (space charge effects).

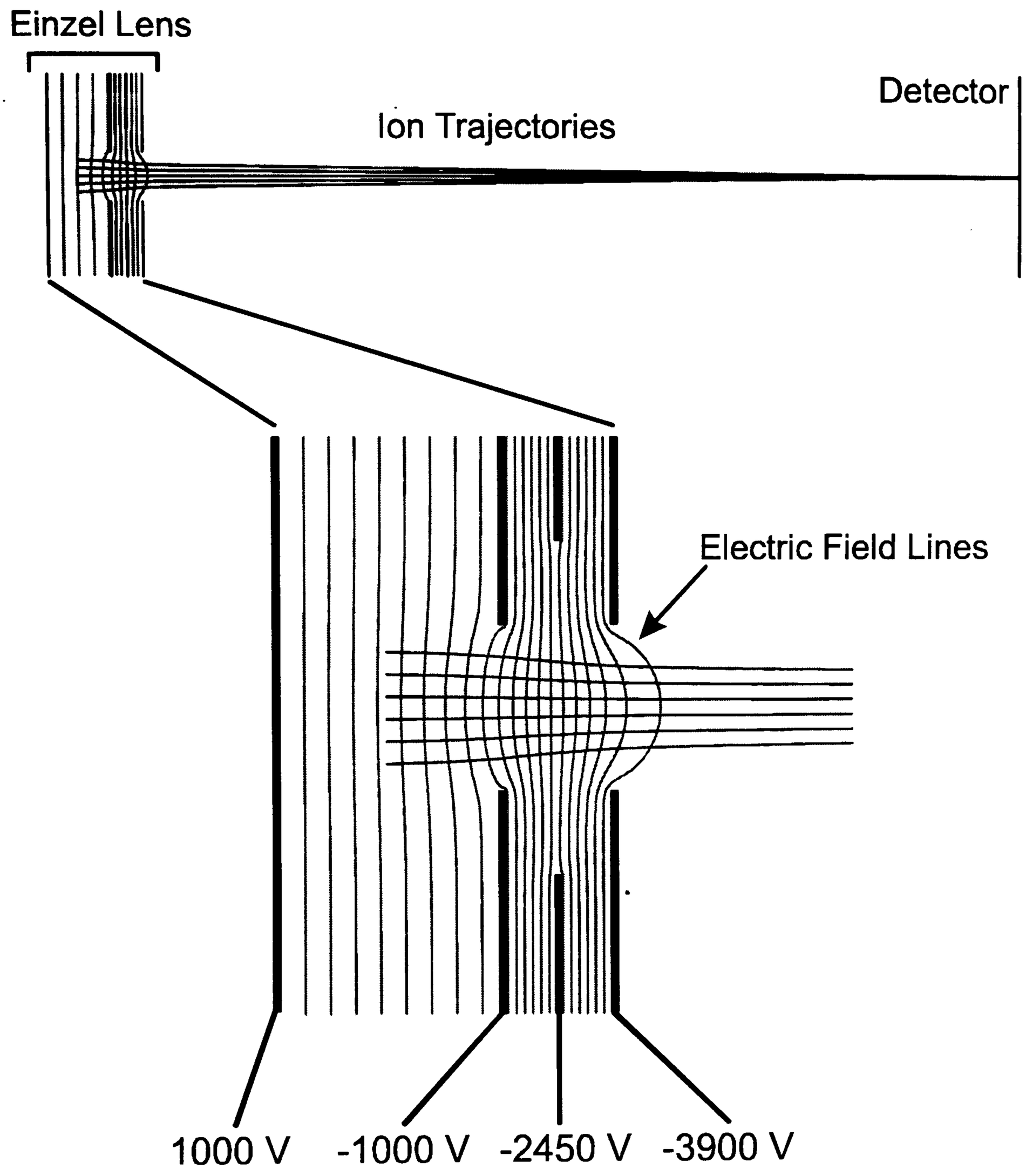

Figure 2.9: Illustrated are the results of the simulation by the SIMION 3D 6.0 computer program of the Einzel lens ion optic set-up. The curved electric field lines produced by the configuration are shown, along with the subsequent ion trajectories.

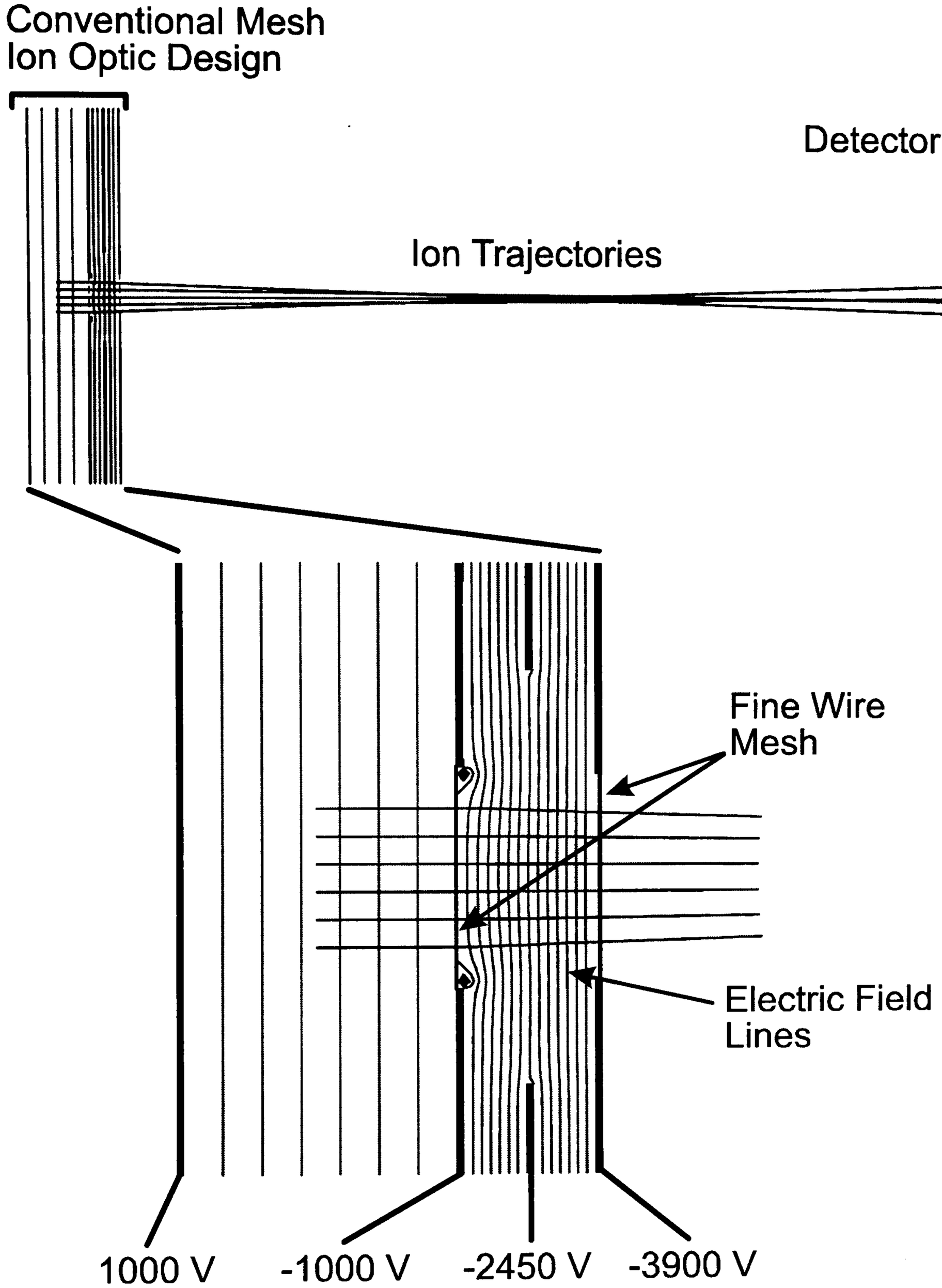

Figure 2.10: Illustrated are the results of the simulation by the SIMION 3D 6.0 computer program of the conventional Wiley-McLaren ion optic set-up. The electric field lines produced by the configuration are shown, along with the subsequent ion trajectories.

Most of these considerations were met by using the Einzel lens ion optic set-up[9] which focuses fragments of the same velocity onto the same point on the detector as well as separating the ions by their mass. This enables the construction of a 'velocity map' of the photofragments produced. The basic design of the TOF mass spectrometer was based on that of a Wiley-McLaren design.[2] The crucial difference between the conventional set-up and the Einzel lens design is illustrated in figures 2.9 and 2.10. The fine metallic meshes that are key in the conventional set-up to keeping the electric field lines as parallel as possible have been removed. As shown in figure 2.9 this creates a curved electric field which acts as a lens to focus the ions onto the detector. The focusing power of the lens is simply adjusted by changing the applied voltages. In the conventional design any adjustment in the applied voltages only changes the TOF of the fragments and does not offer any focusing control. The computer program SIMION 3D 6.0 was used to create figures 2.9 and 2.10. The software enabled construction of the ion optics used in the experiment in the computer, and then calculated the electric field gradients and ion trajectories that resulted from the design.

As well as focusing the ions onto the detector the Einzel lens design has other advantages over the conventional mesh set-up. In practice the meshes reduced the signal arriving at the detector, as transmission of ions through each mesh cannot be 100%, and each of the holes in the grid acted as a small lens in its own right, which spatially distorted the images. Of course with an Einzel lens the problem of transmission through the meshes is totally removed, as is image blurring due to production of ions from a finite volume because of the focusing conditions. However space charge effects arising from the interaction between ions which can cause image blurring are not removed and so care must be taken to work outside this regime.

2.3.3 Data Collection and Analysis

The events produced by the striking of the ions on the MCP's are recorded by collecting the positions of the subsequent light emission from the fast phosphor screen by a CCD camera (Photonic Science). The camera is time gated to only view the events associated with the TOF of the species of interest. A commercial software package PHOTON (Datacell Ltd.) running on a PC was used to establish, on a shot by shot basis, which of the individual ion events in the image satisfy user selected thresholds for minimum size and intensity, and to determine their centroids. The final image is built up by accumulating these centriods, whilst the laser frequency is scanned repeatedly across the Doppler profile of the relevant transition of the species of interest. The three-dimensional (3D) distribution is detected as a two-dimensional (2D) projection in the MCP detector. Given the assumption of axial symmetry around the direction of the electric vector of the photolysis laser beam, a filtered backprojection method is used to reconstruct the initial 3D velocity distribution from the 2D photofragment images. The mathematical transformation is discussed in more detail in appendix A. The reconstruction and analysis was performed by the IMAGE6 program, written by Prof. Y. Matsumi, of Nagoya University, Japan.

2.3.4 Ultraviolet/Visible Absorption Spectra

In the case of ion imaging of BrCl, the molecule was created by mixing Br_2 and Cl_2 in a bulb with an excess of argon. The mixture was then left to equilibrate overnight to form BrCl via the following reaction:

$$Br_2 + Cl_2 \xleftrightarrow{K_{eq}} 2BrCl\ . \qquad (2.4)$$

The equilibrium constant for the reaction (K_{eq}) ~ 7. For the study of Br photofragments the bulb was filled with an excess of Cl_2 so that almost all of the Br_2 would be consumed, this reduced contamination in the Br images due to formation of

Br atoms from photolysis of Br_2. For the study of Cl photofragments a bulb was created with excess Br_2, to consume all the Cl_2, to prevent Cl_2 contamination. To deduce the various concentrations of Br_2, Cl_2 and BrCl in the different gas mixtures a UV/Visible absorption spectrum was taken of the mixtures. This spectrum was then deconvoluted into contributions from Cl_2, Br_2 and BrCl. To make the measurements a sample of the gas mixture was placed in a cell with quartz end windows. A Perkin Elmer Lambda Bio 10 UV/Visible spectrometer utilising Deuterium and Halogen lamps was used to scan the absorption spectra in the range 200 - 600 nm. Examples of the spectra and subsequent deconvolutions are given in chapter 6.

2.4 References

1 K.N. Rosser, Q.-Y. Wang and C.M. Western, *J. Chem. Soc. Faraday Trans.* **89,** (1993) 391.

2 W.C. Wiley and I.H. McLaren, *Rev. Sci. Instrum.* **26**, 1150 (1955).

3 M.T. Duignan, J.W. Hudgens and M.C. Lin, *J. Phys. Chem.* **86**, 4156 (1982).

4 C.S. Dulcey and J.W. Hudgens, *J. Phys. Chem.* **87**, 2296 (1983).

5 G.K. Anderson and S.H. Bauer, *J. Phys. Chem.* **81**, 1146 (1977).

6 S. Arepalli, N. Presser, D. Robie and R.J. Gordon, *Chem. Phys. Lett.* **118**, 88 (1985).

7 S. Arepalli, N. Presser, D. Robie and R.J. Gordon, *Chem. Phys. Lett.* **117**, 64 (1985).

8 B.C. Johnson, V.J. Newell, J.B. Clark and E.S. McPhee, *J. Opt. Soc. Am. B.* **12**, 2122 (1995).

9 A.T.J.B. Eppink and D.H. Parker, *Rev. Sci. Instrum.* **68,** 3477 (1997).

Chapter 3

Resonance Enhanced Multiphoton Ionisation Spectroscopy of ClO

3.1 Introduction

The ClO radical is of great contemporary interest primarily because of its central role in the catalytic destruction of stratospheric ozone by chlorine,[1] via the proposed mechanism:

$$Cl + O_3 \rightarrow ClO + O_2 \quad (\Delta H = -161.5 \text{ kJ mol}^{-1}) \qquad (3.1)$$

$$ClO + O \rightarrow Cl + O_2 \qquad (3.2)$$

$$\text{net:} \quad O + O_3 \rightarrow 2O_2 \qquad (3.3)$$

The above reaction is atmospherically important as it produces ClO in considerable concentrations in the stratosphere, depending on location and season. The observed ClO concentrations are highly anti-correlated to that of ozone concentration and therefore it is generally believed that ClO plays a major role in the catalytic destruction of ozone.[1] The Cl atoms that catalytically convert ozone to O_2 and ClO via (3.1 - 3.3) come from a variety of sources, namely photolysis of chlorine containing molecules in the stratosphere, such as Cl_2, HOCl,[2] Cl_2O_2[3] and chlorofluorocarbons (CFC's).

There has also been much recent interest in the wavelength dependence of the ClO yield and quantum state population distribution when formed in the UV photolysis of molecules such as Cl_2O,[4] OClO[5] and $ClONO_2$.[6] Such studies are possible in part because of the extensive spectroscopic database already available for the ClO radical.

Figure 3.1 shows a schematic of the highest occupied molecular orbitals (MO's) of the ground state of ClO. ClO has an inverted $^2\Pi$ ground state arising from the electronic configuration .....$7\sigma^2 2\pi^4 3\pi^3$, with a ground state spin-orbit splitting constant,[9] A, of $-321.775(26)\ \text{cm}^{-1}$. ClO has been experimentally investigated by many spectroscopic techniques, including UV and VUV absorption studies,[7-12] VUV laser induced fluorescence (LIF) measurements[13] and multiphoton ionisation (MPI) experiments.[14,15] There is only one modern *ab initio* calculation[16]

on the ground state of ClO and ClO^+ giving spectroscopic parameters comparable to those obtained experimentally.

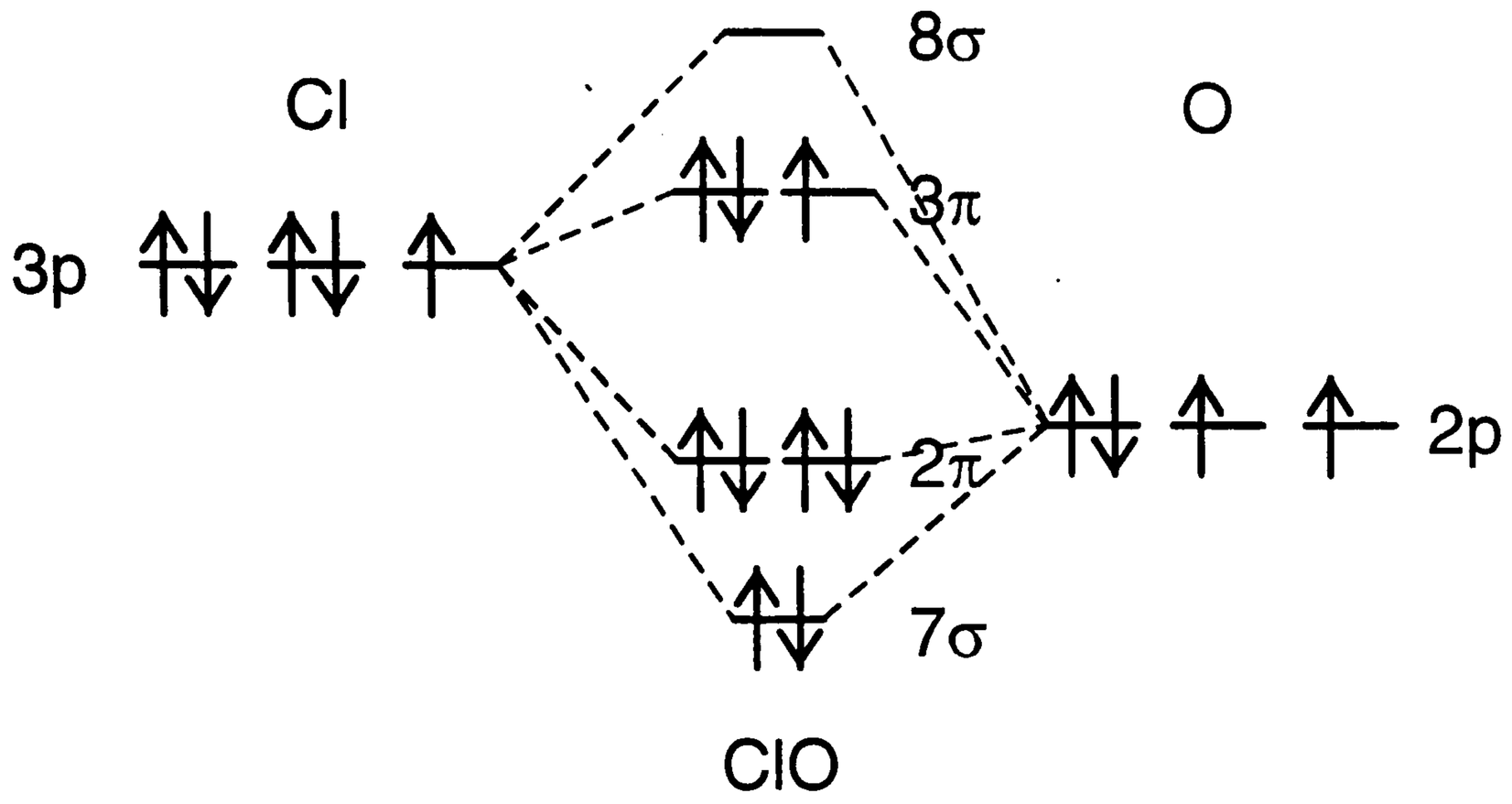

Figure 3.1: Molecular orbital diagram of ClO showing highest occupied orbitals.

The first excited state of ClO is the $A^2\Pi_i$ valence state which has been characterised by analysis of the A–X absorption system which appears as a progression of diffuse bands in the near UV. Transition to the A state arises from the promotion of an electron in the bonding 2π molecular orbital to the antibonding 3π molecular orbital. This additional antibonding nature of the A state weakens the bond between the two atoms, and reduces the vibrational frequency from ~840 cm^{-1}, in the ground state[9], to 519.5 cm^{-1} in the A state[11]. This change is also reflected in the rotational constants (B) for the X and A states, which are 0.62050 cm^{-1} and 0.4450 cm^{-1} respectively[9,11]. A reduction in the value of the rotational constant is indicative of an increase in the bond length of the molecule.

The diffuseness of the A state absorption spectrum reflects the predissociated nature of this excited state, owing to interaction with one (or more) repulsive states correlating with the ground state products $Cl(^2P)$ + $O(^3P)$. Linewidth measurements[11] indicate that the predissociation efficiency increases with increasing v' quantum number up to $v'=6$ (at which stage the level widths are ~

5 cm^{-1}) but thereafter declines (falling to ~ 0.3 cm^{-1} for $v' = 25$,[11] the highest bound vibrational level supported by the A state potential).

The A state is the only bound valence state of ClO that has been fully characterised, however, six Rydberg states of the ClO radical (labelled C to H) have been experimentally investigated to various degrees.

The lowest energy Rydberg state of ClO is the $C^2\Sigma^-$ state, which has been the subject of many spectroscopic investigations including LIF[13] and VUV absorption studies[9] resulting in a wealth of extensive and high resolution data. This has enabled a full characterisation of the spectroscopic constants for the state. The C state has a quantum defect $\delta = 2.07$ (assuming n = 4 and a value of 10.887 ± 0.005 eV for the first ionisation limit[14]), which suggests assignment in terms of the promotion of a 3π antibonding electron into the essentially nonbonding $4s\sigma$ orbital. This promotion of an antibonding electron into a non-bonding orbital results in a increased bond strength, and a decreased bond length of the radical. This is confirmed by the vibrational spacing (ω_e)[9] of the C state which increases, compared to that of the ground state, to 1077.74 cm^{-1}, indicating a stronger bond, and the rotational constant (B)[9] increases to 0.69521 cm^{-1}, indicative of a shorter bond.

The higher lying Rydberg states of ClO have been studied via single (VUV) photon absorption,[8] and via 3+1 REMPI.[14,15] Kinetic energy analysis of the photoelectrons arising in the more recent of these REMPI studies[14] has afforded what, to date, is the most accurate value of the first ionisation potential of ClO of 10.887 ± 0.005 eV. Each of these REMPI studies yielded vibrational but not full rotational resolution. The current consensus attributes the symmetry label $^2\Sigma$ to the D, E and F states, but ambiguity remains as to whether the G state, which the REMPI-PES studies show to involve an excited $^1\Delta$ ionic core,[14] should be viewed as having $^2\Delta$ or $^2\Pi$ symmetry. The nature of the H state remains to be established. Table 3.1 summarises the spectroscopic constants for the known states of the ClO radical.

State	T_e (cm^{-1})	ω_e (cm^{-1})	A_0 (cm^{-1})	B_0 (cm^{-1})	Ref.
$(ClO^+)X^3\Sigma^-$	87800				
H	74131	$\Delta G_{½}$=1023			6
$G\ ^2\Pi/^2\Delta$	73782	1066	35/17.5		6
$F\ ^2\Sigma$	70093	981			13
$E\ ^2\Sigma$	67323	1085			13
$D\ ^2\Sigma$	64484	1052			7
$C\ ^2\Sigma^-$	58490	1077.74		0.69521	7
$A\ ^2\Pi_i$	31750	519.5	-521	0.4450	9
$X\ ^2\Pi_i$	0	853.8	-321.775	0.62050	7

Table 3.1: Overview of the spectroscopic parameters of known electronic states of the ^{35}ClO radical.

There has also been interest in the photodissociation dynamics of ClO at a variety of wavelengths. Davis and Lee[17] reported the photodissociation dynamics of the Cl atom from ClO at 248 nm using photofragment translational spectroscopy and Schindler and co-workers[18] reported the translational energy of O (^1D) and Cl ($^2P_{1/2}$ and $^2P_{3/2}$) atoms from ClO photodissociation in the range 237 nm to 270 nm and at 205 nm.

The results described in this chapter are of a 2+1 REMPI investigation into the Rydberg and ion pair states of the ClO radical. Analysis of the ClO spectra recorded confirmed the previous spectroscopic assignments of the $C^2\Sigma^-$ Rydberg state, as well as providing new spectroscopic data on ion pair states of the radical. The data recorded also provided information on the spectroscopic interplay between different excited states of the radical.

3.2 Experimental

The experimental set-up and procedure followed for the two experiments (in Bristol and at NIST) have already been discussed in detail in chapter 2.

In the case of the Bristol experiment the rotationally cold radicals were created by passing an electric discharge through a gas mixture of 5% Cl_2 and 5% O_2 in argon at a total pressure of 1 atm. At NIST the room temperature ClO radicals were created by two different gas mixtures with both procedures giving the same spectral results.

$$Cl_2 \xrightarrow{\text{microwave}} 2\,Cl \xrightarrow{\text{ozone}} ClO + O_2 \qquad (3.4)$$

$$Cl_2 + O_2 \xrightarrow{\text{microwave}} 2\,Cl + 2\,O \longrightarrow 2\,ClO \qquad (3.5)$$

Firstly, 10% Cl_2 in He was discharged, with the subsequent Cl atoms produced reacted with ozone, to form ClO via (3.4). Secondly, 10% Cl_2 and 10% O_2 in He was discharged directly to produce ClO via (3.5). Both mixtures were run at a total pressure of between 5 and 8 Torr in the flow reactor. All of the room temperature spectra shown here were recorded using the second method of radical production due to the obvious experimental convenience of using Cl_2 and O_2 versus ozone.

3.3 Results and Disscussion

3.3.1 2+1 REMPI of the $C^2\Sigma^-$ Rydberg State

The initial investigation centred on studying the $C^2\Sigma^-$ Rydberg state by [2+1] REMPI. A spectrum of the C state would serve to confirm the production of ClO by the radical sources, and also provide conformation of the previously reported spectroscopic constants for the state.

Figure 3.2 shows a typical time of flight trace from the REMPI of ClO. It can be seen that most of the ClO fragments upon ionisation to form either a Cl^+ or an O^+ ion. Because of this, all of the spectra presented in this work, unless specified otherwise, were created by monitoring the $^{35}Cl^+$ channel in the time of flight spectrum. Monitoring the ClO^+ (m/z 51) channel would have lead to identical spectra, but with a poorer signal to noise ratio. The TOF mass resolution used in this work enabled separate detection of the two isotopes of Cl (35 and 37). All the spectra presented in this thesis are generated by monitoring the stronger m/z 35 peak, with the m/z 37 peak showing identical spectra, albeit at a slightly shifted energy (~ $1cm^{-1}$).

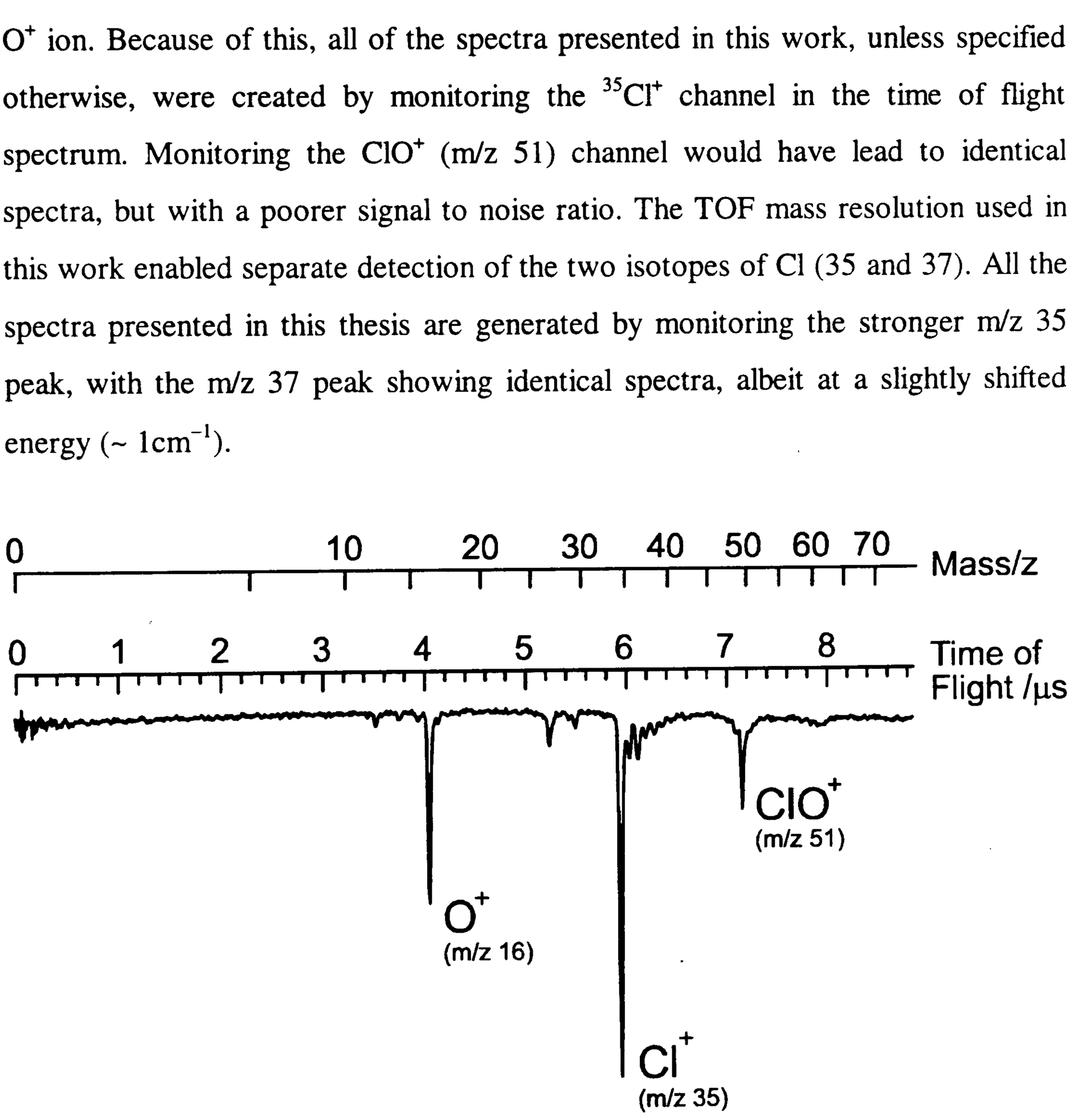

Figure 3.2: Typical REMPI time of flight mass spectrum of the ClO radical.

Figure 3.3(a) shows the observed 2+1 REMPI spectrum of the $C^2\Sigma^-$ state of ^{35}ClO, taken with the room temperature REMPI set-up at NIST. Fig 3.3(b) is a simulation of these C – X two photon bands, using the PGOPHER diatomic simulation program, with previously reported spectroscopic constants. A simulation temperature of 300 K reproduced the observed intensity ratio of the two spin-orbit components of each $C^2\Sigma^-$ - $X^2\Pi_i$ (v', 0) transitions correctly. The observed intensity ratio between the different vibronic transitions is however skewed by the wavelength dependence of the laser power, and the intensities of the different (v',0) transitions in the simulation were adjusted to match the observed spectrum. Figure 3.4 (a) shows a close-up of the experimental $C^2\Sigma^-$ ($v' = 2$ $\Omega = 1/2$) ← $X^2\Pi$ ($v = 0$, $\Omega = 3/2$) transition, along with a simulation (3.4 (b)). Clearly the agreement is not perfect, but no particular care was exercised when recording this rapid survey scan. The key points to note are: a) no alternative band contour (e.g. $^2\Delta$ or $^2\Pi$) has a contour approaching that measured, and b) the rotational contours of the C–X bands are clearly *blue* degraded. This is consistent with the shortening of the internuclear distance that occurs when a π antibonding electron is promoted to a nonbonding Rydberg orbital.

$$X\ ^2\Pi_{1/2}\ (..7\sigma^2 2\pi^4 3\pi^3) \rightarrow C\ ^2\Sigma^-\ (..7\sigma^2 2\pi^4 3\pi^2 8\sigma^1) \qquad (3.6)$$

3.3.2 Ion Pair States of ClO

Prior to this work no spectroscopic information on ion pair states of the ClO radical had been reported. As outlined in chapter 1, this is not altogether surprising due to the experimental difficulties in accessing such states, which usually requires a two colour laser spectroscopy technique. However, it is possible to predict the approximate position of the ion pair states of ClO on a potential energy diagram using the simple two ion model described in chapter 1. Figure 3.5 shows a potential energy diagram for ClO with the ground ($X^2\Pi_i$) and $A^2\Pi_i$ states indicated. The position of the first set of ion pair states, which correlate to ground, and first excited states of the Cl and O ions, are indicated by the asymptotic plots of the

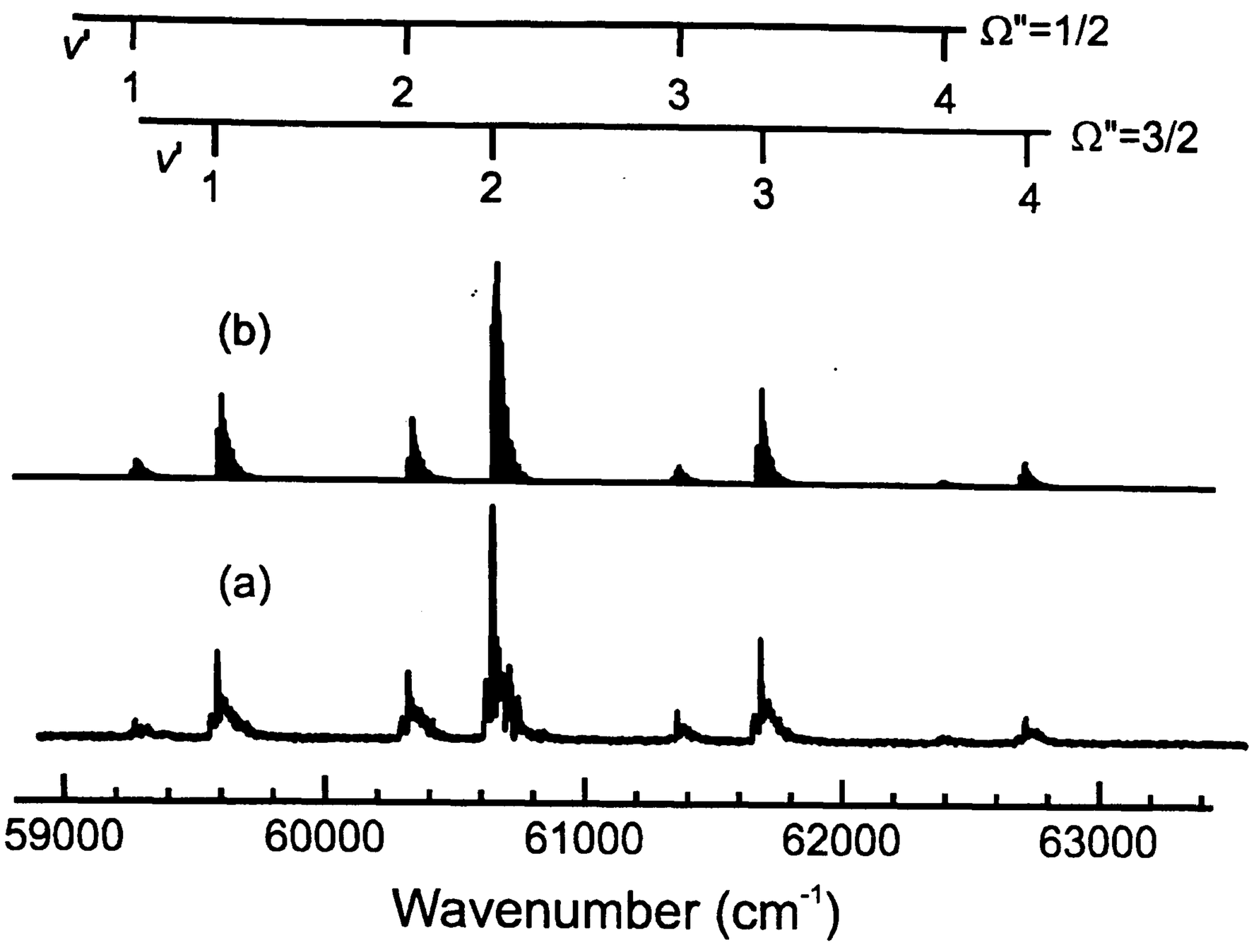

Figure 3.3: The experimental (a) and simulation (b) spectra of the $C^2\Sigma^-$ Rydberg state of ClO.

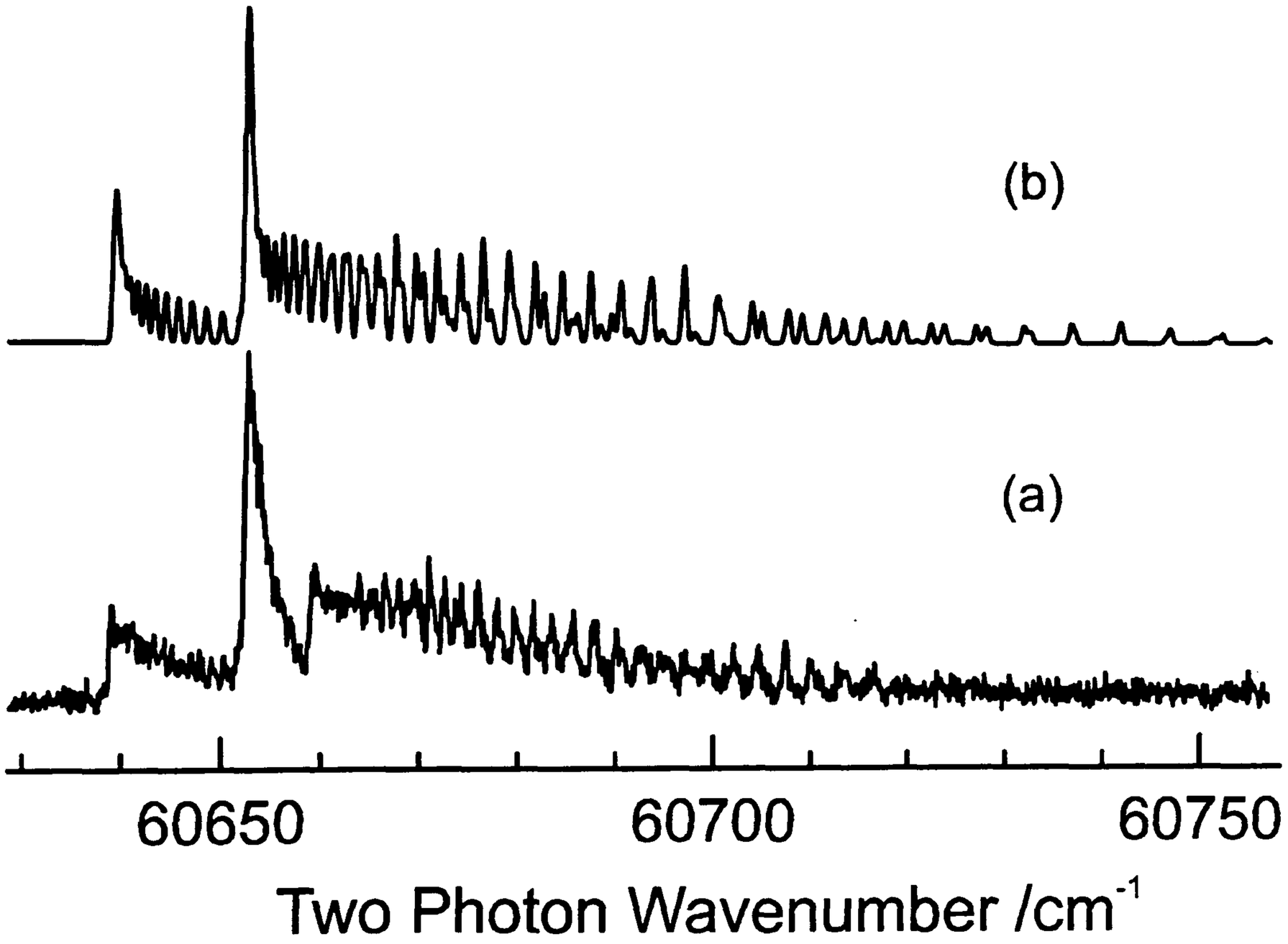

Figure 3.4: The experimental (a) and simulated (b) spectrum of the $C^2\Sigma^-$ (v=2, Ω=1/2) $\leftarrow X^2\Pi$ (v=0, Ω=3/2) transition of ^{35}ClO.

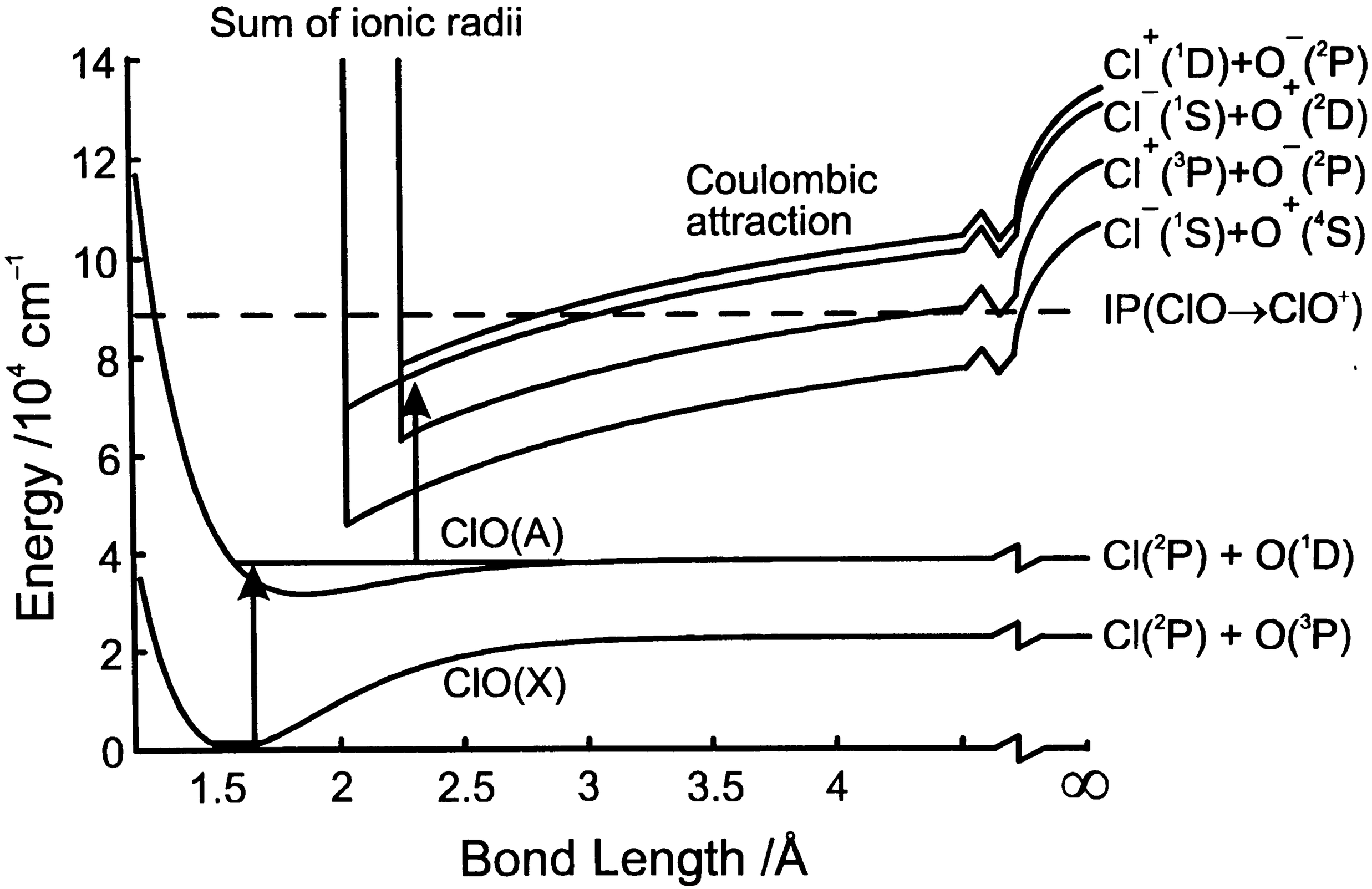

Figure 3.5: Schematic of the potential energy curves of ClO, indicating the possible position of the ion pair states of the radical. The arrows indicate the excitation pathway to the ion pair manifold.

Coulomb attraction of Cl^+ to O^- and Cl^- to O^+. The curves are positioned on the diagram using the values of 251 kJ mol^{-1} and 1314 kJ mol^{-1} for the atomic ionisation energies[19] of Cl and O, and 349 kJ mol^{-1} and 141 kJ mol^{-1} for their respective electron affinities. The estimate of the bond length of the ion pair states is indicated by the vertical lines at the sum of the relevant ionic radii[21], (Cl^+ = 49 pm, Cl^- = 181 pm, O^+ = 22 pm and O^- = 176 pm).

In this work the ion pair states were accessed, not by a 2 colour resonance technique, but by an experimentally simpler, one colour multiphoton scheme utilising the $A^2\Pi_i$ valence state of the molecule. The ClO was first excited into the $A^2\Pi_i$ state by the absorption of a single photon, and then subsequently excited into the ion pair states by absorption of second photon of the same wavelength. The radical was then promoted above the ionisation threshold of the radical by a third photon, resulting overall in a [1+1+1] ionisation process. This scheme is possible due to the fact that, as mentioned previously, the $A^2\Pi_i$ state is predissociated by one or more states, which results in a broad absorption spectrum all the way up to its dissociation limit at ~ 31800 cm^{-1}. The broadness of the absorption spectrum, coupled to the extended bond length of the state, results in good Franck-Condon overlap to the ion pair manifold.

Figure 3.6 shows a room temperature [1+1+1] spectrum of the ion pair states of the radical, from 72200 – 76200 cm^{-1}. The key features to notice in the spectrum are firstly the build-up and then abrupt decrease in signal up to 76200 cm^{-1}. In fact no [1+1+1] signal is recorded at energies > 76200 cm^{-1}. This buildup, and the cut-off of signal can be accounted for by considering the varying enhancement effects the $A^2\Pi_i$ state has on excitation into the ion pair manifold. The A state predissociation efficiency is v' dependent, with a maximum at $v' = 6$ where the lifetime broadened linewidth is ~ 5 cm^{-1}. At long wavelengths the A–X one photon resonances are relatively broad, but sparsely distributed, and the vibrational amplitude within the A state level is comparatively small, so the possibility of double resonant excitation pathways to ion pair states is rather small. Increasing the excitation energy brings us into resonance with higher v' levels of

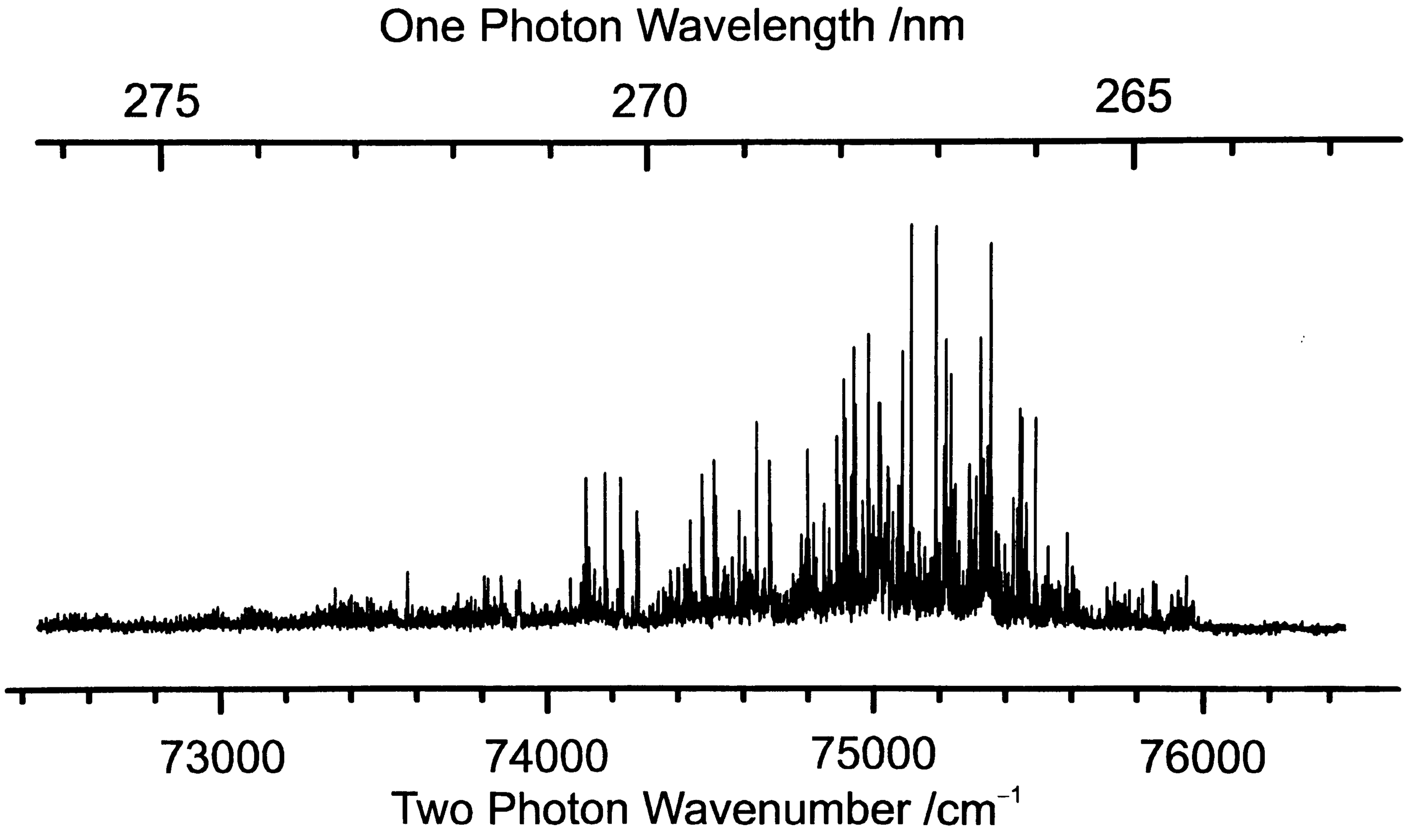

Figure 3.6: Room temperature (~300 K) 2+1 REMPI spectrum of the ClO radical.

the A state which show lesser lifetime broadening, but become progressively more tightly spaced. This relaxes the energy constraints on any accidental double resonance, whilst the increased amplitude of vibrational motion in the intermediate A state can only be of benefit in the second excitation step. Hence the observed growth in REMPI intensity, and the obvious drop in intensity at excitation energies > 38100 cm^{-1} – at which point the Cl + $O(^1D)$ dissociation limit is exceeded. The energy range covered in figure 3.6 spans the one photon range of $A_{v=11-25}$ – X, where the line width of the A state levels falls from 2.2 cm^{-1} for $v = 11$ to 0.3 cm^{-1} for $v = 26$.

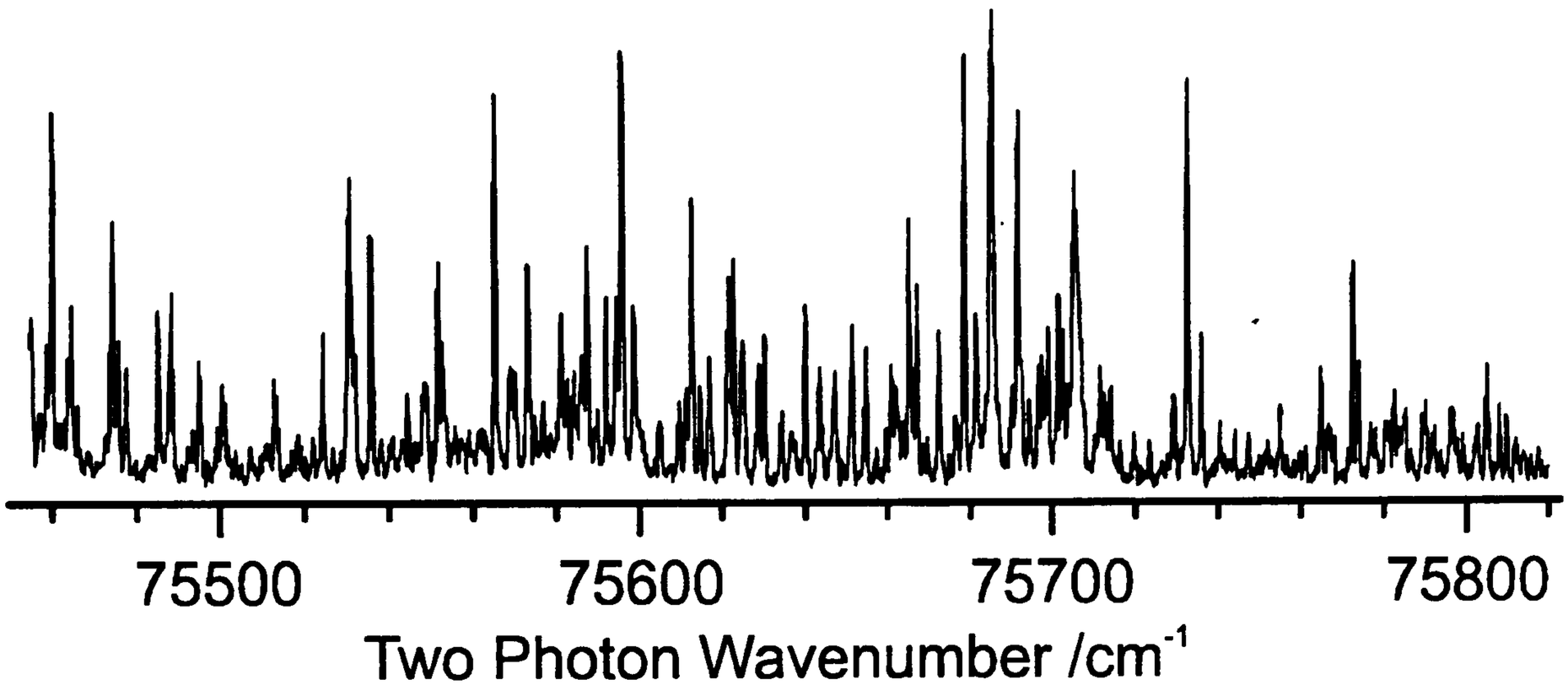

Figure 3.7: Close up of the room temperature REMPI spectrum of ClO.

The second point of interest from figure 3.6, which is illustrated more clearly in a close-up of the spectrum in figure 3.7, is the dense rotational and vibrational structure. In fact the structure is so dense that it precludes assignment in terms of rotational, vibrational and electronic state labelling. This dense structure is not unexpected for the ion pair states, for a few reasons. Firstly, it can be expected that many ion pair states correlate to each ionic limit, and recall that the vibrational spacing for each of these states is typically much less than in ground or Rydberg states, so the vibrational progressions of all of the states are expected to be dense. Secondly the rotational temperature of the radical is ~ 300K, which leads to extended rotational bands, and possible hot band excitation, which will result in overlap of spectral lines from different bands. Finally, as the $A^2\Pi_i$ state is being

used as an intermediate state in the REMPI process the energy range over which the ion pair manifold can be accessed is limited to that over which the $A^2\Pi_i$ state absorbs. The subsequent two photon energy is therefore over an energy range high up in the ion pair manifold, missing the possibly spectroscopically simpler, origin of the ion pair states.

The same spectral region of the ClO radical was also investigated using the molecular beam REMPI apparatus at Bristol University. Figure 3.8 shows the same spectral region as figure 3.6, but now with a rotationally cold (~15K) sample. The spectrum again shows the same cut-off in signal at energies $> 76200\ cm^{-1}$. The relative intensities of the various spectral features have not been normalised to account for varying laser power over the wavelength region studied. The long wavelength part of this spectrum ($\lambda > 270$ nm) was recorded using 532 nm pumping of the dye laser by the Nd:YAG, whilst, for the remainder, it was necessary to use the less intense 355 nm pump wavelength.

Under these rotationally 'cold' conditions, where we might reasonably expect a substantial reduction of most structure associated with hot band excitation (both vibrational hot bands and features originating from the excited $^2\Pi_{1/2}$ spin-orbit component of the ground state), the spectrum still displays a complex pattern of vibronic bands showing no obvious progressions. Nonetheless, the rotational structure associated with the individual bands is sufficiently simple to encourage assignment. Figure 3.9 shows a typical rovibrational band of ClO, alongside a simulation using the PGOPHER simulation program. Of particular note is the fact that the observed bands are *red* degraded, implying a decrease in the rotational constant, B, upon electronic excitation, which is exactly what would be expected for ion pair states of the molecule.

The simulation procedure (and the implicit necessity that known ground state combination differences[9] be satisfied) confirms that the transition originates from the $v'' = 0$ level of the X $^2\Pi_{3/2}$ ground state and involves an excited state of $^2\Pi_{3/2}$ symmetry resonant at the two photon energy. The spectrum is dominated by the Q

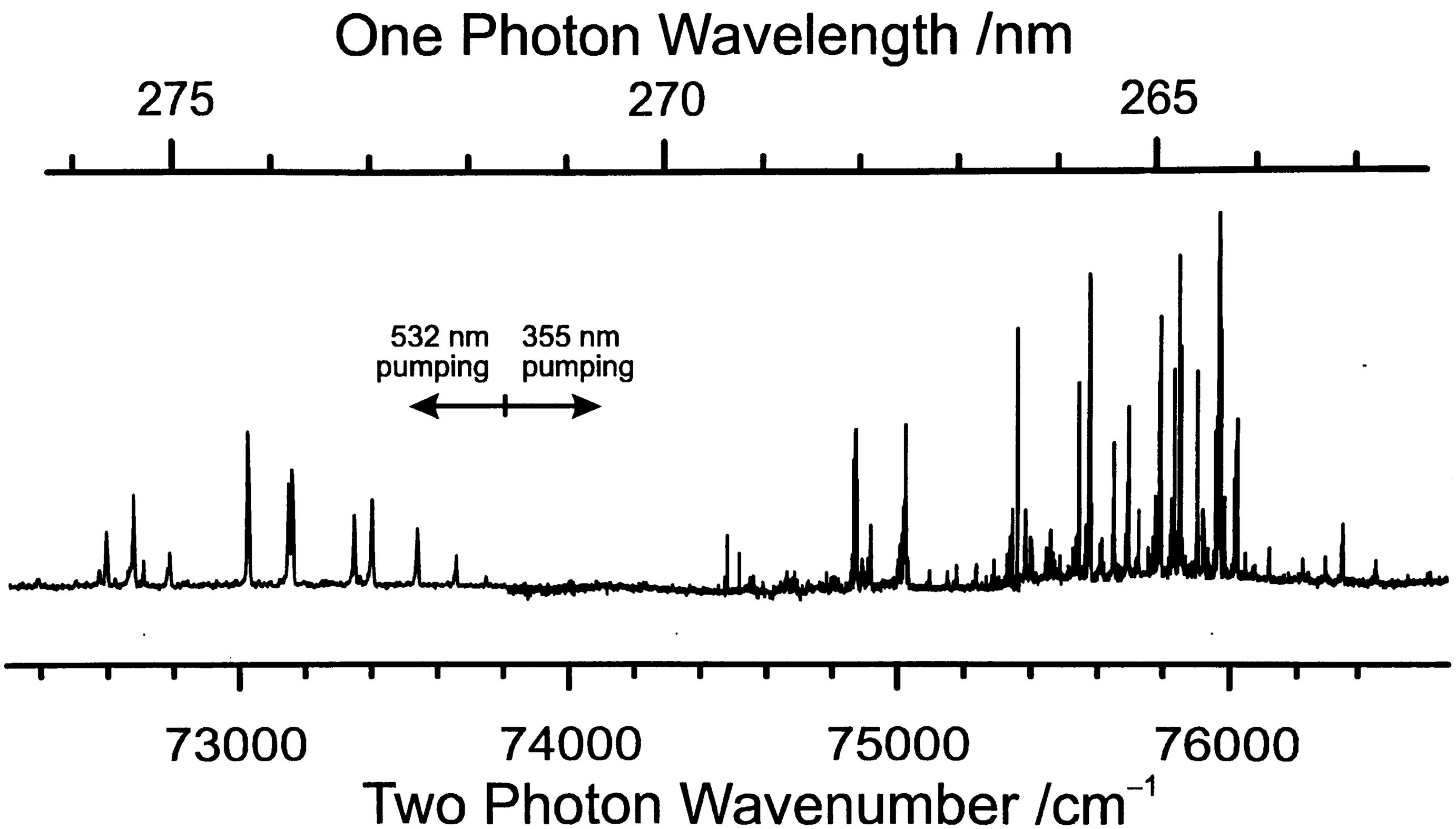

Figure 3.8: Rotationally cold (~15 K) 2+1 REMPI spectrum of the ClO radical.

branch associated with the $T_0^0(\mathbf{A})$ component[20] of the two photon transition tensor but also displays weaker $\Delta J = \pm 1$ and ± 2 branches indicating some contribution from the $T_0^2(\mathbf{A})$ component of the transition tensor. From the fitted value of B' for the band it is possible to calculate a bond length for the state, via the formula:

$$B = \frac{h}{8\pi^2 Ic} \tag{3.7}$$

where:

$$I = \frac{m_1 m_2}{m_1 + m_2} r^2 . \tag{3.8}$$

In the above equations m_1 and m_2 are the masses of the two atoms of the diatomic molecule, r is the mean bond length, h is Planck's constant, and c is the speed of light. The best fit rotational constant, B', for the excited state band shown in fig. 3.9 is 0.24068 cm^{-1}, implying an excited state bond length of 2.43 Å, some 1.6 times that of the X state. This bond length is comparable to the sum of the ionic radii of Cl^+ and O^- (2.25 Å) and of Cl^- and O^+ (2.03 Å),[21] confirming the suggestion that this band, and its neighbours evident in fig. 3.8, are associated with excitation to vibrational levels of one or more ion pair states of ClO. Table 3.2 presents rotational constants for a number of fitted $^2\Pi_{3/2} - X^2\Pi_{3/2}$ bands, with energy levels for the lower state taken from ref. 9. For the upper state the rotational energy is taken simply as $BJ(J+1)$; each sub-band origin in Table 3.2 is quoted as the separation between the lowest rotational levels of the two states, *i.e.* the frequency of the $Q_1(3/2)$ transition.

Even at low temperatures however, the complexity of the rotational band structure precludes a definite vibrational state assignment, even though a rotational characterisation was possible. This is possibly due to the oscillatory nature of the excitation to the ion pair manifold by the $A^2\Pi_i$ state, which will almost certainly not give a full and clear picture of all the vibrational bands associated with the ion pair states. It is possible that Rydberg – ion pair state configuration interaction

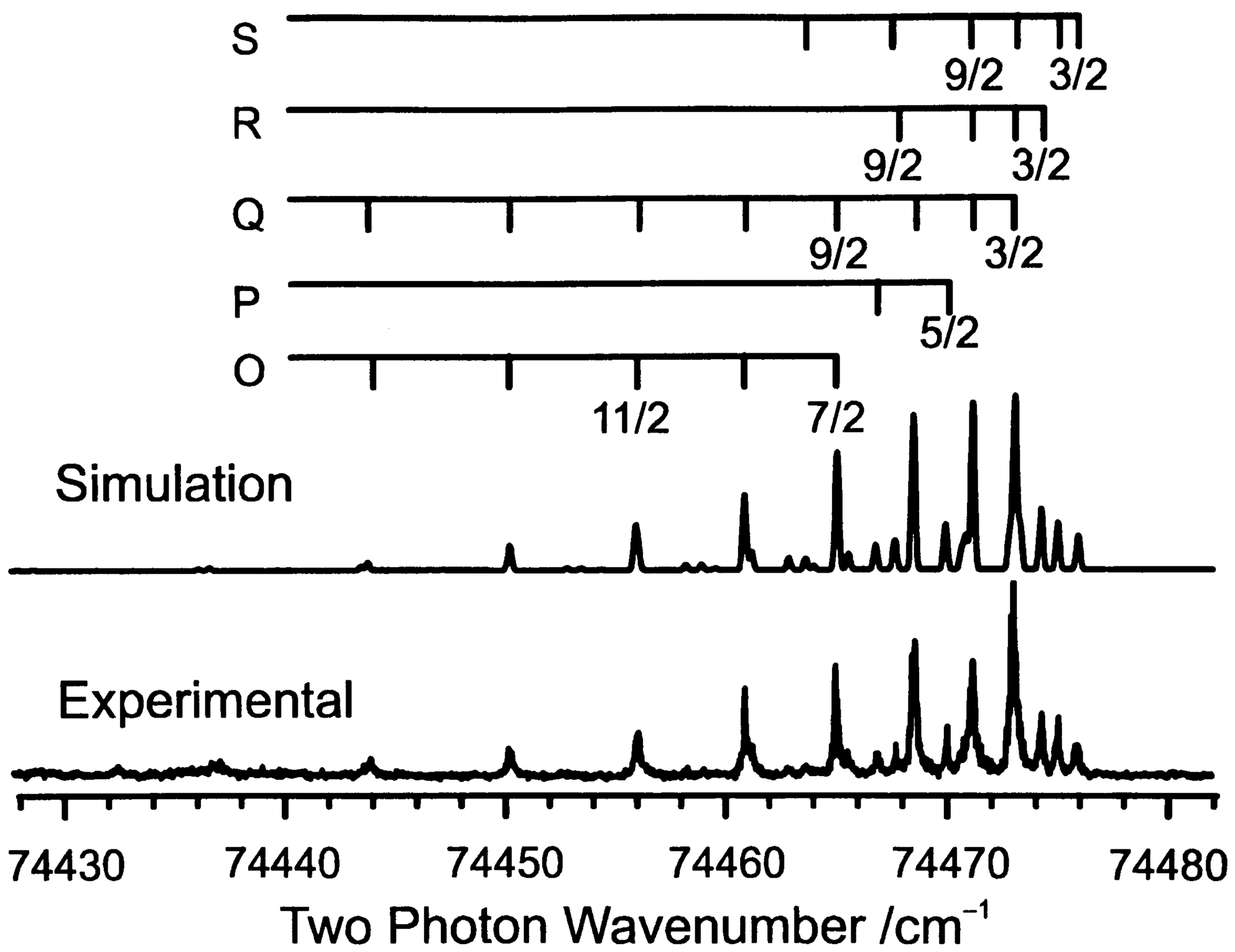

Figure 3.9: A rovibrational band at ~15 K of a $^2\Pi$ ion pair state of ClO. The combs indicate the positions of the different rotational branches, O, P, Q, R and S.

leading to double minimum potentials as seen, for example, in HCl and Cl_2 is likely to lead to further complication of the spectrum. However, as all the bands characterised arose from a $^2\Pi$ excited electronic state configuration, and the $Cl^+(^3P) + O^-(^2P)$ ion limit will support two states of $^2\Pi$ electronic symmetry we might expect the rotational bands characterised in this study to be vibrational components of these states. Further states of $^2\Pi$ symmetry can also be expected in the energy range of interest correlating with the excited asymptotic products $Cl^-(^1S) + O^+(^2D)$, and $Cl^+(^1D) + O^-(^2P)$. The use of the $A^2\Pi_i$ state to access the ion pair states also accounts for the propensity for observing only ion pair states of $^2\Pi$ symmetry. Transitions to ion pair states involve substantial redistribution of electron density along the bond, therefore such transitions are typically parallel (i.e. $\Delta\Lambda = 0$) rather than perpendicular in nature.

Sub-band Origin $^2\Pi_{3/2} - {}^2\Pi_{3/2}$ (cm^{-1})*	B' (cm^{-1})
73336.258(19)	0.2393(13)
73390.169(17)	0.24918(86)
74473.993(13)	0.24068(33)
74867.687(23)	0.2347(14)
75233.294(51)	0.2357(56)
75396.865(19)	0.2282(14)
75572.233(19)	0.22857(60)
75788.545(24)	0.23884(92)
75829.150(24)	0.2244(12)
75899.787(31)	0.2240(16)
75965.385(41)	0.2245(20)
76335.651(30)	0.2247(11)

Table 3.2: Spectroscopic parameters for the various $^2\Pi_{3/2} - {}^2\Pi_{3/2}$ transitions of the ^{35}ClO radical identified in this work. The quoted error bars are one standard deviation in units of the last significant figure.

3.3.3 Higher Rydberg States of ClO

All of the bands characterised in the previous spectra were attributed to ion pair states. None of the two photon features of the spectra recorded could be attributed to the D to H Rydberg states previously identified in VUV absorption[8] and/or 3+1 REMPI.[14,15] Such a striking discrimination between excitations involving odd and even numbers of photons is required by symmetry in molecules with a centre of symmetry, and is also frequently observed in, for example, light hydride molecules where both the combining orbitals are sufficiently 'atomic-like' for a $\Delta\ell$ = odd or even propensity rule to apply.[20,22] Neither seems likely to provide an explanation for the present observations. It is suggested that the non-observation of 2+1 REMPI signal associated with the D to H Rydberg states may be a consequence of the fact that, for these states, the first excitation step will be accidentally near resonant with levels of the A state. This resonance will lead to rapid loss of ClO via absorption to the predissociated A state, but will not enhance two photon absorption to the Rydberg state as the dominant electronic configuration of the A state (.....$7\sigma^2 2\pi^3 3\pi^4$) and those of the known Rydberg states (.....$7\sigma^2 2\pi^4 3\pi^2 n\ell\lambda^1$) differ by more than one electron.

3.4 Conclusions

The current study has yielded new spectroscopic data on the never before investigated ion pair states of the ClO radical, as well as confirming previous assignments and constants of the $C^2\Sigma^-$ Rydberg state. An explanation is also offered as to why the D to H Rydberg states of the radical have been seen in 1 and 3 photon studies, but not in 2 photon investigations.

Due to the combination of spectroscopic congestion that is indicative of ion pair states, and the varying nature of excitation to the ion pair manifold by the $A^2\Pi_i$ state, a full rotational, vibrational and electronic characterisation proved unfeasible. However the knowledge that the $A^2\Pi_i$ state can provide a route to the ion pair states of the molecule, singles out the ClO radical as a prime candidate for investigation using double resonance multiphoton ionisation. A study of this type, should be able to yield a full characterisation of the ion pair states of the radical. One stumbling block to this investigation is however, that the $A^2\Pi_i$ state is short lived and does not fluoresce due to predissociation. This fact makes it more difficult to set up a double resonance scheme, as fluorescence from the valence state is usually used as a guide to setting up the pump laser beam in a double resonance experiment. The short lifetime of the $A^2\Pi_i$ state also means that the double resonance process is competing against the predissociation process and so high powers are also required which means that the one colour process still provides signal. However preliminary work on such a study has been carried out, using a two colour ionisation scheme, where the first photon populates the $A^2\Pi_i$ state, and the second excites from the $A^2\Pi_i$ state into the ion pair manifold. Figure 3.10 shows two, two colour spectra of a rotational band of a ClO ion pair state. The spectra are plotted against probe laser energy, and both spectra show two bands, the one colour band of the type already presented, and a 2 colour double resonance band. The two double resonance peaks are offset from each other in the two spectra by the difference in the pump laser energy.

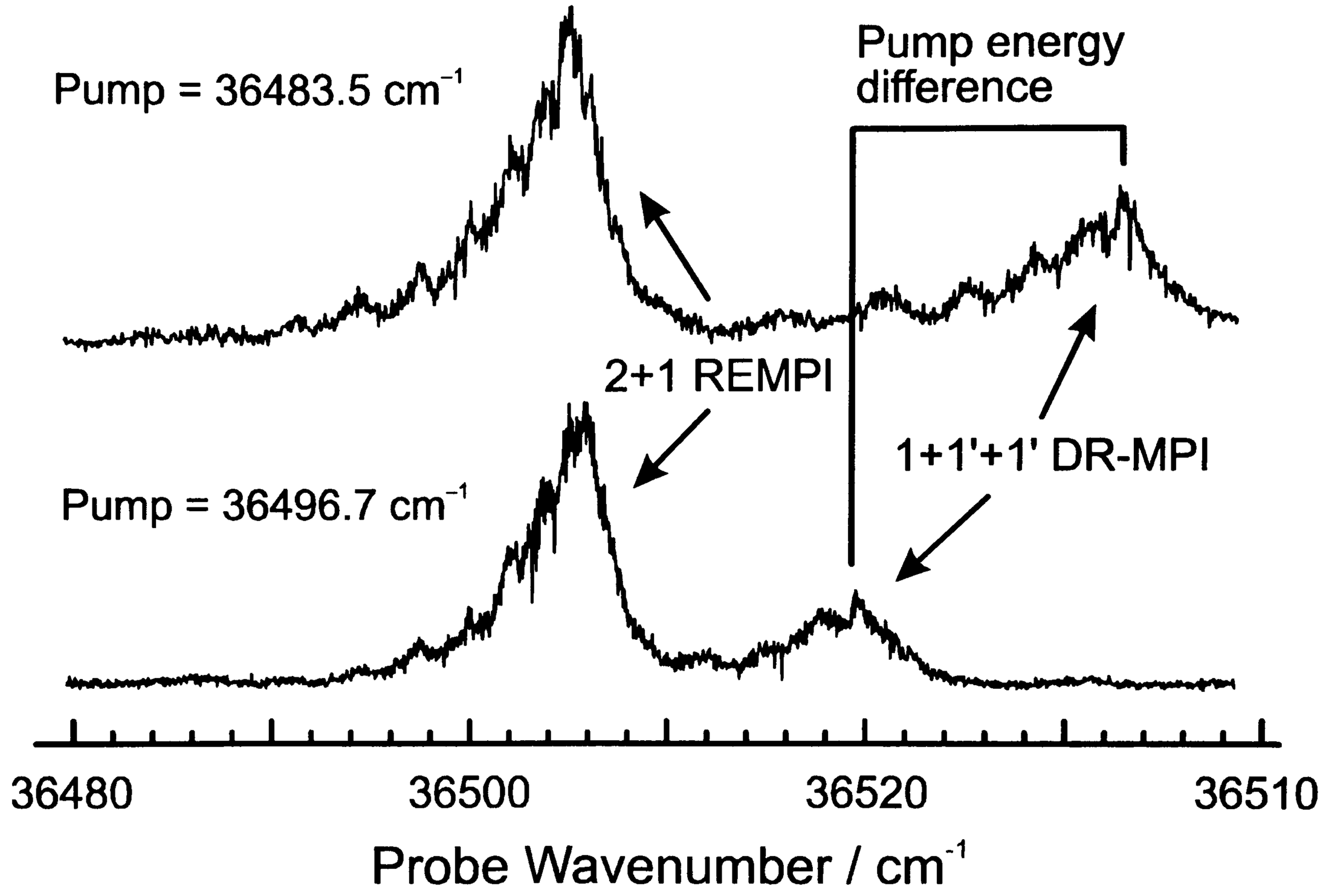

Figure 3.10: Double resonance spectra of the ion pair states of ClO recorded via the $A^2\Pi_i$ state. Both 2+1 REMPI and double resonance signal are recorded in the two spectra, with the double resonance bands offset from each other by the energy difference between the pump photons.

3.5 References

1 R.P. Wayne, G. Poulet, P. Biggs, J.P. Burrows, R.A. Cox, P.J. Crutzen, G.D. Hayman, M.E. Jenkin, G. Le Bras, G.K. Moortgat, U. Platt, and R.N. Schindler, *Halogen Oxides: Radicals, Sources and Reservoirs in the Laboratory and in the Atmosphere*, European Commission, Luxembourg: Office for Official Publications of the European Communities, ISBN 92-827-4642-9, (1996) and references cited therein.

2 R.N. Schindler, M. Liesner, S. Schmidt, U. Kirchner, Th. Benter, J. Photochem. Photobiol. A: Chem. **107**, 9 (1997).

3 M.J. Molina, A.J. Colussi, L.T. Molina, R.N. Schindler, T.L. Tso, *Chem. Phys. Lett.*, **173**, 310 (1990).

4 C.M. Nelson, T.A. Moore, M. Okumura, and T.K. Minton, *J. Chem. Phys.* **100**, 8055 (1994).

5 R.F. Delmdahl, S. Baumgärtel, and K.-H. Gericke, *J. Chem. Phys.* **104**, 2883 (1996).

6 C.M. Nelson, T.A. Moore, M. Okumura and T.K. Minton, *Chem. Phys.* **207,** 287 (1996).

7 G. Porter, *Discuss. Faraday Soc.* **9**, 60 (1950).

8 N. Basco and R.D. Morse, *J. Mol. Spectrosc.* **45**, 35 (1973).

9 J.A. Coxon, *Can. J. Phys.* **57**, 1538 (1979).

10 R.A. Durie and D.A. Ramsay, *Can. J. Phys.* **36,** 35 (1958).

11 J.A. Coxon and D.A. Ramsay, *Can. J. Phys.* **54**, 1034 (1976).

12 P.W. McLoughlin, C.R. Park and J.R. Wiesenfeld, *J. Mol. Spectrosc.* **162**, 307 (1993).

13 Y. Matsumi, S.M. Shamsuddin and M. Kawasaki, *J. Chem. Phys.* **101**, 8262 (1994).

14 N.P.L. Wales, W.J. Buma and C.A. de Lange, *Chem. Phys. Lett.* **259**, 213 (1996).

15 M.T. Duignan and J.W. Hudgens, *J. Chem. Phys.* **82**, 4426 (1985).

16 H.-S. Song and E.-M. Sung, *Bull. Korean Chem. Soc.* **14**, 476 (1993).

17 H.F. Davis and Y.T. Lee, *J. Phys. Chem.* **100**, 30 (1996).

18 S. Schmidt, Th. Benter and R.N. Schindler, *Chem. Phys. Lett.* **282**, 292 (1998).

19 P.W. Atkins, M.J. Clugston, M.J. Fazer and R.A.Y. Jones, *Chemistry*, Longman, ISBN 0-582-35590-7 (1988).

20 M.N.R. Ashfold, S.G. Clement, J.D. Howe and C.M. Western, *J. Chem. Soc., Faraday Trans.* **89**, 1153 (1993).

21 J.E. Huheey, E.A. Keiter and R.L. Keiter, *Inorganic Chemistry: Principles of Structure and Reactivity*, 4th edition, Harper Collins ISBN 0-06-042995-X (1993).

22 R.D. Johnson III and J.W. Hudgens, *J. Chem. Phys.* **94**, 5331 (1991).

Chapter 4

Double Resonance Multiphoton Ionisation Spectroscopy of S_2

4.1 Introduction

The S_2 radical has been the subject of much spectroscopic investigation. S_2 provides an analogue of O_2, which has importance in many areas of chemistry, as well as much of the spectroscopy of S_2 being of interest in its own right. Unlike O_2 however, S_2 is a transient species and is only produced in sulphur flames or discharges,[1-3] or at high temperatures (>800K) in sulphur vapour. S_2 has been previously investigated by a number of techniques including VUV, UV and visible absorption spectroscopy,[4-10] LIF,[11-13] and REMPI.[14] These studies have led to a wealth of spectroscopic information on the valence states of the radical, and a characterisation of many of the Rydberg states. This chapter reports on an investigation into the Rydberg and ion pair states of S_2 using the technique of double resonance multiphoton ionisation. The data presented extends the previous knowledge of the Rydberg states of S_2 as well as, for the first time, characterising ion pair states of the radical.

Figure 4.1 illustrates the ground state molecular orbital occupation of S_2. The $X^3\Sigma_g^-$ state arises from the doubly occupied $4\pi_g^*$ orbital. The ground state has been well characterised from electron paramagnetic resonance (e.p.r.) spectroscopy[15] and microwave studies.[16] The first excited molecular configuration ..... $9\sigma_g^2 3\pi_u^3 4\pi_g^3$ gives rise to 6 states, $B^3\Sigma_u^-$, $c^1\Sigma_u^-$, $A'^3\Delta_u$, $A'^3\Sigma_u^+$, $b^1\Delta_u$ and $^1\Sigma_u^+$.[17] Of these states the $B^3\Sigma_u^-$ state has been the focus of the most investigation due to its strong transition strength.

The B-X transition of S_2 is very strong in the ultra violet and visible region and is the source of the blue colouration of flames containing sulphur species. The transition also has cosmological interest, and was detected by the Hubble Space telescope observing the Shoemaker-Levy comet impacting on Jupiter.[18] It has also been proposed as a candidate for the tuneable chemical laser,[19] due to the wealth of

bands which, at high temperature, produce almost complete coverage of the UV and visible region. High resolution spectroscopic characterisation of the $B^3\Sigma_u^-$ state has been complicated however by the presence of the nearby $B''^3\Pi_u$ state, which arises from the $.....9\sigma_g^2 3\pi_u^4 4\pi_g^1 10\sigma_u^1$ configuration. The two states interact strongly, which leads to large perturbations in the energy levels of both. A deperturbation analysis has however been completed,[11–13] and the subsequent spectroscopic knowledge is crucial as it is these states which serve as the intermediate valence states in this double resonance investigation.

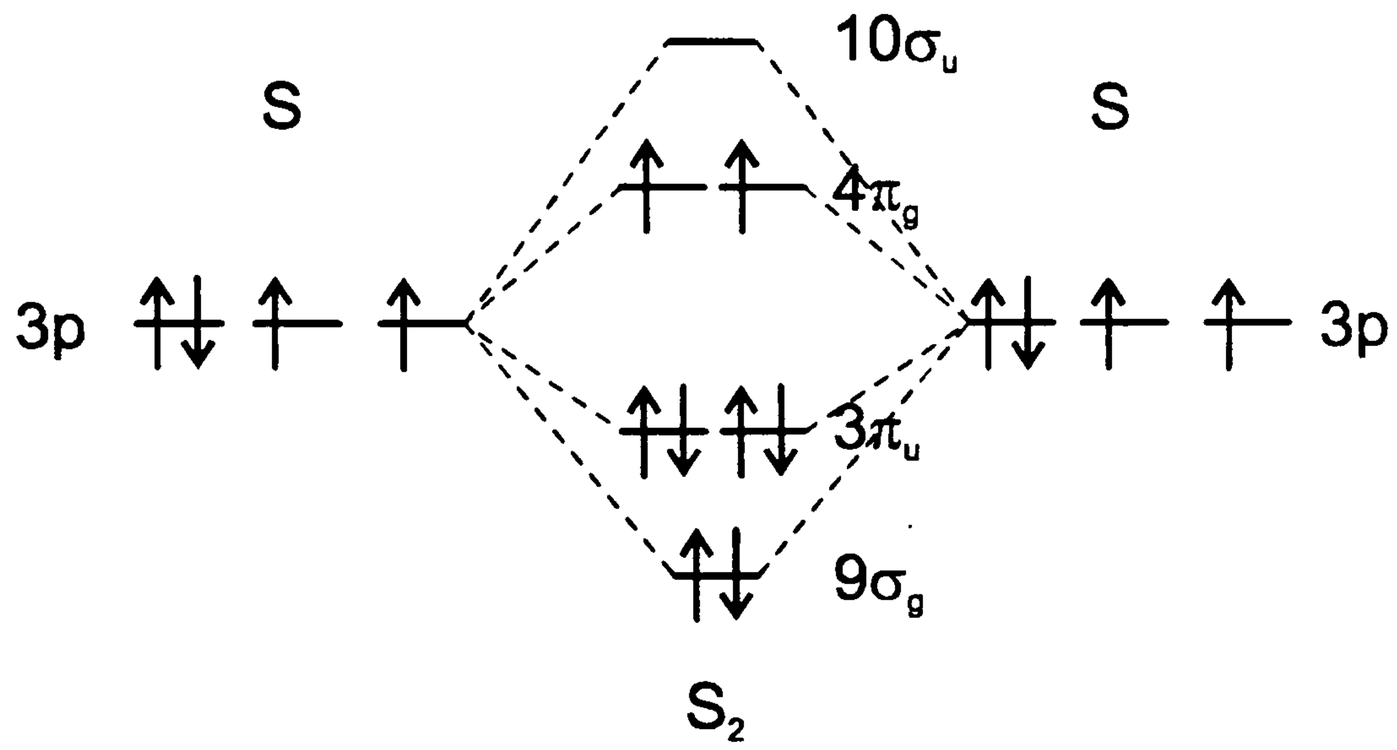

Figure 4.1: Illustration of the highest occupied molecular orbitals of S_2.

The focus of this work is on the Rydberg and ion pair states of S_2. Previously only Rydberg states have been spectroscopically characterised, mostly using single photon VUV absorption techniques. This has lead to the assignment of mainly *u* Rydberg states, due to the $g \leftrightarrow u$ selection rule for single photon transitions. The low lying $C^3\Sigma_u^-$ and $D^3\Pi_u$ states[7–10] and the higher lying E and F states[4–6] have all been investigated and characterised, at least partially, by these single photon absorption methods. The only known *g* Rydberg state of S_2 is the $(3d\pi)^3\Delta_g$ state, which was investigated using 2+1 REMPI.[14] Table 4.1 summarises the known spectroscopic constants for selected states (Rydberg and valence) of S_2 as well as the lower states of

S_2^+. Note from the table the similarity between the rotational and vibrational constants for the Rydberg states and the ground state of the ion. This is typical of Rydberg states, which are essentially made up of the ion core, which dominates the spectroscopic character, orbited by a single non-bonding electron.

$^{32}S_2$	Origin / cm^{-1}	ω_e / cm^{-1}	B_e / cm^{-1}
F	66385		0.3134
E	65876	817.3	0.3081
$(3d\pi)^3\Delta_g$	63478.2	797.8	0.3150
$D^3\Pi_u$	58782	793.8	0.3066
$C^3\Sigma_u^-$	55582	829	0.3219
$B^3\Sigma_u^-$	31835	434	0.224
$B''^3\Pi_u$	30905	339	0.209
$X^3\Sigma_g^-$	0	726	0.295

$^{32}S_2^+$	Origin / cm^{-1}	ω_e / cm^{-1}	B_e / cm^{-1}
$b^4\Sigma_g^-$	30920	580	
$A^2\Pi_u$	22345	553	0.2524
$a^4\Pi_u$	17440	600	
$X^2\Pi_g$	(75500)	806	0.3175

Table 4.1: The spectroscopic constants for selected valence and Rydberg states of $^{32}S_2$ and the lowest states of $^{32}S_2^+$.

Figure 4.2 summarises the relative energies of the more important previously investigated valence and Rydberg states of S_2. The first ionisation energy has been measured as 9.356±0.002 eV by VUV photoelectron spectroscopy[20] and photoionisation mass spectrometry[21] and is indicated in the figure.

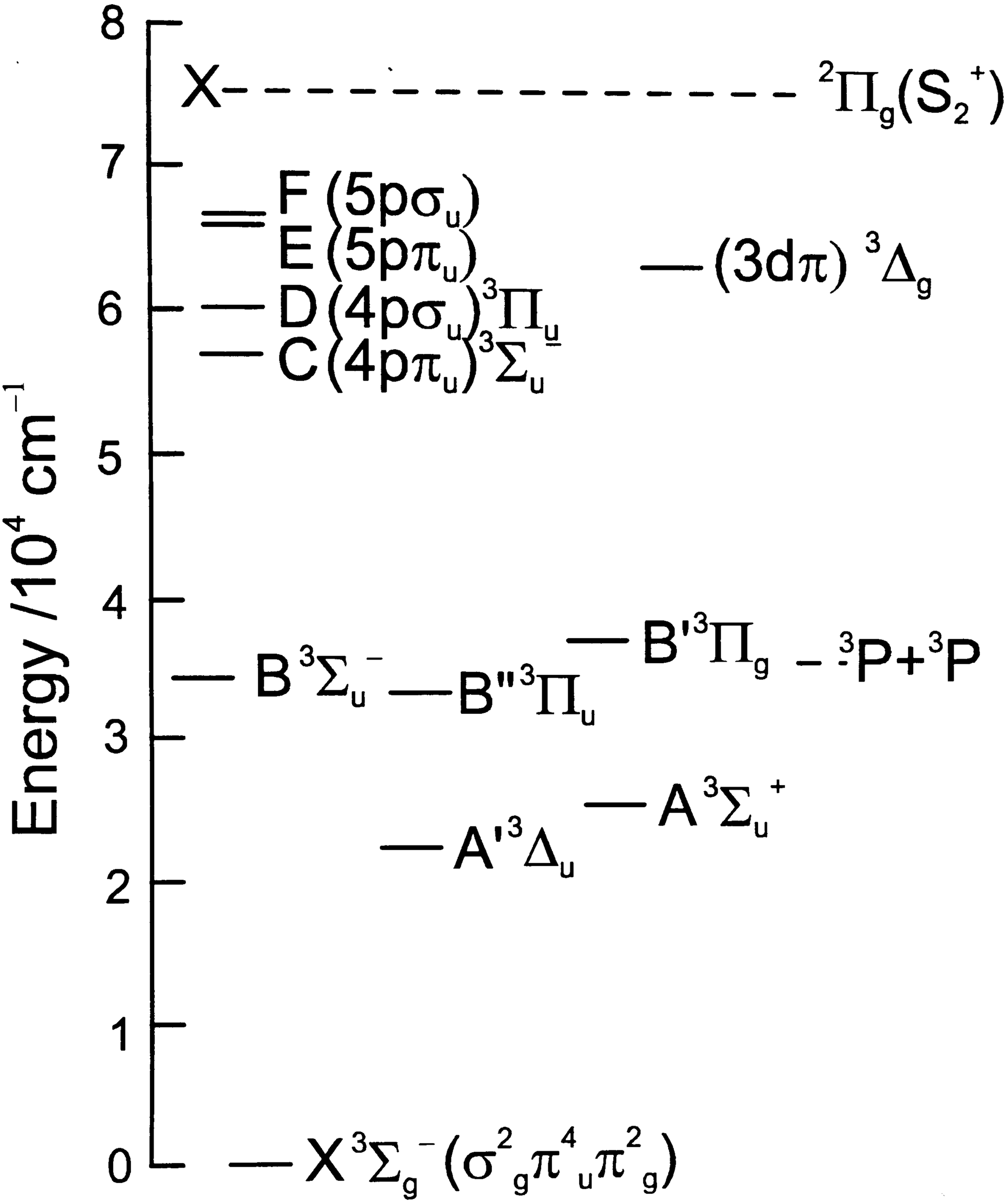

Figure 4.2: Relative energies of the ground and selected valence and Rydberg states of S_2.

The use of the double resonance multiphoton ionisation technique is crucial in the investigation of *g* Rydberg and ion pair states of S_2. As mentioned previously the change in Franck-Condon factors associated with the technique provides access to the ion pair states at extended bond lengths. However for investigations into Rydberg states which do not possess extended bond lengths, it might be envisaged that the simpler technique of 2+1 REMPI may be employed. In the case of S_2 however the 2+1 technique is not useful above the energies of the previous characterisation of the first 3 vibrational levels of the $^3\Delta_g$ Rydberg state. This is due to the wealth of bands in the valence region of S_2, which provide enhancement for the 1+2 REMPI process which produce spurious ion signals in the 2+1 REMPI spectrum. As the laser is scanned to shorter wavelength, the 1+2 peaks become so frequent, as to dominate the spectrum and so mask any 2+1 progressions. This problem is completely removed in the double resonance technique as no multiphoton transitions are used. This allows relaxation of the focusing conditions, which results in a dramatic decrease in the 1+2 transition probability. In fact the wealth of states in the valence region is advantageous to the double resonance process as they provide a host of states at a wide range of energies through which the double resonance scheme can excite.

4.2 Experimental

The experimental procedure and set-up used in the investigation has already been described in chapter 2. To create the rotationally cold S_2 radicals studied in the experiment 5% H_2S in Ar at a total pressure of 1 atm was passed through the electric discharge nozzle. The ions produced by the double resonance process were separated by mass and detected by a TOF mass spectrometer. The LIF from the valence states of the radical was collected and monitored by a photomultiplier tube orthogonal to the laser beams.

Figure 4.3 illustrates a typical TOF spectrum recorded for the double resonance multiphoton ionisation of S_2. All the spectra recorded were created by monitoring the m/z = 64 mass channel, i.e. only $^{32}S_2$. Any signal at a slightly different mass due to the different isotopes of Sulphur were not considered as the natural relative abundance's strongly favour the $^{32}S_2$ combination. Natural relative abundances of the different isotopes of sulphur are: ^{32}S:95.02 %, ^{33}S:0.75 %, ^{34}S:4.21 % and ^{35}S:0.02 %.

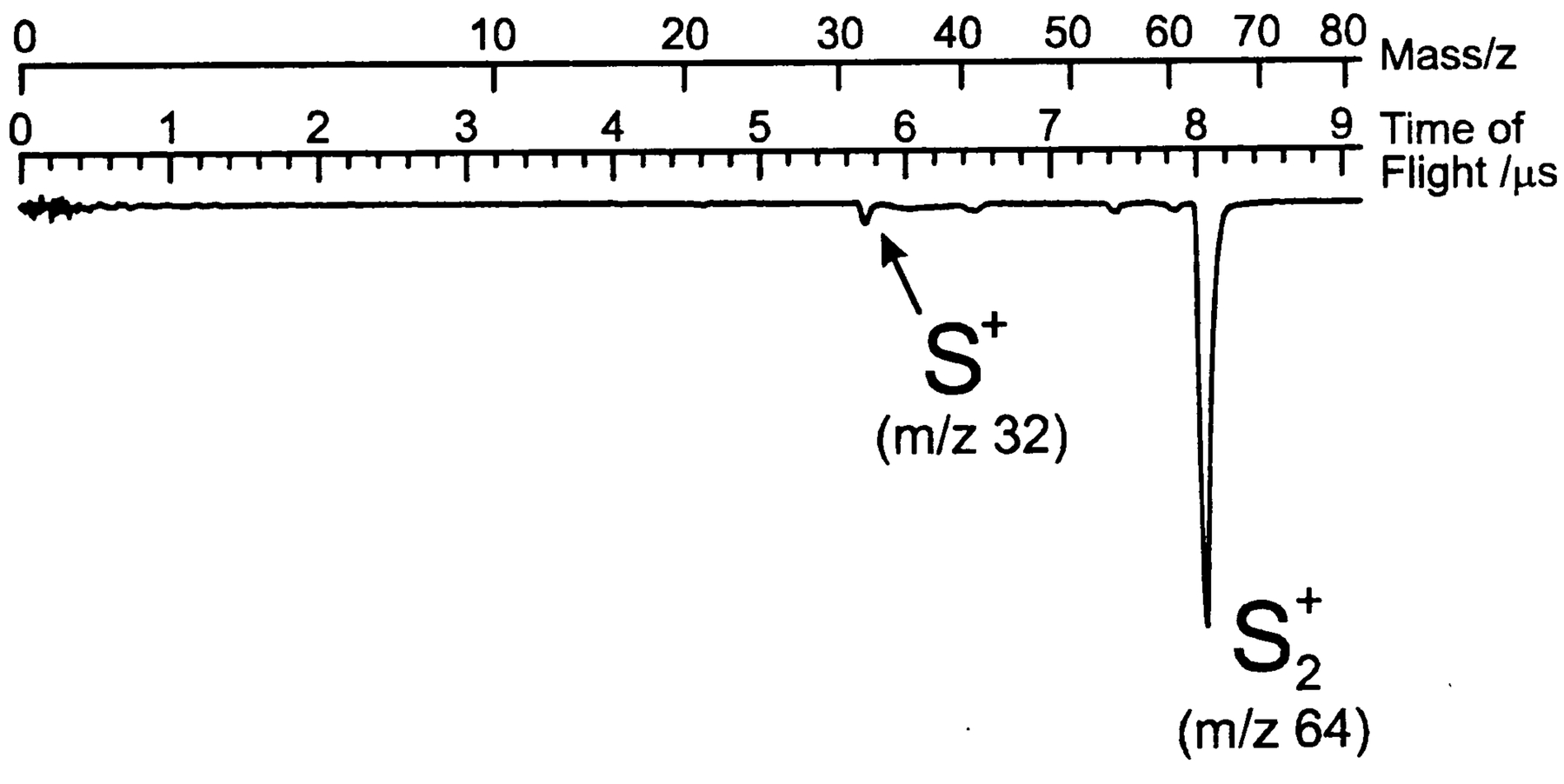

Figure 4.3: A typical TOF mass spectrum resulting from the double resonance multiphoton ionisation of S_2.

4.3 The $(3d\pi)^3\Delta_g$ Rydberg State

Initial work focused on extending the previous characterisation of the $^3\Delta_g$ Rydberg state,[14] of which the lower vibrational bands from $v = 0$ to 2 had previously been identified. Figure 4.4 shows three survey scans for the pump laser set on the three different Ω' components in the B" state. A clear progression with intervals of approximately 800 cm^{-1} is easily identified as higher vibrational levels of the $(3d\pi)$ $^3\Delta_g$ Rydberg state seen by Barnes *et al.*[14] Double resonance spectra were mainly recorded through B" $v' = 15$ $\Omega' = 0$ and 1 and B" $v' = 18$ $\Omega' = 2$. The B" $v' = 18$ $\Omega' = 2$ level was used in place of the $v' = 15$ $\Omega' = 2$ level of the B" $^3\Pi_u$ state as this level lies too close in energy to the $v' = 16$ $\Omega' = 0$ component of the same state. In each case only one Ω'' component of the Rydberg state was seen, implying that the $\Delta\Omega = \Delta\Lambda$ selection rule is strictly followed. Excitation of the $B\,^3\Sigma_u^-$ state gave similar double resonance spectra as for the B" states with the same Ω'. This is consistent with the forbidden nature of a Δ - Σ transition and the known strong B/B" mixing (which is strongest for the states of the same Ω).

Figure 4.5 shows the experimental and simulated spectrum of one individual band of $^3\Delta_2$ $v = 4$ with the pump laser set to populate $J = 4$ to 8 of the B" $^3\Pi_1$ $v' = 15$ state. The line positions were measured for several Rydberg state J'' values using a number of double resonance spectra to populate a range of J' for each Ω' component in the B" state. The spectra were fitted using the following Hamiltonian (ref 11):

$$\hat{\mathbf{H}} = B(\hat{\mathbf{J}} - \hat{\mathbf{S}} - \hat{\mathbf{L}})^2 + A\hat{\mathbf{L}} \bullet \hat{\mathbf{S}} + \tfrac{2}{3}\lambda(3\hat{\mathbf{S}}_z^2 - \hat{\mathbf{S}}^2) \qquad (4.1)$$

Term values for the B" states were taken from ref. 12. The simulation in figure 4.5 shows that these constants reproduce the observed spectrum well. The individual line intensities of the simulated spectrum were adjusted manually to fit the observed spectrum by altering the relative populations of the intermediate state rotational energy

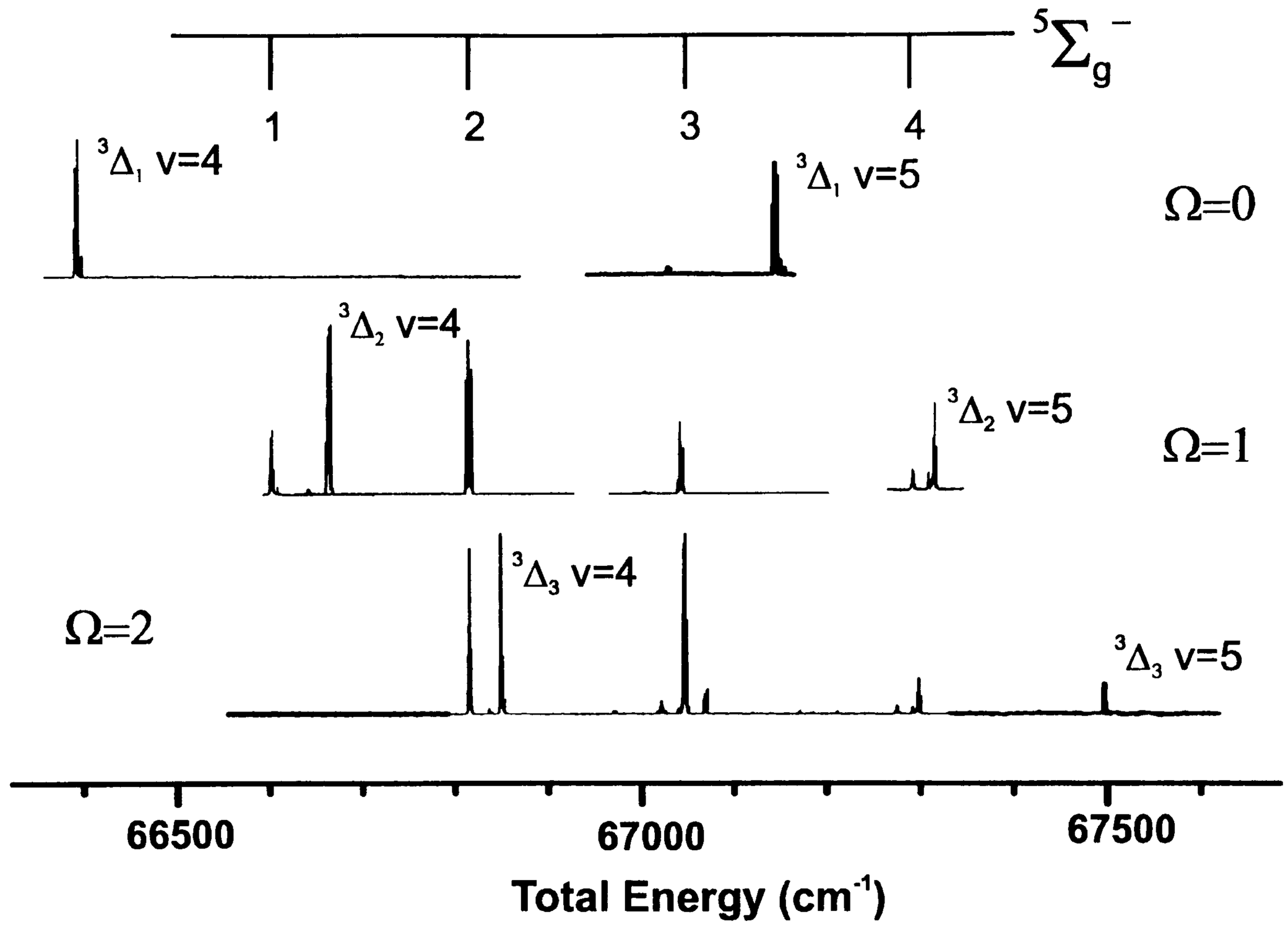

Figure 4.4: A set of double resonance scans through the Ω = 0 and 1 components of the B" v = 15 and the Ω = 2 B" v = 18 component of the intermediate state. The spectra are plotted against the energy of the intermediate state plus the energy of the probe photon, so that transitions to the same final state energy line up.

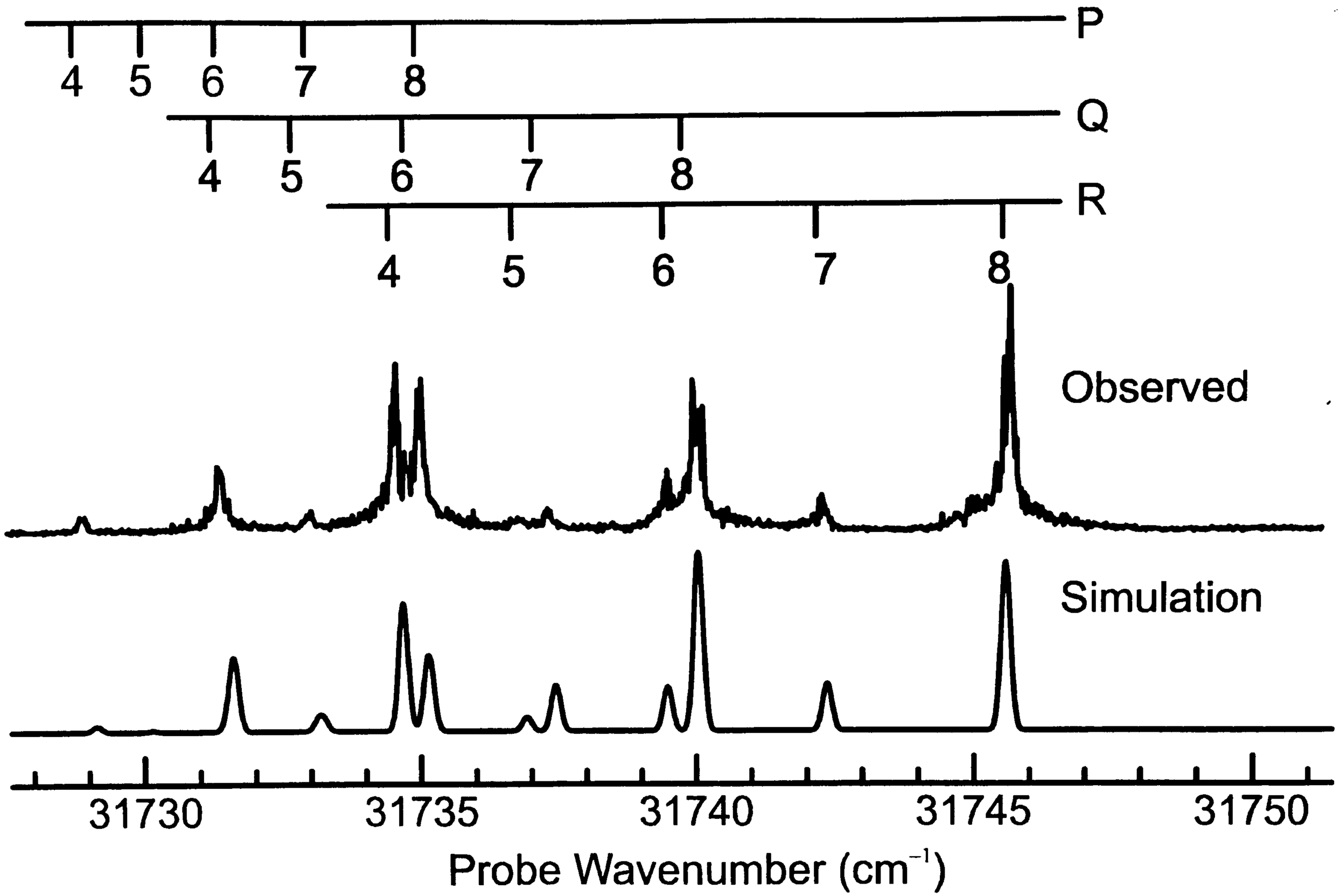

Figure 4.5: Double resonance multiphoton ionisation spectrum of the $^3\Delta_2$ $v = 4$ Rydberg state of S_2. The pump laser is set to populate $J = 4$ to 8 of $B''^3\Pi_1$ $v = 15$.

levels. Table 4.2 summarises the fitted spectroscopic constants for the observed vibrational levels, along with the previously reported values for the lower vibrational states. The value of the rotational constant, B, of 0.315 cm^{-1} indicates a reduction in bond length upon excitation from the ground state by 0.1 Å, which is consistent with the promotion of an electron from an antibonding orbital into a non-bonding Rydberg orbital. Many other g Rydberg states are expected for S_2 in this region, for instance a continuation of the $(3d\pi)^3\Delta_g$ series with the Rydberg electron being promoted to the 4s orbital and so on. However this investigation only revealed partial information on one other Rydberg state, $a^3\Sigma_g^+$ state. The partial spectroscopic data for this state is presented in table 4.3.

v	Origin (cm^{-1})	A (cm^{-1})	λ (cm^{-1})	B (cm^{-1})
0[a]	63449.6(5)	119.4(1)	42.8	0.3142(5)
1[a]	64242.2(5)	119.4(1)	42.6	0.3130(5)
2[a]	65028.9(5)	119.5(1)	43.1	0.3112(5)
2	65039.141(76)	119.998(28)	42.804(43)	0.3204(72)
3	65819.209(16)	119.7917(64)	43.011(10)	0.31031(35)
4	66592.403(11)	119.6114(54)	42.8450(74)	0.30702(19)
5	67358.594(11)	119.4487(57)	42.6006(75)	0.30684(29)
6	68118.0237(90)	119.2535(39)	42.3613(85)	0.30501(17)
7	68870.393(17)	119.081(10)	42.081(13)	0.30271(42)
8	69615.907(23)	118.8410(57)	41.799(20)	0.30112(48)
9	70354.925(14)	[118.56]	[41.50]	0.29798(30)
10	71085.961(13)	118.3793(50)	41.0203(93)	0.29714(35)

Table 4.2: Constants of the $^3\Delta_g$ Rydberg state of S_2.

a: Ref . 14

Error bars are one standard deviation in units of the last significant figure.

v	Origin (cm^{-1})	B (cm^{-1})	λ (cm^{-1})	γ (cm^{-1})
$x+0$	67008.496(20)	0.30863(18)	37.1185(60)	0.130(13)
$x+1$	67861.331(61)	0.30406(18)	70.553(25)	0.611(46)
$x+2$	69256.554(38)	0.29999(17)	15.2621(76)	0.490(24)

Table 4.3: Constants of the $^3\Sigma_g^+$ Rydberg state of S_2.
Error bars are one standard deviation in units of the last significant figure.

4.4 Ion Pair States

4.4.1 Ion Pair State Theory

Using the Wigner-Witmer rules (see appendix B), the lowest ion pair limit of S_2, $S^+(^4S) + S^-(^2P)$, will give rise to 4 *gerade* states: $^5\Pi_g$, $^5\Sigma_g^-$, $^3\Pi_g$ and $^3\Sigma_g^-$, and the four corresponding *ungerade* states. In the work presented here transitions to the $^5\Sigma_g^-$, $^3\Pi_g$ and $^3\Sigma_g^-$ states were directly observed, with possible evidence for the other ion pair state lying in unclassified perturbations in the progressions of the characterised states.

Provided the atoms forming the ion pair states are not too close together, the molecular wavefunctions of each Ω component of the state should be similar to a product of the separate atomic wavefunctions. For example:

$$\left|{}^5\Sigma_g^-\Omega=2\right\rangle = \left|{}^4S, M_S = 3/2\right\rangle \left|{}^2P, M_L = 0, M_S = 1/2\right\rangle. \qquad (4.2)$$

In the above and following expressions the two atomic wavefunctions are expressed in the order $|S^+\rangle|S^-\rangle$. In changing from the atomic to molecular limit M_S transforms as Σ, M_L as Λ and M_J as Ω. Using the lowering operator $\hat{S}_-$ on equation (4.2), expressions can be formulated for each Ω component of the $^5\Sigma_g^-$ state:

$$\left|{}^5\Sigma_g^-\Omega=1\right\rangle = \sqrt{3}/2\left|0,1/2\right\rangle\left|0,1/2\right\rangle + 1/2\left|0,3/2\right\rangle\left|0,-1/2\right\rangle \qquad (4.3)$$

$$\left|{}^5\Sigma_g^-\Omega=0\right\rangle = 1/\sqrt{2}\left|0,-1/2\right\rangle\left|0,1/2\right\rangle + 1/\sqrt{2}\left|0,1/2\right\rangle\left|0,-1/2\right\rangle. \qquad (4.4)$$

Similar expressions describing the molecular orbitals of the $^5\Pi_g$, $^3\Pi_g$ and $^3\Sigma_g^-$ ion pair states have also been derived and are presented in table 4.4. The sign (positive or

State	Ω	Molecular Wavefunction $\lvert\Lambda,S,\Sigma\rangle$	Atomic Combination $S^+\lvert M_L,M_S\rangle S^-\lvert M_L,M_S\rangle$
$^5\Sigma_g^-$	2	$\lvert 0,2,2\rangle$	$\lvert 0,3/2\rangle\lvert 0,1/2\rangle$
	1	$\lvert 0,2,1\rangle$	$\sqrt{3}/2\,\lvert 0,1/2\rangle\lvert 0,1/2\rangle + 1/2\,\lvert 0,3/2\rangle\lvert 0,-1/2\rangle$
	0	$\lvert 0,2,0\rangle$	$1/\sqrt{2}\,\lvert 0,-1/2\rangle\lvert 0,1/2\rangle + 1/\sqrt{2}\,\lvert 0,1/2\rangle\lvert 0,-1/2\rangle$
$^3\Sigma_g^-$	1	$\lvert 0,1,1\rangle$	$\sqrt{3}/2\,\lvert 0,3/2\rangle\lvert 0,-1/2\rangle - 1/2\,\lvert 0,1/2\rangle\lvert 0,1/2\rangle$
	0	$\lvert 0,1,0\rangle$	$1/\sqrt{2}\,\lvert 0,1/2\rangle\lvert 0,-1/2\rangle - 1/\sqrt{2}\,\lvert 0,-1/2\rangle\lvert 0,1/2\rangle$
$^5\Pi_g$	3	$\lvert 1,2,2\rangle$	$\lvert 0,3/2\rangle\lvert 1,1/2\rangle$
	2	$\lvert 1,2,1\rangle$	$\sqrt{3}/2\,\lvert 0,1/2\rangle\lvert 1,1/2\rangle + 1/2\,\lvert 0,3/2\rangle\lvert 1,-1/2\rangle$
	1	$\lvert 1,2,0\rangle$	$1/\sqrt{2}\,\lvert 0,-1/2\rangle\lvert 1,1/2\rangle + 1/\sqrt{2}\,\lvert 0,1/2\rangle\lvert 1,-1/2\rangle$
	0	$\lvert 1,2,-1\rangle$	$1/2\,\lvert 0,-3/2\rangle\lvert 1,1/2\rangle + \sqrt{3}/2\,\lvert 0,-1/2\rangle\lvert 1,-1/2\rangle$
	-1	$\lvert 1,2,-2\rangle$	$\lvert 0,-3/2\rangle\lvert 1,-1/2\rangle$
$^3\Pi_g$	2	$\lvert 1,1,1\rangle$	$\sqrt{3}/2\,\lvert 0,3/2\rangle\lvert 1,-1/2\rangle - 1/2\,\lvert 0,1/2\rangle\lvert 1,1/2\rangle$
	1	$\lvert 1,1,0\rangle$	$1/\sqrt{2}\,\lvert 0,1/2\rangle\lvert 1,-1/2\rangle - 1/\sqrt{2}\,\lvert 0,-1/2\rangle\lvert 1,1/2\rangle$
	0	$\lvert 1,1,-1\rangle$	$1/2\,\lvert 0,-1/2\rangle\lvert 1,-1/2\rangle - \sqrt{3}/2\,\lvert 0,-3/2\rangle\lvert 1,1/2\rangle$

Table 4.4: Each Ω component of the 4 expected *g* ion pairs states is expressed as a sum of contributions by the two, S^+ and S^-, atomic wavefunctions.

negative) of the individual atomic wavefunctions the right hand column in table 4.4 have been chosen to follow the convention that all matrix elements of S_{1z} which are nondiagonal in s are real and positive.

Using the expressions above predictions of the spectroscopic constants of some of the ion pair states can be made. For example the spin-orbit splitting of the $^3\Pi_g$ state can be estimated as follows. The spin-orbit interaction is assumed to have the following form:

$$\hat{\mathbf{H}}_{SO} = \mathbf{h}_{SO}(S^+) + \mathbf{h}_{SO}(S^-). \tag{4.5}$$

However as the S^+ atom has $L = 0$ (as its term symbol is ^4S) the form of the spin orbit interaction is simplified to the following:

$$\hat{\mathbf{H}}_{SO} = \mathbf{h}_{SO}(S^-) = a\hat{\mathbf{L}} \cdot \hat{\mathbf{S}} \tag{4.6}$$

where $\hat{\mathbf{L}}$ only acts on the S^- atom. The spin-orbit splitting in the $^3\Pi_g$ state can then be predicted by evaluating the following:

$$\left\langle {}^3\Pi_2 \left| a\hat{L}_z\hat{S}_z \right| {}^3\Pi_2 \right\rangle = \tag{4.7}$$

$$\left\{\sqrt{3}/2 \left\langle 0, 3/2\right|\left\langle 1, -1/2\right| - 1/2 \left\langle 0, 1/2\right|\left\langle 1, 1/2\right|\right\} a\hat{L}_z\hat{S}_z \left\{\sqrt{3}/2 \left|0, 3/2\right\rangle\left|1, -1/2\right\rangle - 1/2\left|0, 1/2\right\rangle\left|1, -1/2\right\rangle\right\} \tag{4.8}$$

$$= \left(1/4\right)\left(a/2\right) + \left(3/4\right)\left(-a/2\right) = -a/4, \tag{4.9}$$

similarly,

$$\left\langle {}^3\Pi_1 \left| a\hat{L}_z\hat{S}_z \right| {}^3\Pi_1 \right\rangle = 1/2\, a/2 + 1/2\, -a/2 = 0 \tag{4.10}$$

and

$$\left\langle {}^3\Pi_0 \left| a\hat{L}_z\hat{S}_z \right| {}^3\Pi_0 \right\rangle = 3/4\, a/2 + 1/4\, -a/2 = a/4. \tag{4.11}$$

In the above expressions the value of a can be related to the splitting between the two levels, $^2P_{3/2}$ and $^2P_{1/2}$, of the S^- ion. It can be derived by evaluating the spin-orbit interaction in terms of atomic wavefunctions using the following expressions:

$$\left\langle {}^2P_{3/2} \middle| \hat{\mathbf{H}}_{SO} \middle| {}^2P_{3/2} \right\rangle = \left\langle {}^2P_{3/2} \middle| a\hat{\mathbf{L}}\hat{\mathbf{S}} \middle| {}^2P_{3/2} \right\rangle \tag{4.12}$$

$$= \left\langle {}^2P_{3/2} \middle| a[\hat{L}_z\hat{S}_z + \tfrac{1}{2}(L_+S_- + L_-S_+) \middle| {}^2P_{3/2} \right\rangle \tag{4.13}$$

and similarly for $^2P_{1/2}$,

where, $$\left| {}^2P_{3/2} \right\rangle = |1,1\rangle \left| \tfrac{1}{2}, \tfrac{1}{2} \right\rangle \tag{4.14}$$

and, $$\left| {}^2P_{1/2} \right\rangle = \tfrac{1}{\sqrt{3}} |1,0\rangle \left| \tfrac{1}{2}, \tfrac{1}{2} \right\rangle - \sqrt{\tfrac{2}{3}} |1,1\rangle \left| \tfrac{1}{2}, -\tfrac{1}{2} \right\rangle \tag{4.15}$$

The above atomic wavefunctions are expressed in terms of $\left| L, M_L \right\rangle \left| S, M_S \right\rangle$. This results in positions of the levels as $^2P_{3/2} = \frac{1}{2}a$ and $^2P_{1/2} = -a$, therefore the total splitting between the two levels is $\frac{3}{2}a$. The experimentally measured splitting[22] is 483.54 cm^{-1}, so the value of a is –322.36 cm^{-1}. Referring back to equation (4.6) this gives a predicted spin-orbit splitting, A, for the $^3\Pi_g$ ion pair state of 80.59 cm^{-1}. This value compares favourably with the experimentally determined value of 78.770 cm^{-1} for the first vibrational level of the $^3\Pi_g$ state. Similar consideration of the expressions for the $^5\Pi_g$ state also predict A = 80.59 cm^{-1} and for the state to be inverted, although this has yet to be confirmed experimentally. The spin-orbit operator also implies mixing between different electronic states:

$$\left\langle {}^3\Pi_{g2} \middle| \hat{\mathbf{H}}_{SO} \middle| {}^5\Sigma^-_{g2} \right\rangle = \frac{\sqrt{3}}{2\sqrt{2}} a \tag{4.16}$$

$$\left\langle {}^3\Pi_{g1} \middle| \hat{\mathbf{H}}_{SO} \middle| {}^3\Sigma^-_{g1} \right\rangle = -\tfrac{1}{4} a \tag{4.17}$$

$$\left\langle {}^3\Pi_{g2} \left| \hat{\mathbf{H}}_{SO} \right| {}^5\Pi^-_{g2} \right\rangle = -\sqrt{3}/4\, a \tag{4.18}$$

$$\left\langle {}^5\Pi_{g2} \left| \hat{\mathbf{H}}_{SO} \right| {}^5\Sigma^-_{g2} \right\rangle = 1/2\sqrt{2}\, a \tag{4.19}$$

$$\left\langle {}^5\Pi_{g1} \left| \hat{\mathbf{H}}_{SO} \right| {}^3\Sigma^-_{g1} \right\rangle = -1/4\, a \tag{4.20}$$

$$\left\langle {}^3\Sigma^-_{g1} \left| \hat{\mathbf{H}}_{SO} \right| {}^5\Sigma^-_{g1} \right\rangle = 0 \tag{4.21}$$

4.4.2 Ion Pair State Spectra

As mentioned previously direct observations were made of the ${}^5\Sigma^-_g$, ${}^3\Pi_g$ and ${}^3\Sigma^-_g$ ion pair states, to greater or lesser extent (${}^5\Sigma^-_g$ $v = 0$ -15, ${}^3\Pi_g$ $v = 0$ - 12 and ${}^3\Sigma^-_g$ $v = 0$ and 1). These states all interact and perturb each other via the spin-orbit interaction. Because of the presence of perturbations in the observed spectra, the discussion of the experimentally determined constants has been treated in 3 separate ways. Initially the states are considered almost in isolation, where the constants presented just reproduce the observed spectral line positions and energy level patterns, using a minimal set of interactions between the states. The second section describes a deperturbation analysis carried out on all the states simultaneously, with the inclusion of a full set of interactions between all the vibrational levels. The third method is of an analysis of the spectra at the vibrational level, fitting the positions of the various vibrational levels to a set of spectroscopic constants and perturbation interactions (the results of this analysis are presented in appendix C).

4.4.2.1 The Isolated State Model

The $^5\Sigma_g^-$ Ion Pair State

Also indicated in the survey spectrum in figure 4.4. is the start of the $^5\Sigma_g^-$ vibrational progression. It is important to notice that the $^5\Sigma_g^-$ state has a much smaller vibrational spacing of about 230 cm^{-1} compared to the 700 cm^{-1} of the Rydberg states. The state is visible in both the $\Omega' = 1$ and $\Omega' = 2$ spectra, with the transitions from the different intermediate state Ω' values lining up (Note that the double resonance spectra are plotted offset by the intermediate state energy so that transitions to states with the same final energy will line up). This lack of an Ω selection rule (in contrast to transitions to the $^3\Delta_g$ Rydberg state) implies the final state is Hund's case (b). Figure 4.6 shows just one band of the state for a range of intermediate state J'. The observed pattern of alternation of three and four final states for even and odd J' can only be accounted for if the final state term symbol is $^5\Sigma_g^-$.

However such a state should also be accessible through intermediate state $\Omega' = 0$, even though it does not appear so in figure 4.4, where the lower trace shows no sign of signal at the relevant energies. Further experiments were performed via B" $v' = 16$ $\Omega' = 0$ where it is possible to excite $\Omega' = 0^-$ levels (i.e. *f* parity $\Omega = 0$ levels) in addition to those on B" $v' = 15$ $\Omega' = 0$ where it is only possible to excite $\Omega' = 0^+$ levels. These experiments showed that the $^5\Sigma_g^-$ state is accessible through $\Omega' = 0^-$ *but not* $\Omega' = 0^+$ levels. This observation can be accounted for by assuming the transition intensity to the $^5\Sigma_g^-$ state comes from mixing at the valence level between the B" state and a $^5\Sigma_u^-$ repulsive state that goes to the same dissociation limit. The $^5\Sigma_u^-$ state only has $\Omega = 0^-$ and not $\Omega = 0^+$ components and so will only mix with states with $\Omega = 0^-$ (as the strongest mixing occurs between states with the same electronic symmetry). There has been previous evidence for mixing of the B" state with this state in the perturbed pattern of the high vibrational levels from a study of the LIF from the B"

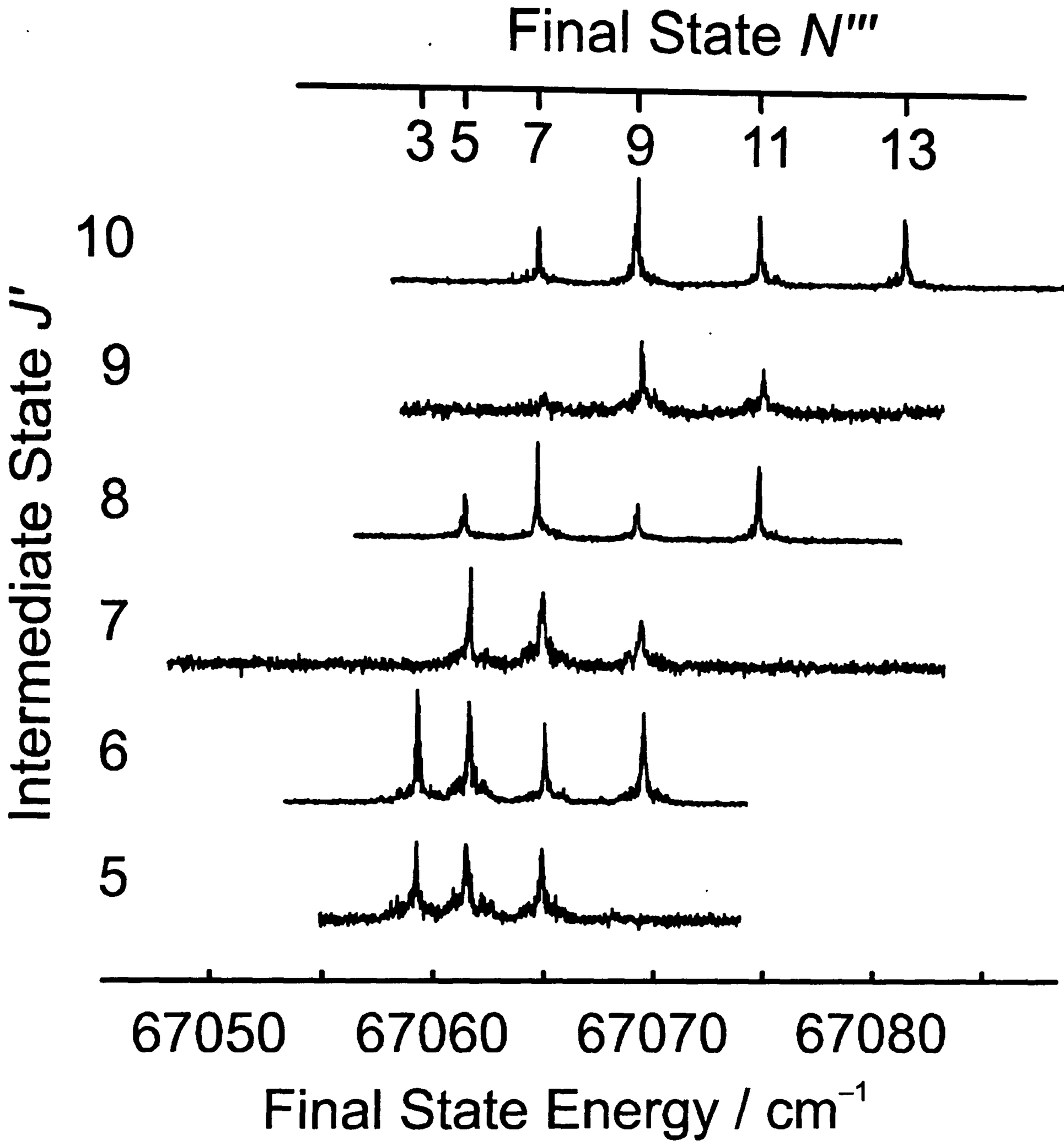

Figure 4.6: Double resonance spectra of the $^5\Sigma_g^-$ $v = 3$ ion pair state taken with a sequence of intermediate state J'. The spectra are plotted against the energy of the intermediate state plus the energy of the probe photon, so that transitions to states with the same final energy line up. Successive spectra show, respectively, 3 and 4 peaks. This is a consequence of nuclear spin statistics (I(^{32}S) = 0) which causes all the even N''' levels to be missing for the $^5\Sigma_g^-$ state.[17]

state. In the LIF study there is also a suggestion of mixing with a $^5\Pi_u$ state going to the same limit, but such a mixing in this case would allow transitions from both $\Omega' = 0$ parities, and so can be said to be spectroscopically insignificant in this case.

Table 4.5 presents an analysis of the rotational structure of the observed bands of the $^5\Sigma_g^-$ state. The Hamiltonian used for the upper state is:

$$\begin{aligned}\hat{H} = B(\hat{J}-\hat{S}-\hat{L})^2 + A\hat{L}\bullet\hat{S} + \tfrac{2}{3}\lambda(3\hat{S}_z^2-\hat{S}^2) + \gamma\hat{N}\bullet\hat{S} \\ + \tfrac{1}{12}\theta(35\hat{S}_z^4 - 30\hat{S}^2\hat{S}_z^2 + 25\hat{S}_z^2 - 6\hat{S}^2 + 3\hat{S}^4)\end{aligned} \tag{4.22}$$

which is as used for the Rydberg state with the addition of an extra terms to account for the quintet nature of the state.[23] The constants are typical of ion pair state character. The small rotational constant (0.13 cm^{-1} compared with 0.31 cm^{-1} for the Rydberg state) corresponds to a bond length of 2.8 Å, which is just slightly longer than the sum of the ionic radii[24] of S^+ and S^- (2.7 Å). The small vibrational spacing of the state (233 cm^{-1} compared with 740 cm^{-1} for the Rydberg state) is again typically ion pair like. Figure 4.7 shows the RKR potentials of the ground, valence, Rydberg and ion pair states pertinent to this study, along with the expected potential energy curve for a Coulombic attraction between $S^+(^4S)$ and $S^-(^2P)$. The ion pair state lies almost on top of the Coulombic curve at bond lengths just longer than the R_e, as predicted by the simple ion pair state model, and the extended bond length limb of the state can be expected to closely follow this potential. The sum of the ionic radii of the two ions is also indicated, which falls in the same region as the ion pair state potential energy minimum.

Electronic configuration considerations reinforce the conclusion that the quintet state is an ion pair state and not a Rydberg state. The lowest Rydberg state, the $C^3\Sigma_u^-$ state, is assigned as a $4p\pi_u$ Rydberg electron with a ground state ion core. Therefore the lowest quintet Rydberg state would arise from a $a^4\Pi_u$ ion core with the

v	Origin (cm^{-1})	B (cm^{-1})	λ (cm^{-1})	θ (cm^{-1})	γ (cm^{-1})
0	66357.4240(25)	0.13075(17)	0.1366(34)	-0.0016(43)	-0.00750(67)
1	66592.785(16)	0.13233(17)	0.0774(67)	-0.0575(10)	-0.00281(72)
2	66826.233(12)	0.13175(18)	0.0720(51)	-0.0144(68)	-0.00236(59)
3	67057.596(12)	0.13137(19)	0.0373(43)	-0.0487(60)	-0.00187(73)
4	67287.044(24)	0.13044(18)	0.0565(14)	0.0082(21)	-0.00402(63)
5	67514.456(14)	0.12921(21)	0.0321(64)	-0.0055(85)	-0.00536(74)
6	67739.533(19)	0.12842(14)	-0.0267(31)	-0.0015(43)	-0.00598(53)
7	67962.289(18)	0.12749(18)	-0.0875(31)	0.0034(32)	-0.00738(74)
8	68182.511(17)	0.12462(27)	-0.2003(58)	0.0196(53)	-0.0101(13)
9	68399.295(15)	0.12495(30)	-0.3517(63)	0.0107(40)	-0.0060(17)
10	68612.243(14)	0.12335(28)	-0.6626(53)	-0.1238(37)	0.4929(16)
11	68823.803(21)	0.12205(77)	0.1238(20)	[0.00]	-0.0176(51)
12	69037.059(48)	0.12046(78)	0.1759(25)	[0.00]	-0.0227(46)
13	69219.430(14)	0.11616(27)	-3.0516(17)	[0.00]	-0.0222(16)
14	69395.311(13)	0.10927(29)	0.5441(69)	[0.00]	0.0032(26)
15	69593.776(31)	0.10739(89)	4.5008(89)	[0.00]	0.0478(80)

Table 4.5: Constants of the $^5\Sigma_g^-$ ion pair state of S_2 as derived using the isolated state model.

Error bars are one standard deviation in units of the last significant figure.

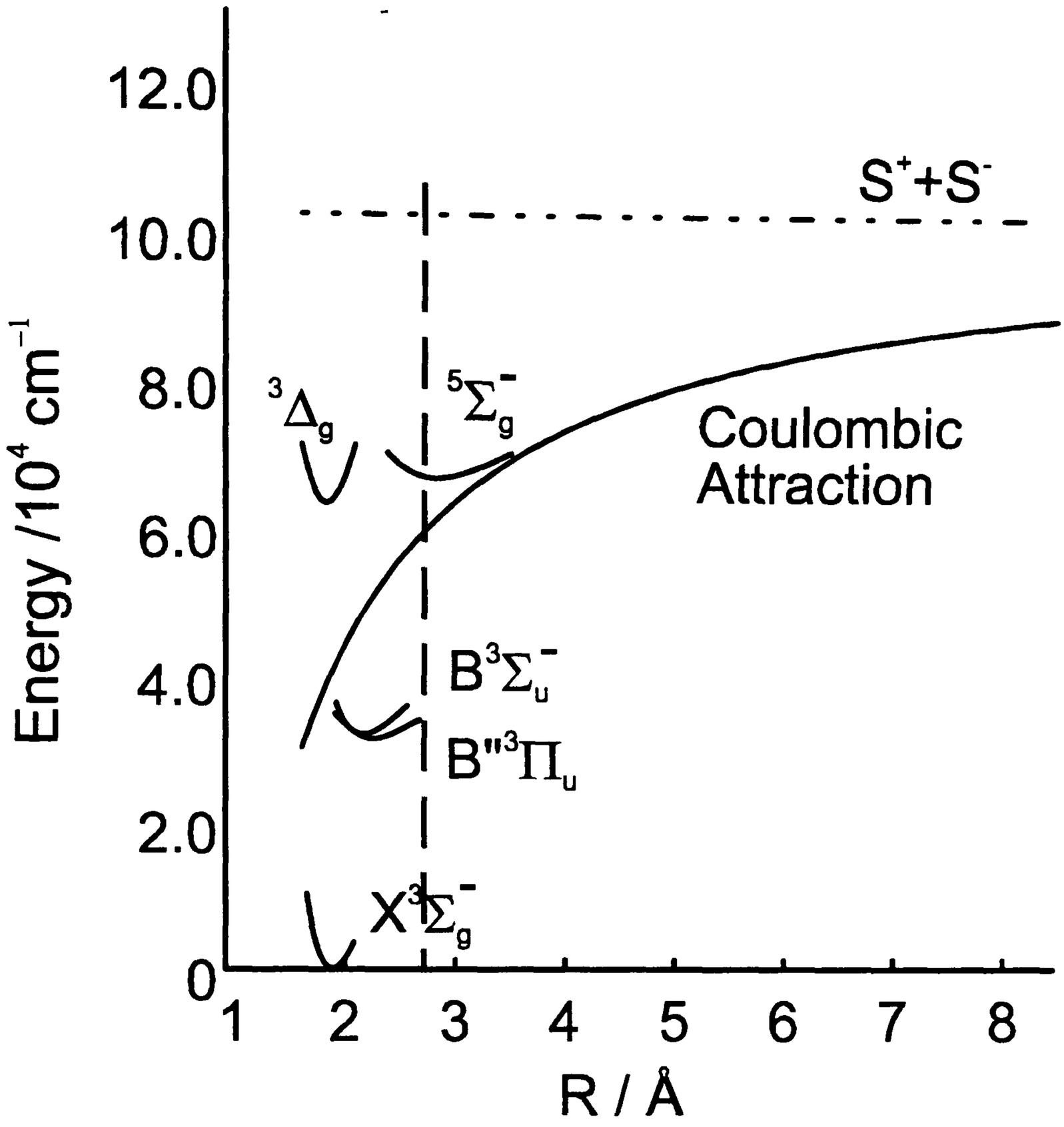

Figure 4.7: RKR potential energy curves for the ground, intermediate, Rydberg and $^5\Sigma_g^-$ ion pair states. The coulombic attraction between an S^+ and an S^- ion is indicated, along with the sum of the ionic radii of an S^+ and an S^- ion (vertical dashed line).

same $4p\pi_u$ Rydberg electron, but the difference in ion core energies should place this state around 72620 cm^{-1}, much higher than the quintet state observed here.

The constants for the lower vibrational levels ($v = 0$ to 10) of the $^5\Sigma_g^-$ state as shown in table 4.5 are extremely regular. All the states have small λ, θ and γ values, which implies little perturbation from neighbouring states, and all the constants vary smoothly with increasing vibrational number. This regularity is illustrated by the energy level plot of $v = 3$ of the $^5\Sigma_g^-$ state in figure 4.8. The vertical energy scale is plotted as a reduced term value, i.e. with $BJ(J+1)$ subtracted from the energy of the states.

However, the smooth variation in the spectroscopic constants ceases abruptly at $v = 11$ from whereon the picture becomes more complex. This is due to the strong interactions between the $^5\Sigma_g^-$ state and the $^3\Pi_g$ ion pair state.

The $^3\Pi_g$ Ion Pair State

Figure 4.9 shows another survey spectrum, much like figure 4.4. Indicated on the spectra is the vibrational origin of the $^3\Pi_g$ ion pair state and the continuing vibrational progression of the $^5\Sigma_g^-$ state. The origin of the $^3\Pi_g$ ion pair state is at 68790 cm^{-1}, and the vibrational progression continues to higher energy with a spacing comparable to that of the $^5\Sigma_g^-$ state. Table 4.6 lists the fitted constants for the observed vibrational levels ($v = 0$ to 12) of the $^3\Pi_g$ ion pair state. Again the constants are typically ion pair like; a low value of B (~0.09 cm^{-1}), and a close vibrational spacing (~200 cm^{-1}). Table 4.6, like table 4.5, is incomplete, this is due to the interaction between the two ion pair states. The interaction between the two states moves the positions of the Ω components away from their predicted positions, and so in some cases not all of the components of a vibrational level could be assigned

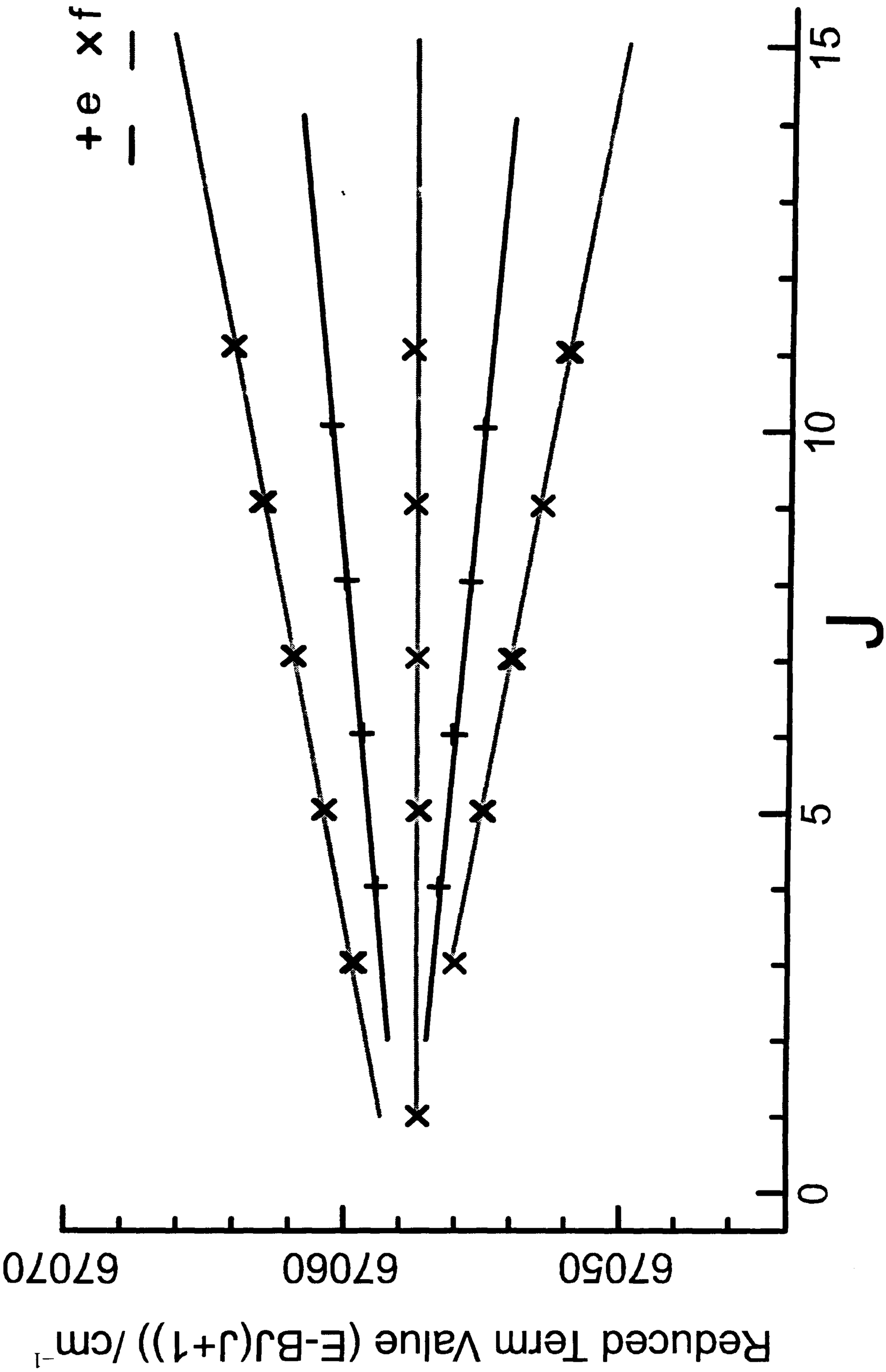

Figure 4.8: Rotational energy level plot of $^5\Sigma_g^-$ $v = 3$. The energy levels of the two different rotational parities are indicated by +'s (e) and x's (f).

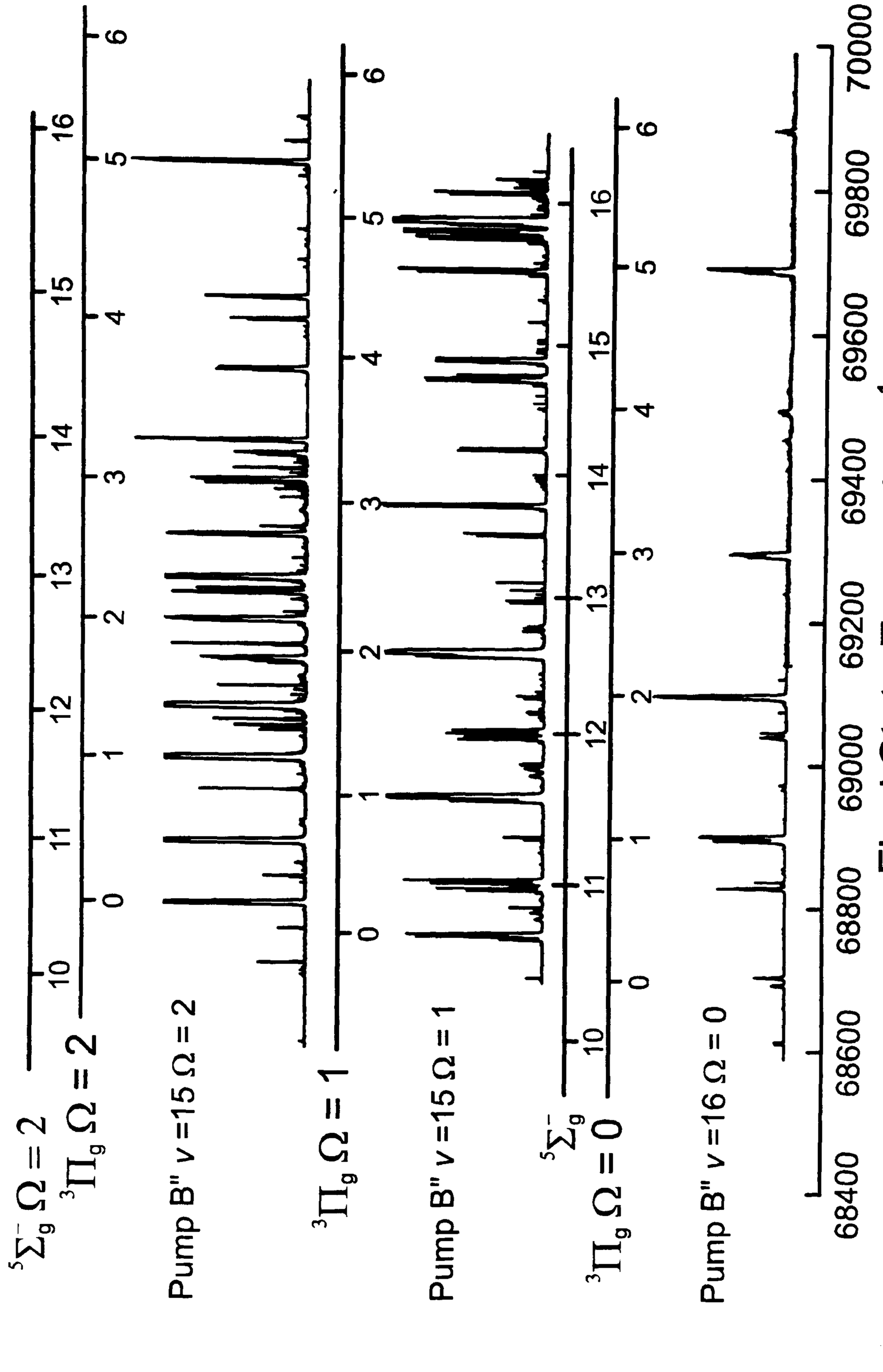

Figure 4.9: A set of double resonance scans through the three different Ω components of the intermediate state. The spectra are plotted against the energy of the intermediate state plus the energy off the probe photon, so that transitions to the same final state line up. The vibrational progressions of the $^5\Sigma_g^-$ and $^3\Pi_g$ ion pair states are indicated by the combs above and below the spectra.

v	Origin (cm^{-1})	B (cm^{-1})	A (cm^{-1})	λ (cm^{-1})	α (cm^{-1})
0	68790.703(69)	0.09704(61)	78.770(84)	-2.311(55)	18.474(41)
1	68965.92(24)	0.09857(59)	58.53(14)	-3.866(26)	2.871(17)
2	69168.715(17)	0.09475(26)	67.793(46)	-0.180(31)	6.054(23)
3	69368.631(23)	0.09417(35)	67.348(26)	-3.650(23)	5.075(26)
4	69564.876(16)	0.09508(29)	68.553(25)	-2.260(27)	3.725(16)
5	69750.444(61)	0.09486(47)	66.733(21)	7.674(21)	1.939(22)
6	69954.079(29)	0.09887(60)	71.762(29)	[7.85]	1.931(18)
7	70143.329(15)	0.09415(45)	72.676(12)	6.348(10)	[1.41]
8	70329.8447(95)	0.09298(15)	[61.19]	[0.00]	[2.51]
9	70519.991(14)	0.09577(37)	64.2272(92)	0.510(11)	1.412(11)
10	70708.3370(81)	0.09392(17)	63.8917(60)	1.0567(62)	2.2346(72)
11	70893.3083(90)	0.09381(12)	61.175(10)	[0.00]	2.5141(63)
12	71074.7224(79)	0.09405(21)	55.9557(69)	-1.5757(54)	2.7910(86)

Table 4.6: Constants of the $^3\Pi_g$ ion pair state of S_2 as derived from the isolated state model.

Error bars are one standard deviation in units of the last significant figure.

unambiguously. Table 4.7 lists the minimal set of interactions between the ion pair states used in the isolated model to reproduce the observed data.

$\hat{H}^{SO}$ /cm^{-1}	$^5\Sigma_g^-$ v	$^3\Pi_g$ v
85.60873	11	0
79.78773	12	1
54.77639	13	2
47.3519	14	3
26.35216	15	4
[5]	16	5
[5]	17	6

Table 4.7: Spin-Orbit interaction values used in the isolated state model between the vibrational levels of the $^5\Sigma_g^-$ and $^3\Pi_g$ states.

The $^3\Sigma_g^-$ and $^5\Pi_g$ Ion Pair States

Two vibrational levels ($v = 0$ and 1) have been assigned of the $^3\Sigma_g^-$ state, the constants for which are presented in table 4.8. However, no spectroscopic features could be assigned as direct evidence of the $^5\Pi_g$ ion pair state which is also predicted to arise from the $S^+(^4S) + S^-(^2P)$ ion pair limit, although one level was observed and assigned as a $^1\Pi_g$ ion pair state which could be one Ω component of the $^5\Pi_g$ state. At these higher energies the spectrum is crowded with features, even with the simplification offered by the double resonance process. It is clear from vibrational and rotational band analysis that other unassigned states are in the region perturbing the ion pair state progressions of the assigned states. However, it should only be a matter of time and effort before the spectrum can be completely accounted for in terms of transitions to ion pair and Rydberg states.

v	Origin (cm^{-1})	*B* (cm^{-1})	λ (cm^{-1})	γ (cm^{-1})
0	69322.654(17)	0.09855(28)	-2.552(17)	-0.0344(40)
1	69537.416(20)	0.10029(41)	-1.056(24)	0.0062(33)

Table 4.8: Constants of the $^3\Sigma_g^-$ ion pair state of S_2.

Error bars are one standard deviation in units of the last significant figure.

v	Origin (cm^{-1})	*B* (cm^{-1})	q (cm^{-1})
?	69439.93(17)	0.09838(23)	0.0059(14)

Table 4.9: Constants of the single ion pair component assigned as $^1\Pi_g$.

Error bars are one standard deviation in units of the last significant figure.

Ion Pair State Interactions

The $^5\Sigma_g^-$, $^3\Pi_g$ and $^3\Sigma_g^-$ ion pair states mix with each other via the spin orbit interaction, leading to perturbations in the vibrational progressions of the states. The largest effect of this interaction is on the positions of the $\Omega = 2$ components of the $^5\Sigma_g^-$ and $^3\Pi_g$ states. The interaction moves the $\Omega = 2$ components significantly away from their expected positions. Figure 4.10 illustrates this effect with two diagrams, 4.10(a) indicating the expected position of the various components of the two states without any interaction, and 4.10(b) showing the experimentally observed positions of the components with the interaction in place.

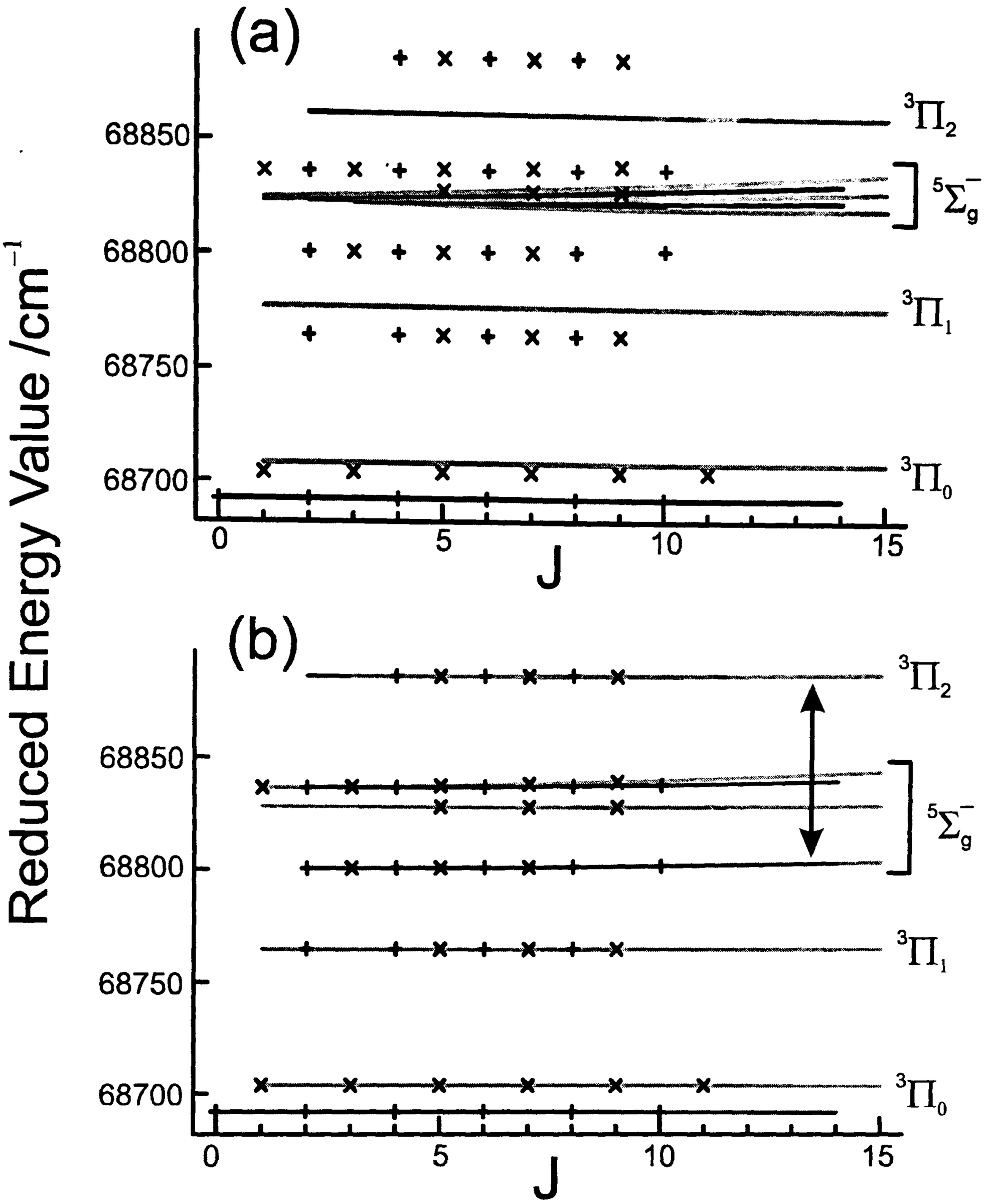

Figure 4.10: The solid lines indicate the positions of the various Ω components of the $^3\Pi_g$ and $^5\Sigma_g^-$ states with the interaction between the two states (a) off and (b) on. The vertical arrow in (b) indicates the large interaction and displacement of the Ω = 2 components of the two states. The observed energy levels of the two different rotational parities are indicated by +'s (e) and x's (f), whereas the solid lines indicate the fitted values.

4.4.2.2 Deperturbation Analysis

Figure 4.11 presents graphs of the variation in selected spectroscopic constants for the vibrational levels of the $^5\Sigma_g^-$ ion pair state presented in table 4.5. For a normal electronic state the constants should vary smoothly with increasing vibrational level. However, as figure 4.11 shows, the constants for the $^5\Sigma_g^-$ state only vary smoothly up to $v=10$, from whereon the constants do not follow a set pattern. This deviation from the expected value is due the interaction with the $^3\Pi_g$ and other ion pair states.

To obtain a more realistic set of spectroscopic constants a deperturbation analysis was performed by creating RKR (Rydberg-Klein-Reese) potential energy curves for the three characterised ion pair states using the computer program AAEE[25] written by Prof. J. Tellinghuisen of Vanderbilt University. Figure 4.12 shows the relative positions of these calculated potential energy curves for the states. The computer program LEVEL[26], written by Prof. R. LeRoy of the University of Waterloo, Canada, was then used to calculate wavefunctions for each vibrational level of the three ion pair states. From these wavefunctions the Franck-Condon overlap between all the various states could be estimated and placed into the overall model.

Figure 4.13 illustrates the overlap between the wavefunctions of the $^3\Pi_g$ and $^5\Sigma_g^-$ states. The figure shows the potential energy curves, vibrational energy levels and wavefunctions for the two states around the vibrational origin of the $^3\Pi_g$ state. With the new interactions between the states in place the constants were refitted to the experimental data. The whole process was then repeated to converge on a set of valid spectroscopic constants, and interaction parameters. To aid the fitting process the value of α of the $^3\Pi_g$ ion pair state was assumed to be zero. α describes the splitting between the two parities of the $\Omega = 0$ component, which usually arises due to interactions with neighbouring Σ states. In this case the observed spectra were

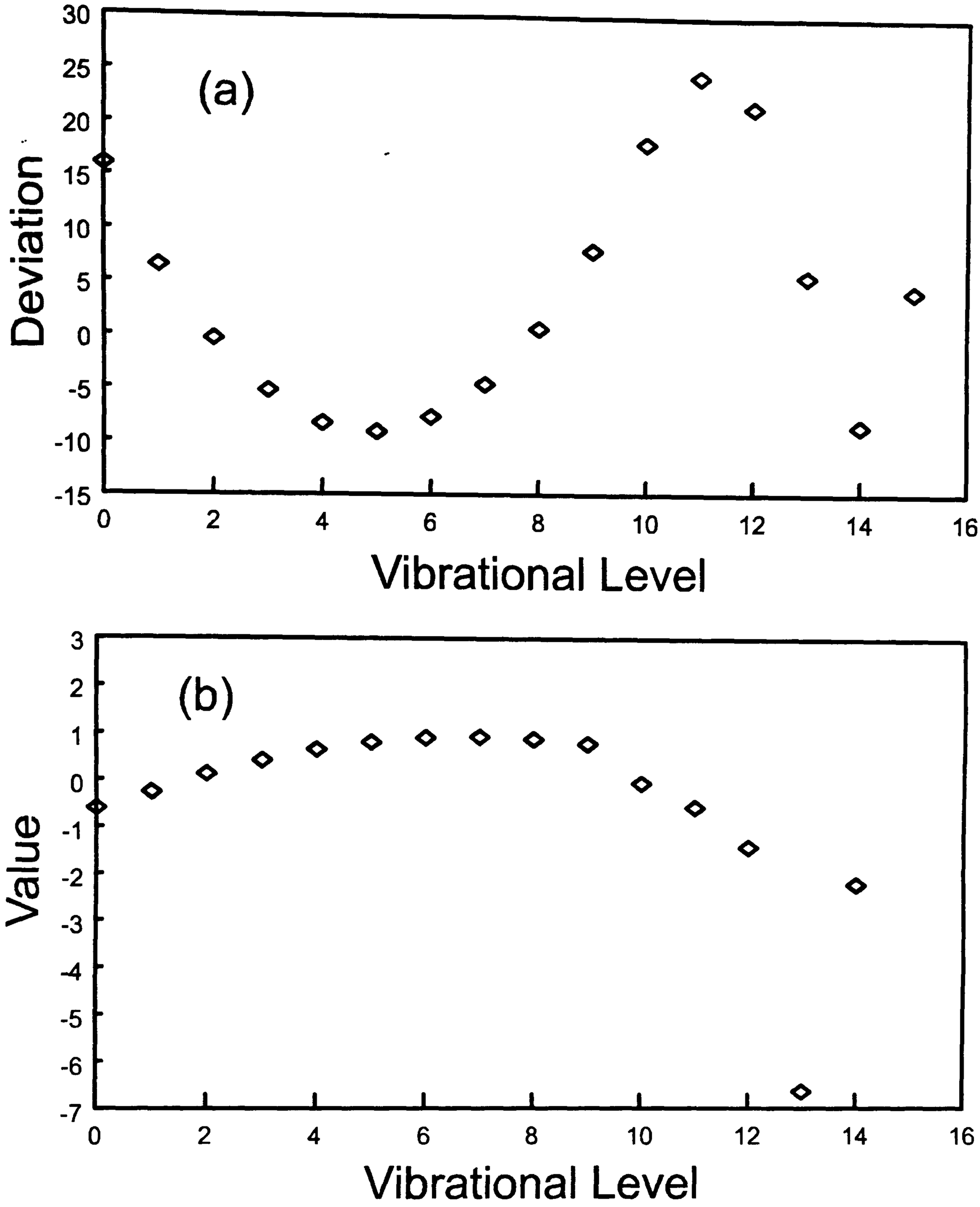

Figure 4.11: The varitaion of the $^5\Sigma_g^-$ ion pair sate constants with increasing vibrational level from the isolated state model. (a) shows the variation of the vibrational state origin from a fitted first order polynomial of the values and (b) graphs the variation in λ. Note how the smooth variation ceases above $v = 10$ where the interaction with the $^3\Pi_g$ begins.

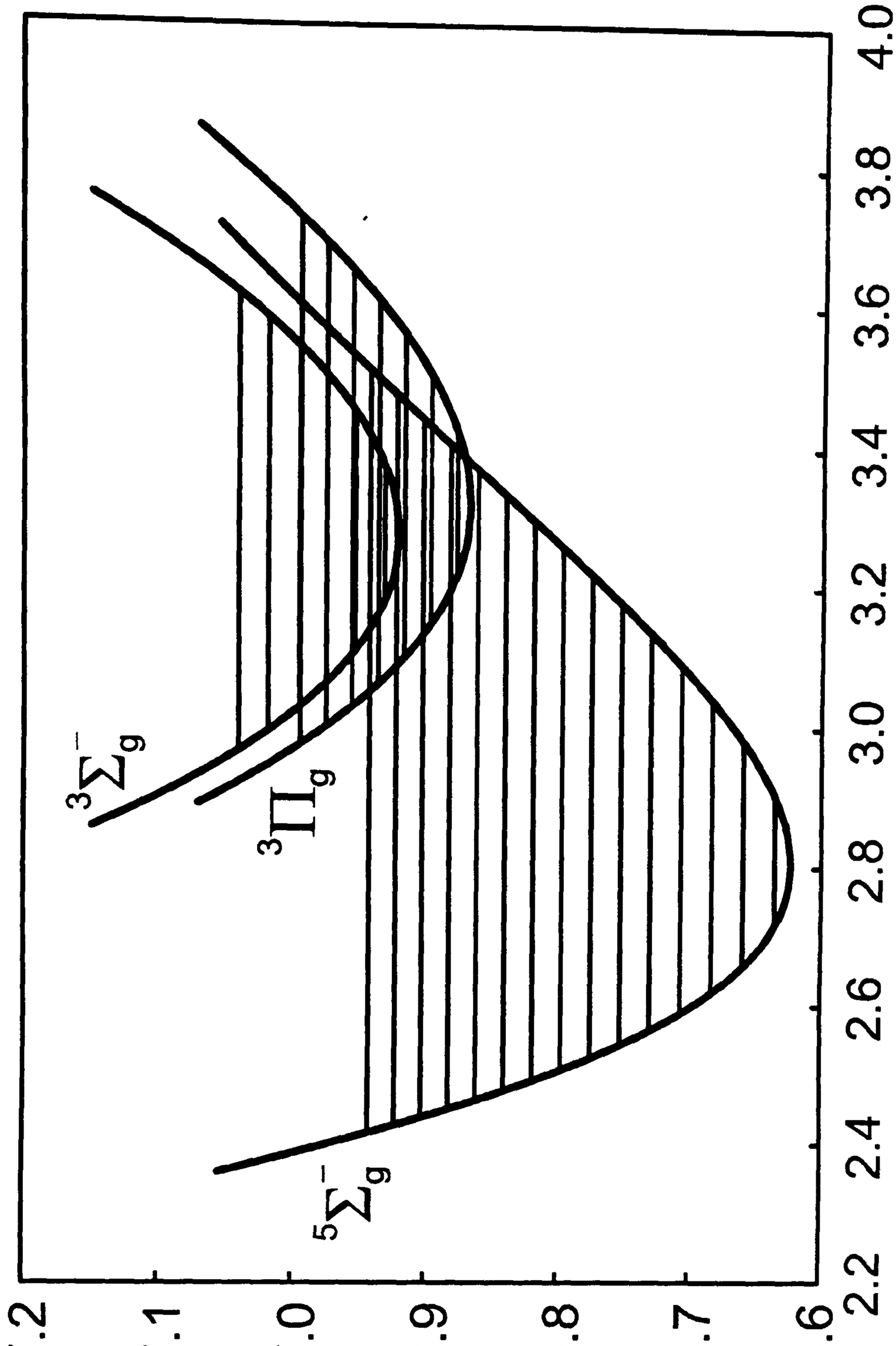

Figure 4.12: The calculated RKR curves for the three ion pair states of S_2 so far characterised, $^5\Sigma_g^-$, $^3\Pi_g$ and $^3\Sigma_g^-$. The constants used to calculate the potential energy curves were taken from the deperturbation analysis.

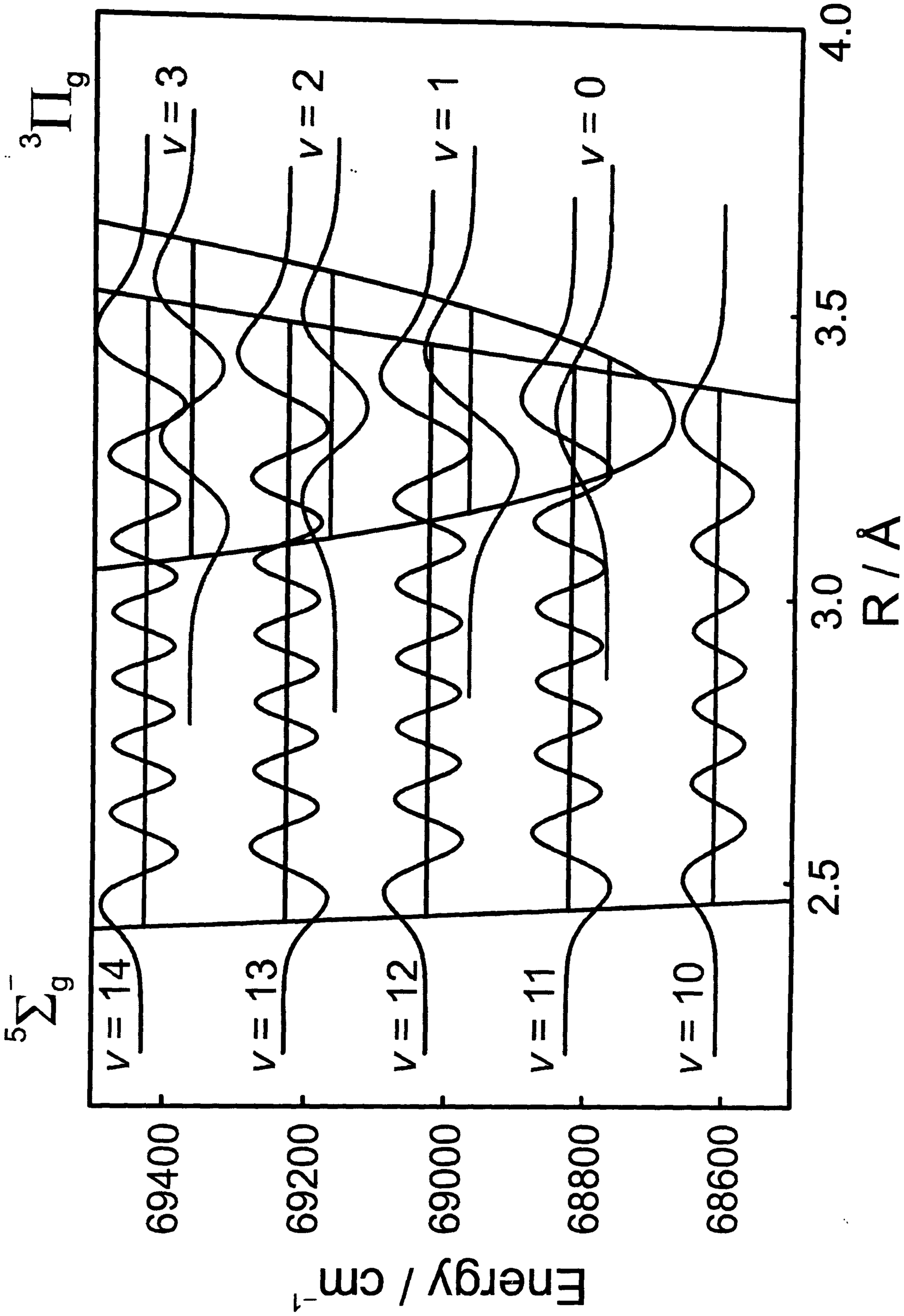

Figure 4.13: Illustration of the potential energy curves and vibrational level wavefunctions calculated by the AAEE and LEVEL computer programs around the origin of the $^3\Pi_g$ ion pair state.

reproduced by varying the interactions between the neighbouring states as well as the spectroscopic constants with α set as 0. Tables 4.10 to 4.12 present the updated set of spectroscopic constants and degrees of interaction calculated from the deperturbation analysis.

The updated constants show that the deperturbation analysis was only successful for all the vibrational levels up to $v = 3$ of the $^3\Pi_g$ state. Above this state the constants again do not vary smoothly with increasing vibrational level. This is due to the lack of spectroscopic data above these levels on all the states in the region. Even though data on the $^3\Pi_g$ and $^5\Sigma_g^-$ states have been calculated to higher energy the $^3\Sigma_g^-$ and $^5\Pi_g$ states are also expected in this region but were not fully characterised. Just two vibrational levels of the $^3\Sigma_g^-$ state were observed and included in the model, and the role of the unseen $^5\Pi_g$ state can only be estimated. This results in a poor set of spectroscopic constants for the higher lying states, although they do reproduce the observed spectral features.

The excited state interactions derived from the experimental data and the calculation are compared to the value predicted by the separated atom model in figure 4.14. The variation in wavefunction overlap can be predicted from the separated ion model of ion pair states introduced in section 4.4.1, by solving the following equation:

$$\begin{aligned}\left\langle {}^5\Sigma_g^-\Omega=2\left|a[\hat{L}_z\hat{S}_z+\tfrac{1}{2}(L_+S_-+L_-S_+)\right|{}^3\Pi_g\Omega=2\right\rangle \\ =(-1)^{S-\Sigma}\begin{pmatrix} S & 1 & S' \\ -\Sigma & q & \Sigma' \end{pmatrix}\left\langle {}^5\Sigma_g^-\Omega=2\left\|\mathbf{H}^{SO}\right\|{}^3\Pi_g\Omega=2\right\rangle\end{aligned} \qquad (4.23)$$

$$\left\langle {}^5\Sigma_g^-\Omega=2\left\|\mathbf{H}^{SO}\right\|{}^3\Pi_g\Omega=2\right\rangle = 441.4\ \mathrm{cm}^{-1} \qquad (4.24)$$

where the left hand side of the expression is solved as before (see equations 4.7 - 4.9) and $\left\langle {}^5\Sigma_g^-\Omega=2\left\|\mathbf{H}^{SO}\right\|{}^3\Pi_g\Omega=2\right\rangle$ is the magnitude of the interaction between the

v	Origin (cm^{-1})	B (cm^{-1})	λ (cm^{-1})	θ (cm^{-1})	γ (cm^{-1})
0	66357.47	0.130753	0.142538	-0.00162	-0.0075
1	66593.14	0.13233	0.120631	-0.05762	-0.002827
2	66827.29	0.131764	0.20019	-0.01446	-0.00239
3	67059.31	0.131392	0.244406	-0.048662	-0.001926
4	67289.03	0.130476	0.2927	0.00703	-0.004101
5	67516.88	0.129255	0.316686	-0.005559	-0.00549
6	67742.8	0.128489	0.34919	-0.001705	-0.0062
7	67966.32	0.127617	0.360946	0.003476	-0.007801
8	68187.88	0.124829	0.358915	0.021324	-0.011186
9	68407.37	0.125467	0.374424	0.023782	-0.009108
10	68625.51	0.124867	-0.289753	0.195239	0.54308
11	68835.72	0.12381	-0.57555	[0.00]	-0.03158
12	69032.61	0.12085	-1.137998	[0.00]	-0.037503
13	69212.22	0.117527	-6.009319	[0.00]	-0.045184
14	69389.45	0.110296	-1.18449	[0.00]	0.001387
15	69589.68	0.1076	3.732642	[0.00]	0.046323

Table 4.10: Constants of the $^5\Sigma_g^-$ ion pair state of S_2 as derived from the deperturbation analysis.

Error bars are one standard deviation in units of the last significant figure.

v	Origin (cm^{-1})	B (cm^{-1})	A (cm^{-1})	λ (cm^{-1})	α (cm^{-1})
0	68771.05	0.096645	83.71184	6.535361	[0.00]
1	68971.96	0.095656	81.28594	5.28994	[0.00]
2	69174.68	0.095468	78.56954	3.950333	[0.00]
3	69361.32	0.093313	68.00728	-2.029638	-2.068624
4	69557.69	0.094783	65.55507	-1.850608	-0.236015
5	69750.24	0.096152	66.73978	7.925914	1.954885
6	69946.31	0.094899	69.44	9.831595	2.267103
7	70143.32	0.094646	72.67887	6.349822	1.407905
8	70328.44	0.092995	61.18939	[0.00]	2.513724
9	70519.99	0.095768	64.22723	0.509769	1.412394
10	70708.34	0.093919	63.8898	1.055722	2.234636
11	70893.32	0.093773	61.18939	[0.00]	2.513724
12	71074.72	0.093978	55.95526	-1.576304	2.79112

Table 4.11: Constants of the $^3\Pi_g$ ion pair state of S_2 as derived from the deperturbation analysis.

Error bars are one standard deviation in units of the last significant figure.

$\hat{H}^{SO}$/cm^{-1}	$^5\Sigma_g^-$	$^3\Pi_g$	$\hat{H}^{SO}$/cm^{-1}	$^5\Sigma_g^-$	$^3\Pi_g$	$\hat{H}^{SO}$/cm^{-1}	$^5\Sigma_g^-$	$^3\Pi_g$	$\hat{H}^{SO}$/cm^{-1}	$^5\Sigma_g^-$	$^3\Pi_g$
0.47	0	0	1.47	0	1	3.53	0	2	6.90	0	3
2.03	1	0	6.03	1	1	12.89	1	2	22.76	1	3
6.03	2	0	16.30	2	1	31.28	2	2	49.21	2	3
14.24	3	0	33.78	3	1	57.92	3	2	78.68	3	3
28.19	4	0	59.17	4	1	85.11	4	2	94.73	4	3
48.18	5	0	84.86	5	1	99.29	5	2	80.58	5	3
72.50	6	0	104.09	6	1	87.45	6	2	32.85	6	3
97.35	7	0	104.84	7	1	46.27	7	2	30.13	7	3
117.71	8	0	82.08	8	1	12.64	8	2	75.46	8	3
128.85	9	0	38.12	9	1	66.03	9	2	76.18	9	3
118.55	10	0	14.92	10	1	90.39	10	2	30.69	10	3
86.35	11	0	105.61	11	1	74.71	11	2	34.06	11	3
104.76	12	0	88.14	12	1	26.24	12	2	79.58	12	3
73.50	13	0	121.16	13	1	59.97	13	2	79.87	13	3
50.95	14	0	109.28	14	1	90.30	14	2	48.86	14	3
32.75	15	0	89.48	15	1	111.18	15	2	28.66	15	3
18.45	16	0	63.26	16	1	110.12	16	2	83.99	16	3
9.55	17	0	39.93	17	1	90.33	17	2	111.03	17	3

Table 4.12: Tables of the spin orbit interactions between the various levels of the $^5\Sigma_g^-$, $^3\Pi_g$, and $^3\Sigma_g^-$ ion pair states.

$\hat{H}^{SO}$ /cm^{-1}	$^5\Sigma_g^-$	$^3\Pi_g$	$\hat{H}^{SO}$ /cm^{-1}	$^5\Sigma_g^-$	$^3\Pi_g$	$\hat{H}^{SO}$ /cm^{-1}	$^5\Sigma_g^-$	$^3\Pi_g$
11.61	0	4	18.51	0	5	26.48	0	6
35.22	1	4	49.24	1	5	63.29	1	6
66.97	2	4	80.93	2	5	87.89	2	6
89.73	3	4	87.73	3	5	71.69	3	6
82.68	4	4	51.42	4	5	9.90	4	6
38.00	5	4	14.99	5	5	53.33	5	6
28.91	6	4	67.28	6	5	67.88	6	6
73.47	7	4	63.85	7	5	16.77	7	6
65.29	8	4	6.06	8	5	49.89	8	6
8.80	9	4	56.64	9	5	65.04	9	6
52.92	10	4	68.25	10	5	14.86	10	6
76.71	11	4	17.92	11	5	53.17	11	6
42.90	12	4	49.36	12	5	64.35	12	6
23.79	13	4	73.84	13	5	11.52	13	6
76.46	14	4	34.47	14	5	56.67	14	6
25.47	15	4	35.41	15	5	69.00	15	6
29.79	16	4	79.74	16	5	17.17	16	6
40.71	17	4	65.91	17	5	54.86	17	6

$\hat{H}^{SO}$ /cm^{-1}		$^3\Pi_g$
0.04	$^1\Pi_g$	3
50.30	$^3\Sigma_g^-$ v=0	2

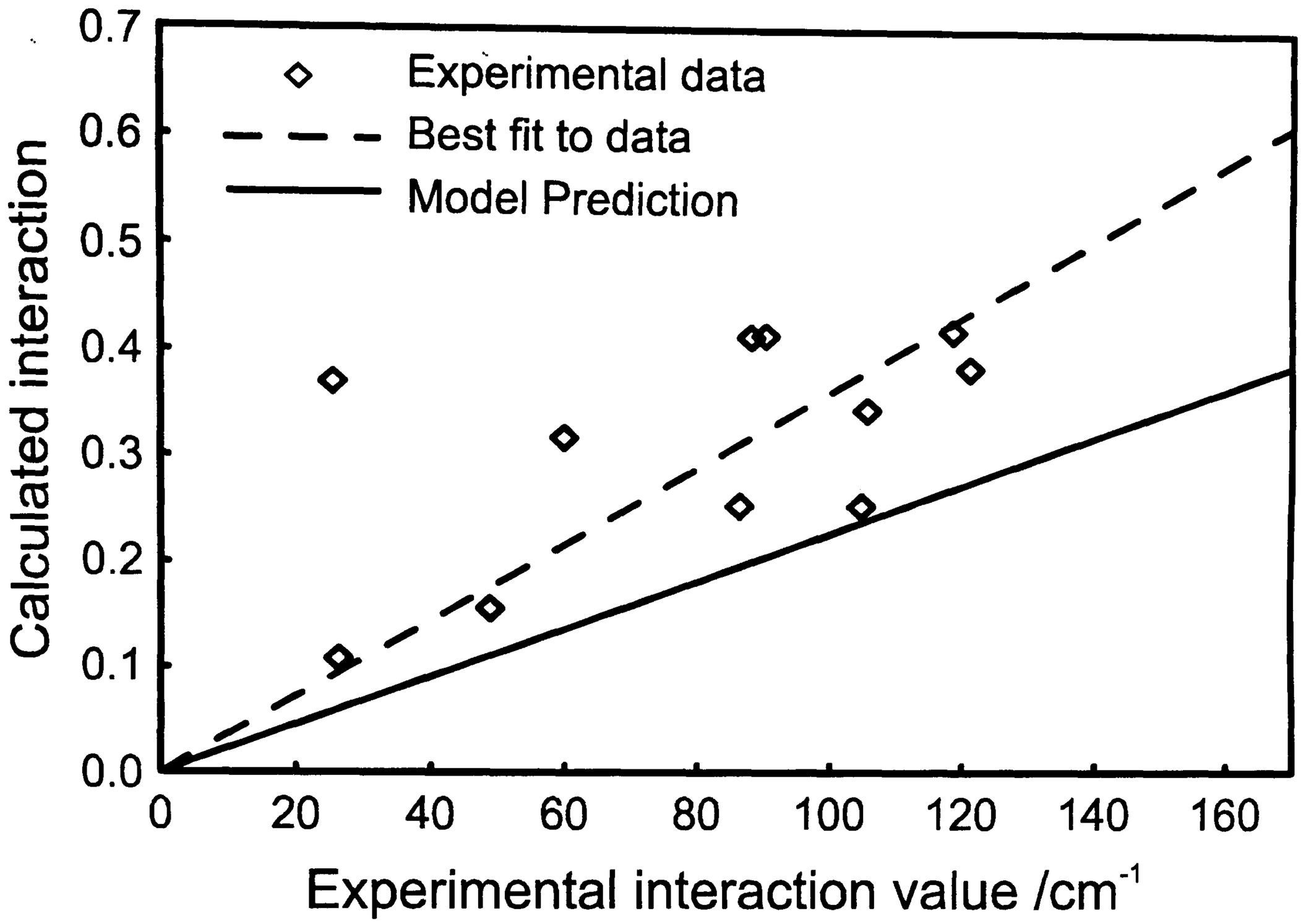

Figure 4.14: Comparison of interaction values between the $^5\Sigma_g^-$ and the $^3\Pi_g$ ion pair states. The solid line is the predicted interaction value from the separated ion model. The plotted points show the experimental interaction values from the deperturbation analysis compared to the values calculated from the vibrational wavefunctions from the LEVEL computer program. The dashed line represents the best fit line through the data points.

states. Similar equations can be solved for mixing between the other Ω components, all giving the same value. This prediction indicated in figure 4.14 is generally below all the observed interactions, but recall that the experimental data is not complete and that the model is only a low level approximation of the interactions occurring.

4.4.3 Ionisation Threshold of S_2 via the $^5\Sigma_g^-$ State

The first ionisation threshold of S_2 has been determined to be 9.356±0.002 eV (75500 cm^{-1})[20,21], with the ground state electronic configuration of the S_2^+ being $X\,^2\Pi_g$. However electronic configuration considerations forbid ionisation of S_2 from the $^5\Sigma_g^-$ state via the $X\,^2\Pi_u$ state as the removal of an electron from the ion pair state will form a quartet state. The first known excited quartet state of S_2^+ is the $a^4\Pi_u$ state,[27] which lies 17440 cm^{-1} above the ground state, with the next quartet state, the $b^4\Sigma_g^-$, lying at 30920 cm^{-1} above the ground state. Table 4.1 summarised the positions of these and other selected states of S_2 and S_2^+.

The observed ionisation threshold from the $^5\Sigma_g^-$ state does not correspond to these limits, where the S_2 is ionised by the absorption of one pump photon and two probe photons. By varying the vibrational level and Ω component of the intermediate and ion pair states, different total energies were investigated with reference to the ionisation limit. For example, a double resonance excitation scheme employing $B''^3\Pi_u$ $v = 14$, $\Omega = 1$ as the intermediate state, and probing $^5\Sigma_g^-$ $v = 1$, results in a total absorption energy 22830 cm^{-1} above the first ionisation threshold, as the intermediate state energy is 34854 cm^{-1} and the ion pair state energy is 66592 cm^{-1}. Therefore lowering the energy of the pump photon (by pumping a different intermediate level) will increase the energy available for ionisation by the same amount.

Table 4.14 presents the total energies available for ionisation through various combinations of intermediate and final states. The numbers not shaded refer to combinations that do ionise, whereas those shaded do not. Two discrepancies are immediately obvious from the table. Firstly the values around which the ionisation threshold seems to occur do not correspond to the previously known ionisation thresholds for quartet states of the ion. This inconsistency may however be a consequence of poor Franck-Condon factors for ionisation to the lower vibrational levels of the $a^4\Pi_u$ state given the large bond length of the $^5\Sigma_g^-$ state compared to the states of the ion.

The second anomaly is that some combinations that do not ionise have a greater total energy available for ionisation than others that do. For example ionisation through $^5\Sigma_g^-$ $v = 0$ via $B''^3\Pi_u$ $v = 15, \Omega = 1$ has a total energy available for ionisation of 22189 cm^{-1} above the first ionisation threshold, but does not ionise, whereas ionisation through the same final state but using $B''^3\Pi_u$ $v = 16$, $\Omega = 1$ as the intermediate state does, with 137 cm^{-1} less available energy. One possible explanation is that three photons of the probe wavelength are being absorbed in some ionisation cases. This process could be envisaged if a third state, which lies just below the ionisation threshold, is populated after absorption of the second probe photon, with subsequent absorption of a third photon ionising the radical.

If the above mechanism is the case, from the information presented in table 4.14, it can only be concluded that the ionisation threshold lies above the highest energy combination that does not ionise, i.e. 22550 cm^{-1} above the first ionisation threshold. An ionisation threshold of 22550 cm^{-1} places the energy required for ionisation between $v = 8$ and $v = 9$ of the $a^4\Pi_u$ state.

$B''^3\Pi_u$			$^5\Sigma_g^-$		
			v=0	v=1	v=2
v	Ω	Energy (cm^{-1})	66358	66592	66827
13	2	34811	22405	22873	23343
14	1	34854	22362	22830	23300
15	1	35027	22189	22657	23127
16	0	35103	22113	22581	23051
15	2	35134	22082	22550	23020
16	1	35164	22052	22520	22990
17	1	35275	21941	22409	22879
18	1	35386	21830	22298	22768
18	2	35422	21794	22262	22732

Table 4.14: Table of energies, above the first ionisation threshold, that different combinations of intermediate and ion pair state reach after the absorption of one pump and two probe photons. The grey shaded combinations do not show an ion signal, whereas the non-shaded combinations do.

4.5 Conclusions

This is this first time an ion pair state of a group VI molecule has been revealed. The double resonance technique is essential in accessing the ion pair manifold, with the B" state acting as a particularly good intermediate level due to the many different types of mixing it experiences. The $^5\Sigma_g^-$, $^3\Pi_g$ and $^3\Sigma_g^-$ states were directly observed, and characterised to greater or lesser extents, along with values for perturbation interactions between vibrational levels of the $^5\Sigma_g^-$ and $^3\Pi_g$ states. The constants deduced from the current study serve as an excellent foundation from which to probe higher into the wealth of ion pair and Rydberg states that lie to higher energy.

The ionisation threshold of the $^5\Sigma_g^-$ state was also investigated, but found not to correlate directly to any known excited state of the ion. This apparent inconsistency may be accounted for by the poor Franck-Condon factors associated with transitions from the $^5\Sigma_g^-$ ion pair state to the states of the ion, as a consequence of the long bond length of the ion pair state.

4.6 References

1 R.B.W. Pearce and A.G. Gaydon, *The Identification of Molecular Spectra*, Chapman and Hall, London (1963).

2 A. Fowler and W.M. Vaïdya, *Proc. R. Soc. A.* **132**, 310 (1931).

3 G. Lakshminarayana and C.G. Mahajan, *J. Quant. Spectrosc. Radiat. Transfer.* **16**, 549 (1976).

4 Y.V. Ramanamma Chaudhri and C.G. Mahajan, *J. Mol. Spectrosc.* **145**, 308 (1991).

5 J. Breton, F. Remy, I. Dubois, H. Bredohl, D. Macau-Hercot, J.M. Esteva and E. Somé, *J. Molec. Spectrosc.* **173**, 49 (1995).

6 R.J. Donovan, D. Husain and C.D. Stevenson, *Trans. Far. Soc.* **66**, 1 (1970).

7 K. WieLand, M. Wehrli and E. Miescher, *Helv. Phys. Acta.* **7**, 843 (1934).

8 R. Maeder and E. Miescher, *Nature.* **161**, 393 (1948).

9 R. Maeder, *Helv. Phys. Acta.* **21**, 411 (1948).

10 Y. Tanaka and M. Ogawa, *J. Chem. Phys.* **36**, 726 (1962).

11 M.E. Green and C.M. Western, *J. Chem. Phys.* **104**, 848 (1996).

12 M.E. Green and C.M. Western, *J. Chem. Soc. Faraday Trans.* **93**, 365 (1997).

13 M.E. Green, *Ph.D. Thesis*, University of Bristol, (1996).

14 M. Barnes, J. Baker, J. M. Dyke and R. Richter, *Chem. Phys.* **166**, 229 (1992).

15 F.D. Wayne, P.B. Davies and B.A. Thrush, *Mol. Phys.* **28**, 989 (1974).

16 H.M. Pickett and T.L. Boyd, *J. Mol. Spectrosc.* **75**, 53 (1979).

17 G. Herzberg, *Molecular Spectra and Molecular Structure I. Spectra of Diatomic Molecules*. Van Nostrand Reinhold Company, New York, (1950).

18 K.S. Knoll, M.A. McGrath, L.M. Trafton, S.K. Atreya, J.J. Caldwell, H.A. Weaver, R.V. Yelle, C. Barnet and S. Edgington, *Science.* **267**, 1307 (1995).

19 S.R. Leone and K.G. Kosnik, *Appl. Phys. Letts.* **30**, 346 (1977).

20 J.M. Dyke, L. Golob, N. Jonathan and A. Morris, *J. Chem. Soc. Farad. Trans.* **7**, 1026, (1975).

21 J. Berkowitz and C. Lifshitz, *J. Chem. Phys.* **48**, 4346 (1968).

22 H. Hotop and W.C. Lineberger, *J. Phys. Chem. Ref. Data*. **14**, 731 (1985).

23 J.M. Brown, A.S-C. Cheung and A.J. Merer, *J. Mol. Spectrosc*. **124**, 464 (1987).

24 J.E. Huheey, E.A. Keiter and R.L. Keiter, *Inorganic Chemistry: Principles of structure and reactivity*, 4th edition, Harper Collins, New York (1993).

25 J. Tellinghuisen, *Comp. Phys. Comm*, **6**, 221 (1973).

26 R.J. LeRoy, LEVEL 6.1, University of Waterloo Chemical Physics Research Report CP-555R (1996).

27 K.P. Huber and G. Herzberg, *Constants of Diatomic Molecules*, Van Nostrand Reinhold, New York (1979).

Chapter 5

Photofragment Ion Imaging of Br_2

5.1 Introduction

The bromine molecule, Br_2, has been the subject of many spectroscopic investigations.[1–4] Central interest lies in its membership of the halogen series, along with the fact that the molecule is stable and readily available. For these reasons past studies have resulted in a wealth of spectroscopic data with which some of the excited states of the molecule have been characterised. Photofragmentation of the diatomic halogens and interhalogens has also been an area of extensive investigation,[5–8] many experimental techniques have been used such as angle-resolved photofragment translational spectroscopy,[9–12] transient absorption of vacuum ultraviolet (VUV) radiation,[13] infrared fluorescence,[14] laser gain vs. absorption spectroscopy[15] and photofragment ion imaging.[16,17] The investigation described in this chapter uses this last technique to investigate the photodissociation dynamics of Br_2.

The bond dissociation energy of bromine, $D_0^0(\text{Br-Br}) = 15890\ \text{cm}^{-1}$.[18] The threshold wavenumbers and wavelengths for producing the three possible combinations of $Br(^2P_{3/2}^o)$ and $Br^*(^2P_{1/2}^o)$ products via photodissociation are:

$$Br_2 \rightarrow Br + Br \qquad 15890\ \text{cm}^{-1}\ (\lambda < 629.0\ \text{nm}) \qquad (5.1)$$

$$Br_2 \rightarrow Br + Br^* \qquad 19580\ \text{cm}^{-1}\ (\lambda < 510.6\ \text{nm}) \qquad (5.2)$$

$$Br_2 \rightarrow Br^* + Br^* \qquad 23265\ \text{cm}^{-1}\ (\lambda < 429.8\ \text{nm}) \qquad (5.3)$$

The ground state of Br_2 has the term symbol $X^1\Sigma_g^+$ which arises from the electronic configuration $.....14\sigma_u^{*2}\ 15\sigma_g^{\ 2}\ 8\pi_u^{\ 4}\ 9\pi_g^{*4}$. The molecular orbital diagram in figure 5.1 illustrates this electronic configuration, with figure 5.2 showing the correlation diagram for the low lying valence states with the predicted dissociation products for Br_2. The second column from the left of figure 5.2 shows the Hund's case (a) notation for the coupling of the electronic angular momenta. This case assumes, that the spin and orbit angular momenta are not coupled together, and are coupled separately to the internuclear axis. This is only valid for Br_2 (and the other halogens and interhalogens) at small bond lengths. At bond lengths around the equilibrium bond

length and longer, the atomic spin-orbit coupling is still partially effective, which results in the molecular spin and orbital angular momenta (Σ and Λ) being poorly defined, and Ω ($= \Sigma + \Lambda$) is the only good quantum number. This coupling regime is known as Hund's case (c), which provides the best description of the momentum coupling at large internuclear distances. For this reason the term symbol for the electronic states of the halogens are often written using mixed case (a) and (c) notation, e.g. $B^3\Pi_u(0_u^+)$. This mixed notation will be used in this and the following chapter (dealing with BrCl). This notation is beneficial as it stresses the Ω quantum number of the state, as it is the change in Ω experienced by the molecule prior to dissociation that ion imaging is particularly sensitive to.

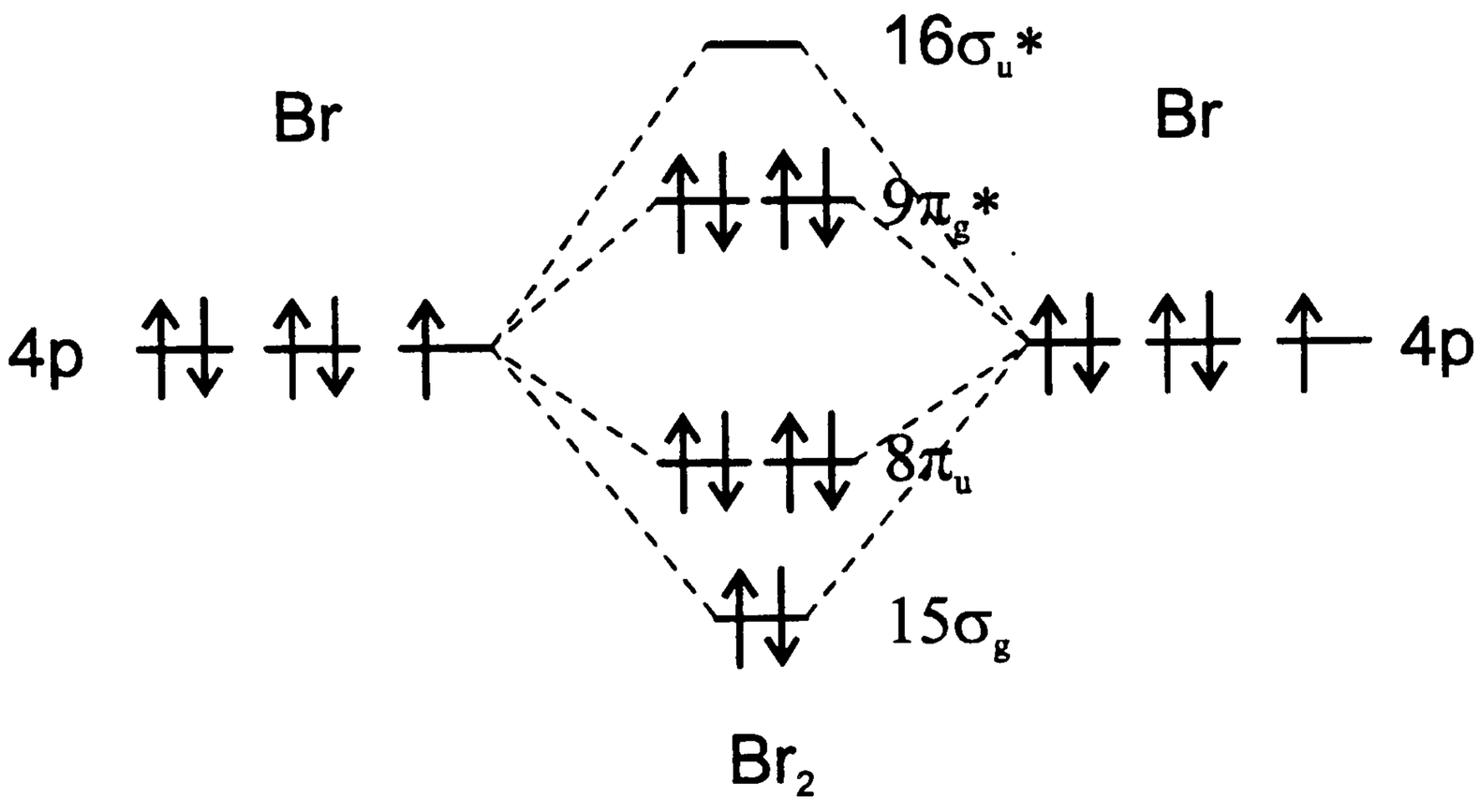

Figure 5.1: Molecular orbital diagram of Br_2 showing highest occupied orbitals.

Of the excited states of Br_2 indicated in figure 5.2 most are repulsive, but the two most important bound states (in terms of the UV/visible) absorption spectrum are the $A^3\Pi_u(1_u)$ and the $B^3\Pi_u(0_u^+)$ states, which both arise from the electronic configuration .....$14\sigma_u^{*2}\ 15\sigma_g^{2}\ 8\pi_u^{4}\ 9\pi_g^{*3}\ 16\sigma_u^{*1}$. Although transitions between the ground state and these two states and are formally spin forbidden they do occur. The intensity of these transitions arises from the mixing of the triplet and singlet states, which is induced by the persistence of the spin-orbit coupling. The near UV and visible absorption spectrum of Br_2 has previously been studied and interpreted by a number of workers.[19–22] Figure 5.3 shows the UV/visible absorption spectrum, along

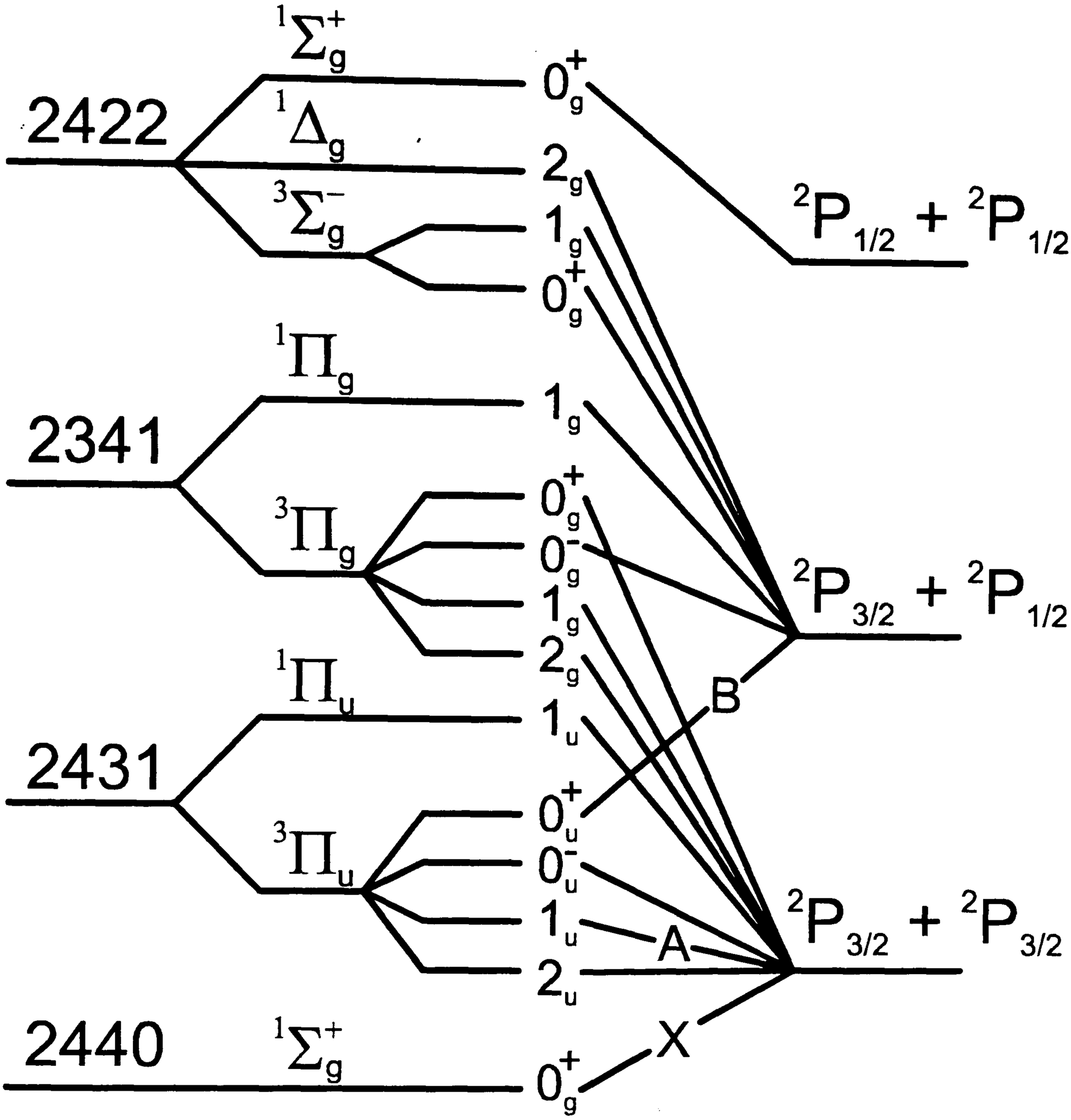

Figure 5.2: Diagram showing the low-lying electronic states of Br_2 and their expected correlations to the three possible asymptotes corresponding to the different spin-orbit states of the $Br(^2P)$ atoms. The four-digit numbers on the left-hand side represent the electronic occupancies of the valence $\sigma_g\pi_u\pi_g^*\sigma_u^*$ orbitals.

with schematic Gaussian curves to represent the contribution to the total absorption from three different excited states of Br_2. It shows resolved rovibronic structure at wavelengths $\lambda > 510$ nm, albeit complicated by the density of rovibronic structure approaching the Br + Br* limit and the presence of three isotopomers - $^{79}Br^{79}Br$, $^{79}Br^{81}Br$ and $^{81}Br^{81}Br$ (with relative weights ~ 1:2:1 in any natural abundance sample). This lower energy region has been assigned in terms of absorption from the $X^1\Sigma_g^+(0_g^+)$ ground state to the $A^3\Pi_u(1_u)$ and the $B^3\Pi_u(0_u^+)$ excited states. Both transitions have been studied in absorption and in laser induced fluorescence (LIF).[1–4,7] All B state levels with $v > 0$ lie above the lowest energy (Br + Br) dissociation limit and are therefore capable of predissociation. Careful measurements of the fluorescence lifetimes of individual B state levels, and the ways in which they vary as a function of both the vibrational (v) and rotational (J') quantum numbers, have been rationalised in terms of rotationally induced predissociation caused by coupling to a repulsive state of 1_u symmetry.[4,23]

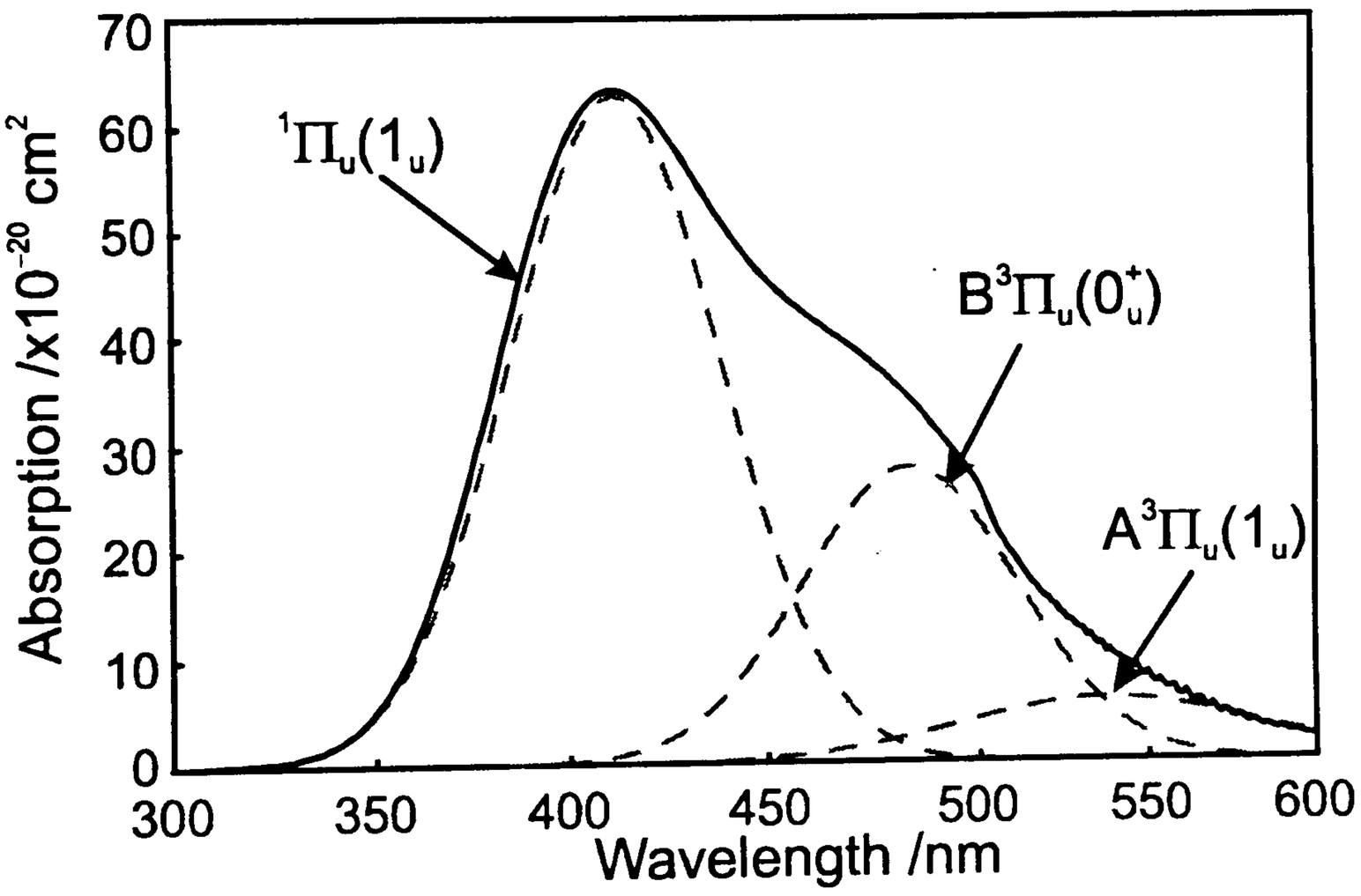

Figure 5.3: The absolute UV/visible absorption spectrum for Br_2 in the wavelength range 300 to 600 nm is shown as the solid line. A schematic deconvolution of the absorption spectrum into contributions from 3 excited states ($A^3\Pi_u(1_u)$, $B^3\Pi_u(0_u^+)$ and $^1\Pi_u(1_u)$) is indicated by the dotted lines.

The schematic deconvolution of the total absorption spectrum shown in fig. 5.3 indicates that the A–X and, particularly, B–X transitions contribute to the continuous absorption at shorter wavelengths; the latter is deemed responsible for the clear inflection in the absorption profile at $\lambda \sim 470$ nm. At still shorter wavelengths the absorption is dominated by excitation to the repulsive $^1\Pi_u(1_u)$ state. Note that the foregoing description of the valence absorption spectrum of bromine in terms of transitions to just three excited states belies the complexity of the electronic structure of the molecule. State counting from figure 5.2 shows that no fewer than 23 excited electronic states[7] correlate with the asymptotes (5.1 - 5.3). Fig. 5.4 shows the relevant potential energy curves correlating to the atomic state asymptotes.

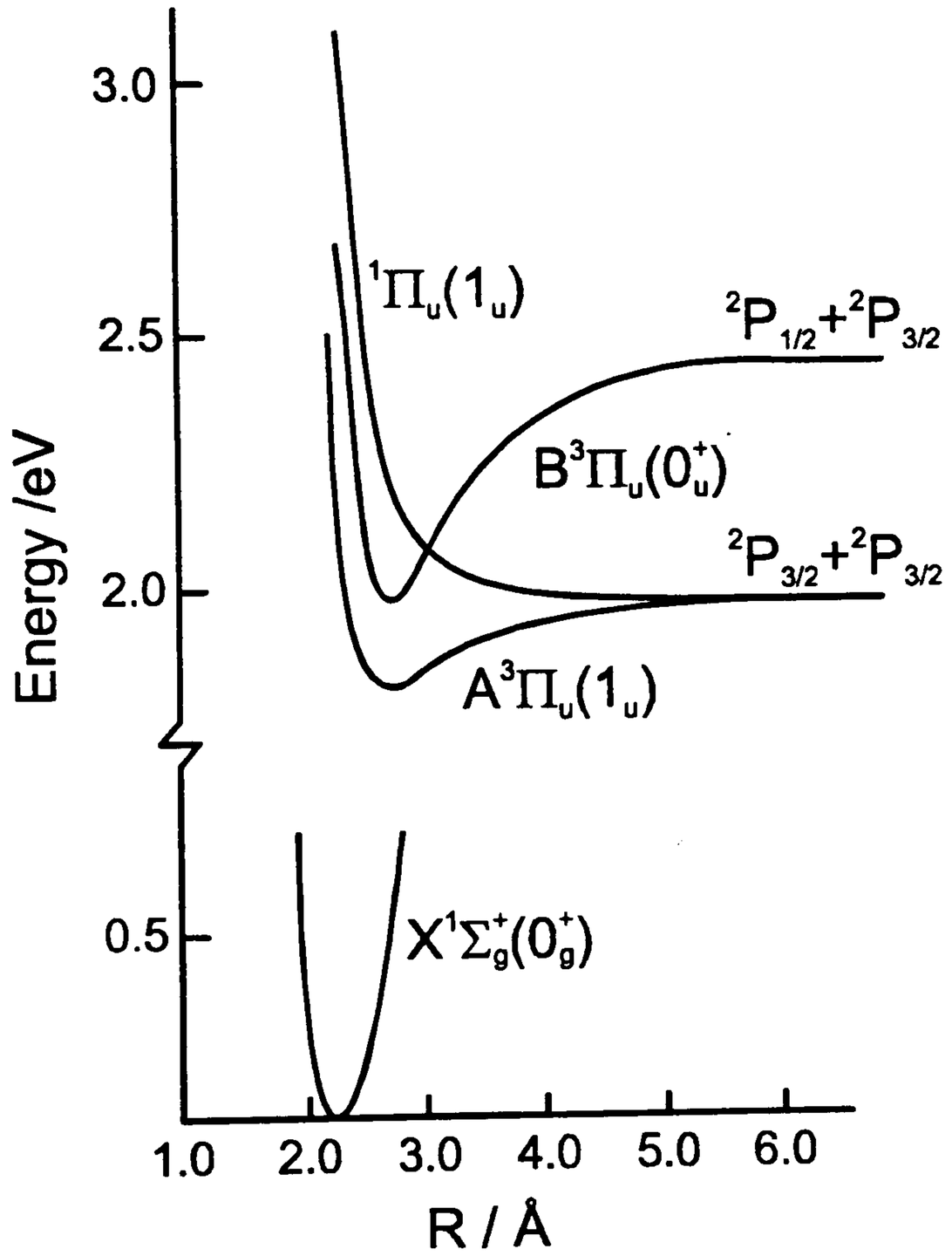

Figure 5.4: A schematic of the potential energy curves accessed in UV/visible excitation of Br_2. Note how the $A^3\Pi_u(1_u)$ and $^1\Pi_u(1_u)$ states correlate to the Br + Br limit, whereas the $B^3\Pi_u(0_u^+)$ state correlates to the Br + Br* limit.

Previous studies of Br_2 photodissociation are comparatively sparse: Wilson and co-workers[10] used photofragment translational spectroscopy (PTS) to study Br_2 photolysis at 532.3, 466.1 and 346.9 nm and determined the angular anisotropy of the distribution of recoiling ground state Br atoms formed at all three wavelengths and of the Br + Br* product channel at λ = 466.1 nm. The angular distribution of ground state products (channel (5.1)) was found to be characterised by an anisotropy parameter, $\beta \sim -1$ at all three wavelengths, indicating that dissociation to these products follows a perpendicular ($\Delta\Omega = \pm 1$) excitation to the $A^3\Pi_u(1_u)$ and/or the $^1\Pi_u(1_u)$ states of the parent Br_2. The angular distribution of the Br + Br* products, in contrast, was found to fit to a positive value of β, leading to the suggestion that these channel (5.2) products arise as a result of dissociation following a parallel ($\Delta\Omega = 0$) transition, most probably involving the $B^3\Pi_u(0_u^+)$ excited state. The photofragmentation of Br_2 has also been investigated by laser gain versus absorption spectroscopy on the $Br \leftrightarrow Br^*$ spin-orbit transition at 3685 cm^{-1}.[15] These measurements enabled determination of the relative quantum yields for forming Br and Br* products, and thus of the relative importance of the Br + Br and Br + Br* product channels, as a function of parent excitation wavelength in the range 445 - 530 nm. A recent one-colour ion imaging study[24] of Br_2 photolysis at $\lambda \sim 265$ nm with detection of both Br and Br* atoms determined channel (5.2) to be dominant and measured anisotropy parameters consistent with excitation to 1_u state, tentatively assigned as the $^3\Sigma_u^+(1_u)$ state arising from the electron configuration $....15\sigma_g^{\,1}\, 8\pi_u^{\,4}\, 9\pi_g^{*4}\, 16\sigma_u^{*1}$.

In this chapter ion imaging studies of the Br and Br* fragments resulting from the photodissociation of Br_2 at 260 nm and at 19 different wavelengths in the range 360 - 580 nm are described. Relative branching ratios for product channels (5.1) - (5.3) and the photofragment recoil anisotropies of the various participating channels at each wavelength were determined, which enabled further characterisation of the nature, roles and interplay of the excited electronic states involved in the photodissociation dynamics of the molecule.

5.2 Experimental

The ion imaging experimental design and set-up has been previously described in chapter 2. Pure Br_2 gas was diluted in argon (typically ~15% in 1 atmosphere) prior to use. Br_2 was photolysed over the range of wavelengths from 260 - 580 nm with two different laser systems employed to span this range. In both cases the Br or Br* photofragments were ionised by 2+1 resonance enhanced multiphoton ionisation (REMPI) via the following transitions:[25]

$$Br\ (4p^5;^2P^o_{3/2}) + 2h\nu\ (\lambda = 260.622\ nm) \rightarrow Br\ (4p^4 5p^1;^2D^o_{3/2}) \qquad (5.4)$$

and $$Br^*\ (4p^5;^2P^o_{1/2}) + 2h\nu\ (\lambda = 262.548\ nm) \rightarrow Br\ (4p^4 5p^1;^2S^o_{1/2}), \qquad (5.5)$$

each followed by $$Br\ (4p^4 5p^1) + h\nu \rightarrow Br^+ + e^-. \qquad (5.6)$$

5.3 Results

A typical observed and manipulated image is shown in figure 5.5. Figure 5.5(a) shows the measured 2-D projection (after symmetrization) of the 3-D recoil velocity distribution of the Br fragments arising from the 460 nm photolysis of Br_2, using vertically polarised laser radiation. Figure 5.5(b) shows the slice through the back-projected image which shows two distinct velocity sub-groups, corresponding to formation of Br + Br (outer ring) and Br + Br* (inner ring).

Not visible in fig. 5.5, but evident in images recorded at higher probe laser intensities is the 'one colour' image resulting from Br_2 photolysis at ~260.662 nm, the REMPI probe wavelength. Velocity analysis of the single ring in the one colour image shows the radius to correspond to formation of one ground state (Br) atom and one excited state (Br*) atom, with maximum photofragment flux perpendicular to the ε vector of the photolysis laser radiation. This image makes an inevitable (albeit very weak) contribution to all two colour images obtained in this work, but its large radius and relative weakness ensures that it is not a source of interference.

Figure 5.6 shows representative samples of 2-D slices through the reconstructed 3-D recoil distributions for both Br and Br* products recorded at six different photolysis wavelengths. Clearly the images change in radius as well as appearance as the wavelength of the photolysis photon is changed. This variation in the image size is indicative of the energy available as kinetic energy in the photofragments. The same amount of energy is needed in each case to break the molecular bond, but as the wavelength of the photolysis photon is lengthened less energy is available as translational energy in the photofragments, which leads to smaller images. Analysis of the Br images taken at short photolysis wavelengths (360 - 400 nm) shows the observed signal to result from dissociation of Br_2 to two ground state Br fragments, with the maximum photofragment flux perpendicular to the polarisation axis of the photolysis laser. As the wavelength of the photolysis laser is increased through the range from 400 nm up to 500 nm a second, smaller, ring can be seen in all of the Br images. This second ring exhibits a different angular distribution, with the maximum

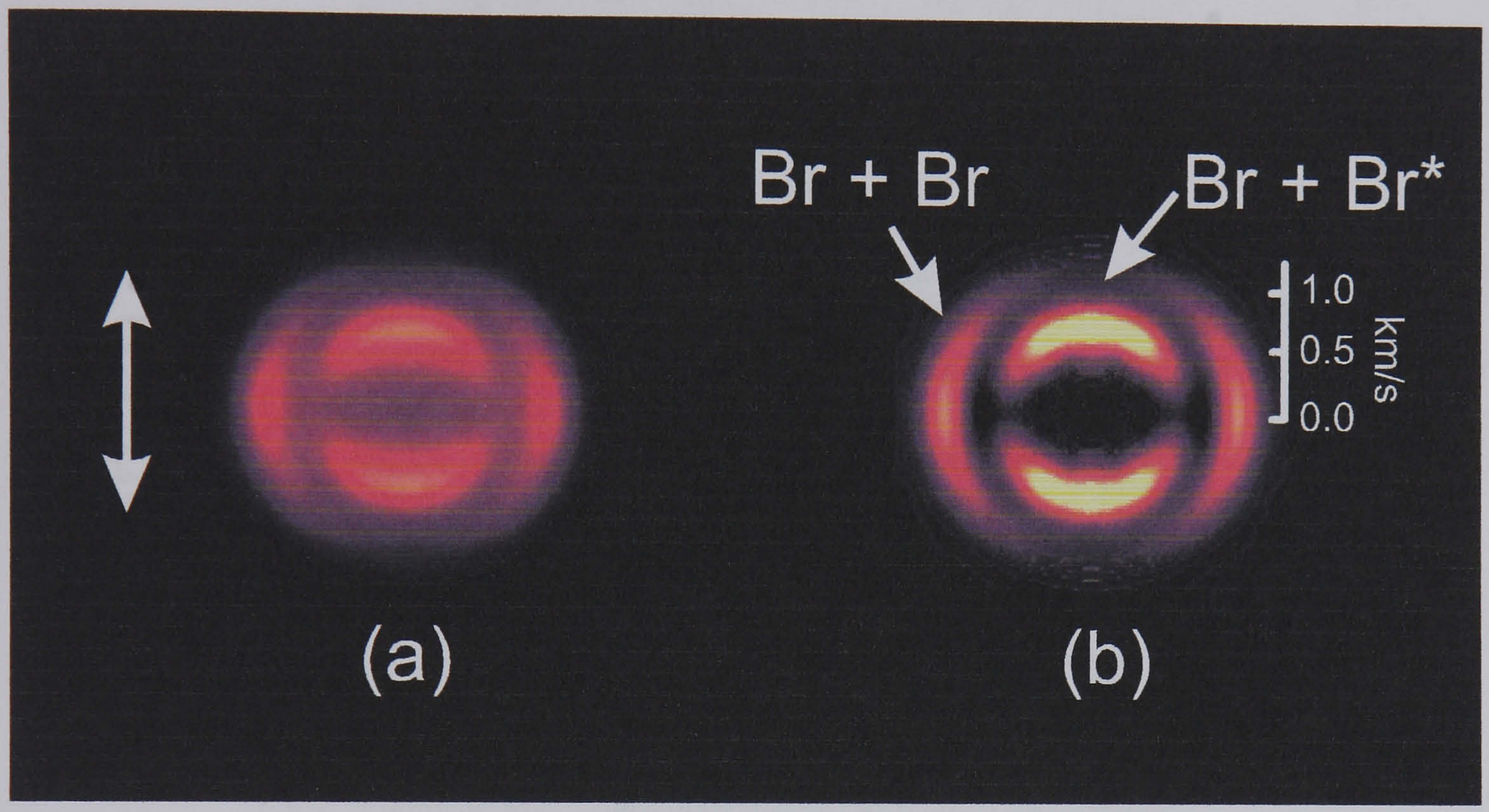

Figure 5.5: The raw image (a) and the 2D slice through the 3D reconstruction of the Br photofragment recoil distribution (b) at 460 nm. The arrow indicates the direction of the photolysis laser polarisation vector. Two velocity subgroups, due to Br + Br and Br + Br*, are clearly visible.

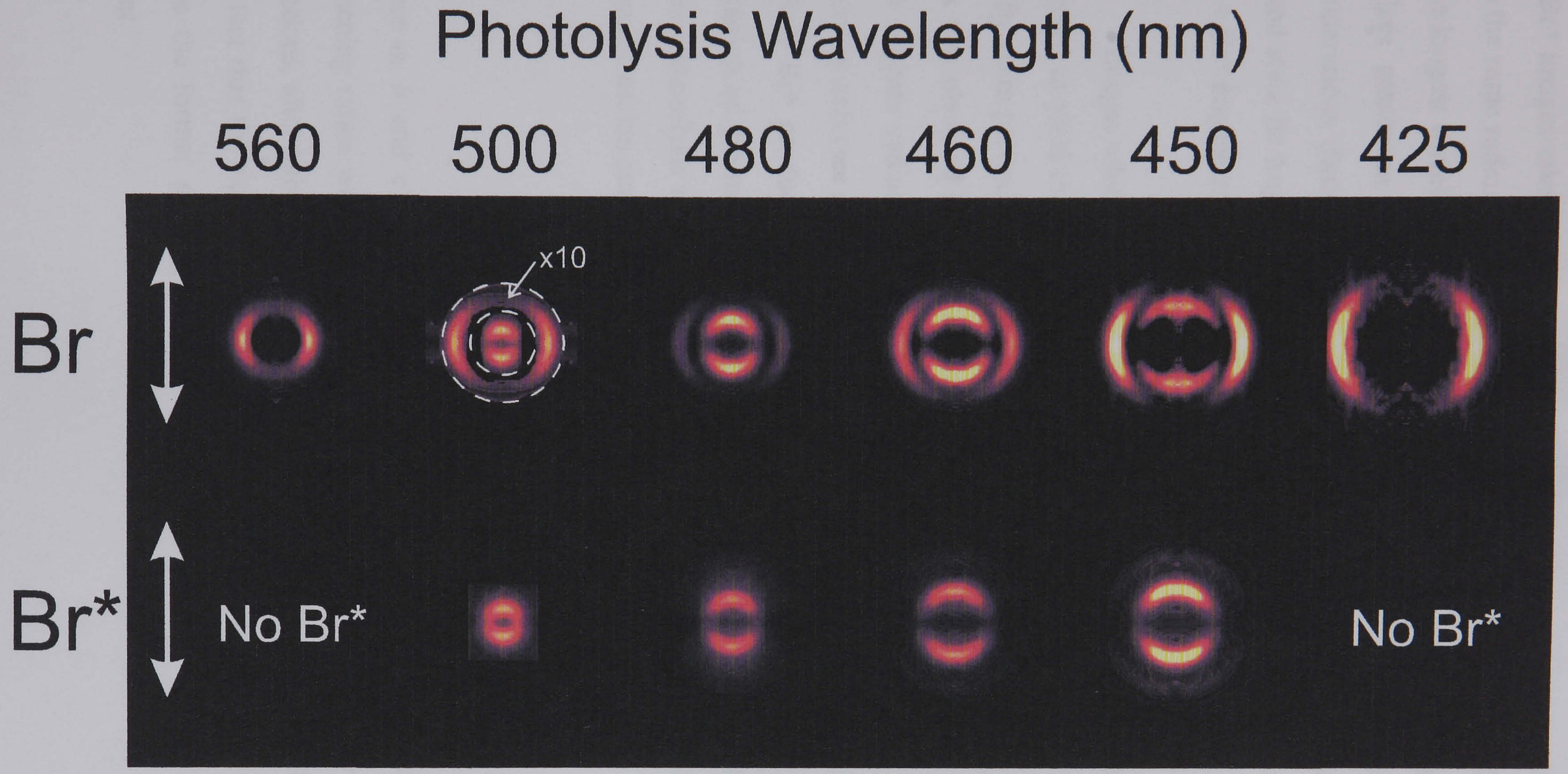

Figure 5.6: 2D slices of the reconstructed 3D ion clouds of both Br and Br* at 6 different wavelengths from 425 - 560 nm. The vertical arrow indicates the direction of the photolysis laser polarisation vector. The intensity of the photofragment flux between the images has not been normalised.

photofragment flux parallel to the photolysis polarisation axis, and is attributed to photodissociation to form Br* + Br atomic products. This assignment is confirmed by the Br* images taken at the same wavelengths, which show only one product channel with the same radius and angular anisotropy as the inner ring of the Br images. Finally, at the longest wavelengths investigated (540 - 580 nm), just one ring is observed. This displays maximum flux perpendicular to the laser beam polarisation. Energetic considerations dictate that this signal is due to Br_2 photodissociation yielding two ground state Br fragments. None of the Br* images show any evidence for an active Br* + Br* fragmentation channel.

Images which reveal the involvement of more than one product channel can be analysed to yield the respective channel branching ratios. Figure 5.7 shows a plot of the Br atom product flux velocity distribution resulting from Br_2 photolysis at 460 nm. This was obtained from the appropriate 2-D slice (fig. 5.5(b)) by integrating all flux with a given radius ρ, appropriately weighted by the distance $r = \rho\sin\theta$ from the symmetry axis (see appendix A). The peak at smaller radius (and hence velocity) is due to Br + Br* product formation, whereas the peak at larger radius is associated with formation of ground state products. To calculate the product branching ratio at the various photolysis wavelengths the experimental velocity plot (as in fig. 5.7) was fitted to two Gaussian curves of the form:

$$f(x) = a\exp(-b(x-c)^2) \qquad (5.7)$$

where a, b and c were all varied to fit the observed data. The product channel branching ratios were then deduced from the relative areas under the two Gaussian functions, after halving the relative weight of the faster (Br + Br) product to allow for the fact that the experiment is twice as sensitive to channel (5.1) as to channel (5.2), since the former pathway produces two Br atomic products per photodissociation event.

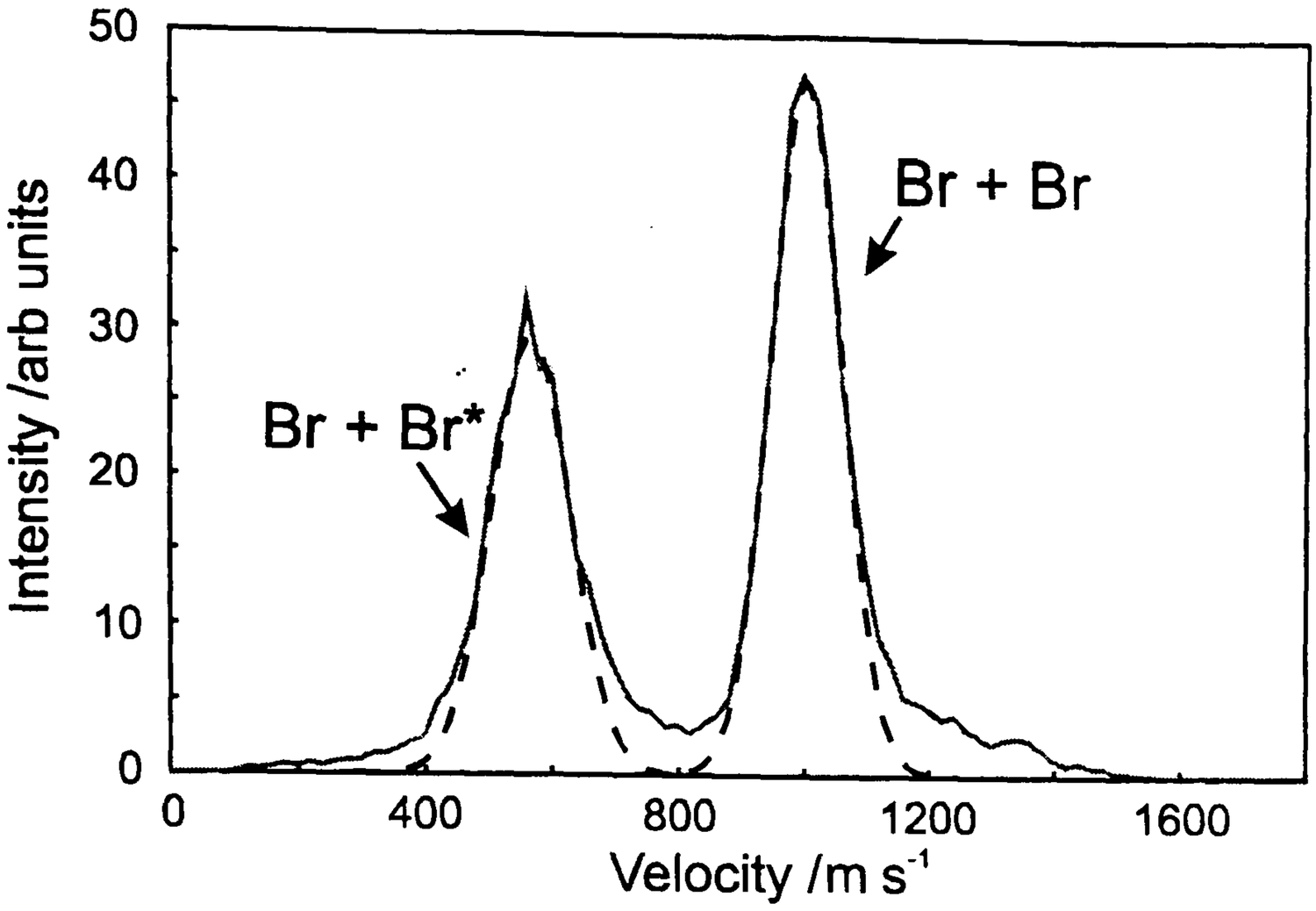

Figure 5.7: The velocity distribution of the Br photofragments from photolysis at 470 nm. The Gaussian fits to the two velocity subgroups (Br + Br and Br + Br*) are indicated. The ratio of the areas of the two Gaussians is directly related to the branching ratio between the two atomic product channels at the photolysis wavelength.

Figure 5.8 shows the channel branching ratios so derived, expressed as

$$\phi(\mathrm{Br} + \mathrm{Br}^*) = \frac{[\mathrm{Br} + \mathrm{Br}^*]}{[\mathrm{Br} + \mathrm{Br}] + [\mathrm{Br} + \mathrm{Br}^*]}, \qquad (5.8)$$

where [Br + Br*] and [Br + Br] are, respectively, the area under the slow peak and half the area under the fast peak in plots such as that shown in fig. 5.7. The data agrees well with the earlier (less extensive) measurements of Leone and co-workers.[15] Photolysis at $360 < \lambda < 400$ nm leads to no observable Br + Br* product formation. This excited product channel first appears in the image recorded at $\lambda = 435$ nm, where it contributes ~5% of the total dissociation flux. ϕ(Br +Br*) increases with increasing wavelength, reaching ~79% of the total product flux at $\lambda = 500$ nm. Images taken at $\lambda = 520$ nm still show a quite intense central 'spot' attributable to Br + Br* products. recalling the threshold wavelengths quoted in section 5.1 it is evident that these must result from hot-band absorptions, or by collision induced dissociation,[26] with the

importance of both effects sensitively dependent upon the molecular beam conditions. For this reason no attempt is made to define branching ratios at $\lambda > 500$ nm in fig. 5.8. Figure 5.9 also illustrates the variation in branching ratio as the photolysis wavelength is changed. Shown are the velocity distributions for Br atoms born from photolysis at 8 different wavelengths. Each velocity distribution shows two peaks to a greater or lesser extent. The slower peak corresponds to Br atoms from dissociation into Br + Br*, whereas the faster peak is due to Br + Br formation. As before the areas under the two peaks are a direct measurement of the branching ratio at each specific wavelength. The peaks that arise from the same dissociation pathway, either Br + Br or Br + Br*, can be seen to move to lower velocity as the wavelength of the photolysis laser is lengthened. This is directly analogous to the shrinking of the images shown in figure 5.6, where longer wavelength photolysis leaves less energy available as kinetic energy of the photofragments after breaking the molecular bond.

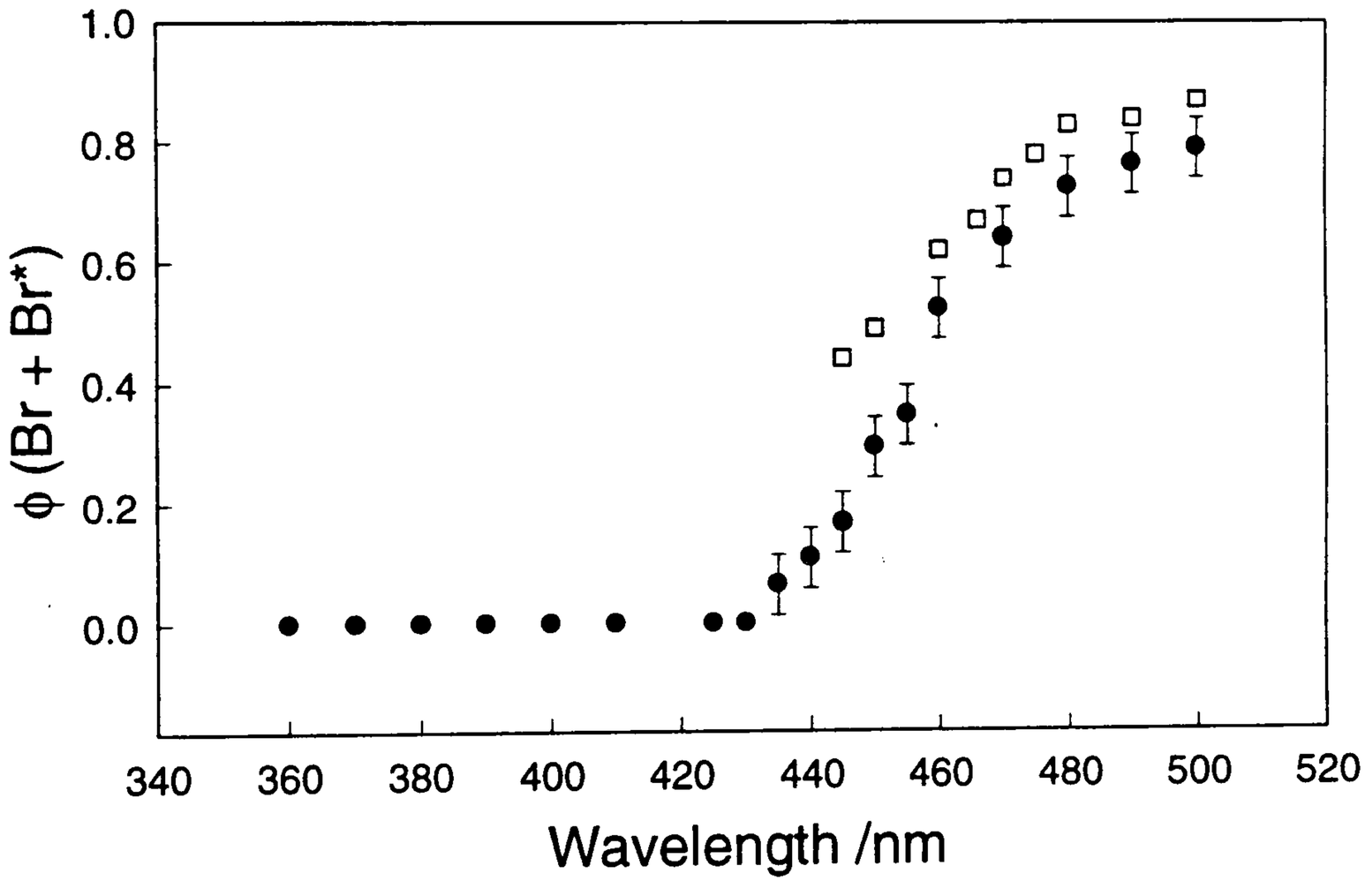

Figure 5.8: Calculated branching ratio of Br_2 (●) into either Br + Br or Br + Br*, shown as %Br + Br* formed, for the photolysis region 360 to 500 nm. The previous measurements by Leone and co-workers[15] are also indicated (❑).

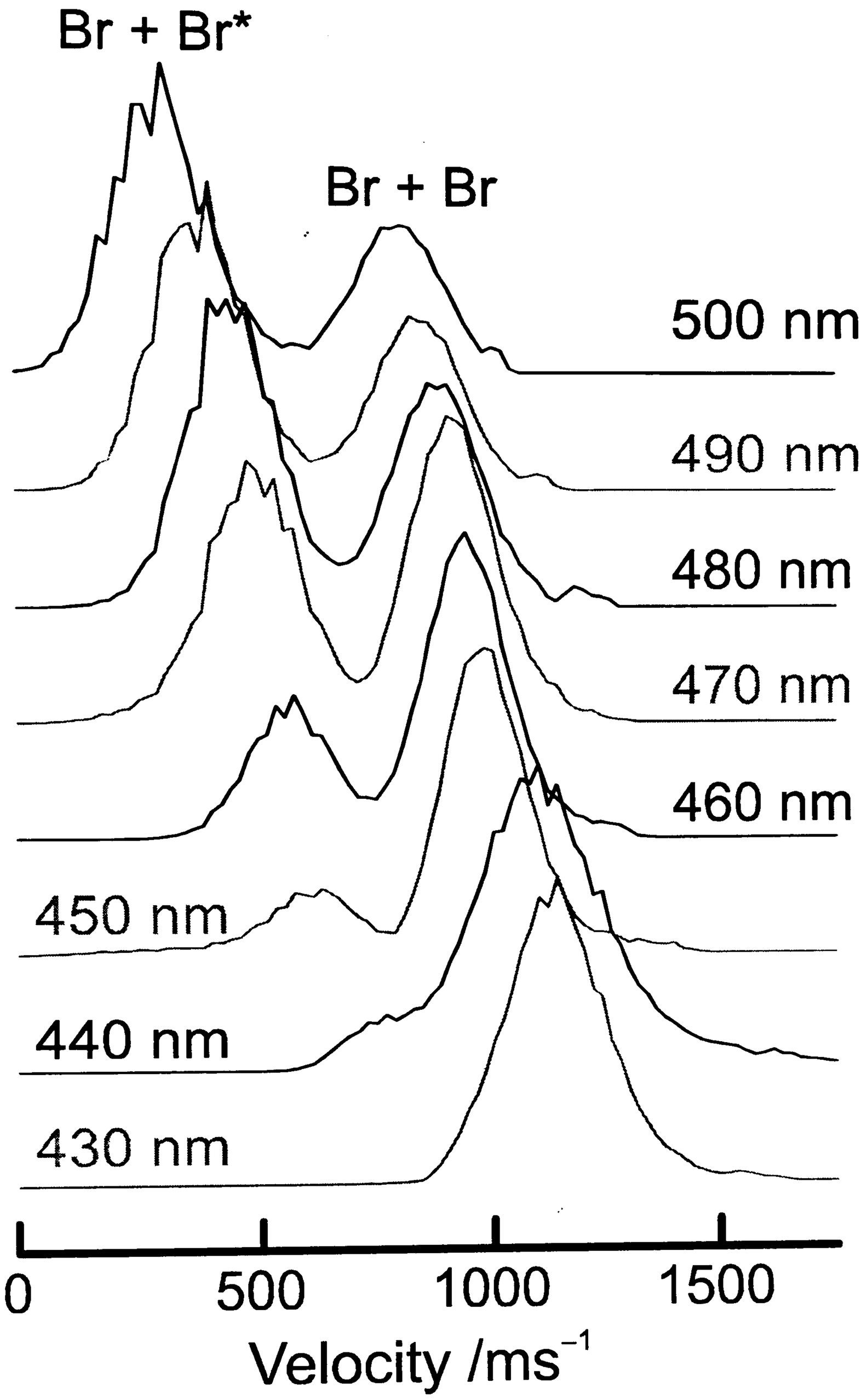

Figure 5.9: The velocity distribution of the Br photofragments is shown at 8 wavelengths between 500 and 430 nm. The peaks at higher velocity correspond to Br from dissociation of Br_2 into Br + Br, whereas the slower peaks correspond to formation of Br + Br*. The areas of the peaks indicate the relative branching ratio of the photodissociation at the different wavelengths into Br + Br or Br + Br*.

The FWHM of the best-fit Gaussian functions created from the experimental data, calculated via:

$$FWHM = 2\sqrt{\frac{\ln 2}{b}} \qquad (5.9)$$

provide a value (± 100 m s^{-1}) for the velocity resolution in the present ion imaging experiments. This velocity spread was found to give a good fit to the back-projected images derived at all photolysis wavelengths used in the study.

The anisotropies of the product recoil velocity distributions obtained at each photolysis wavelength were quantified by fitting the angular distributions of the different velocity sub-groups in terms of the standard expression[27] for the anisotropy parameter, first presented as equation (1.7) in chapter 1.

$$I(v,\theta) = \left(\frac{1}{4\pi}\right).f(v).\left[1+\beta P_2(\cos\theta)\right], \qquad (5.10)$$

Recall that β, the anisotropy parameter, can take the limiting values of +2, corresponding to a prompt dissociation following a parallel photoexcitation, and -1 for a prompt, perpendicular dissociation path. Figure 5.10 shows angular distributions and best fit lines for the Br + Br and Br + Br* product channels arising in the 480 nm photolysis of Br_2, with $\beta_{(Br + Br)} = -1.0 \pm 0.1$ and $\beta_{(Br + Br^*)} = 1.1 \pm 0.1$. The β values derived for the active product channels at all photolysis wavelengths investigated, along with the values reported previously by Wilson and co-workers[10] are summarised in table 5.1 and figure 5.11. The ground state Br + Br product channel is seen to display a limiting β value of ~ -1 except at the very longest wavelength studied, whereas the value of $\beta_{(Br + Br^*)}$ decreases from ~ 1.86 at λ = 455 nm to ~ 0.6 at λ = 500 nm.

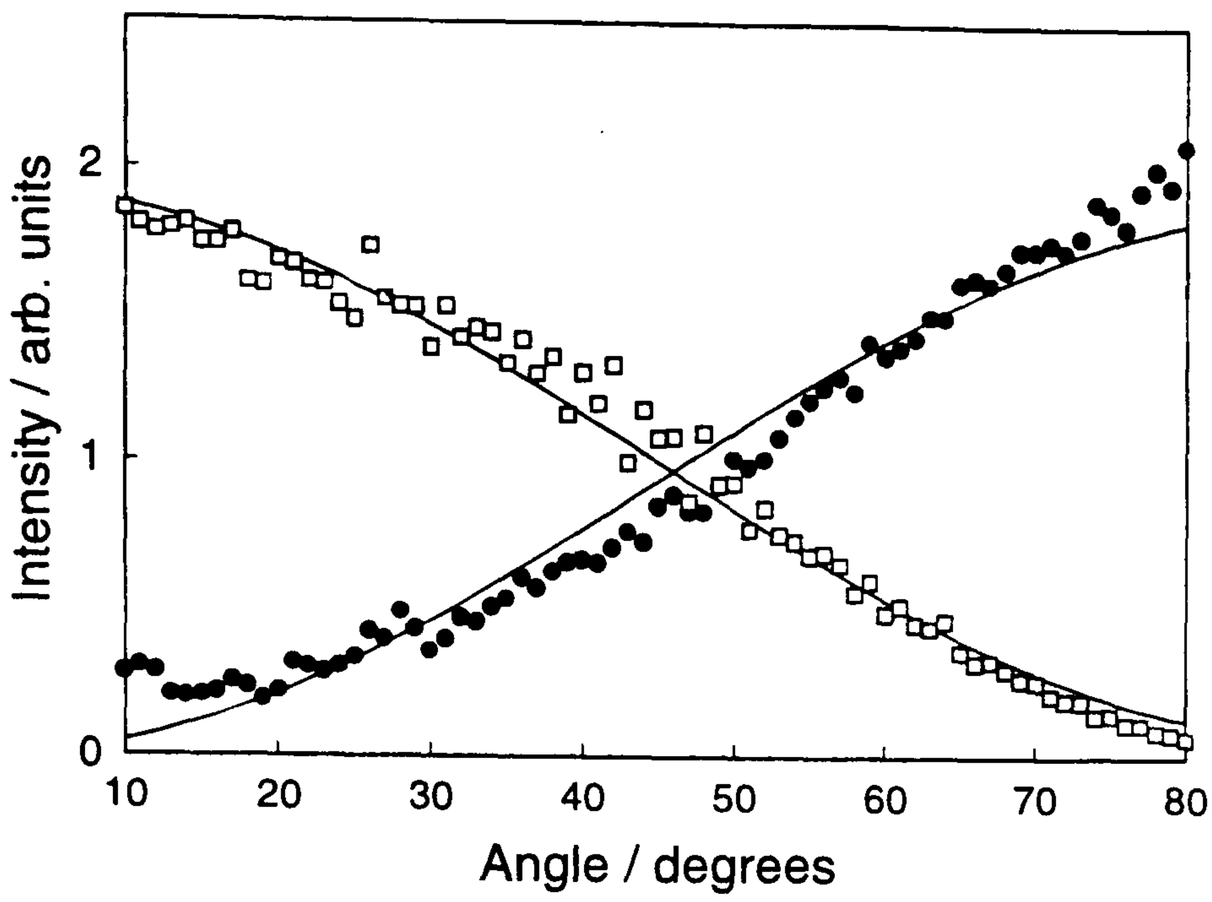

Figure 5.10: Fits to the observed angular intensity of the 2D slices of the images for the Br + Br and Br + Br* channels at 480 nm, β(Br + Br) = -1.0 ± 0.1 (●), and β(Br + Br*) = 1.1 ± 0.1 (□).

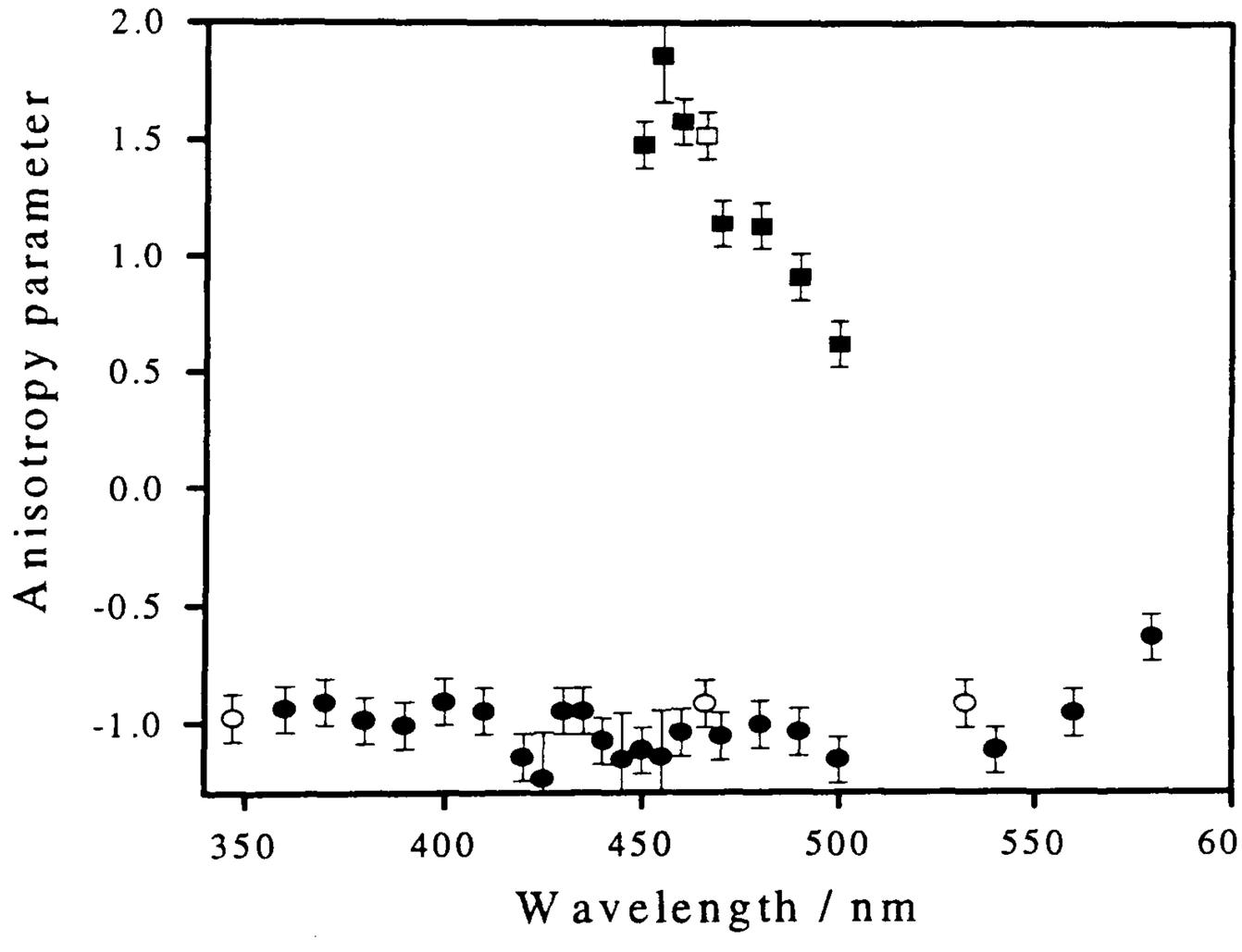

Figure 5.11: Plot of the fitted β values for the various photolysis wavelengths investigated. Indicated are the β values for Br + Br (●) and Br + Br* (■) formation along with the previously reported values[10] (❍,□).

Wavelength (nm)	β (Br + Br) (± 0.1)	β (Br + Br*) (± 0.1)
260.662		-1.03
346.88	-0.98[a]	
360	-0.94	
370	-0.91	
380	-0.99	
390	-1.01	
400	-0.91	
410	-0.95	
420	-1.15	
425	-0.95	
430	-0.95	
435	-0.95	
440	-1.08	
445	-1.16	
450	-1.12	1.48
455	-1.15	1.86
460	-1.04	1.58
466.07	-0.92[a]	1.52[a]
470	-1.06	1.14
480	-1.01	1.13
490	-1.04	0.91
500	-1.16	0.62
532.33	-0.92[a]	
540	-1.12	
560	-0.96	
580	-0.64	

a: Ref. 10

Table 5.1: The variation of β with photolysis wavelength for the two active channels in the UV/visible photodissociation of Br_2.

5.4 Discussion

Table 5.1 shows that at some photolysis wavelengths, non-limiting β values (i.e. not -1 or 2) result from analysis of the recorded photofragment images. Therefore prior to discussion of the derived β's for the various photofragment images and branching ratio data gained from this study, different effects occurring during the ion imaging experiment that result in non-limiting β values should be considered in more detail.

As previously mentioned in chapter 1 section 1.5.2, non-limiting β values can lead to extra information on the photodissociation process. Effects that can cause intermediate β's include: (i) breakdown of the axial recoil approximation due to slow recoil velocities, which will be important in the case of rotationally excited molecules dissociating at energies close above the dissociation threshold; (ii) dissociations that occur on a time scale that is long compared to the rotational period (*i.e.* predissociations) - classically this has the effect of reducing the limiting values of β by up to a factor of four;[27,28] and (iii) spectral overlap of transitions to two (or more) excited states with different Ω both (or all) of which correlate to the same asymptotic products. Mixing between different excited states is also possible, which can complicate the photodissociation dynamics further.

5.4.1 Slow Recoil Model

The slow recoil model describes the β values expected from a photodissociation when the photofragments are moving apart relatively slowly. This occurs when the energy of the photolysis photon is just above the threshold for forming an active product channel. In this situation almost all of the excitation energy is taken in breaking the molecular bond, which leaves little energy to appear as velocities of the photofragments. When the fragments are within this low kinetic energy regime, it is possible for the angular speed of the parent molecule to be similar to the axial recoil velocity of the photofragments. This results in significant displacement of the recoiling fragments from the molecular bond axis and therefore

leads to a reduced β value. Figure 5.12 illustrates this low kinetic energy regime with a velocity diagram.

A classical expression for the reduction in the β parameter as the axial recoil approximation breaks down as derived by Oldman *et al*[10] is shown below:

$$\beta_{obs} = \beta_{\lim} P_2(\cos\alpha) \qquad (5.11)$$

where, $\alpha = \sin^{-1}(v_{\tan} / v_{rec})$ (5.12)

and, $v_{\tan} = \sqrt{\pi kTm_2 / 2m_1(m_1 + m_2)}$. (5.13)

where β_{obs} is the experimentally observed β value, β_{lim} is the expected limiting value (either -1 or 2), v_{rec} is the recoil velocity of the photofragment, v_{tan} is the tangential velocity imparted on the photofragment from parent molecule rotation, m_1 and m_2 are the masses of the two fragments, k is the Boltzmann constant, and T is the rotational temperature of the parent molecule.

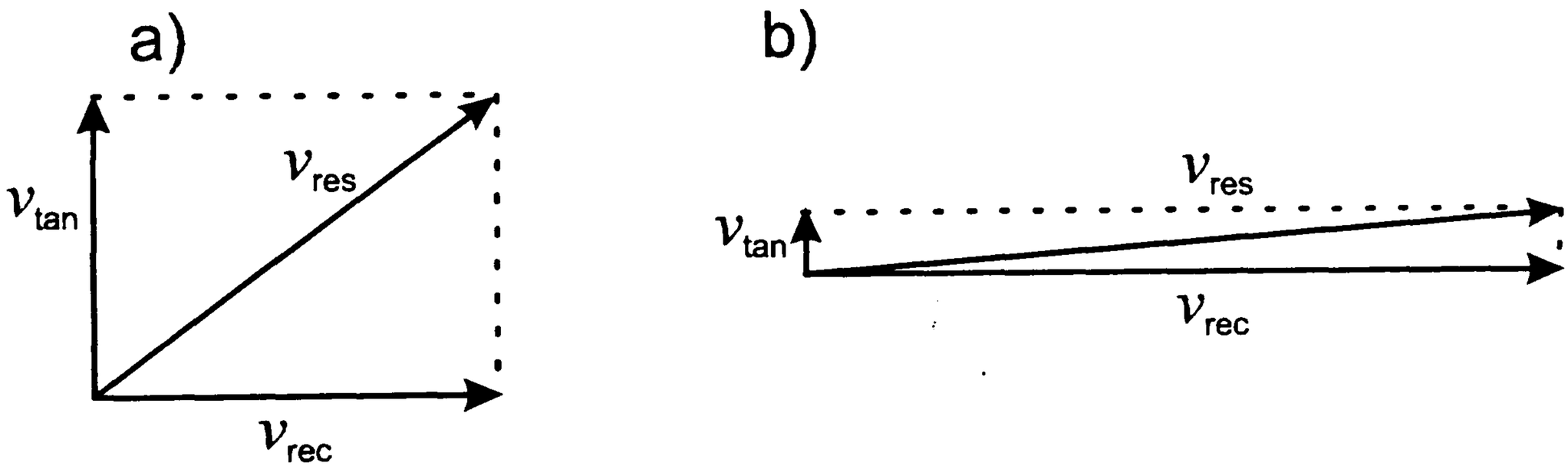

Figure 5.12: Velocity diagram showing the breakdown of the axial recoil approximation at low kinetic energy. a) shows the low kinetic energy regime where the axial recoil and tangential velocities are comparable, whereas b) shows the high kinetic energy regime where the ratio between the two velocities is much greater.

Figure 5.13 shows the reduction in β value expected for a parallel and perpendicular photodissociation respectively for Br_2 at three different parent beam temperatures. The figure shows that the β value is only severely affected at energies just above the formation threshold, and that the change in the β value is highly temperature dependent, with the molecules with the lowest initial internal temperature having the least dramatic effect on the observed β value. Because of this temperature dependence near threshold all ion imaging studies are performed in a molecular beam so as to rotationally cool the parent molecule and reduce this effect.

5.4.2. Predissociation Effects

Non-limiting values of β can also be attributed to predissociation. If a state is accessed in the excitation step that is predissociated then the molecule will not directly dissociate, but will have a finite lifetime in the excited state. Rotation of the molecule during the predissociation event leads to a loss in the angular coherence of the dissociation, which therefore leads to a non-limiting β parameter as the fragments are no longer recoiling away from the molecular bond alignment initially prepared by the excitation. Classical and quantum mechanical expressions for the reduction of β for a predissociating state have been derived.[29] For a long lived predissociation the expected limiting β parameter can be calculated via the following classical expressions:

$$\beta_{//} = 2\frac{\omega^2\tau^2 + 1}{4\omega^2\tau^2 + 1} \tag{5.14}$$

$$\beta_{\perp} = -1\frac{\omega^2\tau^2 + 1}{4\omega^2\tau^2 + 1} \tag{5.15}$$

Where ω is the velocity of the rotating molecule and τ is the lifetime of the excited state. β takes the limiting values of -1 and 2 for a short lifetime state, but approaches $\beta_{\perp} = -¼$ and $\beta_{//} = ½$ as τ increases. This reduction in β from an expected value has been used in previous studies as a 'rotational clock' to estimate predissociative lifetimes of excited states. These above models do not take account of the hyperfine coupling

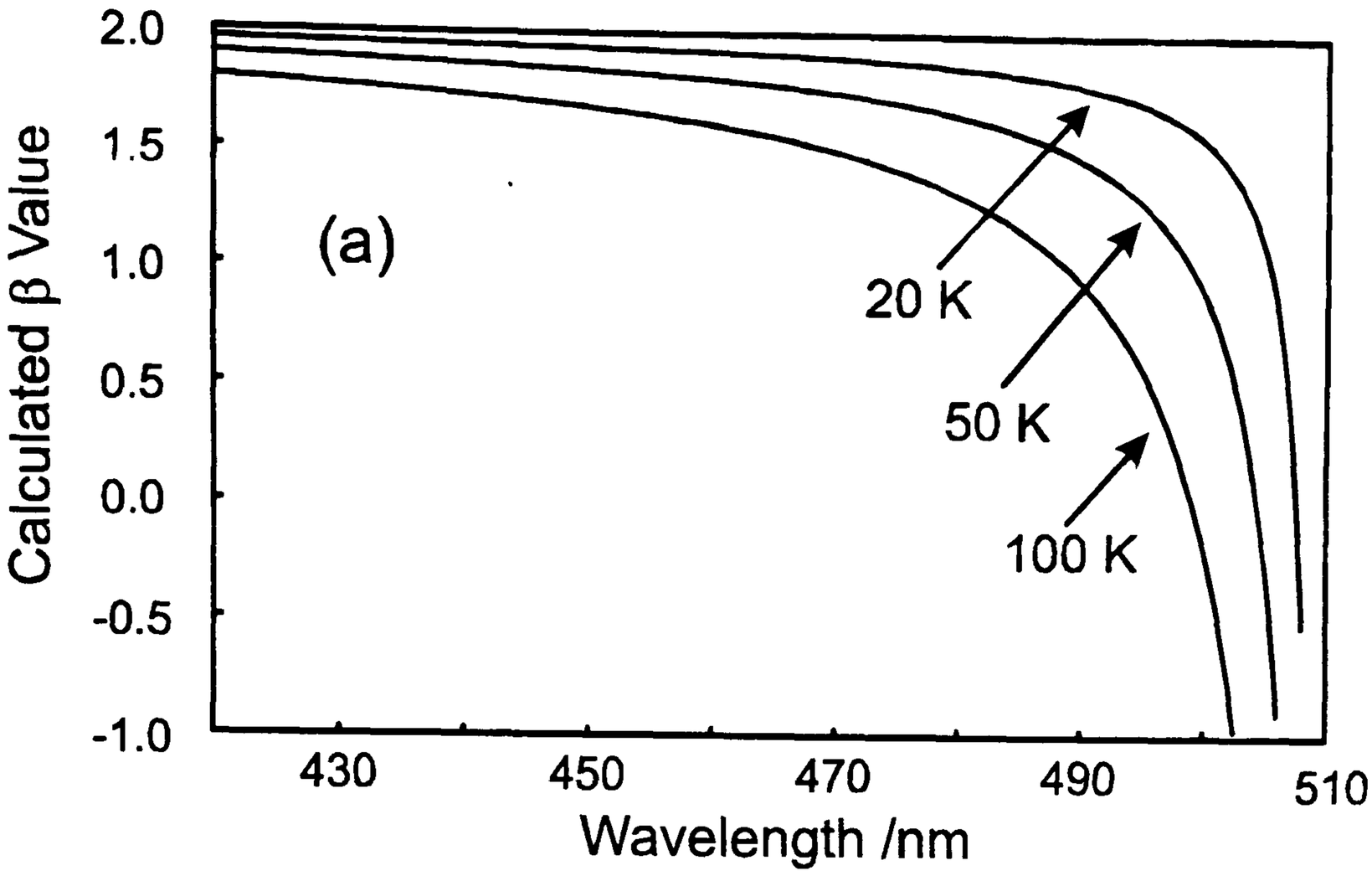

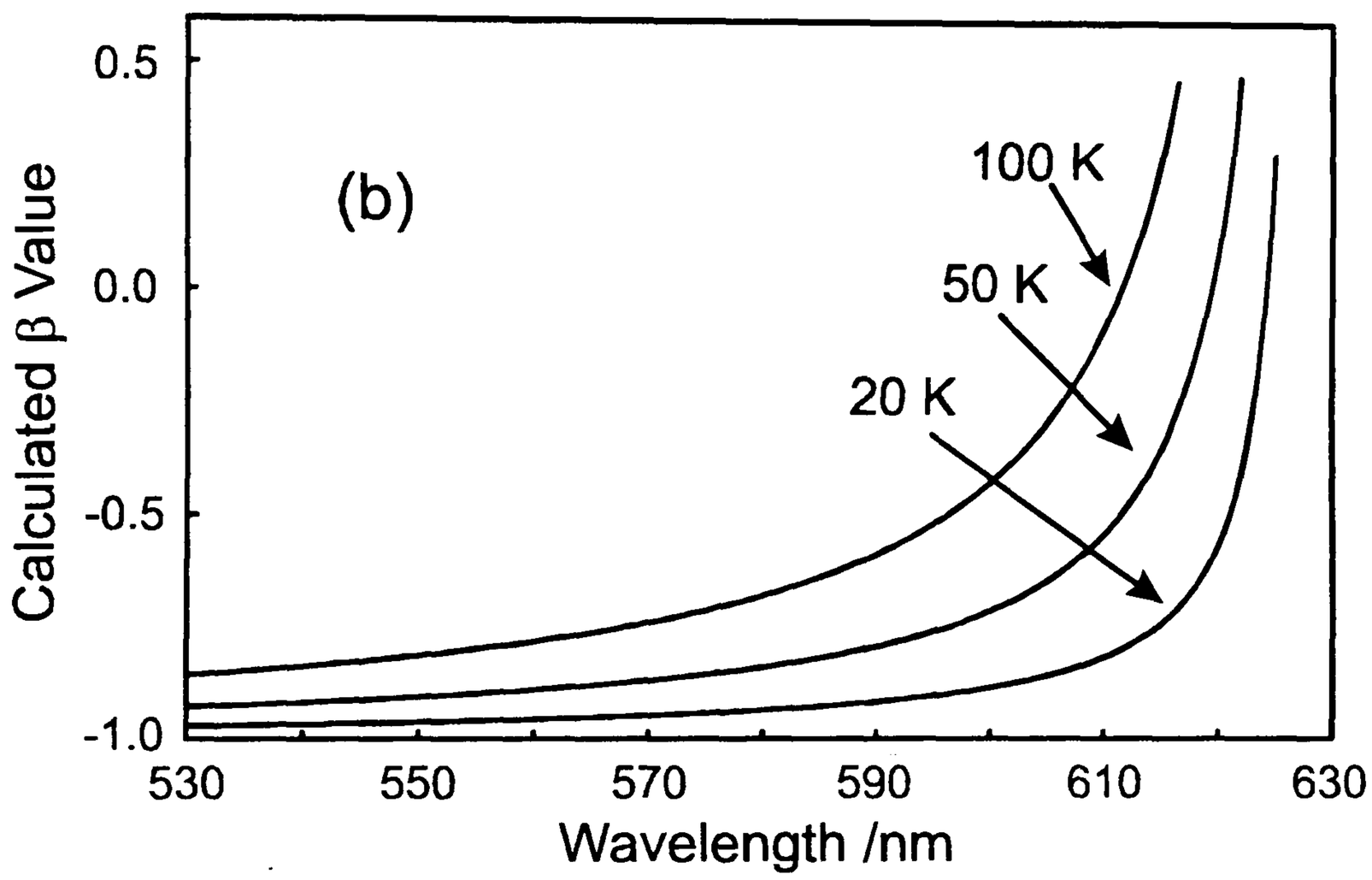

Figure 5.13: Calculated β values, using equation (5.11), for photodissociation of Br_2 just above threshold for forming Br+Br* (510.6 nm), via a parallel transition (a) and for forming Br+Br (629.0 nm), via a perpendicular transition (b).

caused by the non-zero nuclear spins of the atoms produced, which could be significant at low J, and would lead to a further decrease in observed β values. The timescale for such effects is likely to be hundreds of picoseconds or longer, and so would not contribute during the ~10 ns timescale of the photolysis-probe experiment performed here.

5.4.3 Excited State Mixing

Mixed excitation and excited state mixing can have a large and varied effect on the observed β values. The nature of the mixing involved can range from the very simple to the highly complex. Figure 5.14 illustrates one of the simplest examples of mixed excited state effects. If in the excitation step two states of different Ω value are populated, and both correlate to the same atomic products, then neglecting possible interference effects the β value measured for that limit will be a weighted sum of the perpendicular and parallel contributions via the following eqn.:

$$\beta_{obs} = a\,\beta_{\perp} + b\,\beta_{//} \qquad (5.16)$$

$$\text{where: } a + b = 1 \qquad (5.17)$$

with a and b representing the contribution to the dissociation flux from the two states. If a and b are equal, i.e. if the two states contribute equally to the dissociation flux, then $\beta_{obs} = 0.5$. Measurement of β at different excitation wavelengths can provide wavelength dependent information on the relative absorption of the two states.

More complicated mixing schemes can involve 3 or more states, including 'dark states' which are not necessarily accessed in the initial excitation step. Figure 5.15 illustrates an example of excited state mixing where the initial excitation is to two states A and B, which have different Ω values and which dissociate to two different limits. However wavefunction overlap between states A and C is such that photofragment flux can cross into C from A, and dissociate to the same limit as B. In this case the β value measured will be a weighted sum of the two different contributions to the atomic limit from state A (via C) and B. This particular mechanism

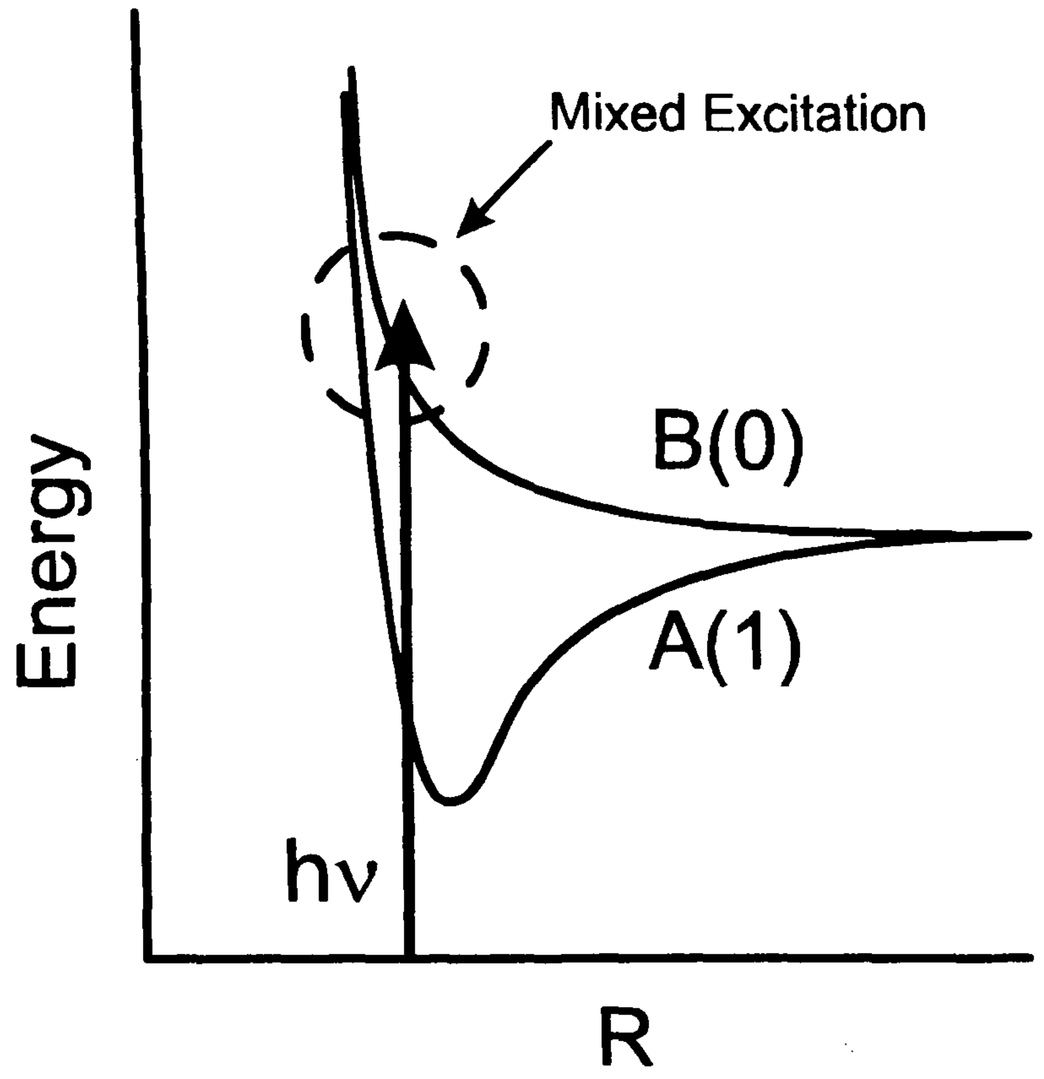

Figure 5.14: Illustration of a mixed excitation, to states A and B, which have different symmetries but both correlate to the same atomic limit, leading to non-limiting β values.

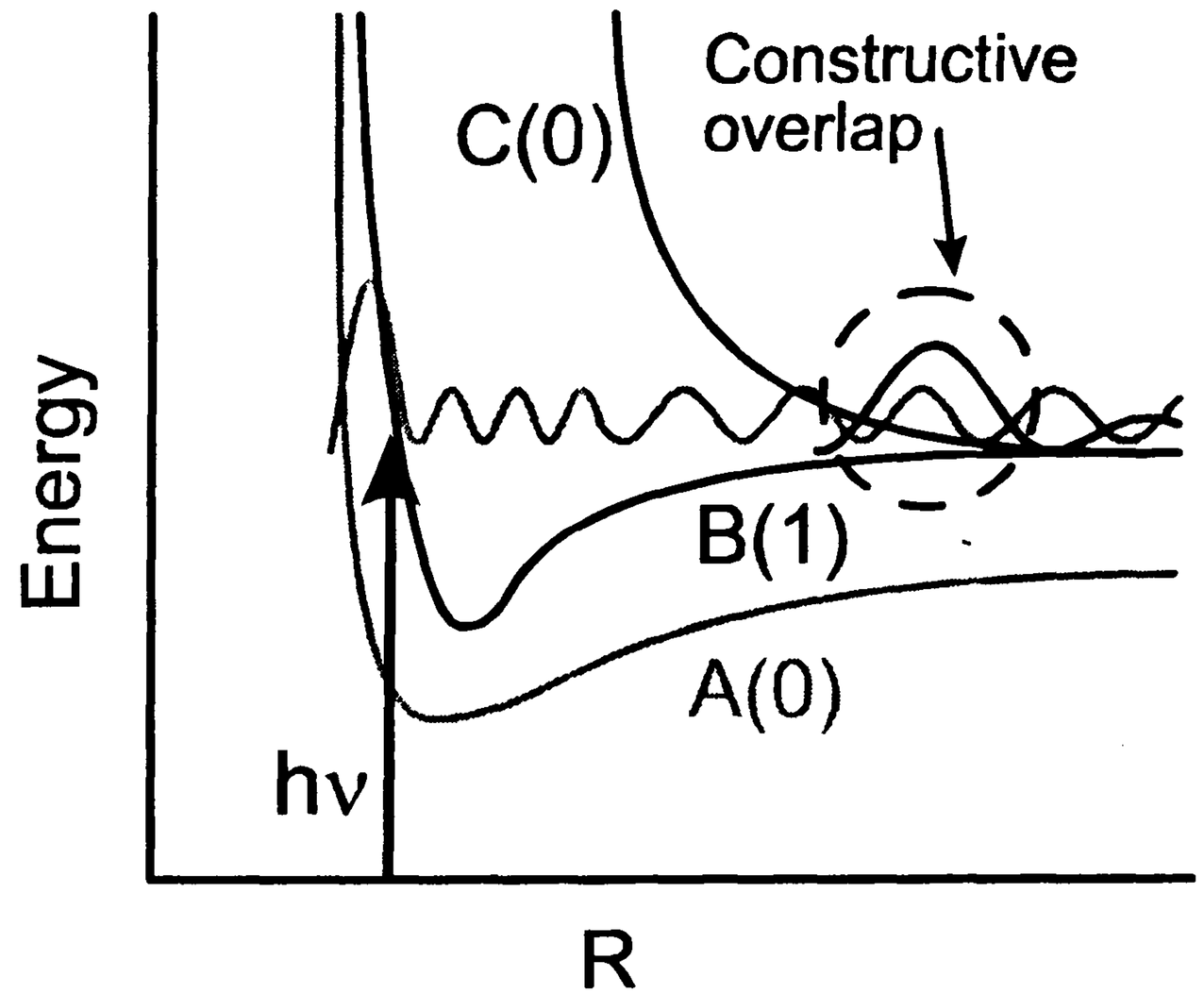

Figure 5.15: Illustration of wavefunction interaction between states A and C, which leads to both parallel and perpendicular flux (from B) dissociating to the same atomic limit.

is only of greatest significance just above the limit for forming a set of atomic products. In this regime it is possible to get a large overlap between the wavefunctions of the two states in question, but as the energy is increased this overlap is likely to become less favourable. There are many other state mixing schemes that can be envisaged via excited state effects such as avoided crossings and inner wall mixing. All of these processes involve the transfer of dissociation flux from one state to another, and all will have an effect on the final observed β value.

Discussion of the Br_2 photofragment branching ratios and recoil anisotropy data is conveniently separated into four different photolysis wavelength regions: $\lambda > 510$ nm, $420 < \lambda < 510$ nm, $\lambda < 420$ nm and at $\lambda = 260.662$ nm, which loosely correspond with the wavelength regions over which different excited states contribute to the total absorption spectrum as shown in figure 5.3.

5.4.4 $\lambda > 510$ nm

From equation (5.2) it can be seen that energetic considerations dictate that two ground state Br atoms are the only possible products from photolysis of Br_2 molecules in their $v''=0$ level at wavelengths $\lambda > 510$ nm. This is consistent with the Br atom image taken at $\lambda = 560$ nm and shown in fig. 5.6, which shows just one ring the radius of which is appropriate for ground state products. The best-fit β value (-0.96±0.1) indicates that these products derive from a perpendicular ($\Delta\Omega$ ±1) photoexcitation process, consistent with fig. 5.3 which suggests excitation to the inner limb of the $A^3\Pi_u(1_u)$ state potential as the most likely route to ground state products at these long wavelengths. However, as Table 5.1 shows, the best-fit β value derived from analysis of the corresponding Br image taken at $\lambda = 580$ nm is less anisotropic.

This non-limiting β could be attributed to predissociation effects as described in section 5.4.2, with transfer of excited state population from one state to another. As figs. 5.3 and 5.4 show, the $B^3\Pi_u(0_u^+) - X^1\Sigma_g(0_g^+)$ transition also contributes to the parent absorption in this wavelength region. The $B^3\Pi_u(0_u^+)$ state correlates diabatically with the products Br + Br*, which are energetically forbidden at these wavelengths,

but it is also known to be predissociated by rotationally induced coupling to the repulsive $^1\Pi_u(1_u)$ state,[4,23] thereby yielding ground state products. This, then, constitutes a route to forming Br + Br products following a parallel ($\Delta\Omega=0$) photo-excitation. However this predissociation will occur on the microsecond timescale, so the Br + Br product arising from this route will be negligible on the 10 ns timescale of the experiments performed here. It is therefore concluded that the most likely reason for the non limiting β value measured for λ = 580 nm is the size of the image. For dissociation at energies just above threshold the image size is so small that after manipulation by the imaging software the two lobes of the image merge, causing the apparent reduction in anisotropy.

5.4.5 420 < λ < 510 nm

Channel (5.2) can now contribute to the dissociation flux at photolysis wavelengths $\lambda < 510$ nm and, indeed, is observed as a second (inner) ring in the Br images recorded at all excitation wavelengths in the range $435 < \lambda < 510$ nm. The recorded images of the Br* products (fig. 5.6) provide further confirmation that this smaller ring corresponds to formation of Br + Br* products. The outer ring, associated with formation of ground state Br + Br products, displays an angular anisotropy that is well described by $\beta = -1$ at all wavelengths in this range implying that, as at longer wavelengths, these products arise as a result of a perpendicular transition to one or more excited states with $\Omega = 1$. Plausibly, excitation at the longer wavelengths is to the $A^3\Pi_u(1_u)$ state but, as the photolysis wavelength is reduced, absorption to the repulsive $^1\Pi_u(1_u)$ state becomes predominant.

As in the long wavelength photolysis image of the Br photofragment discussed previously (λ=580 nm), the Br + Br* photofragment channel also exhibits a non-limiting β throughout this wavelength range. Of particular interest is the observation that the best-fit β parameter is ~ 1.5 at the shorter wavelengths but falls to ~ 0.6 at 500 nm. The $B^3\Pi_u(0_u^+) - X^1\Sigma_g(0_g^+)$ transition, the upper state of which correlates to Br + Br* atomic products, makes a major contribution to the overall absorption in this wavelength region. However, direct absorption and fragmentation via the B state (*i.e.*

a parallel, $\Delta\Omega = 0$, excitation) should lead to Br + Br* products with a product flux recoil velocity distribution characterised by $\beta = 2$. The possible causes for the observation of non-limiting β values in diatomic photodissociation have been summarised previously in section 5.4.2. Each effect is now considered as a possible candidate for the range of β values calculated for this wavelength range (in this case, due to the size of the images involved, β reduction as a result of the small image size is neglected).

Breakdown of the axial recoil approximation cannot account for such marked deviations from the expected $\beta = 2$ value expected in the case of prompt dissociation via a transition with an overall $\Delta\Omega = 0$. Figure 5.13 shows the expected β values for such an effect calculated from equation (5.11), and it is clear that the values predicted do not correspond to those observed.

Predissociation, to the Br + Br* limit, of a bound $\Omega = 0$ state that correlates diabatically to the Br* + Br* limit could lead to reduced, but positive, β parameters. If such a state was to be optically active, however, production of Br* + Br* products at photolysis wavelengths $\lambda < 429.8$ nm (recall eqn. (5.3)) should be expected. This product channel is not observed at any wavelength investigated in the present work. Further, such a predissociated excited state might reasonably be expected to contribute discernible vibronic structure to the parent absorption or dispersed emission spectra; none has been reported.

It is proposed that mixing occurs between two or more excited states, with different values of Ω, which results in dissociation flux arriving at the Br + Br* limit with a reduced β value, as the most likely explanation for the observed β values at the various photolysis wavelengths. The observed $\beta_{(Br + Br^*)}$ values can be accommodated by assuming that most of these products are formed from direct dissociation of Br_2 molecules prepared in the $B^3\Pi_u(0_u^+)$ state, but that an excitation wavelength dependent fraction of the Br + Br* products arise via an alternative, perpendicular, excitation route. Direct simultaneous excitation to the $B^3\Pi_u(0_u^+)$ state and either (or both) of the $A^3\Pi_u(1_u)$ and $^1\Pi_u(1_u)$ states with subsequent transfer of flux between these states (as

has recently been proposed in the case of the heteronuclear species BrCl,[17] see chapter 6) is discounted because, in such a case, the anisotropy parameters for both product channels (1) and (2) should be reduced from their limiting values. Such is clearly not the case for the Br + Br product channel. Direct absorption to the third excited state of 1_u symmetry, that will correlate to the Br + Br* limit[7] is also discounted because this state must lie above the $^1\Pi_u(1_u)$ state and is thus unlikely to be accessible, energetically, at the excitation wavelengths of interest. This mechanism is also dismissed as Franck-Condon factors to such a state would increase with greater photolysis energy, whereas the current study shows a reduction in perpendicular character in the dissociation products as the photolysis wavelength is shortened. Therefore a mixing scheme is required which allows transfer of flux from a 1_u state into the Br + Br* limit, whilst not permitting the reverse transfer of population from the $B^3\Pi_u(0_u^+)$ state into the Br + Br limit. Fig. 5.16 illustrates one possible mechanism by which these criteria might be satisfied, most efficiently at energies just above the Br + Br* asymptote where the experimentally measured $\beta_{(Br + Br^*)}$ shows the greatest deviation from the +2 value expected for a pure parallel production mechanism. The necessary perpendicular contribution arises by assuming constructive interference at extended Br–Br bond lengths between the translational wavefunction associated with the initially populated $A^3\Pi_u(1_u)$ state (or, possibly, the $^1\Pi_u(1_u)$ state) - both of which correlate diabatically with the ground state asymptote - and that of the repulsive 1_u state that correlates to the Br + Br* limit.

Fig. 5.3 suggests a decrease in A←X transition moment with increasing excitation energy (decreasing photolysis wavelength). The efficiency of the translational wavefunction overlap efficiency will also decrease with increasing energy as the curvature of both functions increases. Both factors are consistent with the observed increase in $\beta_{(Br + Br^*)}$ as the excitation wavelength is decreased. Adopting such a model, and assuming only incoherent $\Delta\Omega = 0$ (B←X) and $\Delta\Omega = \pm 1$ (1_u←X) excitations, encourages deconvolution of the measured $\beta_{(Br + Br^*)}$ values into weighted sums of contributions arising from parallel ($\beta = +2$) and perpendicular ($\beta = -1$) transitions using equation (5.17). Therefore the measured value of $\beta_{(Br + Br^*)}$ at $\lambda = 460$ (1.58) would imply $a = 0.86$ and $b = 0.14$, *i.e.* 86% of the Br + Br* product yield

arises from direct dissociation via the $B^3\Pi_u(0_u^+)$ state whilst the other 14% is produced from crossing into the 1_u repulsive curve following initial excitation of the $A^3\Pi_u(1_u)$ or, possibly, the $^1\Pi_u(1_u)$ state. Table 5.2 lists the contributions to the Br + Br* channel by perpendicular and parallel dissociating flux at the various wavelengths investigated.

5.4.6 $\lambda < 420$ nm

Br_2 photolysis in the wavelength range 360 - 420 nm yields images showing just a single ring, the radius of which is indicative of forming ground state products. The best-fit recoil anisotropy parameter $\beta = -1$ throughout, consistent with previous suggestions [10] that these products arise as a result of direct dissociation of the initially populated $^1\Pi_u(1)$ state. No Br* signal is observed in this wavelength range, ruling out any contribution from dissociation channels (5.2) or (5.3). The absence of any detectable Br + Br* product yield at these wavelengths encourages the assumption (above) that the presumed perpendicular contribution to dissociation channel (5.2) at longer excitation wavelengths is due to exit channel mixing with the $A^3\Pi_u(1_u)$ state rather than the $^1\Pi_u(1_u)$ state.

5.4.7 $\lambda = 260.662$ nm

Br_2 absorbs only weakly at this wavelength, and the literature contains little mention of the excited states active in this region of the absorption spectrum. The measured anisotropy of the Br recorded image ($\beta = -1.03 \pm 0.1$) indicates that the bulk of the absorption at this wavelength is to a state with $\Omega = 1$ and the image radius indicates that this 1_u excited state decays via dissociation channel (2) leading to the products Br + Br*. These conclusions agree with a recent one-colour ion imaging study[24] of Br_2 with photolysis wavelengths around 265 nm, for which Br + Br* was the only observed channel, characterised by an anisotropy parameter of $\beta = -0.8 \pm 0.1$ (the non-limiting value was attributed to space-charge effects and cluster formation in the molecular beam). This study concluded that the photodissociation was proceeding via a $^3\Sigma_u^+(1_u)$ state although, as mentioned above, the little absorption in this wavelength region has not been assigned specifically to any excited states.

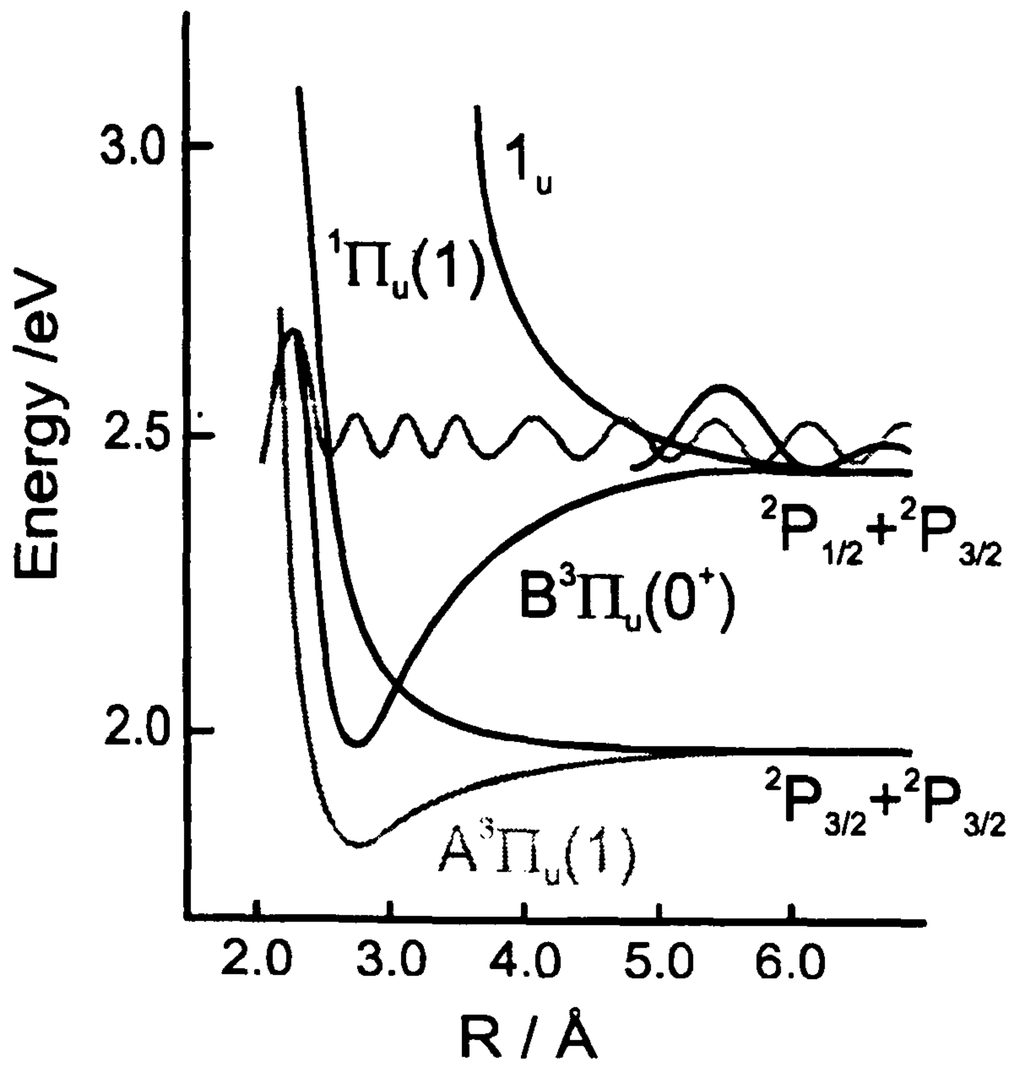

Figure 5.16: A potential energy diagram for the low lying states of Br_2 highlighting the schematic molecular wavefunction overlap between the $A^3\Pi_u(1)$ state with a third 1_u state correlating to the Br + Br* limit. The overlap with the 1_u wavefunction is greatest at energies close to the Br + Br* threshold.

Wavelength /nm	Observed β (Br + Br*)	% Dissociation via $B^3\Pi_u(0_u^+)$	% Dissociation via $A^3\Pi_u(1_u)/^1\Pi_u(1_u)$
450	1.48	82.8	17.2
455	1.86	95.3	4.7
460	1.58	86.1	13.9
470	1.14	71.4	28.6
480	1.12	71.0	29.0
490	0.91	63.5	36.5
500	0.62	54.0	46.0

Table 5.2: Calculated variation in contribution to the total Br + Br* dissociation flux from the $B^3\Pi_u(0_u^+)$ and $A^3\Pi_u(1_u)/^1\Pi_u(1_u)$ states using equations (5.17) and (5.18).

5.5 Conclusions

The technique of photofragment ion imaging has been used to study the photodissociation of bromine at 260.662 nm and at 22 other wavelengths in the range 360 - 580 nm. The resultant angular information derived from the photofragment images assigns the Ω angular momentum symmetry of the various molecular electronic states accessed over the wavelength region investigated. Velocity measurements of the different photofragments have revealed the atomic limits to which the dissociation channels correlate. Interpretation of the data is in general accordance with the previous assignments[19,22] of the Br_2 absorption spectrum, with the $A^3\Pi_u(1_u)$, and the $^1\Pi_u(1_u)$ states dissociating to 2 Br atoms, while the $B^3\Pi_u(0_u^+)$ state produces Br* + Br. It is also suggested that the $A^3\Pi_u(1_u)$ and the $^1\Pi_u(1_u)$ states are mixed with a repulsive 1_u state correlating to Br + Br*. Interpretation of the intensity ratio of the different channels in the images has also allowed branching ratios to be calculated at the various wavelengths. These measurements have served to confirm and extend the previously published results. [10,15]

5.6 References

1 M.A.A. Clyne, M.C. Heaven and E. Martinez, *J. Chem. Soc. Faraday Trans. 2* **76**, 177 (1980).

2 G. Capelle, K. Sakurai and H.P. Broida, *J. Chem. Phys.* **54**, 1728 (1971).

3 K.B. McAfee Jr. and R.S. Hozack, *J. Chem. Phys.* **64**, 2491 (1976).

4 M.A.A. Clyne and M.C. Heaven, *J. Chem. Soc. Faraday Trans. 2* **74**, 1992 (1978).

5 H. Okabe, *Photochemistry of Small Molecules,* (Wiley, New York, 1978).

6 S.R. Leone, in *Dynamics of the Excited State*, edited by K. P. Lawley (Wiley, New York, (1982), p.255.

7 M.C. Heaven, *Chem. Soc. Rev.* **15**, 405 (1986).

8 H. Kato and M. Baba, *Chem. Rev.* **95**, 2311 (1995).

9 J.H. Ling and K.R. Wilson, *J. Chem. Phys.* **65**, 881 (1976).

10 R.J. Oldman, R.K. Sander, and K.R. Wilson, *J. Chem. Phys.* **63**, 4252 (1975).

11 M.S. De Vries, N.J.A. van Veen, and A.E. De Vries, *Chem. Phys. Lett.* **56**, 15 (1978).

12 M.S. De Vries, N.J.A. van Veen, M. Hutchinson, and A.E. De Vries, *Chem. Phys.* **51**, 159 (1980).

13 T. G. Lindemann and R. J. Wiesenfeld, *J. Chem. Phys.* **70**, 2882 (1979).

14 A.B. Petersen and I.W.M. Smith, *Chem. Phys.* **30**, 407 (1978).

15 H.K. Haugen, E. Weitz and S.R. Leone, *J. Chem. Phys.* **83**, 3402 (1985).

16 L.J. Rogers, M.N.R. Ashfold, Y. Matsumi, M. Kawasaki, B.J. Whitaker, *Chem. Phys. Lett.* **258**, 159 (1996).

17 M.J. Cooper, P.J. Jackson, L.J. Rogers, B.J. Whitaker, A.J. Orr-Ewing and M.N.R. Ashfold, *(in press).*

18 K.P. Huber and G. Herzberg, *Constants of Diatomic Molecules* (Van Nostrand Reinhold, New York, 1979).

19 J.A. Coxon, *J. Mol. Spectrosc.* **37**, 39 (1971); **37**, 109 (1971); **41**, 548 (1972); **41**, 566 (1972).

20 R.F. Barrow, T.C. Clark, J.A. Coxon and K.K. Yee, *J. Mol. Spectrosc.* **51**, 428 (1974)

21 R.S. Mulliken, *Phys. Rev.* **57**, 500 (1940).

22 A.L.G. Rees, *Proc. Phys. Soc.* **59**, 1008 (1947).

23 M.A.A. Clyne, M.C. Heaven and J. Tellinghuisen, *J. Chem. Phys.* **76**, 4351 (1982)

24 Y.-J. Jee, M.S. Park, Y.S. Kim, Y.-J. Jung and K.-H. Jung, *Chem. Phys. Lett.* **287**, 701 (1998).

25 S. Arepalli, N. Presser, D. Robie and R.J. Gordon, *Chem. Phys. Lett.* **117**, 64 (1985).

26 J.E. Smedly, H.K. Haugen and S.R Leone, *J. Chem. Phys.* **86**, 6801 (1987).

27 R.N. Zare, *Angular Momentum*, (Wiley, New York, 1988).

28 G.E. Busch and K.R. Wilson, *J. Chem. Phys.* **56**, 3638 (1972).

29 C. Jonah, *J. Chem. Phys.* **55**, 1915 (1971).

Chapter 6

Photofragment Ion Imaging of BrCl

6.1 Introduction

This chapter is concerned with the use of photofragment ion imaging to study the photodissociation of BrCl in the near ultra-violet and visible wavelength range from 235 - 540 nm. Photofragment images of the $Br(^2P^o_{3/2})$, $Br(^2P^o_{1/2})$ and $Cl(^2P^o_{3/2})$, $Cl(^2P^o_{1/2})$ photofragments reveal information on the angular distribution of the photofragment velocities (characterised by the anisotropy parameter β), and the active dissociation pathways as the photolysis wavelength is changed. For conciseness the $Br(^2P^o_{3/2})$ and $Cl(^2P^o_{3/2})$ photofragment will from now on be referred to as Br or Cl, and the $Br(^2P^o_{1/2})$ and $Cl(^2P^o_{1/2})$ photofragment as Br* or Cl*.

The study discussed here on BrCl is analogous to that presented in the previous chapter on Br_2. At first glance BrCl may be expected to show similar photodissociation dynamics. Both molecules contain two halogen atoms, so therefore both have a $X^1\Sigma^+$ ground state electronic state, in the case of BrCl, arising from the electronic configuration .....$9\sigma^2\ 5\pi^4\ 6\pi^{*4}$ as illustrated in figure 6.1.

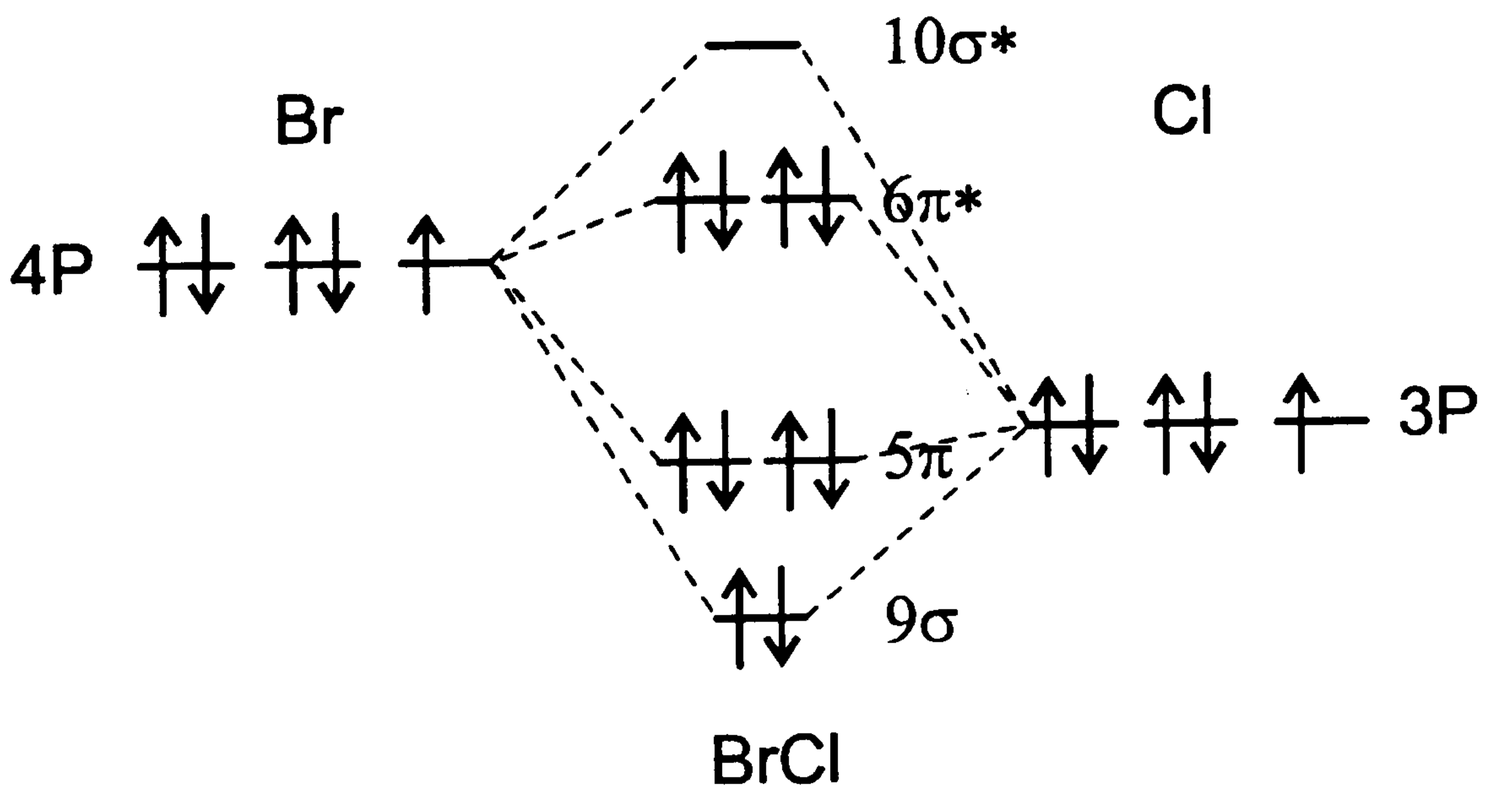

Figure 6.1: Molecular orbital diagram of BrCl showing the highest occupied molecular orbitals.

However, the initial assumption of similarity between the two molecules is lost when the atomic limits associated with the two molecules are considered. In the case of BrCl there are 23 electronic states which correlate to the *four* possible atomic limits

for the ground state (^2P_j) atoms,[1] compared to only *three* atomic limits in the Br_2 case. For BrCl the thermodynamic threshold energies (in energy and wavelength units) for forming the four different combinations of atomic products are as follows:[2]

$$BrCl\ X^1\Sigma^+(0^+) + h\nu \rightarrow \quad Br + Cl \quad E_{th} = 18024\ cm^{-1} \quad \lambda = 554.8\ nm \quad (6.1)$$

$$Br + Cl^* \quad E_{th} = 18905\ cm^{-1} \quad \lambda = 529.0\ nm \quad (6.2)$$

$$Br^* + Cl \quad E_{th} = 21709\ cm^{-1} \quad \lambda = 460.6\ nm \quad (6.3)$$

$$Br^* + Cl^* \quad E_{th} = 22590\ cm^{-1}. \quad \lambda = 442.7\ nm \quad (6.4)$$

The another major difference between the two molecules is the symmetry of the Br_2 molecule (either *g* or *u*) is lost in BrCl. This difference results in a relaxation of the selection rules for transitions between two states, and also allows states which in Br_2 did not mix because of symmetry considerations, to interact. These two considerations result in wholly different photodissociation dynamics for BrCl versus Br_2. The results and discussion of the BrCl study are presented below, and at the end of the chapter the data for the two molecules is compared and contrasted.

Figure 6.2 shows the correlation diagram for BrCl, illustrating the ground state and the 22 excited states which correlate to Cl(^{2}P) and Br(^{2}P) atoms[1,2] (c.f. figure 5.2). However, the UV/visible absorption spectrum of BrCl has typically been deconvoluted into contributions from only three[3] or four[4] different excited states. Figure 6.3 illustrates the proposed contributions[4] to the total absorption cross section made by four different transitions: $D(0^+)$–$X^1\Sigma^+(0^+)$, with peak absorption at $\nu_{max} \sim 43940\ cm^{-1}$ ($\lambda_{max} \sim 228$ nm); $C^1\Pi(1)$–$X^1\Sigma^+(0^+)$, with $\nu_{max} \sim 26850\ cm^{-1}$ ($\lambda_{max} \sim 372$ nm); $B^3\Pi(0^+)$–$X^1\Sigma^+(0^+)$, with $\nu_{max} \sim 22580\ cm^{-1}$ ($\lambda_{max} \sim 442$ nm) and the $A^3\Pi(1)$–$X^1\Sigma^+(0^+)$ transition, with $\nu_{max} \sim 18670\ cm^{-1}$ ($\lambda_{max} \sim 536$ nm).

Schematic potential energy curves for the lower energy states are illustrated in figure 6.4. These curves have been deduced by taking into account data from a number of different studies by different experimental techniques. The B–X system has been studied by Clyne and co-workers in emission[5] and via laser induced fluorescence (LIF).[6–9] These investigations confirmed the parallel (*i.e.* $\Delta\Omega = 0$) character of the B–

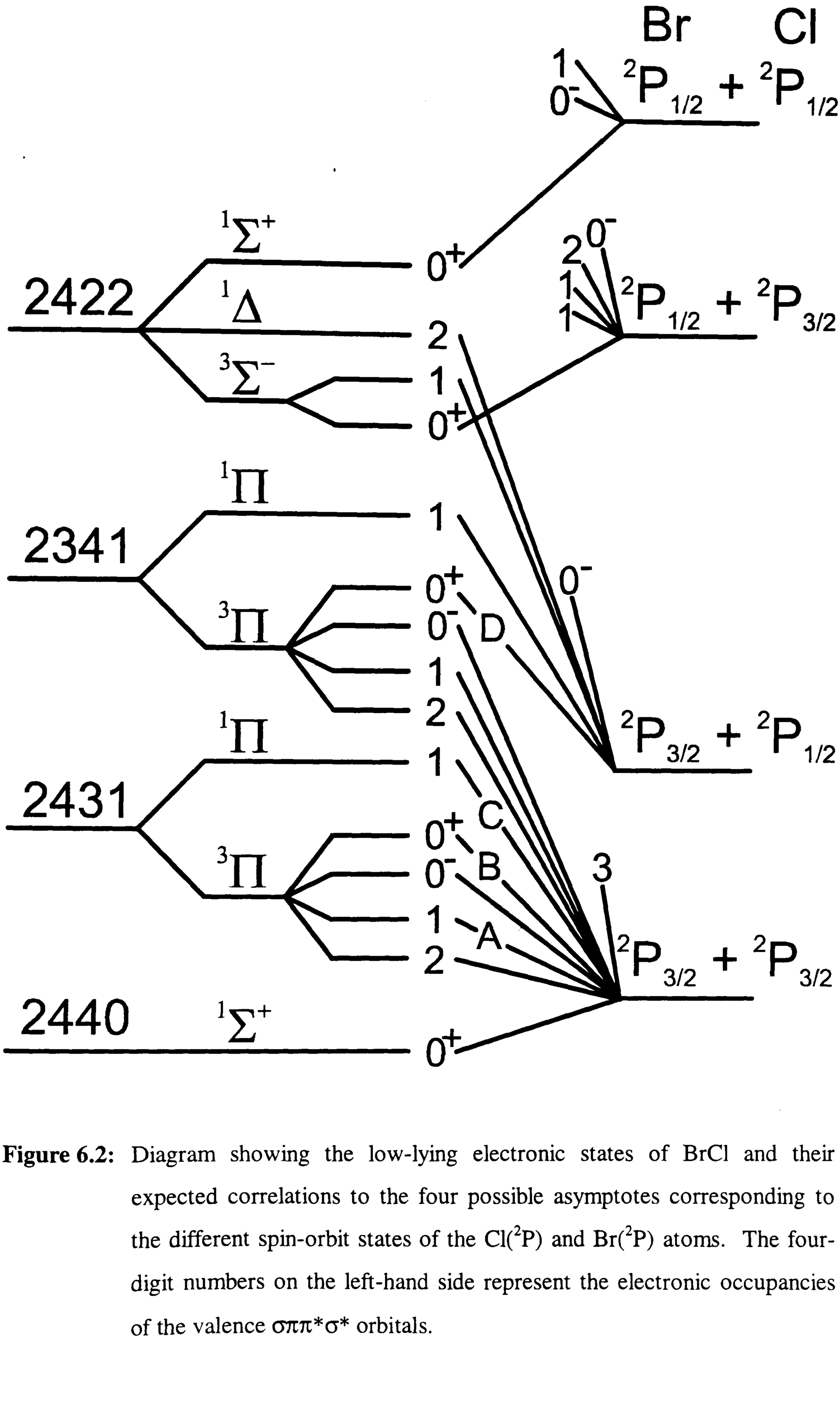

Figure 6.2: Diagram showing the low-lying electronic states of BrCl and their expected correlations to the four possible asymptotes corresponding to the different spin-orbit states of the Cl(^{2}P) and Br(^{2}P) atoms. The four-digit numbers on the left-hand side represent the electronic occupancies of the valence $\sigma\pi\pi^*\sigma^*$ orbitals.

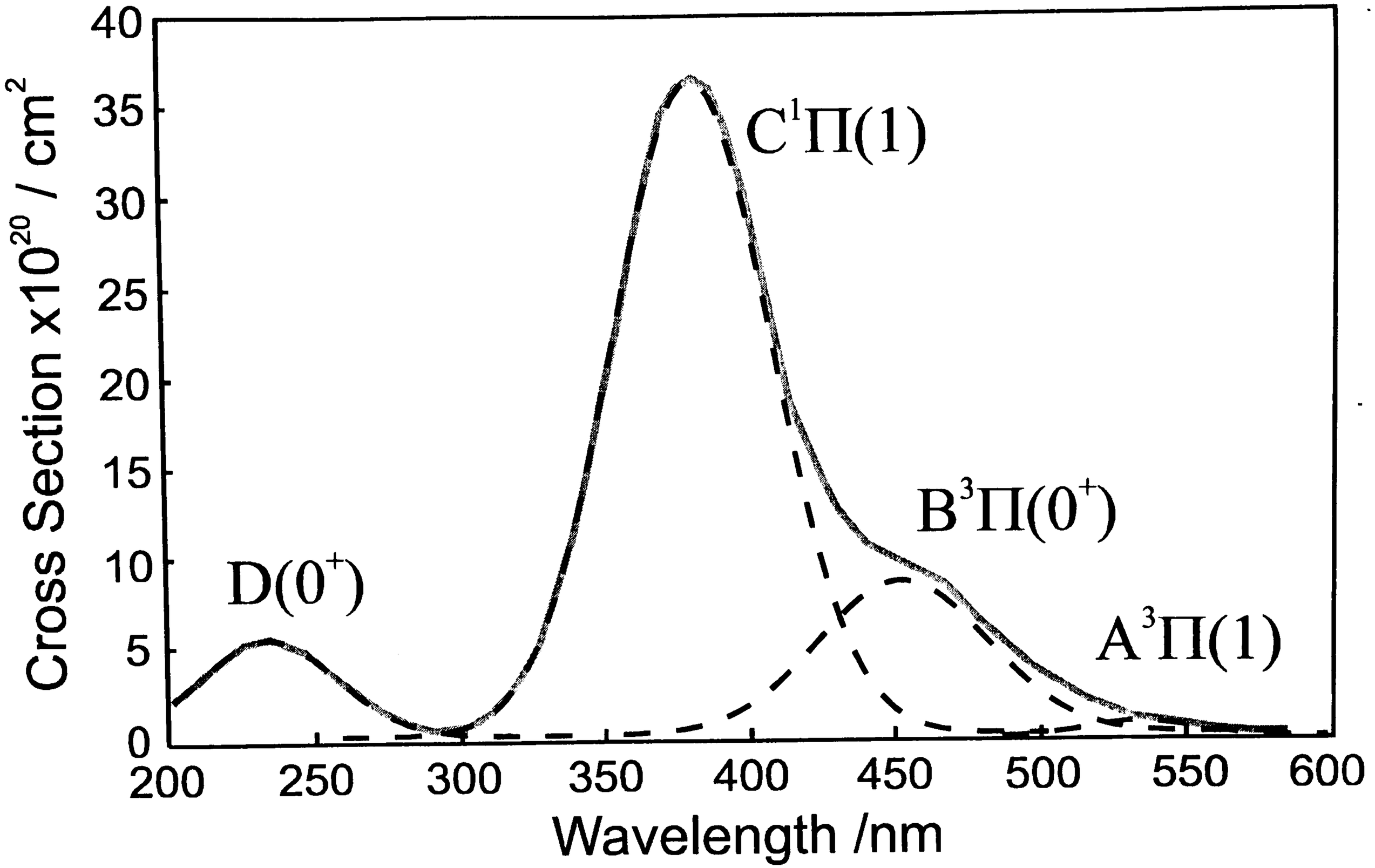

Figure 6.3: The absorption spectrum of BrCl between 200 and 600 nm (solid line), adapted from reference 4. The dashed lines show proposed contributions (also adapted from ref. 4) to the spectrum from excitations from the ground $X^1\Sigma^+(0^+)$ state to the $A^3\Pi(1)$, $B^3\Pi(0^+)$, $C^1\Pi(1)$ and $D(0^+)$ states.

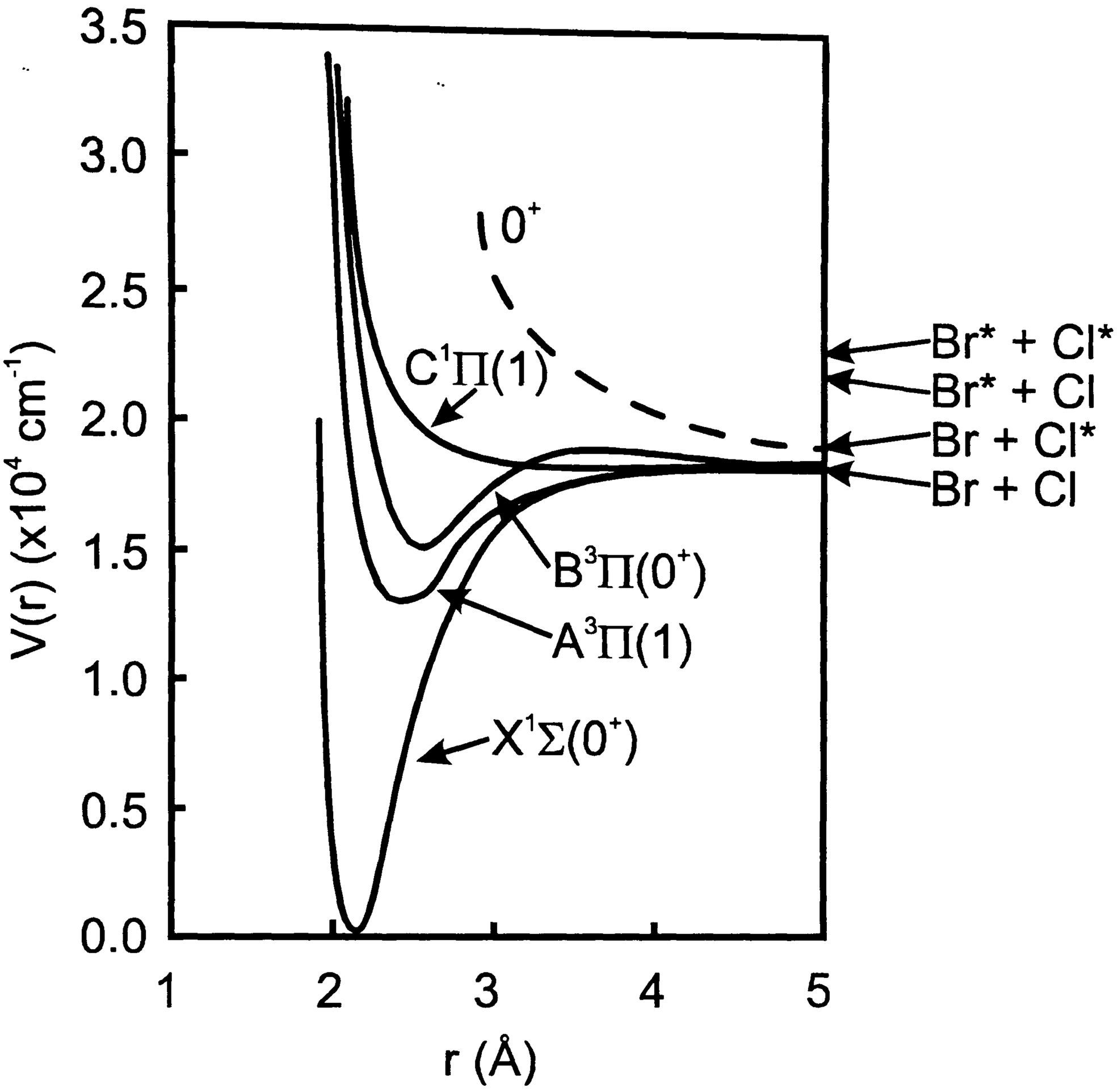

Figure 6.4: Schematic potential energy curves for the low lying electronic states of BrCl pertinent to this work. The figure shows an avoided crossing between the $B^3\Pi(0^+)$ state and a higher lying 0^+ state, giving respective adiabatic correlations to Br + Cl and Br + Cl*.

X transition and identified the onset of predissociation at v'=7 of the B state. From such experiments, Clyne and McDermid[6] estimated a dissociation energy for BrCl dissociating to ground state Br + Cl atoms of $D_0^\circ \leq 18035$ cm^{-1}. The efficiency of this predissociation was observed to be rotational level dependent and to scale with $J(J+1)$, implying that dissociation proceeds via coupling to an Ω = 1 state. Two such non-radiative pathways can be envisaged - coupling to the $A^3\Pi(1)$ state (at the inner turning point of the B state potential energy curve) or an outer limb coupling to the repulsive $1^1\Pi(1)$ potential - both of which correlate to the ground state asymptote. The relative importance of these two possible routes is unclear, though the observed energetic onset of the predissociation does suggest that, for the latter mechanism to be operative, the bound-free crossing would have to occur at, or very close to, the energetic threshold for dissociation. It is therefore clear that the diabatic B state potential must correlate to a higher dissociation limit, probably to Br + Cl* (channel 6.2).[5] Such is consistent with observations of diffuse vibronic structure associated with two higher vibrational levels (v = 8 and 9) of the B state in the wavelength dispersed $E(0^+)$–B emission spectrum.[10] Tellinghuisen and coworkers[10–12] used these data to produce the refined value for D_0°(Br–Cl) = 18024 ± 5 cm^{-1} listed in equation (6.1), and to generate an effective adiabatic potential energy curve for the $B^3\Pi(0^+)$ state which is characterised by a barrier located at 18520 ± 10 cm^{-1} above the ground state minimum (*i.e.* 275 cm^{-1} above the ground state separated atoms asymptote). This barrier is attributable to the effects of an avoided crossing with a repulsive 0^+ state which correlates diabatically with the ground state atomic products.

Absorption studies of BrCl at wavelengths shorter than ~545 nm, i.e. at energies higher than the exit channel barrier on the B state, show no vibronic structure, which suggests rapid dissociation of the parent molecule into atomic products. BrCl has to date not been the subject of many photodissociation investigations.

The Cl/Cl* product branching ratio was investigated at 6 different wavelengths between 389 nm and 500 nm by Qian and co-workers.[13] The branching ratio was deduced to peak at 460 nm, where the ratio Cl*/(Cl+Cl*) ~ 0.6, with the value falling with decreased photolysis wavelength to < 0.2 at 390 nm. The wavelength

dependence of the branching ratio was discussed in terms of possible non-adiabatic transitions between the various excited 0^+ states.

The correlation and interaction between the various low lying electronic states for the interhalogens (XY), where Y is the heavier atom, has been summarised by Child and Bernstein.[14] The suggestion is that states correlating to X + Y* will be hard to observe experimentally as their potential minima will be displaced to longer internuclear separation than the ground state, with the added complication that the states are likely to be predissociated. The potentials for different combinations of XY molecules, typically involve a $B^3\Pi(0^+)$ state which correlates diabatically to X* + Y, but which has an avoided crossing with a second 0^+ state resulting in an adiabatic correlation to X + Y. This picture however is far from concrete, as in studies of IBr, where the molecule is excited above the I + Br* limit, the dissociating flux preferentially remains on the diabatic potential giving rise to Br*. This has led Child to argue that the avoided crossing between the B state and the second 0^+ state is best described using an intermediate coupling regime.[15] The theoretical treatment has proved consistent with experimental results in the case of Br* vs. Br yields from IBr in the photolysis region from 450 - 530 nm.[16,17] Work has also been carried out on other interhalogens using ion imaging, probing shorter wavelengths, such as the photodissociation of ICl at wavelengths from 235 - 248nm.[18,19] Orbital alignment and coherence effects are also now receiving attention, such as in the production of Cl from the photolysis of ICl at 532 nm. Such studies only serve to highlight the complexity of the photodissociation dynamics of interhalogens in the vicinity of the $B^3\Pi(0^+)$ state.[20]

The study described in this chapter entailed the collection and analysis of photofragment images of the various atomic products of BrCl at 26 different wavelengths in the range from 235 - 540 nm. Subsequent analysis of the images of the various photofragments produced provided an insight into active product channels at different photolysis wavelengths as well as information on interactions between the various excited states of the molecule.

6.2 Experimental

The ion imaging experimental design and set-up has been previously described in chapter 2. BrCl was prepared by mixing Br_2 and Cl_2 gases in a 5ℓ glass bulb and leaving the mixture for at least 12 hours to equilibrate. The resultant $BrCl/Cl_2/Br_2$ mixtures were diluted in argon (typically 50 % in 1 atmosphere) prior to use. BrCl was photolysed over the range of wavelengths from 235 - 540 nm, and two different laser systems were employed to span this range. The atomic fragments were probed by 2+1 REMPI using the following electronic transitions:[21,22]

$$Cl\ (3p^5;{}^2P^o_{3/2}) + 2h\nu\ (\lambda = 235.336\ nm) \rightarrow Cl\ (3p^4 4p^1;{}^2D^o_{3/2}), \quad (6.5)$$

or $$Cl^*(3p^5;{}^2P^o_{1/2}) + 2h\nu\ (\lambda = 235.205\ nm) \rightarrow Cl\ (3p^4 4p^1;{}^2P^o_{1/2}), \quad (6.6)$$

each followed by $$Cl\ (3p^4 4p^1) + h\nu \rightarrow Cl^+ + e^-, \quad (6.7)$$

and $$Br\ (4p^5;{}^2P^o_{3/2}) + 2h\nu\ (\lambda = 260.622\ nm) \rightarrow Br\ (4p^4 5p^1;{}^4D^o_{3/2}), \quad (6.8)$$

or $$Br^*(4p^5;{}^2P^o_{1/2}) + 2h\nu\ (\lambda = 262.548\ nm) \rightarrow Br\ (4p^4 5p^1;{}^2S^o_{1/2}), \quad (6.9)$$

each followed by $$Br\ (4p^4 5p^1) + h\nu \rightarrow Br^+ + e^-, \quad (6.10)$$

The mixture of BrCl, Br_2 and Cl_2 in the sample gas inevitably meant that, in regions of strong Cl_2 or Br_2 absorption, images of Cl and Br atoms from BrCl photodissociation will be superimposed on images from, respectively, Cl_2 and Br_2 photolysis. The different bond strengths and cofragment masses of the homonuclear and heteronuclear halogen molecules ensured that at most wavelengths the velocities (and hence the image diameters) of the photofragments from different parent molecules could be separated, and indeed the photodissociations of Cl_2 and Br_2 provided calibrations of the proportionality between the radii of the ion images and photofragment velocities. To minimise contributions from Br_2 photolysis to the ion images obtained by detection of Br atoms, and from Cl_2 photolysis to images of Cl photofragments, gas samples rich in Cl_2 and Br_2, respectively, were prepared. UV/visible spectra of the $BrCl/Br_2/Cl_2$ gas mixtures were subsequently recorded to quantify their composition.

6.3 Results

6.3.1 Absorption Spectra

As described previously, two gas mixtures, one Cl_2 rich and one Br_2 rich were used, so as to reduce the contamination in the images by photodissociation of Br_2 or Cl_2. The various concentrations of the three species in the two mixtures were deduced by running absorption spectra of pure Cl_2, Br_2 and the mixtures. For reference figure 6.5 shows the absolute absorption cross sections for Cl_2, Br_2 and BrCl. The absorption spectrum of the mixtures were deconvoluted into contributions from the three species using the Br_2 and Cl_2 spectra recorded and the previously known BrCl absorption cross sections.[4] Figures 6.6 and 6.7 show the absorption spectra for the Br_2 rich and the Cl_2 rich mixture respectively. Indicated on the figures are the contributions to the overall absorption by the three components, Br_2, Cl_2 and BrCl. For the Cl_2 rich bulb relative concentrations of Cl_2 : Br_2 : BrCl were found to be 2.719 : 0.055 : 1, with the Br_2 rich bulb having the ratios 0.125 : 1.1 : 1.

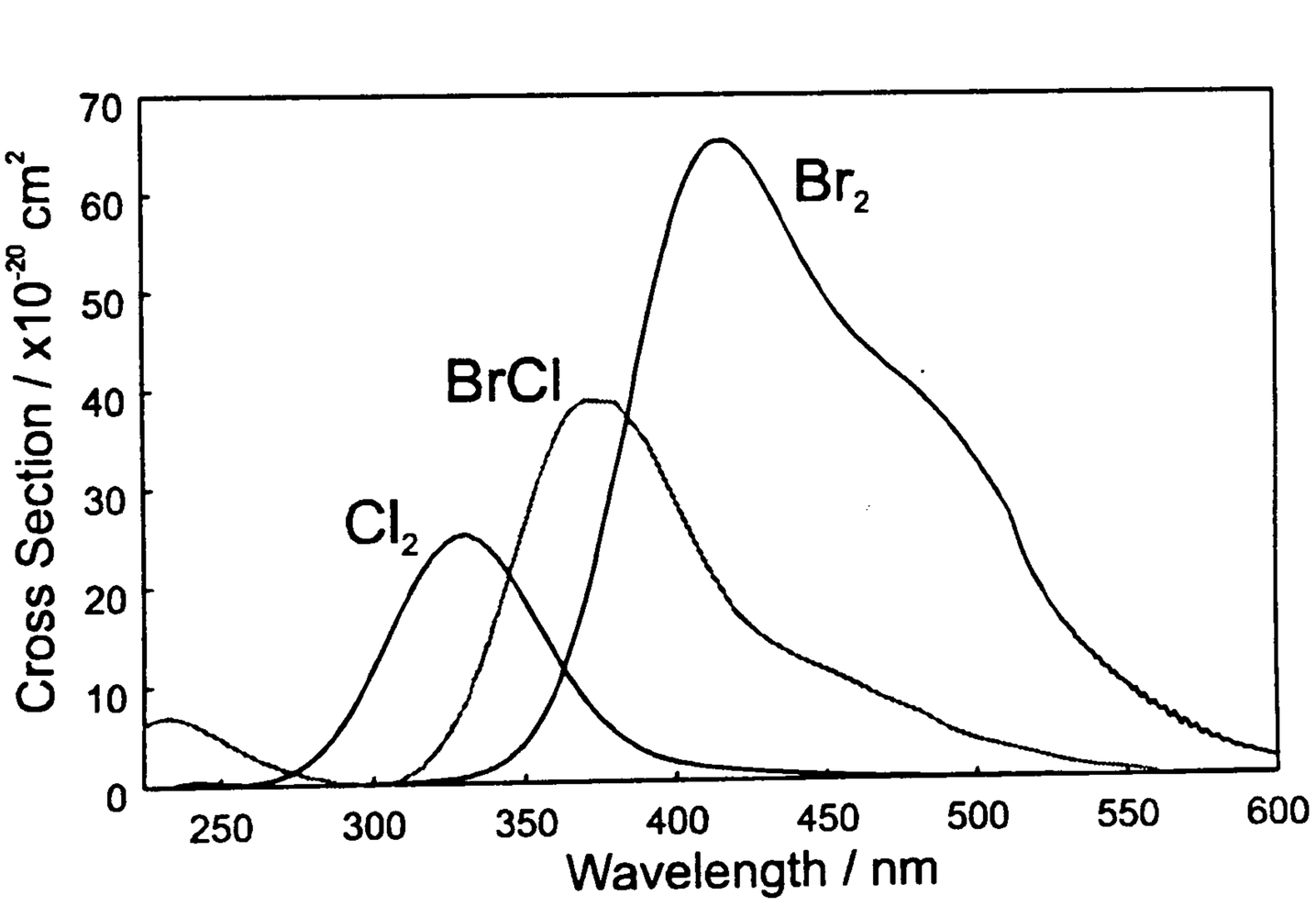

Figure 6.5: Absolute UV/visible absorption cross sections for Br_2, Cl_2 and BrCl.

As for the Br_2 results, the BrCl results have been split up into photolysis wavelength regions within which common photodissociation dynamics occur.

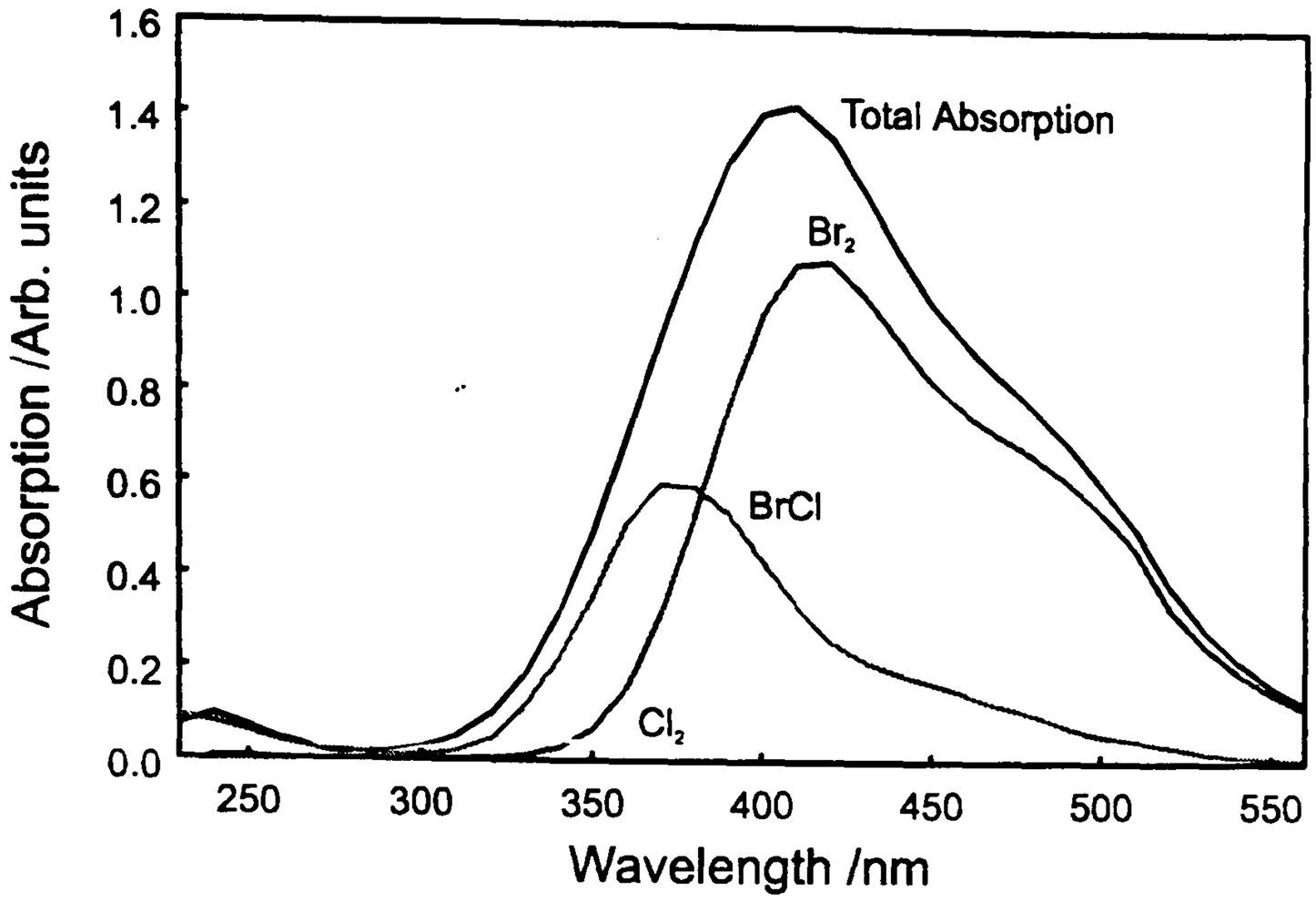

Figure 6.6: Absorption spectrum of the Br_2 rich gas mixture used, indicating the various contributions by the three component species. Deconvolution of the absorption spectrum results in a gas ratio, Cl_2 : BrCl : Br_2, of 0.125 : 1 : 1.1.

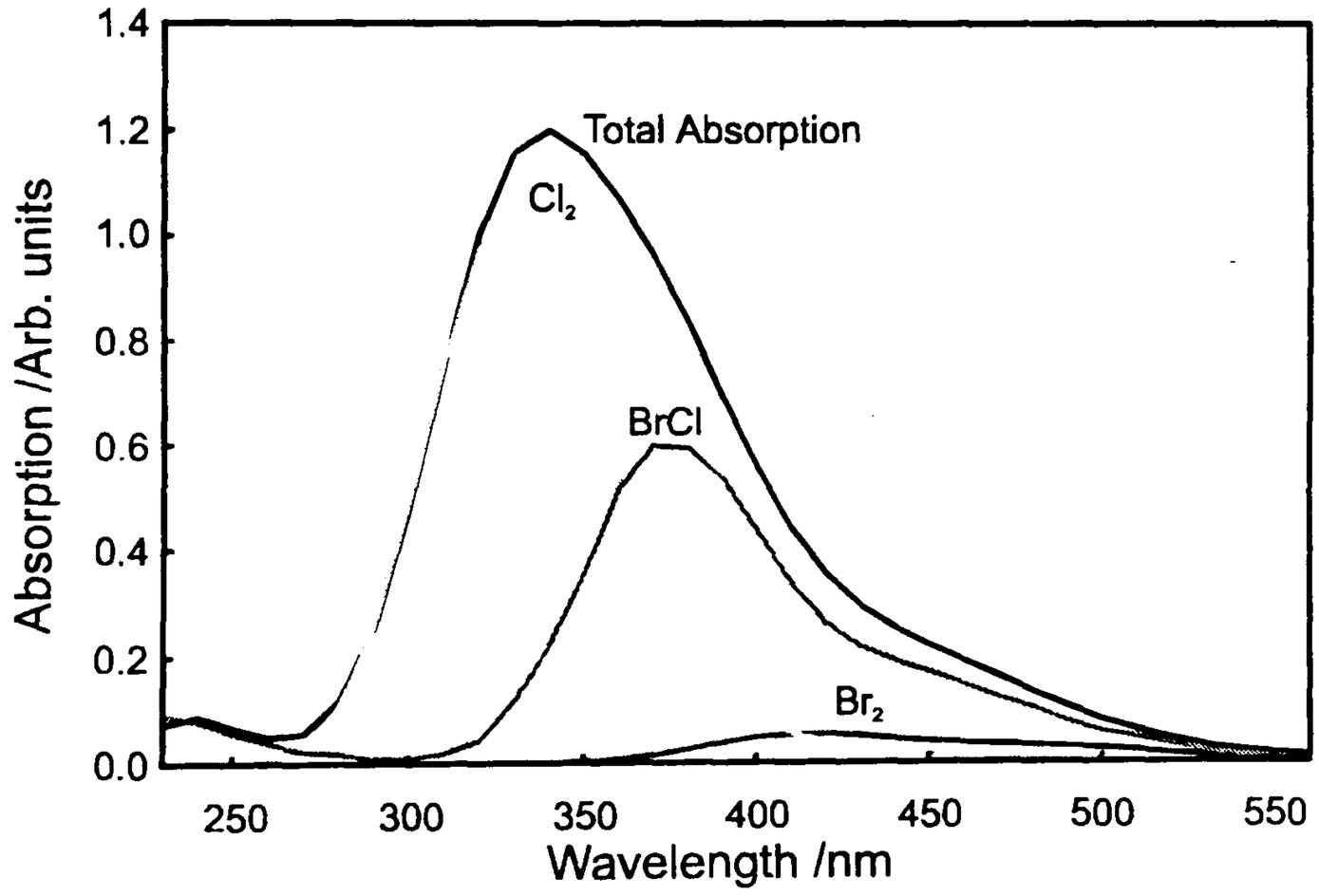

Figure 6.7: Absorption spectrum of the Cl_2 rich gas mixture used, indicating the various contributions by the three component species. Deconvolution of the absorption spectrum results in a gas ratio, Cl_2 : BrCl : Br_2, of 2.719 : 1 : 0.055.

6.3.2 Short-wavelength photodissociation: $\lambda \leq 262.5$ nm

One-colour BrCl photodissociation and photofragment detection experiments were performed at $\lambda = 262.5$ nm with detection of Br* via (6.9), $\lambda = 260.6$ nm with detection of Br atoms via (6.8), $\lambda = 235.3$ nm with detection of Cl via (6.5), and $\lambda = 235.2$ nm with detection of Cl* via (6.6). Figure 6.8 shows raw (2D) ion images and reconstructed slices through the 3D images, obtained from the 2D images by filtered back projection, at wavelengths of 262.5 nm (Br* detection) and 235.3 nm (Cl detection). Images of Cl* at $\lambda = 235.2$ nm were too large to fit completely on the detector, given the necessary ion acceleration voltages to provide good velocity mapping, and hence only partial images were recorded. The Br and Cl* signals were much weaker than the signal observed for Cl and Br* atoms under identical experimental conditions. Analysis of the radius of the single ring arising from detection of Cl from BrCl photolysis shows that the Cl has a mean speed of 2900 m/s with a distribution of speeds about this mean caused by the initial spread of parent internal energies and instrumental blurring. The single 2900 m/s Cl atom speed is consistent with the Cl atoms being formed in conjunction exclusively with Br* atoms. The partial image of Cl* photofragments shows just a single photofragment speed and the larger radius than for Cl images demonstrates that the Cl* is formed with Br cofragments. The images for Br and Br* photofragments also show a single speed group, but the resolution of the instrument is insufficient to determine whether the Br/Br* is formed in coincidence with Cl or Cl* atoms, or both. This lack of resolution is a consequence of the smaller spin-orbit splitting of $Cl(^2P)$ (881 cm^{-1}) compared to $Br(^2P)$ (3685 cm^{-1}). At a photodissociation wavelength of 260 nm the recoil speeds of Br atoms formed via channels (6.1) and (6.2) are calculated respectively as, 1371 and 1341 m/s, and the resolution of the ion-imaging apparatus is estimated to be $\pm$ 100 m/s. The image obtained from detection of Cl at $\lambda = 235.3$ nm demonstrates however, that channel (6.1) forming Cl + Br is not significant at this wavelength, and likewise Cl* detection at $\lambda = 235.2$ nm shows that channel (6.4) does not occur. It is therefore proposed that at the shortest wavelengths ($\lambda \sim 235$ nm) employed, photofragmentation of BrCl proceeds via channels (6.2) and (6.3) with little or no contribution from channels (6.1) and (6.4). The image intensities confirm that the dominant process is channel (6.3). Figure 6.9 shows plots of the angular variation of the Cl (+ Br*) recoil

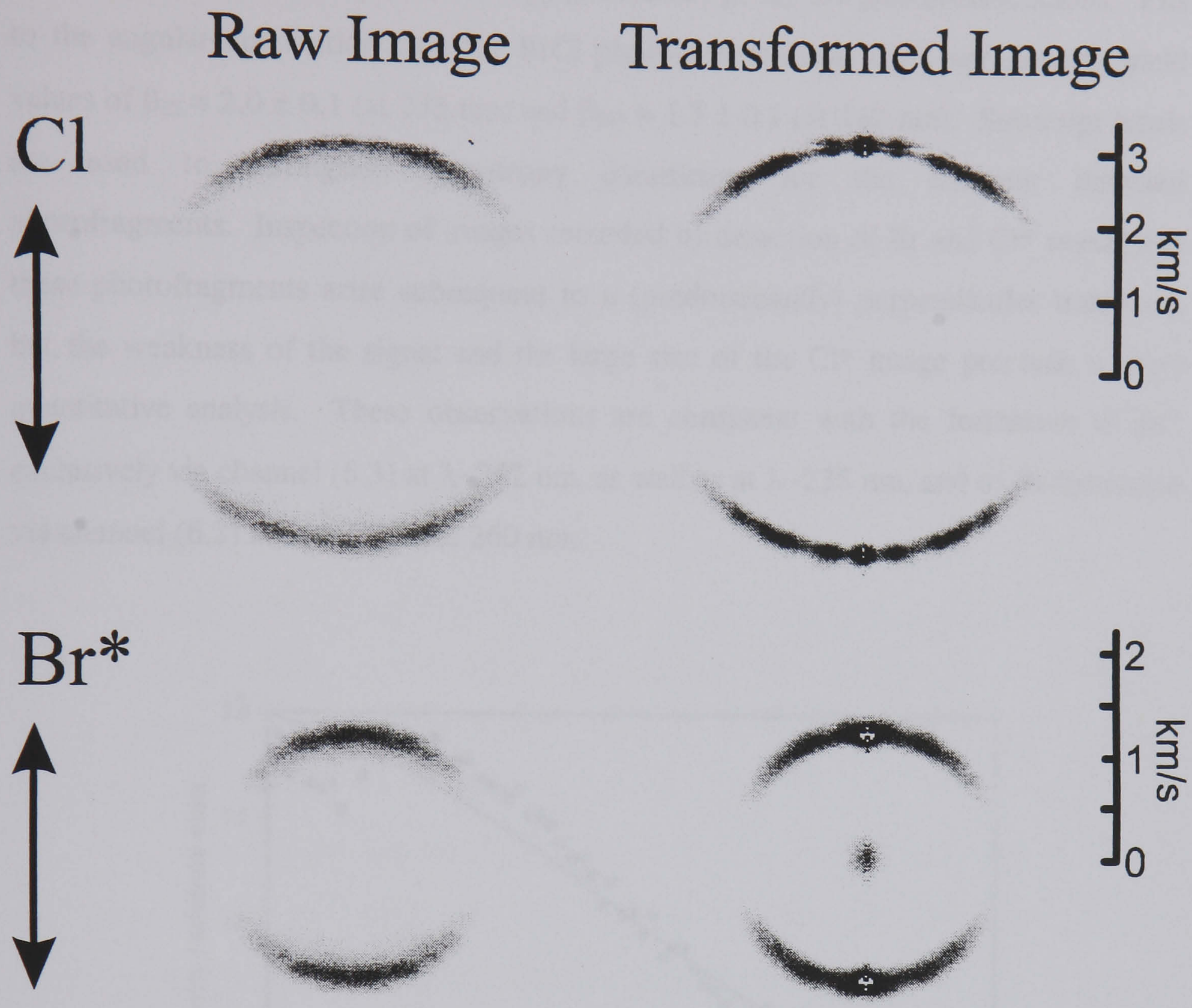

Figure 6.8: Raw, two-dimensional ion images and slices through the reconstructed 3D images of Cl and Br* atoms from the photolysis of BrCl. Top: Cl at 235.3 nm; Bottom: Br* at 262.548 nm. In all images, the linear polarization vector of the photolysis laser is parallel to the vertical arrow. The right-hand scale shows how distance from the centres of the images relates to the photofragment speeds. The angular variation of the intensities of the reconstructed slices are used to obtain photofragment recoil anisotropy parameters.

velocities, derived from the reconstructed images in figure 6.8, along with the fit to the distributions to calculate the anisotropy parameter, β, for the photodissociations. Fits to the angular-distribution data for BrCl photolysis at these short wavelengths yield values of $\beta_{Cl} = 2.0 \pm 0.1$ (at 235 nm) and $\beta_{Br^*} = 1.3 \pm 0.1$ (at 262 nm). Subscript labels are used to distinguish anisotropy parameters for the different detected photofragments. Inspection of images recorded by detection of Br and Cl* reveal that these photofragments arise subsequent to a (predominantly) perpendicular transition, but the weakness of the signal and the large size of the Cl* image preclude a more quantitative analysis. These observations are consistent with the formation of Br* exclusively via channel (6.3) at λ~262 nm, as well as at λ~235 nm, and of Br formation via channel (6.2) at both 235 and 260 nm.

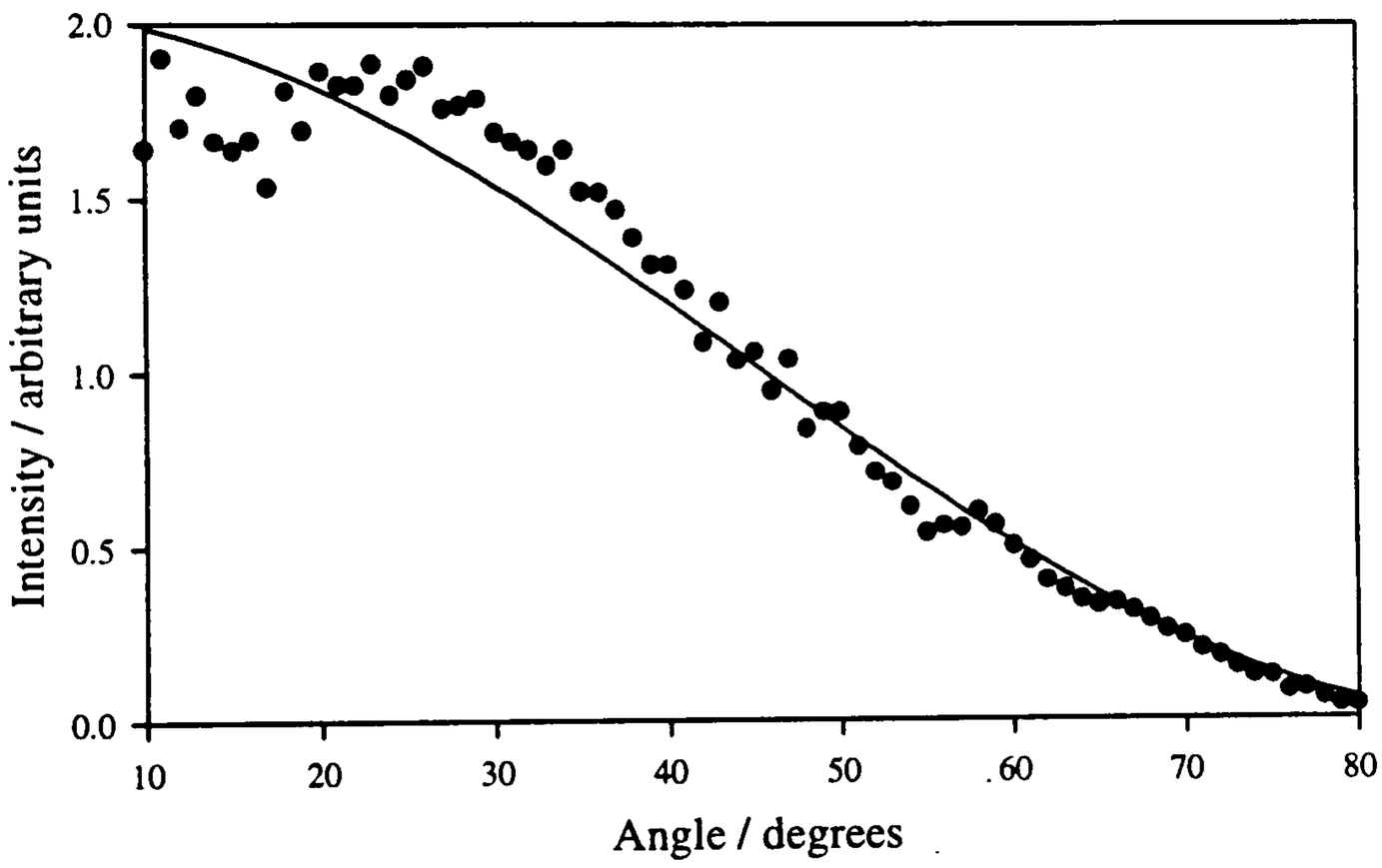

Figure 6.9: Angular distributions of Cl photofragments derived from the reconstructed image in figure 6.8. The solid line is a fit to the data performed using the standard equation for the anisotropy parameter, β, defined in equation (1.7). Data points from 0 - 10° and 80 - 90° have been excluded from the figure and fit because the mathematical reconstruction of the 2D slice from the raw data introduces noise in these angular regions.

6.3.3 Long wavelength photodissociation: $\lambda \geq 320$ nm

Numerous images for the different atomic fragments from BrCl photolysis were recorded at wavelengths between 320 nm and 540 nm. Figure 6.10 shows illustrative examples for Cl and Cl* detection at 5 representative wavelengths. The images clearly evolve both in radius and in anisotropy as the photolysis wavelength is changed. Images were taken of the Cl, Cl* and Br photofragments to obtain as complete as possible a picture of the photodissociation processes, and were analysed both to deduce the cofragment (and hence the dissociation channel) and the anisotropy of the recoiling photofragments. Attempts were made to image Br* atoms from photodissociation in this wavelength range but no signal was detected. The observed changes in the radii of the images are a result of energy conservation as the photolysis wavelength changes. Figure 6.11 shows examples of fits to angular distributions used to determine β parameters with figure 6.12 and table 6.1 summarising the values the obtained for the various photofragments.

At wavelengths shorter than 410 nm, the Cl products show a limiting anisotropy of $\beta_{Cl} = -1.0 \pm 0.1$. The limiting anisotropy parameters are indicative of Cl formation via prompt dissociation following excitation on a perpendicular ($\Delta\Omega = \pm 1$) transition. From 415 - 450 nm the perpendicular anisotropy evolves gradually to a near-isotropic angular distribution ($\beta_{Cl} \sim 0$) and for wavelengths longer than 450 nm, β_{Cl} remains close to zero (in the range 0 to – 0.2) with no apparent wavelength dependence. In marked contrast, the Cl* images show a positive, but non-limiting anisotropy parameter ($\beta_{Cl^*} \sim 1$ to 1.5) for wavelengths longer than 400 nm, with, perhaps, a gentle decline in β_{Cl^*} values as the wavelength increases. At wavelengths shorter than 400 nm little or no Cl* is detected, consistent with the measurements of Cao *et al.*[13] of the branching between Cl and Cl* products from BrCl photodissociation. The angular anisotropy of the Br photofragments changes from a distribution characteristic of a perpendicular excitation ($\beta_{Br} \sim -1$) at wavelengths shorter than 400 nm to a preferentially parallel (but, again, non-limiting) distribution as the photodissociation wavelength increases. The β_{Br} values change rapidly with wavelength from 400 nm to 480 nm, but there is an inevitable contribution to the Br images at the longer wavelengths from photolysis of the Br_2 present in the gas sample.

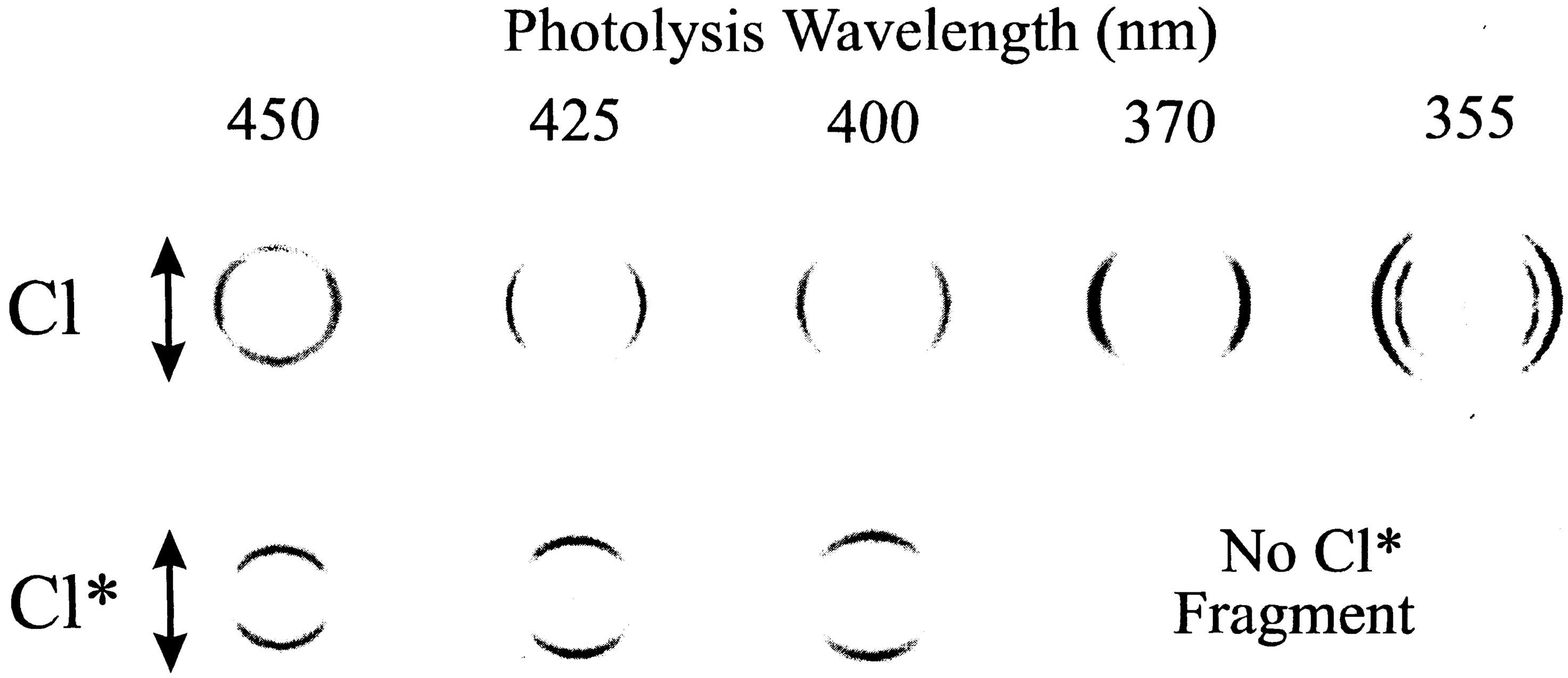

Figure 6.10: Reconstructed, three-dimensional images of Cl and Cl^* from BrCl photolysis at five photolysis wavelengths from 450 - 355 nm. Little or no Cl* was observed for wavelengths shorter than 400 nm. In all images, the linear polarisation vector of the photolysis laser lies vertically as indicated by the arrow. The double ring in the 355 nm image is a result of Cl formation from photolysis both of BrCl (outer ring) and Cl_2 (inner ring).

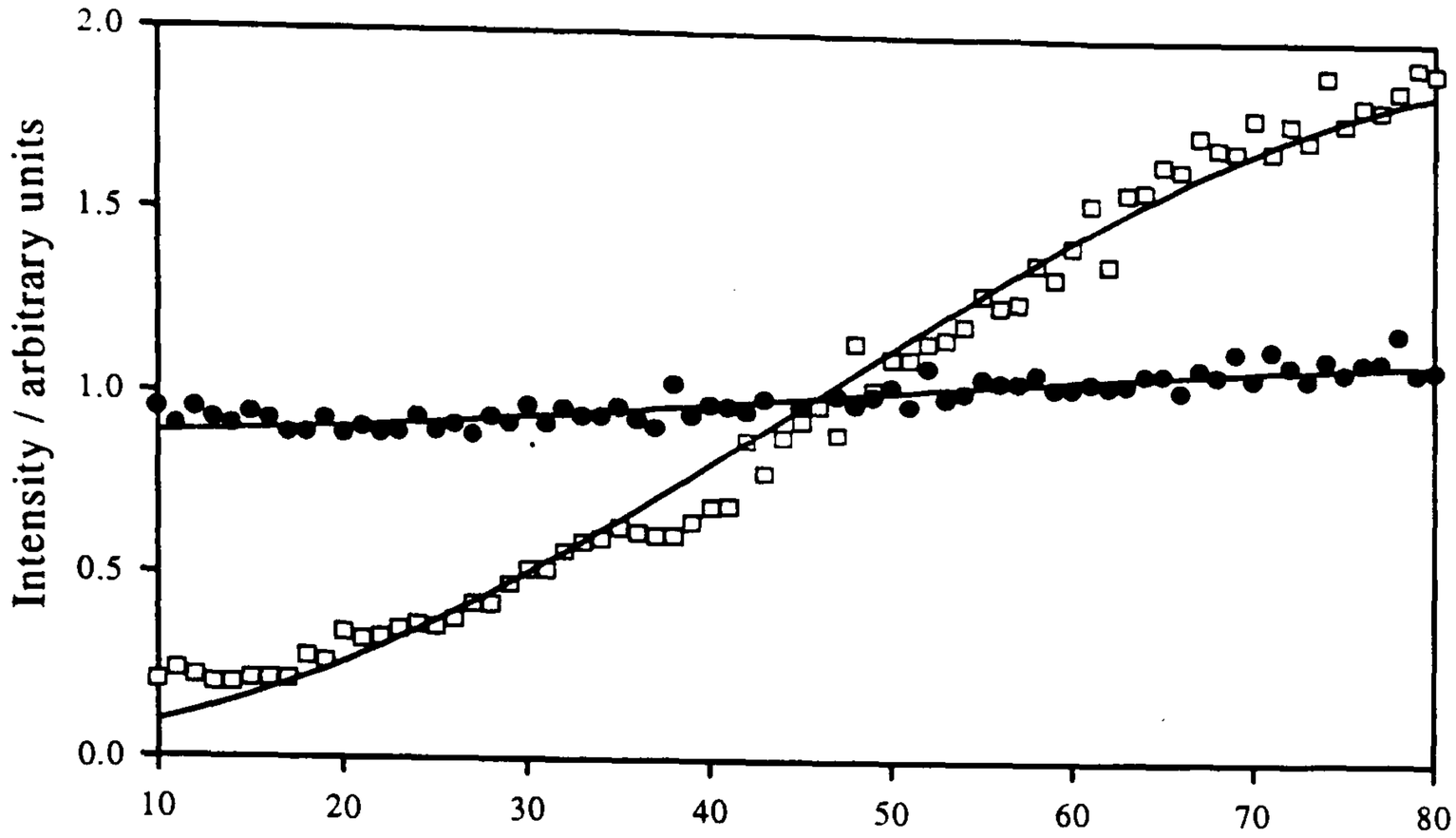

Figure 6.11: Angular distributions of Cl photofragments derived from reconstructed images for λ = 400 (□) and 530 (●) nm. The solid lines are fits to the data performed using equation (1.7) of the text. As in figure 6.9, the plots and fits were restricted to the angular range 10 - 80°.

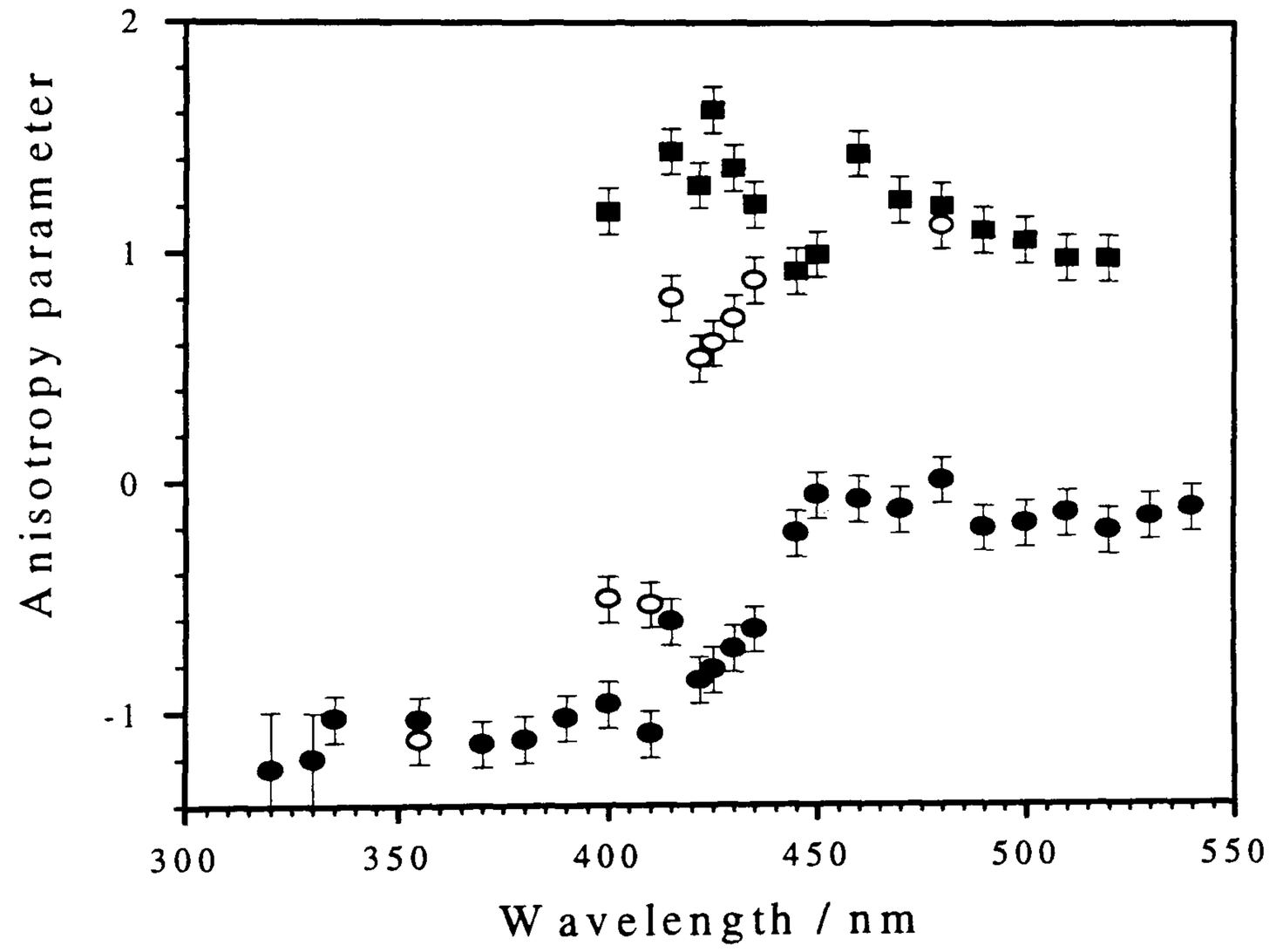

Figure 6.12: Anisotropy parameters, β, determined for the Cl (●), Cl*(■) and Br(○) fragments from BrCl photodissociation at photolysis wavelengths from 320 - 545 nm. Error bars are estimated uncertainties in β based on the reproducibility of the images and exceed the standard deviations obtained from fits to the individual photofragment angular distributions.

Wavelength /nm	β_{Cl} (± 0.1)	β_{Cl^*} (± 0.1)	β_{Br} (± 0.1)	β_{Br^*} (± 0.1)
540	-0.11			
530	-0.15			
520	-0.21	0.98		
510	-0.13	0.98		
500	-0.18	1.06		
490	-0.20	1.10		
480	0.01	1.21	1.12	
470	-0.12	1.23		
460	-0.08	1.43		
450	-0.06	1.00		
445	-0.22	0.92		
435	-0.64	1.21	0.88	
430	-0.73	1.37	0.71	
425	-0.82	1.62	0.61	
421.6	-0.86	1.29	0.54	
415	-0.61	1.44	0.80	
410	-1.10		-0.53	
400	-0.97	1.18	-0.51	
390	-1.03			
380	-1.12			
370	-1.14			
355	-1.04		-1.12	
335	-1.03			
330	-1.20			
320	-1.25			
262				1.30
235	2.01			

Table 6.1: Fitted anisotropy parameter (β) values for the Cl, Cl*, Br and Br* photofragments from the photodissociation of BrCl in the wavelength range 235 - 540 nm.

The extent to which Br_2 photolysis affects the measured β_{Br} values is discussed in section 6.4.7. An interpretation of the strong variations of β parameters both with probed photofragment and with photolysis wavelength is given in section 6.4.

6.4 Discussion

Discussion of the images centres around accounting for their appearance in terms of the postulated form of the potential energy curves of BrCl, and the suggested deconvolution of the absorption spectrum into contributions from transitions to just 4 states. Recall figure 6.4, which shows schematic potential energy curves for the electronic states of BrCl that have, to date, been implicated in its UV and visible photochemistry. Consistent with the correlation diagram in figure 6.2, it shows the $B^3\Pi(0^+)$ state correlating diabatically with the Cl* + Br asymptote rather than the Cl + Br* asymptote tentatively suggested by Brown *et al.*,[10] but with an avoided crossing with another 0^+ state leading to an adiabatic correlation to Cl + Br. Figure 6.4 is also consistent with interpretations of the potentials of other interhalogens such as IBr and ICl, for which the $B^3\Pi(0^+)$ states are postulated to correlate diabatically with the lower in energy of the two possible $^2P_{3/2}$ + $^2P_{1/2}$ asymptotes. As mentioned previously, and illustrated in figure 6.3, fits of the BrCl absorption spectrum permitted assignments[3,4] of portions of the continuous UV/visible band to excitations from the ground $X^1\Sigma^+(0^+)$ state to the $A^3\Pi(1)$, $B^3\Pi(0^+)$, $C^1\Pi(1)$ and $D(0^+)$ states at wavelengths from 540 - 230 nm. The discussion of the experimental results are divided into wavelength regions corresponding to likely excitation to these various states, starting with the short wavelength data. The discussion concentrates first on the measurements of Cl and Cl* anisotropies and fragmentation channels, and at the end of the section information contained within the Br data concerning branching ratios is addressed.

6.4.1 $\lambda \sim 235$ nm and $\lambda \sim 260$ nm

Based on the analysis of the BrCl absorption spectrum shown in figure 6.3, it might be anticipated that photodissociation at wavelengths near 235 nm and 260 nm follow excitation to the $D(0^+)$ state as the band in the absorption spectrum centered at 43940 cm^{-1} (228 nm) has been assigned to the $D(0^+)$ - $X^1\Sigma^+(0^+)$ transition.[4] Therefore the photofragments might be expected to show a limiting anisotropy parameter characteristic of a parallel excitation (i.e., $\beta = 2$). Such a value of β is indeed observed for the production of Cl atoms (which, as discussed in section 6.3.2, are formed in

coincidence with Br*). However, the open channel corresponding to formation of Cl* (together with Br atoms) shows an angular distribution characteristic of a perpendicular excitation ($\beta_{Cl^*} \sim -1$). Very similar behaviour was recently reported in a one-colour ion-imaging study of the 235 nm photodissociation of ICl, for which only channels leading to I + Cl* and I* + Cl were observed, with these two pathways resulting from, respectively, perpendicular and parallel excitations.[19] From comparisons with calculated potential curves for the low-lying excited states of ICl,[18,23] the perpendicular excitation leading to I + Cl* products was attributed to transition to a $^1\Pi(1)$ excited state which correlates adiabatically with the observed products. The upper state of the parallel excitation producing I* + Cl products must have 0^+ symmetry, but could be ascribed to the $2^3\Pi(0^+)$ state (thought to make at most only a minor contribution) or, more likely, the $1^3\Sigma^-$ (0^+) state. The data for BrCl photodissociation show many parallels with the studies of ICl at similar wavelengths, and demonstrate that the BrCl absorption in the wavelength range 235 - 262 nm cannot be solely due to absorption to a 0^+ state, but rather that it must also include a perpendicular component to a state with $\Omega = 1$. Excitation to the $C^1\Pi(1)$ state can be discounted since it correlates with Cl + Br products, but a likely candidate is the $1^3\Sigma^-$ (1) state. The relative contributions of parallel and perpendicular excitations to the absorption spectrum cannot be quantified from the measurements however, since no effort was made to calibrate the magnitudes of the signals for Cl and Cl* formation against one another, but the relative weakness of the Cl* signal as compared with the Cl signal indicates that the perpendicular excitation is a minor contributor to the absorption at 235 nm.

If, as is suggested in section 6.3.2, Br* is formed together with Cl *via* channel (6.2) both at 235 nm and at 262.5 nm, it might be expected that $\beta_{Br^*} = 2.0$ at the longer wavelength, consistent with $\beta_{Cl} = 2.0$ at $\lambda = 235$ nm. The cause of the non-limiting, but positive value, $\beta_{Br^*} = 1.3 \pm 0.1$ at 262.5 nm, is most likely a consequence of the parallel excitation to the $D(0^+)$ state being overlapped by a weaker perpendicular transition also resulting in Br* photofragments. What fractions of these Br* products are formed in association with Cl or Cl* co-fragments, i.e. *via* channel (6.3) or (6.4), cannot be determined from the data.

6.4.2 $320 < \lambda < 400$ nm

The strong feature in the BrCl absorption spectrum peaking at 372 nm (26850 cm^{-1}) and extending to λ ~300 nm has been assigned to the $C^1\Pi(1) - X^1\Sigma^+(0^+)$ transition.[4] The $C^1\Pi(1)$ state is repulsive and correlates with ground state Cl + Br fragments (channel (6.1)). Cao *et al.*[13] have reported that the formation of Cl* from BrCl photodissociation falls off sharply at wavelengths shorter than about 450 nm and the yield of Cl* is only ~10% of the total $Cl(^2P)$ formed at 390 nm. This is consistent with excitation to the $C^1\Pi(1)$ state in the Franck-Condon region followed by the majority of the dissociating flux following this potential curve. The observation that Cl atoms are formed with $\beta_{Cl} = -1.0 \pm 0.1$, independent of wavelength over the range 320 - 410 nm, and with Br cofragments only (channel (6.1)) can be readily explained if their formation is attributed to dissociation following excitation via the perpendicular $C^1\Pi(1) - X^1\Sigma^+(0^+)$ transition. Figure 6.13 shows the Cl atom velocity plot resulting from photodissociation at 355 nm. The peak at higher velocity is due to Cl + Br formation, whereas the slower peak is due to Cl atoms from the photodissociation of Cl_2. The lack of observed Br* and Cl* products in this wavelength range strongly supports the notion that the fragmentation proceeds diabatically on the $^1\Pi(1)$ surface, with little or no transfer of flux onto potentials correlating with upper spin-orbit components of the two atoms.

6.4.3 $400 < \lambda < 540$ nm

To wavelengths longer than 400 nm, two features distinguish the BrCl photodissociation dynamics from those observed in the 320 - 400 nm range: firstly, the yield of Cl* products increases, with Cl* being formed only via channel (6.2) in conjunction with Br, and secondly, β_{Cl} becomes less negative, reaching a value close to zero at 450 nm that is maintained for all longer wavelengths. No Cl* fragments were observed at wavelengths longer than 530 nm, consistent with the threshold for channel (6.2) being 529 nm. These observations are interpreted as indicators of the declining contribution to BrCl absorption *via* the $C^1\Pi(1) - X^1\Sigma^+(0^+)$ transition and the increasing

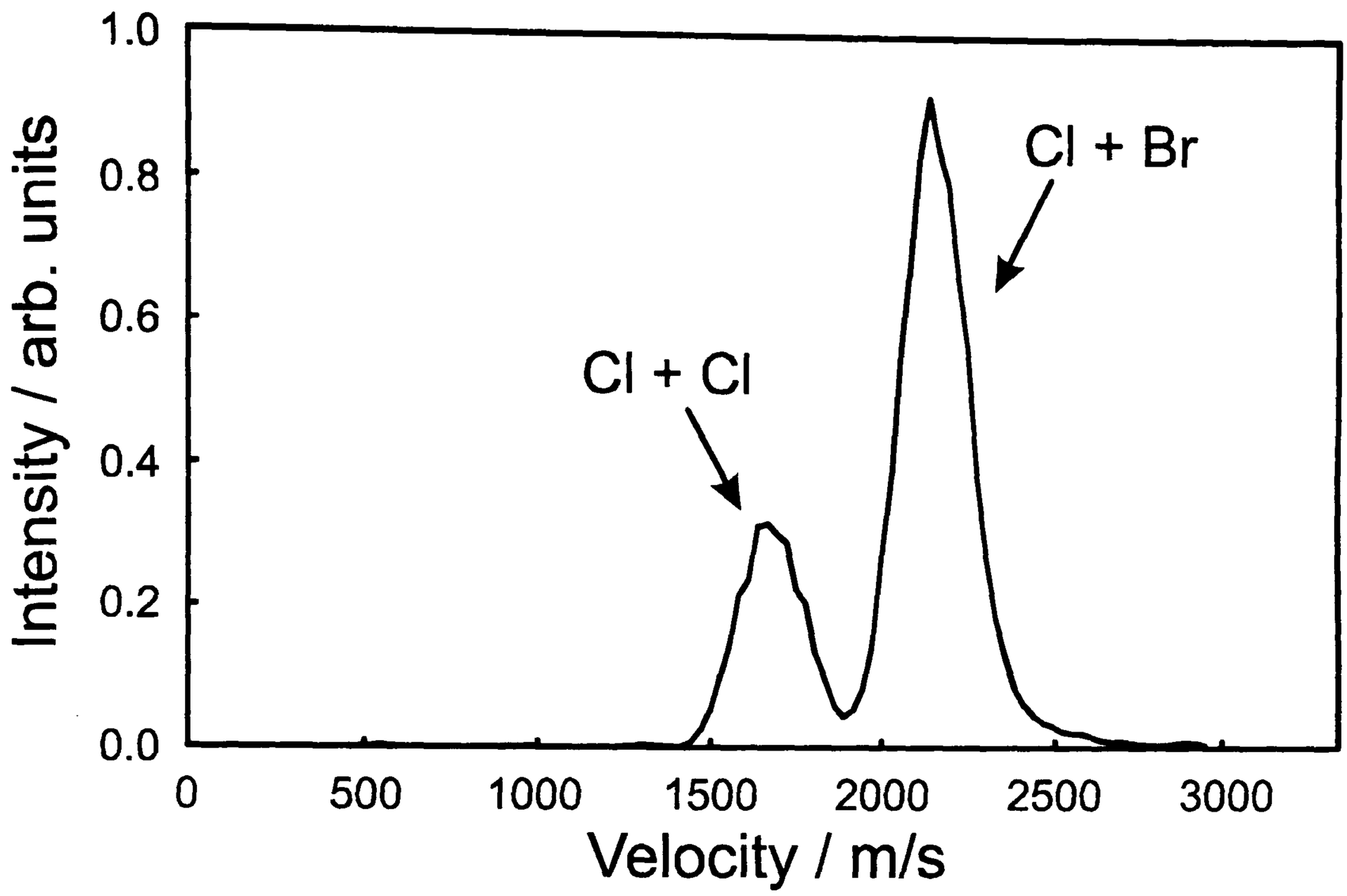

Figure 6.13: Velocity plot of the Cl atoms resulting from the photodissociation of BrCl and Cl_2 at 355 nm. The slower peak is due to Cl_2 photolysis, whereas the faster peak results from BrCl photodissociation.

contribution of the $B^3\Pi(0^+)$ - $X^1\Sigma^+(0^+)$ and $A^3\Pi(1)$ - $X^1\Sigma^+(0^+)$ absorptions as the photodissociation wavelength increases.

Firstly the declining anisotropy of the Cl atoms is considered. The BrCl absorption spectrum in the wavelength range 400 - 450 nm is traditionally interpreted in terms of contributions from both the $C^1\Pi(1)$ - $X^1\Sigma^+(0^+)$ and $B^3\Pi(0^+)$ - $X^1\Sigma^+(0^+)$ transitions with the former dominant at shorter wavelengths.[3,4] As the photolysis wavelength is increased from 400 - 450 nm, the Cl atom velocities are therefore anticipated to show a spatial anisotropy that evolves gradually from perpendicular ($\Delta\Omega$=1, $\beta_{Cl} = -1$) through zero (where perpendicular and parallel components sum to give a net isotropic distribution of photofragments) to parallel ($\Delta\Omega$=0, β_{Cl}=2). The first phase of this evolution is consistent with the experimental results but the model of increasing absorption to the $B^3\Pi(0^+)$ state alone as the wavelength increases cannot account for the fact that $\beta_{Cl} \sim 0$ to -0.2 values are observed for all wavelengths longer than 450 nm.

As previously mentioned, the observation of non-limiting β values for a photodissociation process is indicative of excited state interactions and dynamics. The three different mechanisms of slow recoil, predissociation and excited state mixing will all be considered in turn as candidates for non-limiting effects in β_{Cl} values seen here.

Recall that the axial recoil approximation breaks down when the molecule is excited just above an energy threshold for forming a set of atomic products. For a slowly recoiling system the nascent rotation of the parent molecule can lead to significant tangential motion of the photofragments away from the molecular axis, and so lead to reduced β values. Using the classical expression for the reduction in β as derived by Oldman *et al*[24] (recall from chapter 5, equation (5.11)), the expected β values were calculated for a range of beam temperatures up to 100K. Figure 6.14 illustrate the results of such a calculation for a parallel and perpendicular near threshold photodissociation of BrCl, with parent molecular beam temperatures of 20, 50 and 100 K. Even at the warmest beam temperatures considered, the calculated

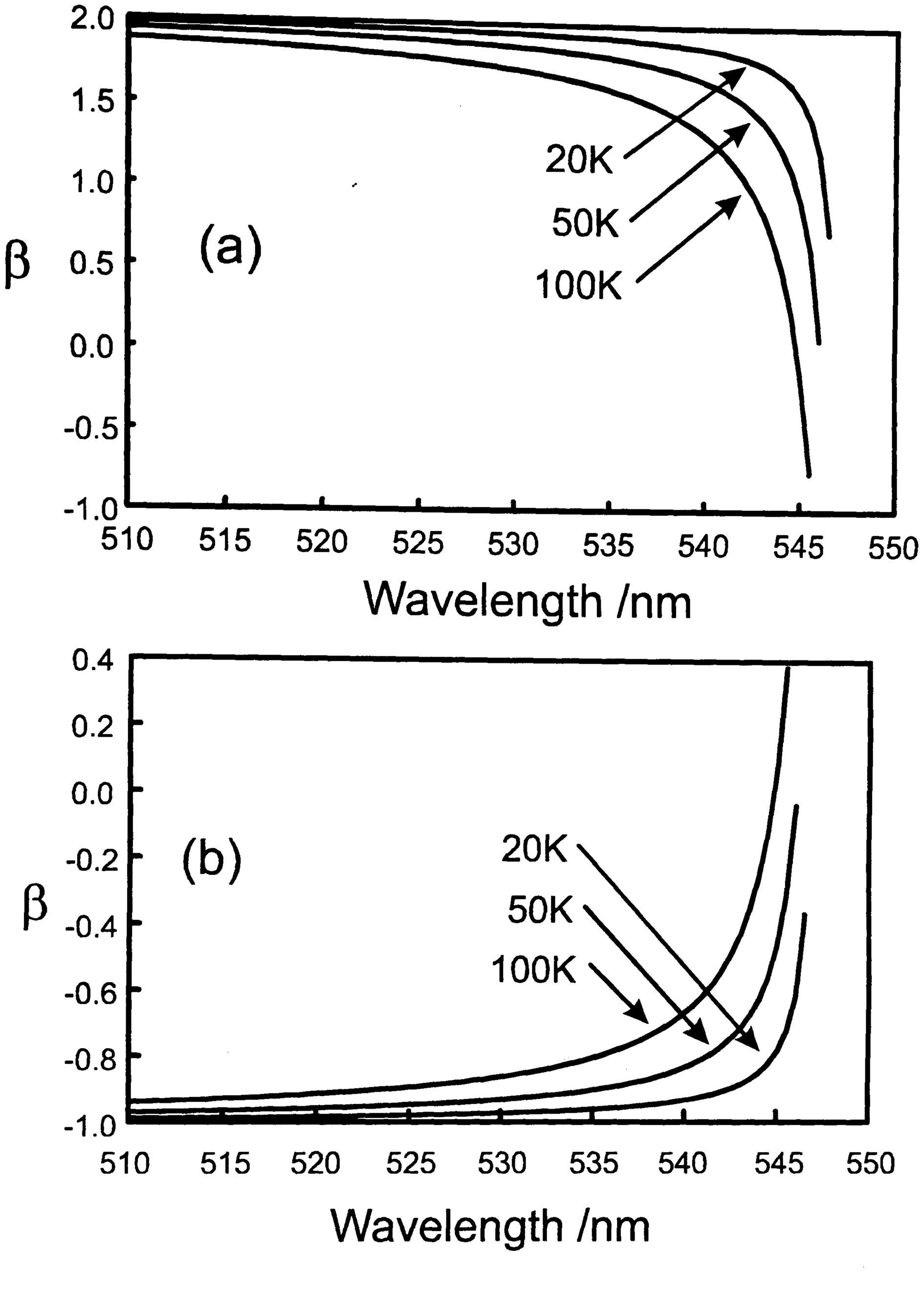

Figure 6.14: Calculated β values using equation (4.11) for photodissoiation of BrCl just above threshold for forming Br + Cl (554.8 nm), via a parallel (a) and perpendicular (b) transition.

reductions in photofragment anisotropies could not account for the small values of β_{Cl} measured experimentally at wavelengths longer than 450 nm.

Alternatively, anisotropy parameters substantially reduced from their limiting values can result from pure parallel or perpendicular excitations if the upper state is predissociated, where the excited state in the transition has a lifetime that is long in comparison with the rotational period of the molecule. In fact values of β less than the limit expected for prompt dissociation can be used as a "rotational clock" to estimate predissociative lifetimes of excited states.[25] The threshold for channel (6.1) lies at 18024 cm^{-1} (λ = 555 nm) and excitation at 450 nm (22222 cm^{-1}) gives an excess energy above this threshold of 4198 cm^{-1}, which exceeds the threshold for channel (6.3) and is close to the threshold for channel (6.4). It could be postulated that the low Cl-atom anisotropies for λ = 450 - 540 nm could result from excitation to a bound state with lifetime longer than the molecular rotational period. If this were the case then the (hypothetical) excited, bound state would correlate asymptotically with Br* + Cl* products and must be predissociated by a state correlating to Br + Cl products. Such a correlation would be consistent with the observation that the β_{Cl} values start to fall from near-zero toward −1 at wavelengths shorter than 450 nm, since the excitation energy then starts to exceed the threshold for channel (6.4). However, this explanation leads to some apparent contradictions which lead it to be discounted. The first objection is that excitation to this postulated state above the channel (6.4) asymptote should form measurable quantities of Br*, yet Cl* images at $\lambda < 450$ nm show only Br cofragments. The second objection is that a bound state would be expected to give vibrational structure in the absorption spectrum, but no such structure has been reported in this wavelength range. It is conceivable, however, that the structure is washed out by a combination of dense rovibronic spectral features, line-broadening from rapid predissociation and isotope shifts for the four possible common isotopomers of BrCl. Finally, recall from chapter 5 that predissociation of a long-lived state does not necessarily lead to near-zero anisotropy parameters: in the high-J limit, states accessed respectively by a perpendicular or parallel excitation should show anisotropy parameters $\beta_{\perp} = -0.25$ and $\beta_{//} = 0.5$.[26] At low J, these β parameters can take more extreme values, but, for simultaneous excitations on P, Q and R branches the

parameters rapidly approach the high-J limit.[27] Thus it might be expected that for predissociation of BrCl on a timescale longer than the rotational period, values of $\beta_{Cl} \sim 0$ would not be observed. The full analysis is, however, complicated by the effects of hyperfine coupling caused by the non-zero nuclear spins of Cl and Br, which could be significant at low J in reducing β_{Cl}. The timescale for such hyperfine effects is likely to be hundreds of picoseconds or longer, and states with such long lifetimes should be evident using LIF or dispersed emission from higher-lying states, yet no such states have been reported.

Discounting both slow recoil and predissociative effects leads to the preferred mechanism for the origin of β_{Cl} values close to zero, namely of multiple excited state population and mixing. The observed results are due to a mixed parallel and perpendicular excitation, which results in formation of both Cl and Cl* atoms with anisotropies reduced from their limiting values. The rapid increase in the yield of Cl* that occurs as the photolysis wavelength is increased from 400 nm and which, according to Cao *et al.*,[13] peaks at about 60% of the total Cl(^{2}P) yield at $\lambda \sim 450$ - 470 nm, was attributed by these authors to extensive non-adiabatic transitions following $B^3\Pi(0^+)$ state excitation. This picture was based on the speculation by Brown *et al.*[10] that the diabatic dissociation limit of the $B^3\Pi(0^+)$ state might be the Br* + Cl asymptote rather than the Br + Cl* asymptote. An avoided crossing with another, repulsive, 0^+ state, however, leads to a suggested adiabatic correlation of the $B^3\Pi(0^+)$ state with the Br + Cl products of channel (6.1). Thus, in the picture of Cao *et al.*, substantial flux must transfer from the adiabatic $B^3\Pi(0^+)$ state *en route* to Br + Cl products to give the 60% Cl* yield.

A slightly different picture is used to explain the current set of results, in which the $B^3\Pi(0^+)$ state is assumed to correlate diabatically to Br + Cl*. This revised correlation does not substantially affect the arguments presented below to account for the data, but simplifies the interpretation. The significant formation of Cl* + Br products following $B^3\Pi(0^+)$ state excitation above the threshold for channel (6.2) can be accounted for if it is assumed that the crossing of the $B^3\Pi(0^+)$ state and the 0^+ state correlating with Br + Cl is only partially or weakly avoided (c.f. the mixed coupling

invoked for IBr[15]). The simplest route to Cl* formation is then *via* excitation to the $B^3\Pi(0^+)$ state and dissociation on the diabatic potential. Hence, the Br + Cl* products should exhibit a positive anisotropy parameter as observed in the experiments: the magnitude of β_{Cl*} evidently shows that the Cl* does not arise from a predissociated state, such as is considered above as a possible route for Cl formation at these wavelengths. The anisotropy parameter does not, however, take the limiting value of +2 at any wavelength, and as shown below, a mechanism involving mixed parallel and perpendicular absorptions can account for the measured, non-limiting values of β_{Cl*}, together with the near-zero values for β_{Cl} and the branching ratio data of Cao *et al.*[13]

The observed β_{Cl*} and β_{Cl} values can be explained by the model potentials shown schematically in figure 6.15, where the thicker lines represent adiabatic potentials which will be followed by dissociating flux if the crossing of the $B^3\Pi(0^+)$ and higher-lying 0^+ state is strongly avoided. The thinner lines in the region of the crossing show the diabatic correlations, more appropriate for interpreting the dissociation dynamics if the crossing is only very weakly avoided. These limiting models are discussed in turn below. The primary excitation for BrCl at wavelengths longer than about 440 nm is traditionally attributed to absorption on the $B^3\Pi(0^+)$ - $X^1\Sigma^+(0^+)$ transition, yet observations of near-zero values for β_{Cl} and non-limiting, but positive values for β_{Cl*} can be most simply explained if a contribution to the two channels is invoked from both a parallel and a perpendicular excitation. The most likely candidate for a perpendicular transition at wavelengths longer than 450 nm is excitation to the continuum of the $A^3\Pi(1)$ state, which correlates with Cl + Br products (although the possible role of the $C^1\Pi(1)$ state is discussed at the end of this section). The $\Omega = 0$ and $\Omega = 1$ components of the $^3\Pi$ state will be mixed by molecular rotation through the operation of the S-uncoupling operator,[28] $J_+S_- + J_-S_+$, and in principle for excitation of a near-equal mixture of the $\Omega = 0$ and $\Omega = 1$ components for a rotating molecule, the photofragments will show reduced anisotropy parameters very much as seen here for Cl and Cl* (appendix C describes the effect of the S-uncoupling operator in more detail). For rotating molecules the correlations shown in figure 6.2 become inappropriate because of mixing of different components of the same multiplet electronic state. Therefore the term adiabatic is used to describe the state correlations

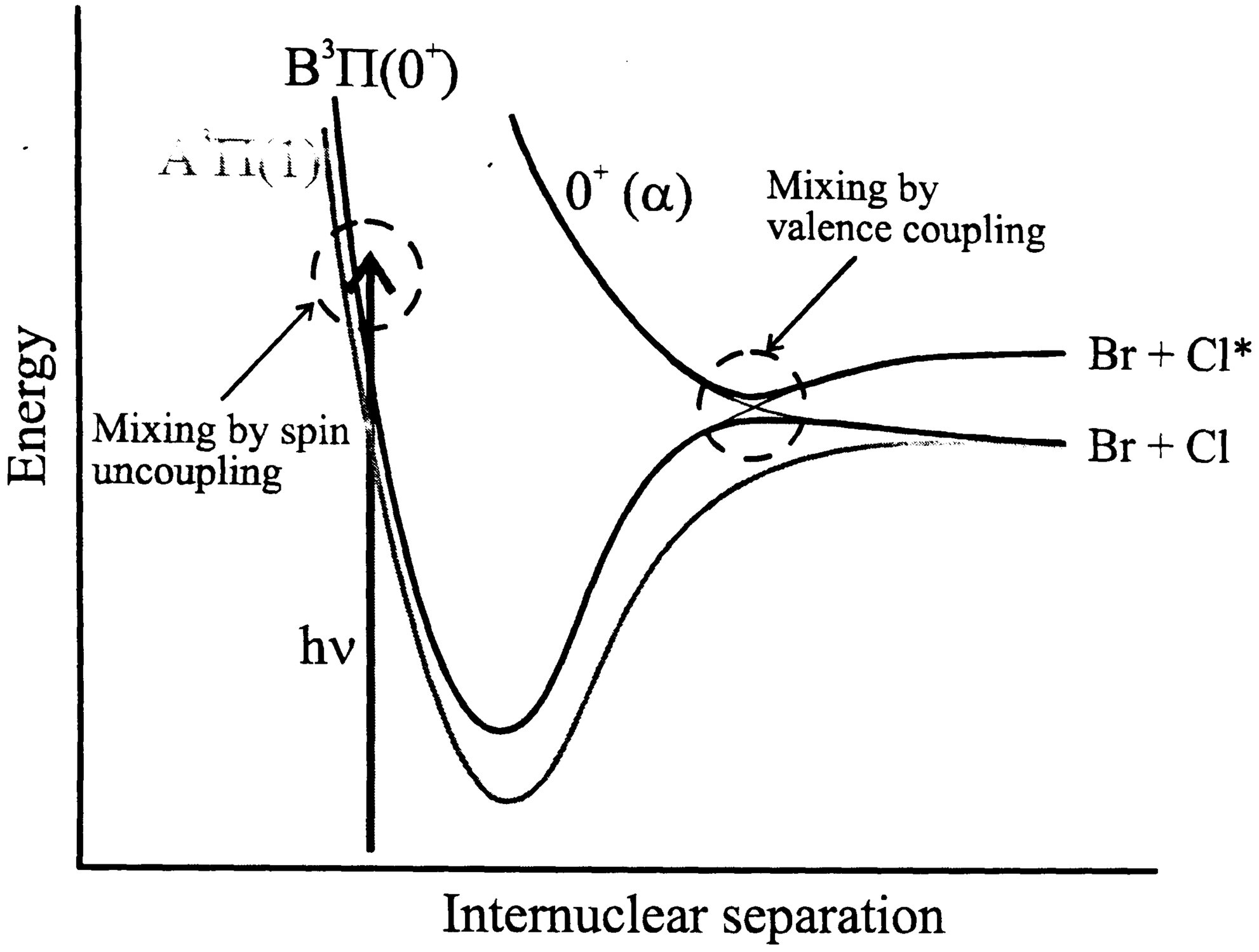

Figure 6.15: Schematic diagram of the potentials used to interpret observed β parameters for BrCl photodissociation at wavelengths longer than 400 nm. Excitation (shown as a vertical arrow) occurs via both a parallel transition to a state with $\Omega=0$ (the $B^3\Pi(0^+)$ state) and a perpendicular transition to a state with $\Omega=1$ (the $A^3\Pi(1)$ state). The bold lines represent adiabatic potentials and the thinner lines show the diabatic correlations of the $B^3\Pi(0^+)$ state and a second 0^+ state to the Br + Cl* and Br + Cl asymptotes respectively. Mixing of the $A^3\Pi(1)$ and $B^3\Pi(0^+)$ states at short internuclear separation, and the avoided crossing of the two 0^+ states are indicated by dashed circles.

of figure 6.15 in the absence of molecular rotation. The extent of the rotational mixing depends on the rotational angular momentum of the molecules and hence the molecular beam temperature. For substantial rotational cooling within a molecular beam, the rotation-induced mixing should be small, but for the halogen-rich mixtures used in the experiments reported here, the estimated beam temperatures could be as high as 50 - 100 K, which may result in significant rotation-induced mixing. It will be greatest at short internuclear separations both because the magnitude of the coupling depends on the rotational constant, and because the potentials are near-degenerate. Figure 6.15 therefore shows schematic mixing *via* spin-uncoupling at the inner walls of the $B^3\Pi(0^+)$ and $A^3\Pi(1)$ states.

To illustrate how the excitation to Ω=0 and Ω=1 components can give the observed anisotropy parameters, the molecular absorption at $\lambda \geq 450$ nm is approximated as being to individual $B^3\Pi(0^+)$ and $A^3\Pi(1)$ states, and the mixing treated as flux transfer between the two states. In addition, the possible role of the second, higher-lying 0^+ state shown in figure 6.15 is considered, in determining measured anisotropy parameters and Cl* branching fractions. The precise details of the model treatment differ for the limits of weakly and strongly avoided crossing of the two 0^+ states, but have the common feature of invoking excitation in the wavelength range between 400 nm and 540 nm to two electronic states, one with $\Omega = 1$ and the other with $\Omega = 0$.

6.4.4 Model for a weakly avoided crossing

To illustrate how the reduced anisotropy of both Cl and Cl^* recoil can arise from the schematic potentials of figure 6.15, the simple limiting case in which the crossing between diabatic 0^+ states is only weakly avoided is firstly considered. In this case most of the dissociating flux on the $B^3\Pi(0^+)$ state will follow the diabatic pathway to Br + Cl*. The dissociation dynamics can be treated as occurring *via* excitation to the $A^3\Pi(1)$ and $B^3\Pi(0^+)$ states, with transfer of flux between these two potentials at short internuclear separation, followed by evolution to atomic products corresponding to channels (6.1) and (6.2) on, respectively, $\Omega = 1$ and $\Omega = 0$ diabatic curves. If the

relative probabilities of absorption to the $A^3\Pi(1)$ and $B^3\Pi(0^+)$ states are taken as P_1 and P_0, with possibility of crossing of flux between the two curves at short range accounted for by defining P_{01} as the probability that excitation to the $\Omega = 0$ state results in formation of Cl + Br products, and P_{10} as the probability that excitation to the $\Omega = 1$ state forms Cl* + Br. Excitation to the $\Omega = 0$ state has $\beta_0 = 2$ whereas excitation to the $\Omega = 1$ state has $\beta_1 = -1$. If interference between the wavepackets evolving on the two coupled electronic states is neglected, following expressions can be formulated for β_{Cl}, β_{Cl^*} and the % yield of Cl*, $\sigma_{Cl^*}/(\sigma_{Cl} + \sigma_{Cl^*})$, determined by Cao *et al*:

$$\beta_{Cl} = P_1(-1)(1-P_{10}) + P_{01}P_0(2) \qquad (6.11)$$

$$\beta_{Cl^*} = P_2(2)(1-P_{01}) + P_{10}P_1(-1) \qquad (6.12)$$

By searching the multidimensional space spanned by the various probabilities the values for P_{01} and P_{10} necessary to account for the measurements can be estimated. To simplify the formulation, it is assumed that values of P_{01} and P_{10} are equal, which results in calculated anisotropy parameters of $\beta_{Cl} = 0$ to -0.2 and $\beta_{Cl^*} = 1.2$ to 1.4 if $P_0 \approx 0.56$, $P_1 \approx 0.44$ and $P_{10} = P_{01} \approx 0.3$. The calculated % yield of Cl* is then ~53 %, close to the measurements of Cao *et al.* Therefore, the non-limiting experimental values of β_{Cl} and β_{Cl^*} can be readily explained in terms of the model illustrated in figure 6.15 in the limit of weak interaction of the two 0^+ states, with a (rotation-induced) crossing between $B^3\Pi(0^+)$ and $A^3\Pi(1)$ state potentials with probability ~ 0.3.

6.4.5 Model for a strongly avoided crossing

The detailed analysis by Tellinghuisen and coworkers[10–12] of emission on the BrCl $E(0^+)$ - $B^3\Pi(0^+)$ transition suggests that the crossing between the $B^3\Pi(0^+)$ and 0^+ states that diabatically correlate, respectively, with the Br + Cl* (or possibly Br* + Cl) and Br + Cl asymptotes is strongly avoided. The resultant adiabatic $B^3\Pi(0^+)$ state correlates to the Br + Cl asymptote. This model is clearly in conflict with the above discussion that supposes a weakly avoided crossing of the $B^3\Pi(0^+)$ and 0^+ states. The bold curves in figure 6.15 represent schematic potentials consistent with the picture of a strongly avoided crossing: in the figure the upper 0^+ state is shown correlating

adiabatically with the Br + Cl* asymptote. Using adiabatic potentials constructed by Tellinghuisen[12] from spectroscopic data, values of the adiabaticity parameter $\xi = R\Delta E/\hbar v$ were calculated, where ΔE is the energy separation of the two potentials at the avoided crossing, R is the extent of the interaction region of the two 0^+ potentials, and v is the photofragment velocity through this region. Values obtained for ξ were greatly in excess of unity for the photodissociation wavelengths in the current study, suggesting that the dissociating flux will almost exclusively follow the adiabatic curves, i.e., in the absence of further exit-channel surface hopping, excitation to the $B^3\Pi(0^+)$ state will result in Br + Cl photofragments. As before, excitation to the $B^3\Pi(0^+)$ state alone cannot be responsible for the measurements since to obtain non-limiting values of β_{Cl} and β_{Cl^*}, a perpendicular transition must also contribute to the absorption. Therefore it is again assumed that the optically bright states are the $A^3\Pi(1)$ and $B^3\Pi(0^+)$ states, with relative excitation probabilities P_1 and P_0 respectively, and allow for transfer of flux from the $A^3\Pi(1)$ and $B^3\Pi(0^+)$ adiabatic states to potentials (denoted as α and α') that correlate with Br + Cl*, with respective probabilities $P_{1\alpha}$ and $P_{0\alpha'}$. The likely assignment of state α', which couples to the $B^3\Pi(0^+)$ state, is the 0^+ state shown in figure 6.15, but coupling of the $A^3\Pi(1)$ state to this 0^+ state would require rotation-induced mixing at large internuclear separation. The precise nature of the α and α' states is not, however, critical to the current analysis and hence discussion is deferred until section 6.4.6. To keep the model simple and to isolate the effects of the adiabatic correlations and possible non-adiabatic transitions, the short-range rotational coupling of the $A^3\Pi(1)$ and $B^3\Pi(0^+)$ states is neglected. The following expressions for the contributions to the observed β values can then be formulated:

$$\beta Cl = P_1(-1)(1-P_{1\alpha}) + P_0(2)(1- P_{0\alpha'}) \qquad (6.13)$$

$$\beta Cl^* = P_1P_{1\alpha}(-1) + P_0P_{0\alpha'}(2) \qquad (6.14)$$

A similar search of the probability values to that described above yields a range of values that can satisfy the experimental measurements of β_{Cl}, β_{Cl^*} and the % yield of Cl*. It is found that P_0 ranges from 0.55 to 0.65 (hence $P_1=1-P_0$ lies between 0.35 and 0.45), $P_{0\alpha'} \sim 0.75$ to 0.8 and $P_{1\alpha} \sim 0.35$ to 0.4. The large values of $P_{0\alpha'}$ show that

this model requires a substantial transfer of flux from the adiabatic $B^3\Pi(0^+)$ state to the α' state (i.e., probably the 0^+ state) upon fragmentation. Whether that flux transfer is through the avoided crossing, or further out towards the potential asymptotes is unclear but calculations of adiabaticity parameters imply that the former possibility can be discounted. Again, absorption to the $A^3\Pi(1)$ and $B^3\Pi(0^+)$ states with similar cross sections must be invoked to account for the measured anisotropy parameters.

Overall the above models must be regarded as limiting cases, with the likely origin of reduced magnitude ansiotropy parameters being both a consequence of rotational coupling at small internuclear separation and a predominantly adiabatic evolution of dissociating flux through the avoided crossing (giving both parallel and perpendicular components to the Br + Cl asymptote), together with some flux transfer to one or more states correlating to Br + Cl*. It is concluded that the estimated excitation probabilities to the $B^3\Pi(0^+)$ and $A^3\Pi(1)$ states should be comparable over the wavelength range 450 - 540 nm since both models require that $P_0 \sim 0.55$ to 0.65. Such a conclusion is consistent with the proposed strong mixing at short internuclear separation of the $A^3\Pi(1)$ and $B^3\Pi(0^+)$ states by molecular rotation. While at the longer wavelength end of this range, fits to the BrCl absorption spectrum (figure 6.3) suggest a roughly equal contribution from these two states,[4] at 450 nm the fits imply that excitation to the $A^3\Pi(1)$ state is negligible. Hence, the ion-imaging data cast doubt on the validity of the interpretation of spectral fits at wavelengths around 450 nm where absorption has previously been attributed almost exclusively to excitation to the $B^3\Pi(0^+)$ state. The view that results from the current study, is that the $A^3\Pi(1)$ state absorption extends to shorter wavelength than is suggested by figure 6.3, which is supported by the expected energy separation of the different Ω components of the $^3\Pi$ state. The minima of the $^3\Pi(0^+)$ and $^3\Pi(1)$ states should be separated by an energy substantially less than the (881 cm^{-1}) spin-orbit splitting of Cl atoms: for Hund's case (a) wavefunctions, the energy gap is estimated[28] to be $\sim 300\ cm^{-1}$. Hence, the absorption maxima of the $A^3\Pi(1)$ and $B^3\Pi(0^+)$ states should lie closer together than the 3900 cm^{-1} illustrated in figure 6.3 (which is based on the analysis of reference 4). Comparison can be made with Br_2, for which the energy minima of the equivalent

$A^3\Pi_u(1)$ and $B^3\Pi_u(0^+)$ states are separated by 1997 cm^{-1},[29] compared to a $Br(^2P)$ spin-orbit splitting of 3685 cm^{-1}.

6.4.6 The possible role of other dissociative states

To account for the perpendicular component in the images recorded for Cl* photofragments formed *via* channel (6.2), in sections 6.4.4 and 6.4.5 excitation to the $A^3\Pi(1)$ state followed by coupling to some state (either the $B^3\Pi(0^+)$ state or denoted α) correlating diabatically or adiabatically with the Br + Cl* channel was invoked. The less than limiting value of β_{Cl^*} extends out to wavelengths for which excitation to the $A^3\Pi(1)$ state has not previously been thought to be significant (i.e., to wavelengths shorter than ~ 500 nm, as shown in figure 6.3). Therefore, although it has been argued that the likely cause of non-limiting anisotropies for the fragments of channels (6.1) and (6.2) at wavelengths longer than 410 nm is most probably due to simultaneous excitation to states with $\Omega = 0$ and $\Omega = 1$, two questions still remain. The first is whether the $A^3\Pi(1)$ state is indeed the $\Omega = 1$ state to which absorption occurs at all $\lambda > 410$ nm, and the second is whether the transfer of flux from the $\Omega = 1$ state to a state correlating with the Br + Cl* asymptote occurs *via* rotation-induced coupling (to an $\Omega = 0$ state), or by mixing with another $\Omega = 1$ state.

Inspection of the correlation diagram in figure 6.2 shows that the only other likely optically bright $\Omega = 1$ state at wavelengths greater than 410 nm is the $C^1\Pi(1)$ state, which also correlates to Br + Cl products. Other $\Omega = 1$ states will lie higher in energy than the $C^1\Pi(1)$ state and cannot cross it. It has been previously stated that the $C^1\Pi(1)$ state correlates with Br + Cl products, and that Cl* photofragments are not observed at short wavelengths where the excitation is predominantly to this state. It is noted, however, that one possible mechanism for formation of Cl* + Br products following excitation to the $A^3\Pi(1)$ or the $C^1\Pi(1)$ states is *via* direct coupling to an additional $\Omega = 1$ state correlating with the Br + Cl* asymptote, and one such state (denoted as $^1\Pi(1)$) is evident in figure 6.2. Such a mechanism was proposed to account for the non-limiting anisotropy parameters observed for Br + Br* atoms formed by the photodissociation of Br_2 (see chapter 5). As is believed to be the case

for Br_2, the mixing of the $C^1\Pi(1)$ and repulsive $^1\Pi(1)$ states of BrCl will be greatest at energies just above the threshold for channel (6.2). This mechanism therefore offers a route to formation of Br + Cl* fragments with perpendicular character subsequent to $C^1\Pi(1)$ state excitation, but with a likelihood that falls sharply as the photodissociation wavelength is decreased. Such a route to Br + Cl* is also highly plausible following excitation to the $A^3\Pi(1)$ state, in which case α (from section 6.4.5) would identified as the repulsive $^1\Pi(1)$ state.

6.4.7 Anisotropy parameters for Br formation

The measurements of β_{Br}, as illustrated in figure 6.12 and listed in table 6.1, show extensive variation with photolysis wavelength. No formation of Br* is observed from the photolysis of BrCl over the wavelength range 320 - 540 nm and hence it should be possible to explain the observed values for β_{Br} in terms of the relative contributions of Cl and Cl* forming channels and their respective anisotropies. The ion imaging technique can, in principle, distinguish between Br atoms formed via channels (6.1) and (6.2) since the Br will be formed with different speeds in the two cases, but, as mentioned previously, the resolution of the instrument was insufficient to make the distinction.

In the range 320 - 400 nm, where only channel (6.1) is active, limiting values of $\beta_{Br} = -1.0 \pm 0.1$ are observed, entirely consistent with the measurement of $\beta_{Cl} = -1.0 \pm 0.1$ in this range which, as discussed earlier, is attributed to dissociation subsequent to excitation to the $C^1\Pi(1)$ state. At longer wavelengths, where channels (6.1) and (6.2) both contribute to the photofragmentation, if interference effects between dissociation pathways are neglected, it can be approximated that

$$\beta_{Br} = \frac{a\beta_{Cl} + b\beta_{Cl^*}}{a+b} \qquad (6.15)$$

where a and b are the relative yields of Cl and Cl* respectively. Thus, from measurements of β_{Cl} and β_{Cl^*}, combined with branching ratio data[13] for channels (6.1)

and (6.2) the expected values of β_{Br} can calculated. In table 6.2 these calculated anisotropy parameters are shown, together with the experimental measurements of β_{Br}. The major discrepancies between the measured and predicted values for β_{Br} occur at all wavelengths where the anisotropy of the Br products is larger than expected based on the results for Cl and Cl*. This discrepancy can be accounted for if additional contribution to the Br images is allowed from photodissociation of Br_2 at these wavelengths.

Wavelength /nm	Cl*/Cl ratio[a]	Calculated β_{Br}	Measured β_{Br} (± 0.1)
500	1.04	0.45	
490	1.13	0.49	
480	1.50	0.73	1.12
470	1.56	0.70	
460	1.63	0.86	
450	1.63	0.59	
445	1.56	0.47	
435	1.38	0.43	0.88
430	1.32	0.47	0.71
425	1.22	0.52	0.61
421.7	1.0	0.22	0.54
415	0.82	0.31	0.80
410	0.59		-0.53
400	0.35	-0.41	-0.51

[a] Values taken from Cao *et al.*[13]

Table 6.2: Comparison of the anisotropy parameters for Br fragments from BrCl photodissociation measured by ion imaging with values calculated from branching ratios and anisotropy parameters for Cl and Cl* photofragment using equation (6.11) of the text.

The BrCl samples used in the study were made from an approximately six-fold excess of Cl_2 over Br_2 with the intention of consuming almost all of the Br_2 in the sample, but measurements of the UV/visible absorption spectrum described in section 6.3.1 show that the ratio of BrCl to Br_2 in these samples was still only ~ 18:1. Therefore, in wavelength regions where the Br_2 absorption cross sections are comparable to, or larger than the BrCl cross sections, measurable contributions from Br_2 photolysis can be expected in the images: these contributions are quantified below. In general, the different speeds expected for Br atoms from Br_2 and from BrCl photolysis at a particular photolysis wavelength should be sufficient to separate them at the detector, but in the wavelength region around 430 - 500 nm where larger than expected β_{Br} values are observed, the speeds of the Br atoms from BrCl and from the $Br_2 \rightarrow Br + Br^*$ channel lie coincidentally close together, as illustrated by figure 6.16. Br_2 fragmentation at these wavelengths to yield Br + Br* involves a parallel photoexcitation process[30] and hence any unresolved contributions to the images of Br (+ Br*) photofragments from Br_2 photolysis will tend to increase the measured values of β_{Br}. As relative amounts of Br_2 and BrCl in the samples were measured, and the variation of the absorption cross sections of the two gases with wavelength is known, the magnitudes of the contributions to β_{Br} from BrCl and Br_2 photolysis can be predicted. For example, at $\lambda = 480$ nm, the absorption cross sections for Br_2 and BrCl are in the ratio 6:1, and Br_2 photolysis via the channel forming Br + Br* has $\beta_{Br} = 1.1$.[30] For a concentration ratio for the Cl_2-rich sample of Br_2:BrCl = 0.055:1, and for BrCl photolysis via channel (6.1) and channel (6.2) (with respective anisotropy parameters $\beta_{Cl} = 0.0 \pm 0.1$ and $\beta_{Cl^*} = 1.2 \pm 0.1$) having a branching ratio of 1:1.5, the expected β_{Br} (which is a sum of contributions from $BrCl \rightarrow Br + Cl$, $BrCl \rightarrow Br + Cl^*$ and $Br_2 \rightarrow Br + Br^*$) is 0.80 compared to a measured value of 0.97 ± 0.1. Bearing in mind the errors inherent in all the values used in this calculation, this result indicates overall consistency between the ion images recorded via Br, Cl and Cl* detection at a photolysis wavelength of 480 nm.

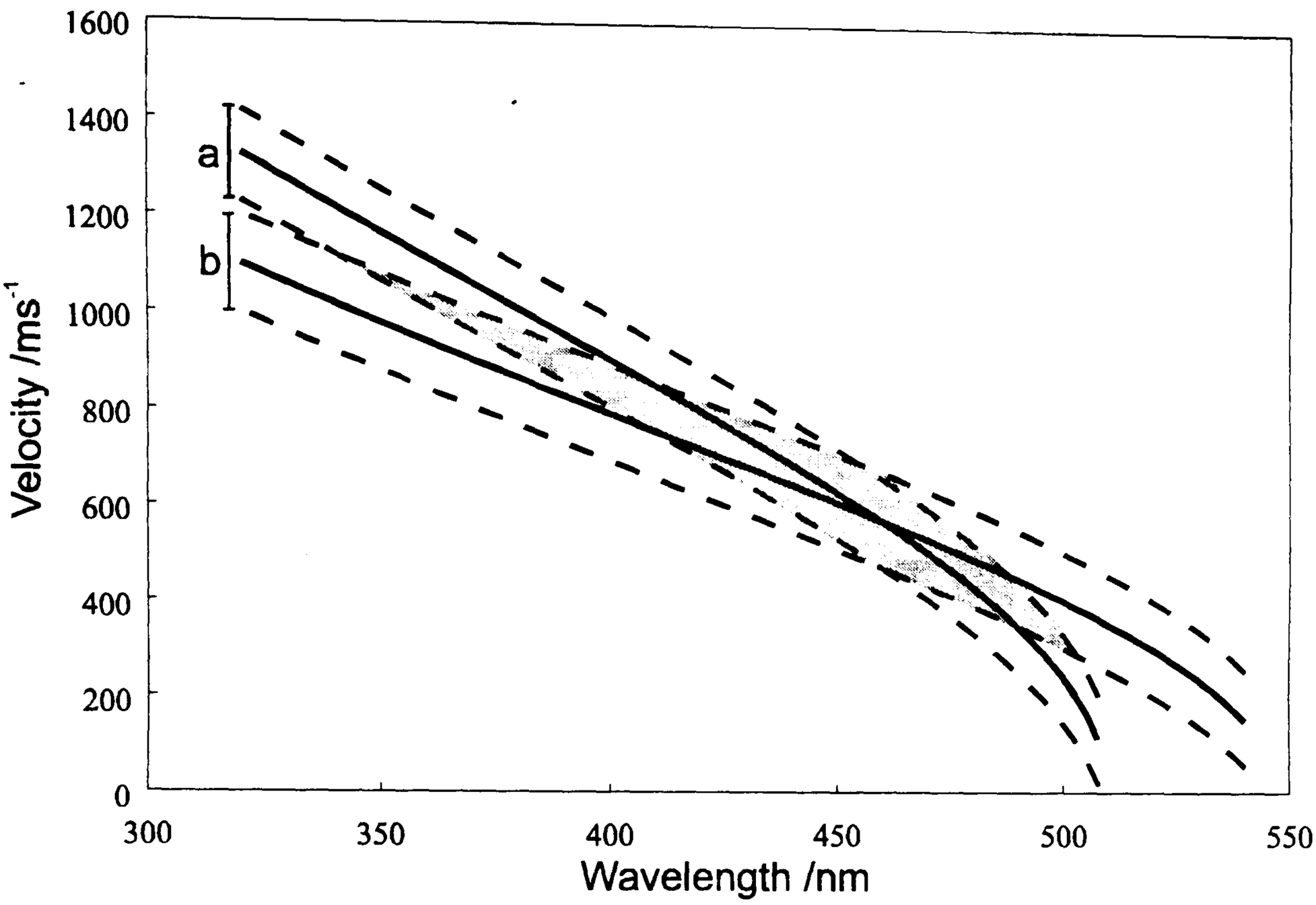

Figure 6.16: Calculated speeds of Br atoms from the two photodissociation processes (a) $Br_2 + h\nu \rightarrow Br + Br^*$ and (b) $BrCl + h\nu \rightarrow Br + Cl$ at wavelengths from 300 to 550 nm plotted as solid lines. The lightly dashed lines about each velocity plot represent the ± 100 m/s instrumental resolution of the ion-imaging experiment. In regions where Br atoms formed from the two processes both have velocities lying within the overlap of the bands defined by the dashed lines (the heavily shaded region), the experiment cannot distinguish Br atoms formed from BrCl or Br_2 photolysis.

6.5 Conclusions

The technique of photofragment ion imaging has been used to study the photodissociation dynamics of BrCl at 26 excitation wavelengths between 235 nm and 540 nm, with detection of Cl, Cl*, Br and Br* atom products. The ion images reveal the spin-orbit states of both fragments at each wavelength and, in addition, the angular distribution of photofragment velocities. Anisotropy parameters for the various $Cl(^2P)$ and $Br(^2P)$ spin-orbit components show extensive variation with wavelength which can be largely understood in terms of excitation to the $A^3\Pi(1)$, $B^3\Pi(0^+)$, $C^1\Pi(1)$ and $D(0^+)$ states as the wavelength is reduced. At wavelengths between 235 nm and 262 nm, where excitation is nominally to the $D(0^+)$ state, predominantly Br* + Cl photofragments formed *via* a parallel transition is seen. Formation of Cl* + Br constitutes a minor channel but exhibits an anisotropy parameter $\beta = -1.0 \pm 0.1$, indicative of an underlying perpendicular transition to a state with $\Omega=1$. Fragmentation to form Br + Cl and Br* + Cl* products is not observed.

Over the wavelength range 540 - 320 nm, corresponding to excitation to the $A^3\Pi(1)$, $B^3\Pi(0^+)$, and $C^1\Pi(1)$ states, no Br* formation is observed. For excitation wavelengths from 320 nm up to 400 nm, dissociation from the $C^1\Pi(1)$ state gives ground state Cl + Br products with an anisotropy parameter of $\beta = -1.0 \pm 0.1$, characteristic of a perpendicular transition. As the photolysis wavelength is increased beyond 400 nm, the onset of excitation to the $B^3\Pi(0^+)$ state is observed, with an associated change in β_{Cl} toward zero and a rise in the value of β_{Br}. The onset of this excitation also coincides with a rapid rise in the yield of Cl* fragments (with $\beta_{Cl^*} \sim 1.0$ to 1.4) which is attributed either to a diabatic dissociation on the $B^3\Pi(0^+)$ state potential to Br + Cl* products through a weakly avoided crossing, or, if the crossing is strongly avoided, to non-adiabatic transitions to another 0^+ state. To all wavelengths longer than 450 nm, β_{Cl} takes values between 0 and –0.2, independent of wavelength, and β_{Cl^*} values remain at ~ 1.2 to 1.4, perhaps showing a slow decline with increasing wavelength. These two observations and the relative yields of Cl* and Cl can be explained in terms of excitation in this wavelength range to both an $\Omega = 0$ and an $\Omega = 1$ state that correlate adiabatically to Cl + Br, with mixing between these states

and possible transfer of flux to a 0^+ state and a repulsive $\Omega = 1$ state that correlate adiabatically with Br + Cl*. It is suggested that the excitations are to the repulsive walls of the $A^3\Pi(1)$ (or $C^1\Pi(1)$ at shorter wavelengths) and $B^3\Pi(0^+)$ states, with approximately equal probabilities, and that either a rotationally-induced transfer of approximately 30% of the dissociating flux between the two curves at the inner, repulsive walls of the potentials, or crossing to states correlating with Br + Cl* *en route* to the atomic asymptotes accounts for the observed anisotropy parameters.

Br images from BrCl photolysis are contaminated by overlapping signal from Br_2 photolysis at wavelengths longer than 400 nm. The measured β_{Br} values can be understood in terms of contributions from the three processes $Br_2 + h\nu \rightarrow Br + Br^*$, $BrCl + h\nu \rightarrow Br + Cl^*$ and $BrCl + h\nu \rightarrow Br + Cl$, with the relative contributions of the latter two dissociations largely consistent with previous measurements of the Cl*/Cl branching ratio.

The analysis of the results highlights some of the many ways in which molecular rotation can complicate the interpretation of photofragment anisotropy parameters. As is well known, rotation can decrease the magnitude of β parameters from the limits expected for parallel or perpendicular transitions, either *via* breakdown of the axial recoil approximation, or if the excitation is to a state with lifetime comparable to or longer than the rotational period. A different influence of molecular rotation is inferred, however, for BrCl photodissociation at wavelengths longer than 450 nm, for which the absorption is assigned to transitions to the $A^3\Pi(1)$ and $B^3\Pi(0^+)$ components of a $^3\Pi$ state. Rotation-induced mixing of the $\Omega = 0$ and $\Omega = 1$ components could substantially reduce the measured β_{Cl} and β_{Cl^*} values, and the molecular rotation might also induce coupling to higher-lying adiabatic states in the exit channel for the dissociation.

In comparison to the previous investigation into Br_2 photodissociation at similar wavelengths, the two molecules have very different photodissociation dynamics. The difference arises because the dissociation dynamics of a molecule are determined by the correlations the excited states posses and the interactions the states

undergo with each other. It is therefore not surprising that the photodissociation dynamics of the two molecules differ so much, as the lower excited states of the molecules have very different interactions and atomic correlations. The main difference in the potential energy curves of the excited states of the molecules is that the $B^3\Pi(0^+)$ state in BrCl has an avoided crossing with a second 0^+ state, which leads to correlation to Cl + Br, whereas in Br_2 the $B^3\Pi_u(0^+)$ state correlates diabatically with the first set of excited state products Br + Br*. This is a consequence of the relaxation in the symmetry considerations that arise when comparing homonuclear and heteronuclear diatomic molecules. This change in correlation behaviour leads to the difference in observed β parameters for the different atomic limits in the two molecules, i.e. in Br_2 the lowest atomic limit (Br + Br) always has a $\beta = -1$, whereas the lowest atomic limit in BrCl (Br + Cl) has a β which evolves with wavelength from -1 to 0.

6.6 References

1 M.C. Heaven, *Chem. Soc. Rev.* **15**, 405 (1986).

2 G. Herzberg, *Molecular Spectra and Molecular Structure I: Spectra of Diatomic Molecules*, Krieger Publishing Company, Florida (1989).

3 D. Maric and J.P. Burrows, *J. Phys. Chem.* **100**, 8645 (1996).

4 S. Hubinger and J.B. Nee, *J. Photochem. Photobiol. A*, **86**, 1 (1995).

5 M.A.A. Clyne and J.A. Coxon, *Proc. R. Soc. London A*, **298**, 424 (1967).

6 M.A.A. Clyne and I.S. McDermid, *J. Chem. Soc. Faraday Trans. II*, **74**, 798 (1978).

7 M.A.A. Clyne and I.S. McDermid, *J. Chem. Soc. Faraday Trans. II*, **74**, 807 (1978).

8 M.A.A. Clyne and I.S. McDermid, *Faraday Disc. Chem. Soc.* **67**, 316 (1979).

9 M.A.A. Clyne and L.C. Zai, *J. Chem. Soc. Faraday Trans. II*, **78**, 1221 (1982).

10 S.W. Brown, C.J. Dowd and J. Tellinghuisen, *J. Mol. Spectrosc.* **132**, 178 (1988).

11 J. Tellinghuisen, *J. Chem. Phys.* **89**, 6150 (1988).

12 J. Tellinghuisen, *J. Mol. Spectrosc.* **173**, 223 (1995).

13 J. Cao, H.P. Loock and C.X.W. Qian, *Can. J. Chem.* **72**, 758 (1994).

14 M.S. Child and R.B. Bernstein, *J. Chem. Phys.* **59**, 5916 (1973).

15 M.S. Child, *Mol. Phys.* **32**, 1495 (1976).

16 M.S. deVries, N.J.A. van Veen and A.E. deVries, *Chem. Phys. Lett.* **56**, 15 (1978).

17 H.K. Haugen, E. Weitz and S.R. Leone, *J. Chem. Phys.* **83**, 3402 (1985).

18 K. Tonokura, Y. Matsumi, M. Kawasaki, H.L. Kim, S. Yabushita, S. Fujimura and K. Saito, *J. Chem. Phys.* **99**, 3461 (1993).

19 L.J. Rogers, M.N.R. Ashfold, Y. Matsumi, M. Kawasaki and B.J. Whitaker, *Chem. Phys. Lett.* **258**, 159 (1996).

20 T.P. Rakitzis and R.N. Zare, private communication.

21 S. Arepalli, N. Presser, D. Robie and R.J. Gordon, *Chem. Phys. Lett.* **118**, 88 (1985).

22 S. Arepalli, N. Presser, D. Robie and R.J. Gordon, *Chem. Phys. Lett.* **117**,

64 (1985).

23 K. Balasubramanian, *J. Mol. Spectrosc.* **110**, 339 (1985).

24 R.J. Oldman, R.K. Sander and K.R. Wilson, *J. Chem. Phys.* **63**, 4252 (1975).

25 G.E. Busch and K.R. Wilson, *J. Chem. Phys.* **56**, 3638 (1972).

26 C. Jonah, *J. Chem. Phys.* **55**, 1915 (1971).

27 R.N. Zare, *Angular Momentum. Understanding spatial aspects in physics and chemistry*, (Wiley, New York, 1988).

28 H. Lefebvre-Brion and R.W. Field, *Perturbations in the spectra of diatomic molecules*, (Academic Press, Orlando 1986).

29 K.P. Huber and G. Herzberg, *Molecular Spectra and Molecular Structure, IV. Constants of Diatomic Molecules* (van Nostrand Reinhold, New York 1979).

30 M.J.Cooper, A.J. Orr-Ewing and M.N.R. Ashfold, to be published.

Appendix A

A.1 Transformation of 2D Images into 3D Distributions

The mathematical reconstruction of the initial 3D ion distribution from the recorded 2D image is achieved by using the filtered back-projection method.[1,2] This method assumes that the image is cylindrically symmetric about the z axis, which is defined along the polarization vector of the dissociating laser beam. In all the images shown in this work this vector is aligned vertically in the plane of the image. The x axis is defined as being perpendicular to the z axis, but also lying in the plane of the image. The image reconstruction is performed by breaking the 2D image up into horizontal rows and mathematically transforming each one. The addition together of all the row by row transformations results in the construction of the 3D distribution from the 2D image. The details of the mathematical transformation are as follows.

The intensity distribution of one row of the 2D image along the x axis is $p(x)$, and the intensity distribution of the corresponding row across the 2D slice through the 3D distribution is $q(r)$, where $r \equiv \sqrt{x^2 + y^2}$. Therefore the function $p(x)$ is the 2D projection of the function $q(r)$ rotated about the z axis, i.e.:

$$p(x) = \int_{-\infty}^{\infty} q(x^2 + y^2)^{1/2} dy \,. \tag{A.1}$$

In polar co-ordinates (A.1) becomes,

$$p(x) = 2\int_{x}^{\infty} \frac{q(r) r dr}{\sqrt{r^2 - x^2}} \tag{A.2}$$

with the Fourier transform $P(\xi)$, of $p(x)$ given by,

$$P(\xi) = \int_{-\infty}^{\infty} p(x) \exp(-i\xi x) dx \,. \tag{A.3}$$

where ξ is the frequency co-ordinate in Fourier space which corresponds to the x co-ordinate in position space.

The filter back-projection method is then employed to create the 2D slice through the 3D distribution $q(r)$, from the 2D projection $p(x)$. This transform is achieved by defining the inverse Fourier transform of $|\xi|P(\xi)$ as,

$$s(x) = \int_{-\infty}^{\infty} |\xi| P(\xi) e^{i\xi x} d\xi = 2\int_{0}^{\infty} \xi P(\xi) e^{i\xi x} d\xi \qquad \text{(A.4)}$$

where $P(\xi)$, the Fourier transform of $p(x)$, is an even function around the origin $\xi = 0$. Substituting the variables then leads to the final 3D distribution, $q(r)$,

$$q(r) = \frac{1}{2\pi}\int_{-x}^{x} \frac{s(x)}{\sqrt{r^2 - x^2}} dx = \frac{1}{\pi}\int_{0}^{\pi/2} s(r\cos\theta) d\theta \qquad \text{(A.5)}$$

were the identity $x = r\cos\theta$ is used.

The entire calculation shown above is automated by the IMAGE6 computer program written by Prof. Y. Matsumi of the University of Nagoya, Japan. Figure A.1 illustrates the mathematical transformation process used by the program. (a) shows the smoothed and symmetrised 2D recorded image, in this case of Cl atoms from Cl_2 photodissociation at 355 nm. (b) shows the final 2D slice through the reconstructed 3D distribution, made by mathematically transforming individual rows of the 2D image. (c) shows the result of the transformation on the intensity distribution from one of the rows of the 2D image into the corresponding row of the 3D distribution.

A.2 References

1 T.F. Budlinger and G.T. Gullberg. *IEEE Trans. Nucl. Sci.* **NS-21**, 2 (1974)

2 Y. Sato, Y. Matsumi, M. Kawasaki, K. Tsukiyama and R. Bersohn, *J. Phys. Chem.* **99**, 16307 (1995).

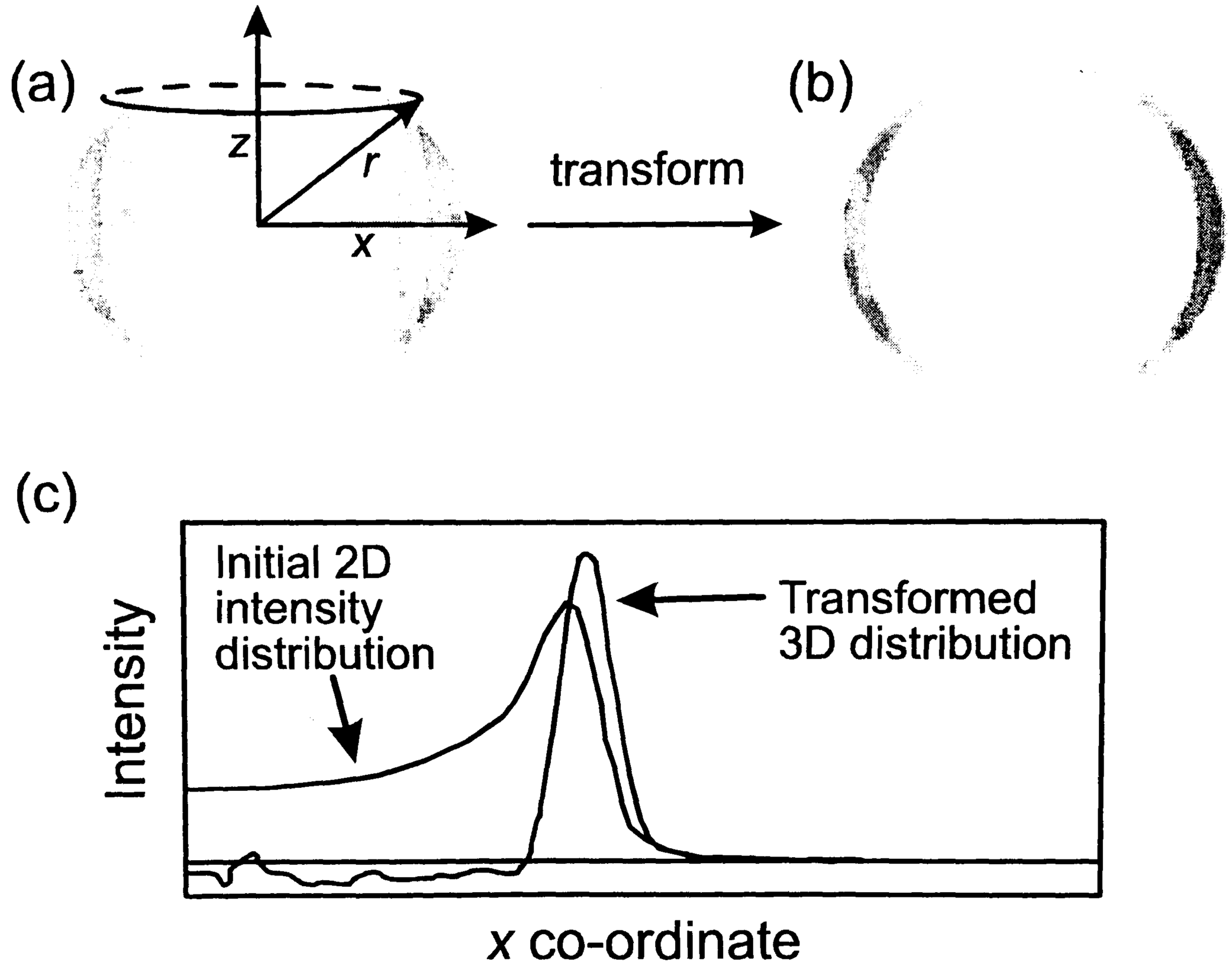

Figure A.1: The raw image in (a) is transformed by the IMAGE6 program line by line into the 2D slice through the 3D reconstruction shown in (b). The initial and final intensity distributions for a particular line of data across the raw image are shown in (c).

Appendix B: Wigner - Witmer Rules

The Wigner - Witmer rules[1] are used to determine the molecular states that correlate to a given combination of atomic states of two separate atoms. These correlations rigorously correct provided the states follow the adiabatic potential energy curves. The rules are separated into those for two unlike atoms, and for those for two like atoms were the effect of whether the states are odd or even have to be accounted for.

B.1 Unlike Atoms

B.1.1 Determination of Molecular Orbital Angular Momentum, Λ

The approach of two atoms to one another, which have total atomic orbital angular momentum L_1 and L_2, and total atomic spin angular momentum S_1 and S_2, creates an inhomogenous electric field. The electric field created has the effect of space quantising L_1 and L_2 into their projections onto the molecular axis, M_{L1} and M_{L2}. This results in a total molecular orbital angular momentum, Λ, given by:

$$\Lambda = |M_{L1} + M_{L2}|. \qquad \text{(B.1)}$$

Combination of all possible M_{Li} values, results in the production of all possible molecular Λ values. The resulting values of Λ correspond to different energies of the molecular states in the electric field. As the electric field increases in magnitude, i.e. as the atoms move closer together, the difference in energy between the different Λ values will increase. These facts led to the conclusion that from a pair of separated atoms in a particular combination of atomic states, the value of Λ derived from the coupling of the different M_{Li} values can have some meaning at short internuclear distances, where the atomic values of L_i and M_{Li} are meaningless.

Consider the example of $Cl(^2P)$ approaching $O(^3P)$ to form the molecule ClO. In this case M_{L1} and M_{L2} both have the values +1, 0, -1, as L is 1 for both atoms. Figure A.1 illustrates the combination of these M_{Li} values to give different values of Λ.

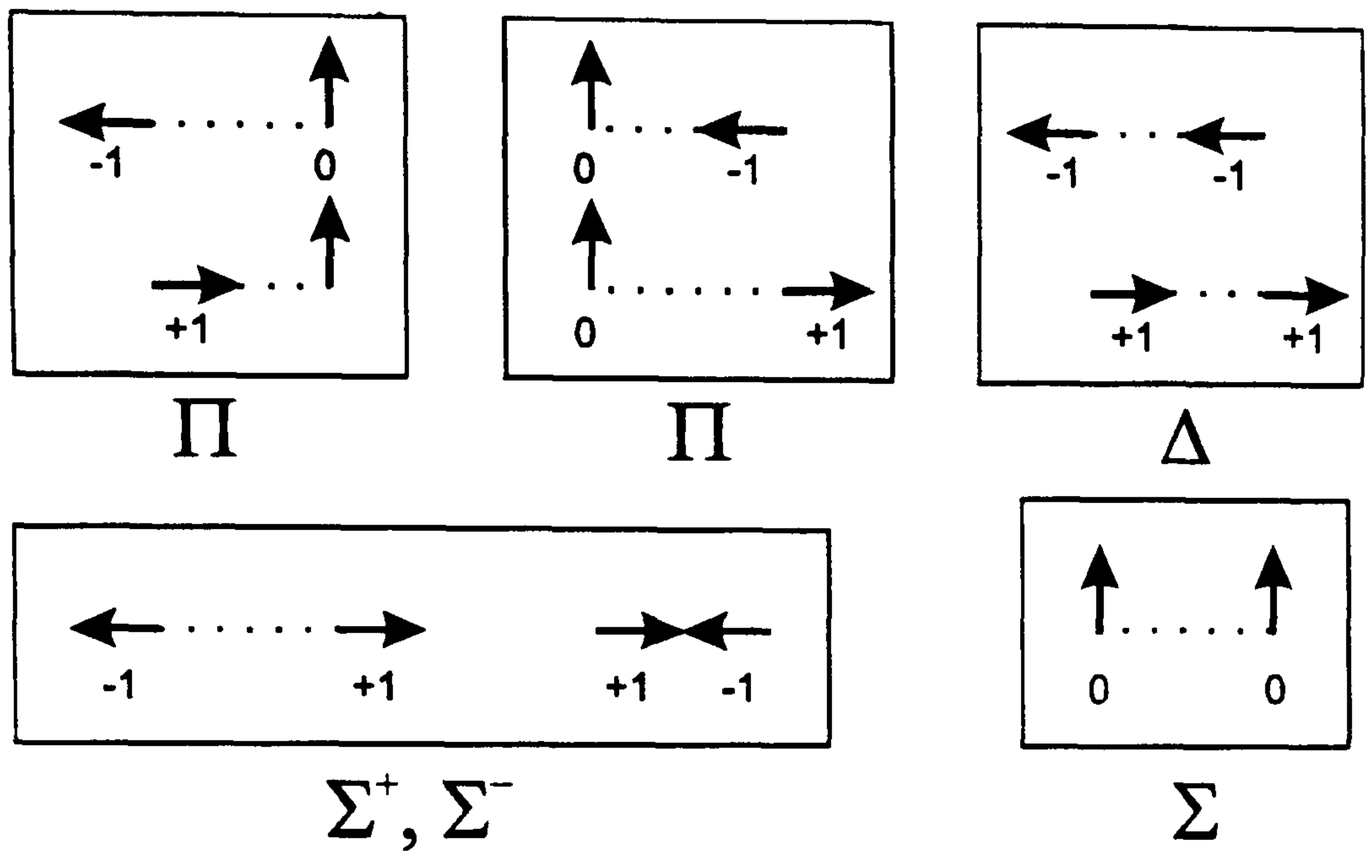

Figure B.1: Vector diagram showing the different values of L, and hence molecular states derived from the combination of $Cl(^2P)$ and $O(^3P)$ atoms.

There are nine possible values of Λ, +2, +1 (x2), 0 (x3), -1 (x2), and -2, which result in a Δ state, two Π states and three Σ states. It is important to note that two states which differ only in the sign of both M_{L1} and M_{L2} have equal energy and are degenerate. Of the three Σ states determined above, one will be Σ^+, and one Σ^-, but the symmetry of the final Σ state cannot be determined by elementary means. From ref. 1, the state will be Σ^+ when $L_1 + L_2 + \Sigma l_{i1} + \Sigma l_{i2}$ is even, and Σ^- when this sum is odd. Therefore the symmetry of the Σ state will depend on the L values of the two atoms involved as well as if the atomic states have odd or even value of atomic parity l. For $Cl(^2P) + O(^3P)$ the above sum will be 1 + 1 + 7 + 6 = 15 (i.e. odd), so the single Σ state will be Σ^-.

B.1.2 Determination of Molecular Spin, *S*.

The determination of the molecular multiplicity, given by $2S+1$, is slightly more straightforward. As spin is not effected by the electric field created by the two atoms approaching each other, the overall values the molecular spin, S, can take are just the vector sums of the two spin vectors of the separated atoms, i.e.:

$$S = (S_1 + S_2), (S_1 + S_2 - 1), (S_1 + S_2 - 2), \ldots\ldots, |S_1 - S_2|. \qquad \text{(B.2)}$$

For a given value of Λ, all the values of S are possible. Using again the example of $Cl(^2P)$ approaching $O(^3P)$, S will take the values 4 and 2; a quartet and a doublet.

Overall the combination of $Cl(^2P)$ and $O(^3P)$ will give twelve different states; $^4\Sigma^+$, $^2\Sigma^+$, $^4\Sigma^-$ (x2), $^2\Sigma^-$ (x2), $^4\Pi$ (x2), $^2\Pi$ (x2), $^4\Delta$, and $^2\Delta$.

B.1.3 Determination of Electronic Angular Momentum, Ω.

In the case where coupling between S and L in the separated atoms is strong in comparison to the coupling of L to the internuclear axis, then space quantization of J rather than L takes place in the electric field produced by the approaching atoms. The electric angular momentum Ω (which includes spin) is then defined as:

$$\Omega = |M_{J1} + M_{J2}| \qquad \text{(B.3)}$$

which is analogous to the definition of Λ in (A.1). For every combination of two M_J values there corresponds a different molecular state, except in the case where the two values differ only in sign, where they form a degenerate pair. In this regime Hund's case (c) usually applies, i.e. Only Ω and not Λ is defined.

B.2 Like Atoms

In the case of two like atoms approaching each other the same above rules apply for determining the overall values that Λ and S can take. In the case of homonuclear diatomics, however, the symmetry of the molecular states, with respect to the centre of inversion, must also be determined, either *gerade, g*, or *ungerade, u*.

When two like atoms approach each other and are in different atomic states, twice as many molecular states are produced as in the unlike atom case. This is because each molecular state is derived using exactly the same rules described above but is now split into two, a *g* and a *u*.

In the case of two like atoms which are both in the same atomic state, the resulting states are as derived for the unlike case, but some will be *g*, and some *u*. As in the case of the symmetry of the lone Σ state above, calculating which states are what is not an elementary task, but the results for various common combinations of atomic states have been determined and tabulated for reference.[1,2]

B.3 References

1 E. Wigner and E.E. Witmer, *Z. Physik*, **51**, 859 (1928).

2 G. Herzberg, *Molecular Spectra and Molecular Structure I: Spectra of Diatomic Molecules*, Van Nostrand Reinhold Company, New York (1950).

Appendix C: Ion Pair State Vibrational Level Analysis

A vibrational level, i.e. rotationless, analysis was performed on the S_2 experimental data as a full rotational analysis of the states proved difficult due to the lack of available information. The analysis was performed by calculating initial RKR potentials for the 4 ion pair states, $^5\Pi_g$, $^5\Sigma_g^-$, $^3\Pi_g$ and $^3\Sigma_g^-$ using the molecular state constants from the deperturbation analysis. From these RKR curves the positions and wavefunctions of the vibrational levels of each state were calculated. The calculated positions of the levels were then compared and fitted to the experimental data by varying the RKR coefficients using a least squares fitting process. Excited state interactions were modelled as a single value which was then scaled by the Franck-Condon overlap and energy gap between the states. The whole fitting process was automated by using the program DIMODEL written by Dr. Colin Western.

C.1 The Lower States

Initially the fitting process centred on the lower vibrational levels ($v = 0$ to 9) of the $^5\Sigma_g^-$ ion pair state. These levels are all very regular and are only slightly perturbed by the higher lying states. The fitted RKR curve for this state was almost identical to that initially derived from the constants alone. Figure C.1 shows the magnitude of the error in the calculated positions of the three Ω components of the vibrational levels as compared to the experimental data for two separate fits. Plot (a) shows the errors with interactions with neighbouring states in place, whereas (b) plots illustrates errors without. Clearly including the interactions reduces the errors dramatically especially for the higher vibrational levels which lie closer in energy to the perturbing states. In this case only the interaction with the $^3\Pi_g$ state was varied, with the other state interactions included but held at the values calculated by the ion pair state model. The fitted value of the $^5\Sigma_g^- - ^3\Pi_g$ interaction was 272.17 cm^{-1}, compared with 441 cm^{-1} as calculated by the ion pair model and 278.16 cm^{-1} as the average value of the experimental data. It is important to notice the similarity between the value from

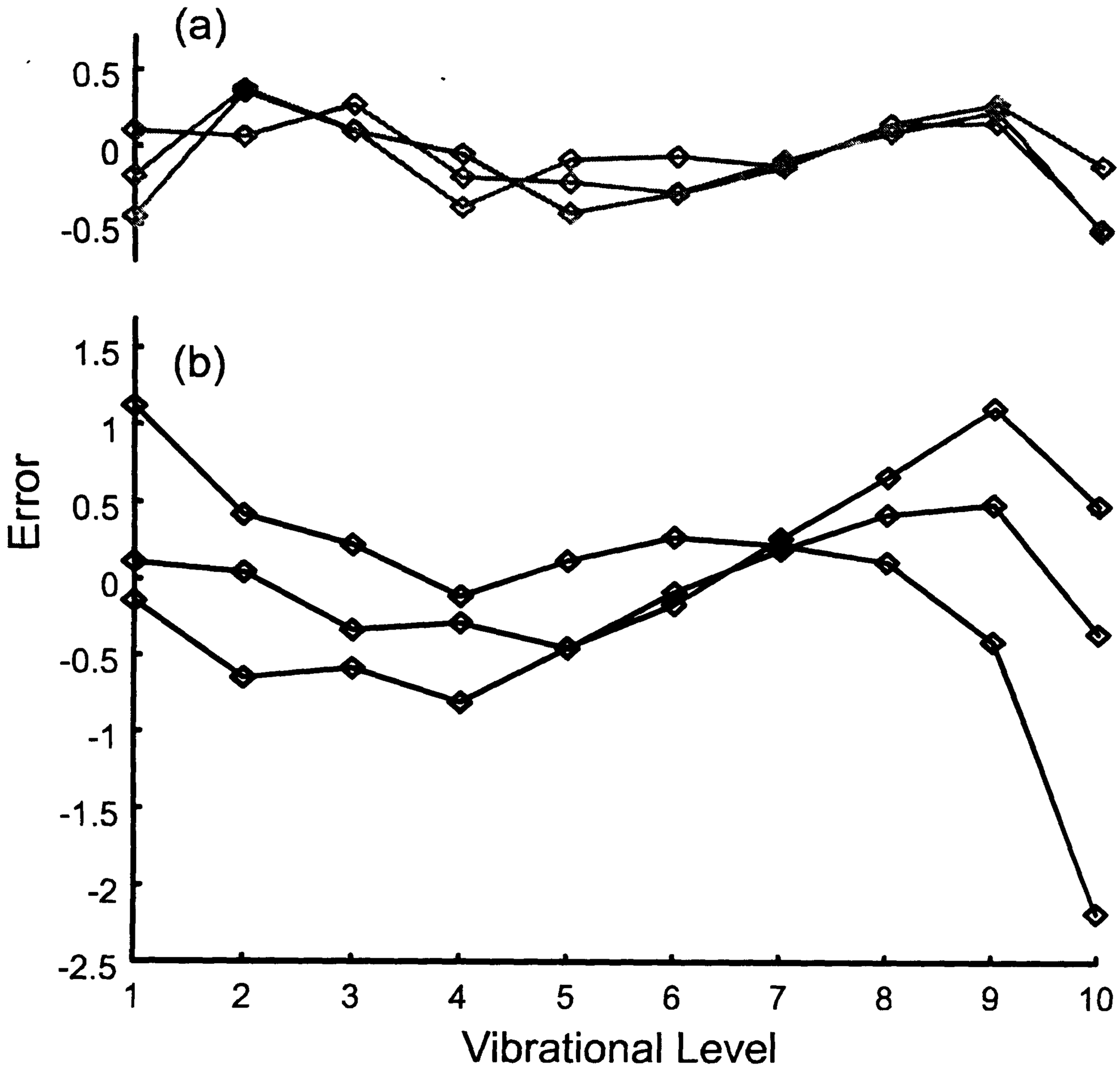

Figure C.1: Error plots from the fit of the lower vibrational levels, v = 0 to 9 of the $^5\Sigma_g^-$ ion pair state. The fit shown in (a) includes interactions with other ion pair states, whereas (b) does not.

this fit and the average value from the experimental data, which included data on higher vibrational levels.

C.2 The Higher States

In the case of the higher lying vibrational levels, again, the lack of data precluded a full analysis. A fit was performed including $v = 0$ - 13 of the $^5\Sigma_g^-$ state and $v = 0$ - 2 of the $^3\Pi_g$ state. Again the RKR curves produced were very similar to those previously calculated. The perturbation interaction between the $^5\Sigma_g^-$ and $^3\Pi_g$ state in this case rose slightly, compared to the previous lower state fit, to 286.40 cm^{-1}.

C.3 Conclusions

The method of analysing the experimental data by calculating and fitting to RKR curves has proven successful, but has not provided any extra insight into the ion pair state spectra then the previous methods. A full analysis of the ion pair spectra can be performed by any of these measures in the future, once a more complete set of data has been obtained on the higher lying electronic states.

Appendix D: Rotational Hamiltonian Operator and Spin-Orbit Interactions

D.1 Rotational Hamiltonian Operator

The rotational part of the Hamiltonian is given as:

$$\mathbf{H}^{\mathbf{ROT}} = (1/2\mu R^2)\mathbf{R}^2 \qquad \text{(D.1)}$$

where **R** is the nuclear rotation angular momentum operator. The total angular momentum, **J**, is defined as:

$$\vec{\mathbf{J}} \equiv \vec{\mathbf{R}} + \vec{\mathbf{L}} + \vec{\mathbf{S}} \qquad \text{(D.2)}$$

which can then be used to express $\mathbf{H}^{\mathbf{ROT}}$ in its more conventional form:

$$\mathbf{H}^{\mathbf{ROT}} = (1/2\mu R^2)[(\mathbf{J}_x - \mathbf{L}_x - \mathbf{S}_x)^2 + (\mathbf{J}_y - \mathbf{L}_y - \mathbf{S}_y)^2 \qquad \text{(D.3)}$$

$$= (1/2\mu R^2)[(\mathbf{J}^2 - \mathbf{J}_z^2) + (\mathbf{L}^2 - \mathbf{L}_z^2) + (\mathbf{S}^2 - \mathbf{S}_z^2) + \qquad \text{(D.4)}$$

$$(\mathbf{L}^+\mathbf{S}^- + \mathbf{L}^-\mathbf{S}^+) - (\mathbf{J}^+\mathbf{L}^- + \mathbf{J}^-\mathbf{L}^+) - (\mathbf{J}^+\mathbf{S}^- + \mathbf{J}^-\mathbf{S}^+)].$$

The first three terms of $\mathbf{H}^{\mathbf{ROT}}$ have only diagonal matrix element terms. The diagonal part of $\mathbf{H}^{\mathbf{ROT}}$ is the rotational energy of the $|JM\Omega\Lambda S\Sigma\rangle$ basis function, which then results in the rotational equation:

$$(1/2\mu R^2)[(\mathbf{J}^2 - \mathbf{J}_z^2) + (\mathbf{L}^2 - \mathbf{L}_z^2) + (\mathbf{S}^2 - \mathbf{S}_z^2)] = \mathbf{E}^{\mathbf{ROT}}(R)|JM\Omega\rangle. \qquad \text{(D.5)}$$

Integration of (D.5) over the vibrational co-ordinate leads to:

$$\mathbf{E}^{\mathbf{ROT}}(\nu,J) = B_\nu[J(J+1) - \Omega^2 + S(S+1) - \Sigma^2]. \qquad \text{(D.6)}$$

The above equations (D.5) and (D.6) make up one form of the Born-Oppenheimer approximation for the rotational part of the Hamiltonian, where the final three terms in equation (D.4) are ignored. These terms lead to coupling between the orbital, spin and

total angular momenta which results in perturbations between different electronic states.

a) $+(1/2\mu R^2)\mathbf{L}^{\pm}\mathbf{S}^{\mp}$ results in homogeneous spin-electronic perturbations between basis functions with the same value of Ω and S, but different values of Λ and Σ.

b) $-(1/2\mu R^2)\mathbf{J}^{\pm}\mathbf{S}^{\mp}$ results in heterogeneous electronic-rotational perturbations between basis sets of different Ω, which have identical values of S and Λ, but different values of Σ. This operator is known as the **S**-uncoupling operator.

c) $-(1/2\mu R^2)\mathbf{J}^{\pm}\mathbf{L}^{\mp}$ results in heterogeneous electronic rotational perturbations between states of different Ω, which have identical values of S and Σ, but different values of Λ. This operator is known as the **L**-uncoupling operator.

It is the **S**-uncoupling operator listed in b) that leads to mixing between the $^3\Pi_1$ and $^3\Pi_0$ states in BrCl. Consideration of the S-uncoupling operator leads to the equation:

$$\begin{aligned} &\langle {}^{2S+1}\Lambda_{\Omega,v}|-B(\mathbf{J}^{+}\mathbf{S}^{-}+\mathbf{J}^{-}\mathbf{S}^{+})|{}^{2S+1}\Lambda_{\Omega+1,v+1}\rangle \\ &\quad = -B[J(J+1)-(\Omega+1)\Omega]^{1/2} \\ &\quad \times[S(S+1)-(\Omega-\Lambda-1)(\Omega-\Lambda)]^{1/2} \end{aligned} \qquad \text{(D.7)}$$

Equation (D.7) shows that the interaction caused by the **S**-uncoupling operator will be J dependant, and so be greater for states with a larger value of J.

D.2 Spin-Orbit Interactions

Perturbations between different electronic states also arise from considerations of the electronic Hamiltonian. One for the most important terms arises from the interaction between the spin and orbital angular momentum of the nuclei and the

electrons of the molecule. This is known as the spin-orbit operator, $\mathbf{H}^{SO}$, and it has the form:

$$\mathbf{H}^{SO} = \sum_i \hat{a}_i \mathbf{l}_i \bullet \mathbf{s}_i \qquad \text{(D.8)}$$

where:
$$\hat{a}_i \mathbf{l}_i = \sum_K \frac{\alpha^2 Z_{eff,K}}{2r_{iK}^3} \mathbf{l}_{iK} . \qquad \text{(D.9)}$$

$\mathbf{l}_{iK}$ is the orbital angular mometum of electron *i* about nucleus K and $Z_{eff,K}$ is the effective charge of the K^{th} nucleus. An effective charge is used as the nuclear charge seen by electron *i* is screened by other electrons by typically 20 - 50%. The selection rules for matrix elements of $\mathbf{H}^{SO}$ are as follows:

$\Delta J = 0$ $\quad \Delta\Omega = 0 \Delta S = 0$ or ± 1 $\quad \Delta\Lambda = 0$ or ± 1

$g \not\leftrightarrow u$ $\quad e \not\leftrightarrow f$ $\quad \Sigma^+ \leftrightarrow \Sigma^-$

Therefore the $\mathbf{H}^{SO}$ operator has the effect of mixing together states that differ in Λ or *S* by up to 1, but have the same Ω. One of the important consequences of this interaction is the that formally spin forbidden transitions can now take place. The $\mathbf{H}^{SO}$ interaction is what mixes the same Ω components of the $^5\Sigma_u^-$ and $^3\Pi_u$ valence states and the $^5\Sigma_g^-$ and $^3\Pi_g$ ion pair states in S_2.